



FILTRATION MODELING USING ARTIFICIAL NEURAL NETWORK (ANN)

By Dr. Awatif Soaded Alsaqqar

University of Baghdad/ College of Engineering/ Civil Engineering Dept.

ABSTRACT

In this research Artificial Neural Network (ANN) technique was applied to study the filtration process in water treatment. Eight models have been developed and tested using data from a pilot filtration plant, working under different process design criteria; influent turbidity, bed depth, grain size, filtration rate and running time (length of the filtration run), recording effluent turbidity and head losses. The ANN models were constructed for the prediction of different performance criteria in the filtration process: effluent turbidity, head losses and running time. The results indicate that it is quite possible to use artificial neural networks in predicting effluent turbidity, head losses and running time in the filtration process, with a good degree of accuracy reaching 97.26, 95.92 and 86.43% respectively. These ANN models could be used as a support for workers in operating the filters in water treatment plants and to improve water treatment process. With the use of ANN, water systems will get more efficient, so reducing operation cost and improving the quality of the water produced.

KEY WORDS: Artificial Neural Network, modeling, water treatment, filtration, turbidity, head losses, running time.

الخلاصة

في هذا البحث جرى تطبيق تقنية الشبكات العصبية الاصطناعية لدراسة عملية الترشيح في معالجة المياه. بنيت ثمانية نماذج و اختبرت باستعمال النتائج العملية من منظومة ريادية للترشيح والتي تعمل تحت ظروف تصميمية: الكدرة، عمق المرشح، حجم مادة الترشيح، سرعة الترشيح و فترة الترشيح و تسجيل الكدرة للماء الراشح والفقدان في الشحنة. هذه النماذج بنيت للتنبؤ بعكورة الماء الراشح، الفقدان في الشحنة و فترة الترشيح. وأظهرت النتائج بان هذه النماذج لها القابلية للتنبؤ بدرجة كبيرة تصل إلى 97.26% للكعورة، 95.92% لفقدان بالشحنة و 86.43% لفترة الترشيح. هذه النماذج تساعد الفنيين في تشغيل المرشحات في محطات معالجة المياه و لتحسين عمليات المعالجة. استعمال تقنية الشبكات العصبية الاصطناعية، تجعل هذه الأنظمة كفوءة وبذلك تنخفض كلفة التشغيل وتحسين نوعية الماء الناتج.

INTRODUCTION

Hard work has been done to predict the relationship between water quality parameters and the most efficient points in water treatment plants. The progress in such work was carried out using multi varied regressions. Nowadays artificial intelligence techniques such as Artificial Neural Networks (ANNs) and Genetic Algorithms can contribute for optimizing performance and operation in water treatment plants (Fernandez and Galvis, 2002).

Over the past two decades, there has been an increased interest in the new class of intelligent systems known as the Artificial Neural Networks (ANNs). These networks are found to be powerful tools for organizing and correlating information in ways, which have proved to be useful for solving problems too complex to understand, too poorly to analyze or too resource-intensive to tackle using more traditional computational methods (TRB, 1999). ANNs have a wide range of scientific applications among them is in different engineering aspects.

In river sanitation, Stewart used ANN for predicting dissolved oxygen concentrations in the Tualatin River, Oregon, USA. The ANN model was constructed using air temperature, solar radiation, rainfall and stream flow as input data. The model predicted the dissolved oxygen concentrations with acceptable accuracy and high correlation reaching 0.83 and absolute error less than 0.9 mg/l (Stewart, 2002). Kanani and his team used multi layer perception (MLP) neural network and input delay neural network (IDNN) for predicting total dissolved solid (TDS) in the Achechay River in Iran. The two models showed acceptable precision

in predicting TDS in the study area and the results can be utilized in optimized management and planning of water recourses (Kanani et al., 2008).

Another application of ANN is the modeling of water distribution systems. In 2003, a team of engineers made use of linear regression models and multi layer perceptron artificial neural networks, to predict chlorine concentrations in the Hope Valley water distribution system, located in Adelaide, south of Australia. The inputs required to feed the models were, WTP chlorine concentration, WTP water temperature, WTP flow, chlorine concentration at the inlet tank and water temperature and chlorine concentration at the sampling points in the distribution system. The multi layer perceptron ANN was found to consistently outperform traditional linear regression models (Gibbs et al., 2003). The ANN can be an online tool to aid in the determination of the required chlorine dosing rates in water distribution network. Another case study was conducted by Memon and his group in 2008 for the prediction of the electrical conductivity (EC) in drinking water flowing in the network of Hyderabad, Pakistan. In this study a Radial Basis Function (RBF) network was applied. The model had the powerful looming of predicting EC in the flowing water, taking into account the parameters turbidity, pH, chloride and alkalinity at the sampling points as input data in the network (Memon et al. in 2008).

In water treatment, ANN was used in some aspects also. Nicolas and Thierry applied ANN techniques for coagulation control in the drinking water treatment plant of Viry-Chatillon near Paris, France. They developed a software sensor including a self organizing map (SOM) for

sensor data validation and missing data reconstruction, and a multi layer perceptron (MLP) for modeling the coagulation process. The important objective of this study is to automatically validate the sensor measurements to provide reliable inputs to the automatic coagulation control system (Nicolas and Thierry, 2001). In 2002, Fernandez and Galvis showed that ANNs are capable of identifying usable relationships between optimal doses of coagulants and inflow water quality in Puerto Mallarino water treatment plant in Cali. According to the results the online ANN model implementation, in real time, coupled with the alum ejector of the plant, could save around 10% in alum dosage applied in the coagulation process (Fernandez and Galvis, 2002).

In this study the ANN technique is used in modeling the filtration process in rapid sand filters in drinking water treatment plants. Filtration is considered a polishing process which removes the remaining colloidal particles from water. The main objective of this process is to reduce the turbidity of water to drinking water specifications providing long filtration runs with low head losses. These ANN models may help to control the filtration process and improve the performance of the system.

ARTIFICIAL NEURAL NETWORKS (ANNs)

ANN models are specified by network topology, node characteristics and training or learning rules. It is an interconnection set of weights that contains the knowledge generated by the model (Hafizan et al., 2004). Different types of ANNs exist; the most common type is the feed forward network termed the multilayer perceptron. In this network, the artificial neurons or

processing units are arranged in a layered configuration as shown in Figure 1:

Input layer - connecting the input information to the network.

Hidden layer (one or more) – acting as the intermediate computational layer.

Output layer – producing the desired output.

Units in the input layer introduce normalized or filtered values of each input into the network. Units in the hidden and output layers are connected to all of the units in the preceding layer. Each connection carries a weighting factor. The weighted sum of all inputs to a processing unit is calculated and compared to a threshold value. An activation signal then is passed through a mathematical transfer function to create an output signal that is sent to processing units in the next layer. Training an ANN is a mathematical exercise that optimizes all of the network weights and threshold values, using some fraction of the available data. ANN learns as long as the input data set contains a wide range of patterns that the network can predict. The final model is likely to find those patterns and successfully use them in its prediction (Stewart, 2002).

CASE STUDY

Preliminary design of rapid filters in water treatment consists, of several tasks including (Crittenden et al., 2005):

- Performance criteria such as, effluent water quality mainly turbidity, filter run length and recovery (ratio of net to total water filtered).
- Selecting process design criteria such as, required level of pretreatment (influent turbidity), filter media type, size & depth, filtration rate and available head.

Filter efficiency is a function of these design criteria and the best way to determine the factors that influences this process is by a pilot plant study (Qasim et al., 2000). The data required as inputs to the ANN models were collected from filtration pilot plants. In such plants the filtration units are columns of different materials, glass or plastic that contain the filter media. In this study, Iraqi sand used in water treatment plants, was tested under different working conditions. Table 1 describes the case study which was selected as the input data for the ANN models.

A total number of 15 filtration runs were performed testing the filtration process, recording effluent turbidity and head losses under different process design criteria; influent turbidity, bed depth, grain size, filtration rate and running time (length of the filtration run). The operation of a filter must focuses on head loss, filter run length and effluent turbidity. Improper operation of filtration units can result in poor quality of the filtered water and may damage the filter bed.

ARTIFICIAL NEURAL NETWORKS (ANN) MODELS

Several neural network software are available; Neuframe 4 has been used in this study. Three ANN models were constructed for the prediction of different performance criteria in the filtration process: prediction of effluent turbidity, prediction of the head loss and prediction of the length of the filter run.

-Effluent water quality (turbidity)

The most common measurement of particulate matter in water is turbidity. Filtered turbidity can vary due to changes in raw water quality and utilities need some latitude to respond to these changes.

Most utilities set their turbidity goal below 0.3 NTU with a typical goal being 0.1 NTU (Crittenden et al., 2005).

- Head loss

Throughout a filter run, solid particles are deposited in the pores of the filter bed and cause a decrease in the porosity and an increase in the head loss through the filter bed. The head loss at the end of the filter run is to be calculated when designing the filter. This could be done using some empirical equations depending on the porosity at the end of the filter run. The maximum head loss in rapid filters may reach 2 to 3 m. Accurate estimates of head loss values can be determined from pilot plant studies (Qasim et al., 2000).

-Filters run length (running time)

The length of the filter runs dictates how often backwashes must be performed and has an impact on recovery. The frequency of washing has a direct impact on the quantity of labor involved in filter operation. Typically the minimum filter run is one day, with some designs it is also common to reach four days (Crittenden et al., 2005).

The first step for the determination of ANN model is the selection of the data to be the input variables, they were provided from the pilot plant as mentioned in Table 1. The data for each model is shown in Table 2.

The data have to be divided to three sets, training, testing and validation. This step is achieved by trial and error to select the best division with respect to the lowest testing error followed by training error and high correlation coefficient of the validation set. The general strategy adopted for finding the optimal network architecture and internal parameters that control the training process is by trial and

error using the default parameters of the software. In this step first the nodes of the hidden layer are increased until no significant improvement is gained in the model performance. Then the model is tested by changing the default parameters of the software, the momentum term which is 0.8 and the learning rate 0.2. Finally the transfer functions of the input and hidden layers are tested where the default functions of the software are, linear in the input layer and sigmoid in the hidden layer. The default alternatives of the software are to test the following functions: linear, sigmoid and hyperbolic tangent (tanh). The effect of the different combinations of these parameters is summarized in Table 3 which shows the best model performance recording the lowest testing error and the highest correlation coefficient. In each step the testing errors were recorded and the reduction percentages were calculated to see how the improvement is gained in the model performance, this is shown in Table 4.

RESULTS AND DISCUSSION

Prediction of Effluent turbidity

Three models were determined for the prediction of the effluent turbidity of the filtered water which is illustrated in Table 3. All models had one hidden layer but with different number of nodes. In model tur and tur3 one node was used and two nodes in tur2 were required. The momentum rate was high, reaching 0.98 and 0.92 in models tur and tur2 respectively; these values are higher than the default value of the software 0.8 (momentum rate represents the weight change which is in a direction that is a combination of the current gradient descent. This approach is beneficial when some training data are very different from

the majority of the data. The momentum rate is added to obtain a faster convergence. Sivanandam and Paulraj, 2004). The learning rate values were around the default 0.2 only in model tur2 it reached 0.7 (weight changes are proportional to the negative gradient of the error. This guideline determines the relative changes that must occur in different weights when a training samples(s) is presented. These magnitudes changes are dependent on the learning rate. Sivanandam and Paulraj, 2004). The method for adopting the learning rate was increasing it in order to improve the performance of the model by decreasing the testing error and increasing the correlation coefficient. Finally the transfer functions were tested, for the three models, the function of the input layer was tanh and in the hidden layer it remained sigmoid as it is a default function in the software. The reduction percentages in the testing error, as shown in Table 4, were small when increasing the number of nodes in the hidden layer. When testing the effect of increasing the momentum rate, only in model tur it reduced the testing error by 4.58%. A reduction of 4.73% was recorded in model tur2 for a tanh function of the input layer. Finally the correlation coefficient in models tur and tur2 reached 97.26 and 92.84 % respectively.

Prediction of Head loss

For the prediction of the head loss at the end of the filtration run, three models were also constructed. Table 3 illustrates the architecture of each model. The number of nodes in the hidden layer reached five in model hl and two in models hl2 and hl3. The momentum rate ranged 0.68 to 0.92, where the learning rate kept near to the default value of 0.2. The reduction in the

testing rate was, 2.18% in model hl at momentum rate 0.92 and 6.65% for being the two transfer functions tanh in the input and hidden layers in model hl2. The models hl and hl2 gave the highest correlation coefficients recording 95.92 and 93.06 %respectively.

Prediction of Running time (filtration length)

As for predicting the filtration length, two models were only constructed. As shown in Table 3, one or two nodes are required in the hidden layer where it reduced the testing error 10.38 % in model hl-rt. The momentum rate was high in the two models, reaching 0.9 and 0.96. The learning rate kept near to the default value of 0.2. The transfer functions in the input and hidden layer were tanh where it reduced the testing error by 8.25 %. The model hl-rt predicted the running time with a correlation coefficient 86.43%.

A total data of 127 were exploited to build the different models of this study. In these models, 68-70% of the input data were used for training, 19-21% for testing and the remaining 10-13% for validation. The models developed were tested to show the best models to predict the effluent turbidity, head losses and running time. The model tur showed the best agreement between the predicted and measured effluent turbidity which is shown in figure 2. This figure illustrates the hourly variation of the predicted and measured turbidity for one of the experimental runs in the pilot filtration plant. These final predictions appear to be accurate enough to be useful. The models for predicting the head losses also gave good agreement between the predicted and measured head losses from the experimental work as shown in figure 3, the best model was hl2. Figure 4 shows the best model for

predicting the running time (rt) or the length of the filtration run, which was hl-rt.

The results indicate that it is quite possible to predict effluent turbidity, head losses and running time in the filtration process using intelligent data driven methods such as artificial neural networks.

CONCLUSIONS

The results of this study indicate that it is quite possible to predict effluent turbidity, head losses and running time in the filtration process using intelligent data driven methods such as artificial neural networks, and the following conclusions are brought out:

- The data used to build the ANN models were distributed, 68-70% used for training, 19-21% for testing and the remaining 10-13% for validation.

- Models predicting effluent turbidity, had 1-2 nodes in the hidden layer, high momentum rate reaching 0.98, learning rate within 0.2 and the testing error was low 4.65% with a correlation coefficient of 97%.

- Models predicting the head losses, had 2-5 nodes in the hidden layer, high momentum rate reaching 0.92, learning rate within 0.2 and the testing error was low 4.46% with a correlation coefficient of 95%.

- The model for predicting the running time or the length of the filtration run had 2 nodes in the hidden layer, 0.96 momentum



rate, 0.22 learning rate where the testing error was 5.93% which gave a correlation coefficient of 86%.

-All models gave good agreement between the predicted and measured data from the experimental work.

REFERENCES

- Crittenden J. C., R. R. Trussel, D. W. Hand, K. J. Howe and G. Tchobanoglous, (2005), Water Treatment Principles and Design .2nd edition, USA.
- Fernandez E. and Galvis A .(2002), Artificial Neural Network Model used for Clear Water Treatment Plants. Seminario Internacional La Hidroinformatica en la Gestion Integrada de los Recursos Hidricos
- Gibbs M. S., N. Morgon, H. R. Maier, G. C. Dandy, M. Holmes and J. B. Nixon (2003), Use of Artificial Neural Networks for Modeling Chlorine Residuals in Water Distribution Systems.
- Hafizan Juahir, Sharifuddin M. Zain, Mohd Ekhwan, Mazlin Mokhtar and Hasfalina Man (2004), Application of Artificial Neural Network Models for Predicting Water Quality Index. Journal Kejuruteraan Awam 16(2): 42-55.
- Kanani, S., G. Asadollahfardi and A. Ghanbari (2008), Application of Artificial Neural Network to Predict Total Dissolved Solid in Achechay River Basin. World Applied Science Journal 4 (5):646-654.
- Memon N., M. A. Unar, A. K. Ansari, G. B. Khaskheli and B. A. Memon (2008), Prediction of Parametric Value of Drinking Water of Hyderabad City by Artificial Neural Networks Modeling. WSEAS Transactions on Environment and Development, Issue 8, volume 4, August.
- Nicolas Valentin and Thierry Denceux (2001), A Neural Network Based Software Sensor for Coagulation Control in a Water Treatment Plant. Intelligent Data Analysis 5 23-39 IOS Press.
- Qasim S. R., E. M. Motley and G. Zhu (2000), Water Works Engineering Planning, Design and Operation. Prentice Hall PTR. USA.
- Sivanandam S. N. and M. Paulraj (2004), Introduction to Artificial Neural Networks. Vikas Publishing House PVT LTD New Delhi.
- Stewart A. Rounds (2002), Development of a Neural Network Model for Dissolved Oxygen in the Tualatin River, Oregon. Proceedings of the 2nd Federal Interagency Hydrologic Modeling Conference, Las Vegas, Nevada July 29- August 1.
- TRB (1999), Use of Artificial Neural Network in Geomechanical and Pavement Systems. Transportation Research Circular No. e-c 012.

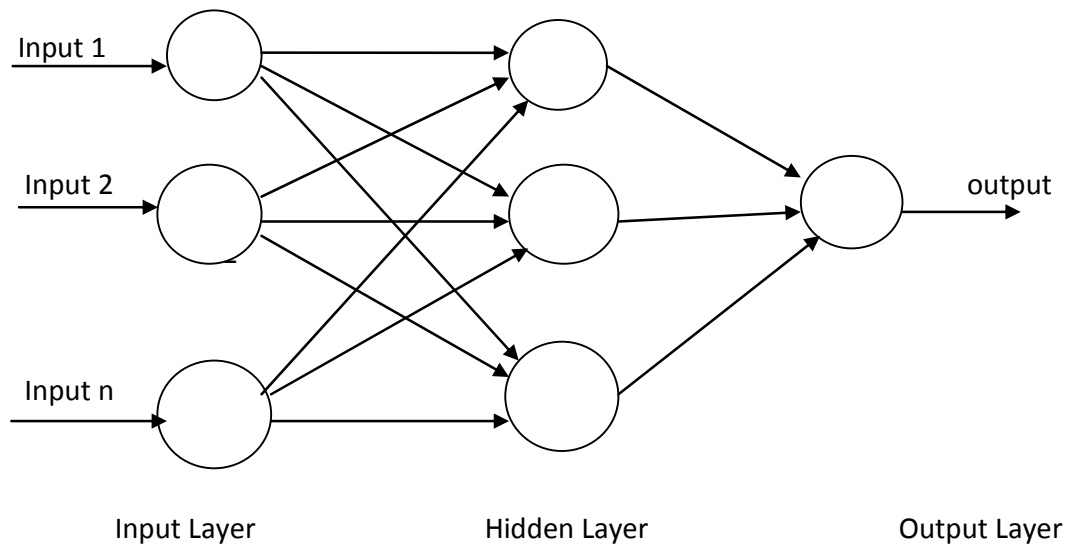


Fig. 1 Multi layer neural network

Table 1 Description of the case study

Filtration rate (m/hr)	Bed depth (cm)	Grain size (mm)	Influent	No. of runs	Running time (hr)
5, 7.5, 10, 15	70	0.72	The same water to the filters of Alwathba WTP with variable turbidity ranging 3.7 to 27 NTU	15	1 to 30

Table 2 Data used in ANN models

Model	Input data
	Prediction of Effluent turbidity (tur)
tur	Running time, filtration rate, bed depth, grain size and influent turbidity
tur-2	Influent turbidity, filtration rate, bed depth, grain size and head loss
tur-3	Running time, filtration rate, bed depth, grain size ,influent turbidity and head loss
	Prediction of Head loss (hl)
hl	Running time, filtration rate, bed depth, grain size , influent and effluent turbidity
hl-2	Running time, filtration rate, bed depth, grain size and influent turbidity
hl-3	Influent turbidity, filtration rate, bed depth, grain size and effluent turbidity
	Prediction of Running time (rt)
tur-rt	Influent turbidity, filtration rate, bed depth, grain size and effluent turbidity
hl-rt	Influent turbidity, filtration rate, bed depth, grain size and head loss

**Table 3 Models Architecture, Optimization and Stopping Criteria**

Model	Input layer	Hidden layer	Momentum rate	Learning rate	Testing error (%)	Training error (%)	Correlation coefficient (R%)
Prediction of Effluent turbidity (tur)							
tur	5 tanh	1 sigmoid	0.98	0.18	4.6509	5.6430	97.26
tur2	5 tanh	2 sigmoid	0.92	0.7	4.6132	5.7169	92.84
tur3	6 tanh	1 sigmoid	0.76	0.24	5.2271	5.3156	79.56
Prediction of Head loss (hl)							
hl	6 linear	5 linear	0.92	0.2	4.4668	5.5207	95.92
hl2	5 tanh	2 tanh	0.8	0.18	4.6637	5.4402	93.06
hl3	5 tanh	2 sigmoid	0.68	0.2	7.7716	9.1015	68.78
Prediction of Running time (rt)							
tur-rt	5 linear	1 tanh	0.9	0.22	11.9993	12.4373	69.86
hl-rt	5 tanh	2 tanh	0.96	0.22	5.9355	6.3205	86.43

Note: default values of the software, momentum rate= 0.8 & learning rate= 0.2

Table 4 Reduction in the testing error (%)

Model	Nodes in the hidden layer	Momentum rate	Learning rate	Transfer function
tur		4.58 (0.98)	0.21	0.05
tur2	0.08	0.84	3.99 (0.7)	4.73 (1 st tanh)
tur3	0.67	0.01	0.02	0.14
hl	0.73	2.18 (0.92)		0.72 (2 nd linear)
hl2	0.89		0.17	6.65 (1 st & 2 nd tanh)
hl3	0.15	0.09		4.81 (1 st tanh)
tur-rt		0.37	0.03	0.04 (2 nd tanh)
hl-rt	10.38 (2 nodes)	2.04 (0.96)	0.06	8.25(1 st & 2 nd tanh)

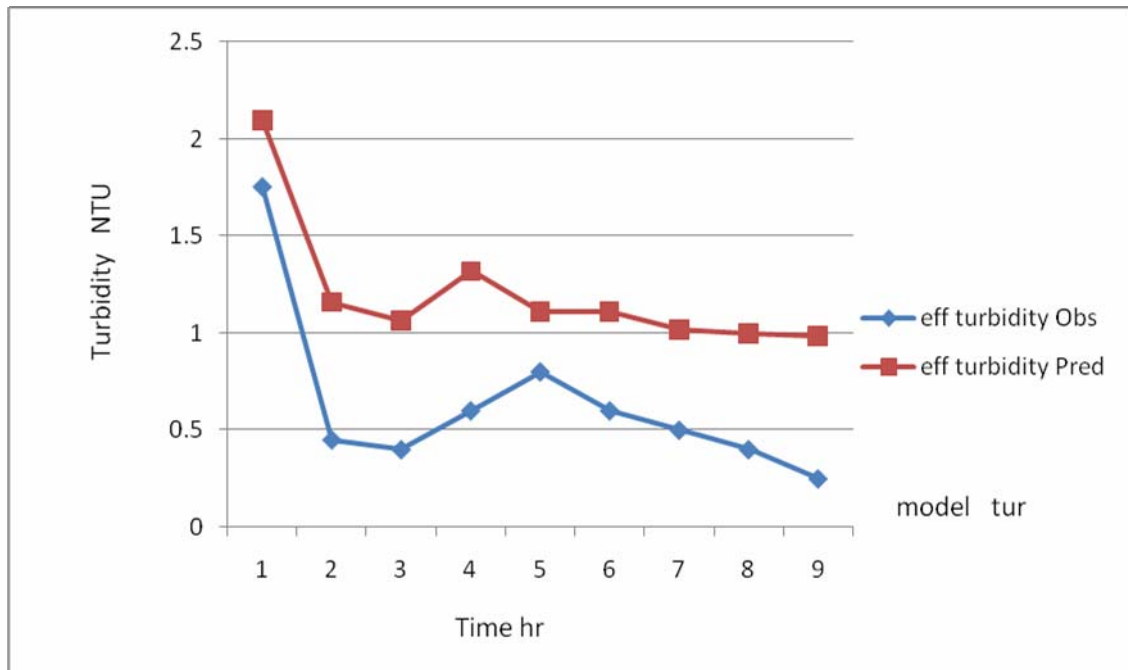


Fig.2 Hourly variation of the predicted and measured turbidity

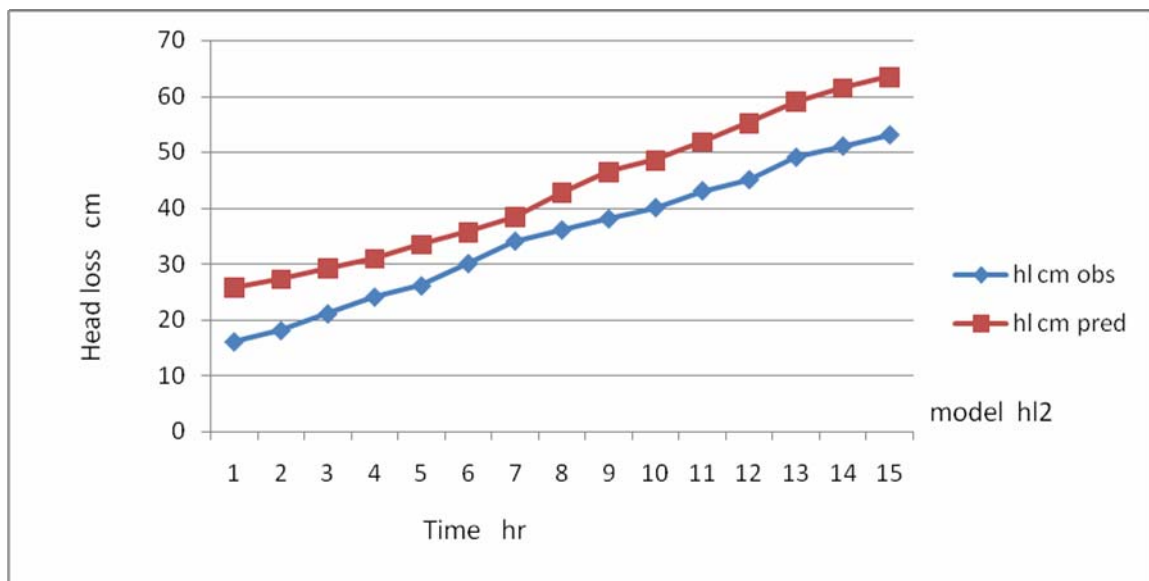


Fig.3 Hourly variation of the predicted and measured head losses

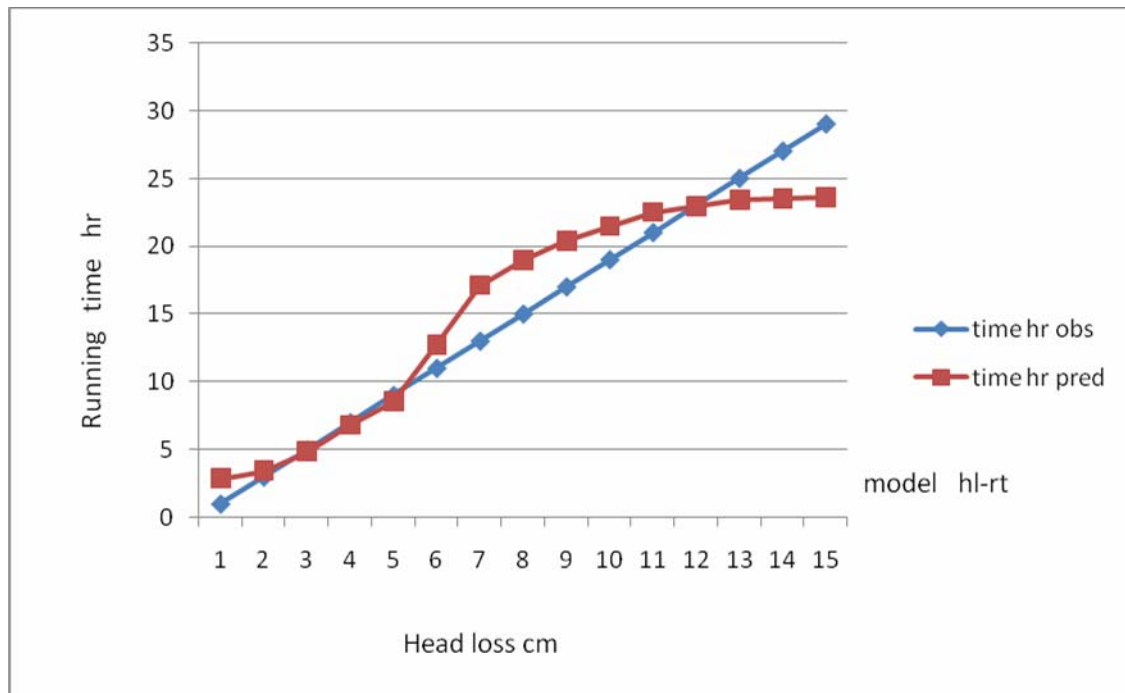


Fig.4 Variation of the predicted and measured running time



ANALYSIS OF GEOTEXTILE EMBANKMENT BY ANSYS

By

Dr. Zainab Ahmed Alkaissi
Lecturer (Civil Eng. Dep. University
of Al-Mustansiriya)

ABSTRACT:

The major objectives of this research are to analyze the behavior of road embankments reinforced with geotextiles constructed on soft soil and describe the finite element analysis by using ANSYS program ver. (5.4). The ANSYS finite element program helps in analyzing the stability of geo- structure (embankment) in varied application of geotextiles reinforcement to enhance the best design for embankment.

The results of analysis indicate that one of the primary function of geotextiles reinforcement was to reduce the horizontal displacement significantly. With the inclusions of reinforcement, the horizontal displacement reduced by about (81%), while the vertical displacement reduced by (32%). The effect of geotextiles stiffness modulus on horizontal and displacement is quite significant even a very high modulus of geotextile will have relatively little effect on vertical displacement. Also it is observed from the obtained results that the maximum displacement occurred at the toe of embankment for both horizontal and vertical movement, then decrease gradually to a negligible value for the layer reinforced case. Also the reinforcement reduces the shear stress developed in the foundation soil.

الخلاصة:

ان الهدف الرئيسي من هذا البحث هو لتحليل تصرف تعلبات الطريق المسلحة بالياف والتي تنشأ فوق التربة الضعيفة ووصف تحليل برنامج ANSYS ver (5.4) العناصر المحددة. برنامج العناصر المحددة ANSYS يساعد في تحليل ثبوتية المنشآت الجيو تكنولوجية (التعلبات) مع تطبيقات مختلفة من الياف التسليح (geotextiles) لاختيار التصميم الافضل للتعلبات. ان نتائج التحليل تبين ان احد اهداف الياف التسليح هو لتقليل الازاحة الافقية بصورة ملحوظة. مع وجود التسليح ، الازاحة الافقية تقل بحوالي (81%) ، بينما تقل الازاحة الشاقولية بحوالي (31%). ان تاثير معامل صلادة الياف التسليح على الازاحة الافقية يكون ملحوظا بصورة واضحة اما تاثير القيم العالية لمعامل صلادة الياف التسليح يكون قليل على الازاحة الشاقولية. وكذلك تم ملاحظة من النتائج المستحصلة ان اعلى قيمة للازاحة تحدث في حافة التعلبة بالنسبة لكل من الحركة الافقية والشاقولية، ثم تقل تدريجيا حتى تصل الى قيمة مهملة بالنسبة لحالة تسليح الطبقات. كذلك ان التسليح يقلل اجهادات القص المتولدة بتربة الاساس.

KEY WORDS: Embankment; reinforced; geotextiles; finite element; numerical analysis; soft soil; displacements.

INTRODUCTION

The most common analysis method used for designing geotextile reinforced embankment fall into two broad categories, namely, conventional limit equilibrium and finite element methods. Limit equilibrium approaches are the most numerous (*e.g., Haliburton 1981; Fowler 1982; Jewell 1982*) and attractive because of their simplicity.

However there are inherent difficulties in the limit equilibrium methods to take into consideration the soil- geotextile interaction. The main advantage of finite element analysis over conventional method is that complete interaction of the embankment foundation system can be simulated.

Several investigators (*e.g., Andraws et al 1980, Bell et al. 1977, Rowe, 1984*) have used finite element techniques for the analysis of geotextile - soil systems. They are not all suitable for the analysis of reinforced embankments on soft or compressible or plastic failure with the soil. *Kamal, et al. (2005)* conducted a parametric study of reinforced and unreinforced embankment using finite element (Sage Crisp) program. Construction sequence and consolidation during construction were modeled using Cam Clay model, it was found that the mode of embankment failure occurred in the form of circular shape with base heave occurring near the toe of the embankment. *Cudny and Neher (2003)* studied the behavior of a test reinforced road embankment constructed on soft soil deposits at Haarajaki. The numerical calculations are completed with finite element method program capable to perform coupled static/ consolidation analysis of soils.

- Geotextiles Reinforcement

The development of geotextiles utilities in subsurface construction works has been generally increased in the solution of engineering problems. Geotextiles used with foundation soil, rock, or any other geotechnical structure or system (*ASTM D4439*). The polymers used in manufacture of geotextiles fiber are made from polymer

materials. Its properties could be shown in Table (1).

Geotextiles improve the total system by increasing its strength which, created by introducing the geotextiles into a soil or other disjointed and separated material. Soils have no or little tensile strength (due to appearance cohesion). Because of that, a geotextiles placed horizontally in the direction of principle stress in the soil mass will improve the tensile property of soil (*Koerner, 1990*). Thus the geotextile acts as reinforcement so any normal applied load on the reinforced soil mass will mobilize tensile forces in the geotextile through friction, and therefore limiting the lateral deformation of the soil mass.

In design, the geotextile reinforcement to enhance soil stability, various factors involve, stiffness of reinforcement in relation to the surrounding soil, orientation of the reinforcement on the purpose embankment, form of reinforcement, creep performance of the reinforcement during the life time of the embankment and corrosion resistance during life time. Figure (1) shows the common scheme use in designing the reinforcement layers.

- Finite Element Analysis

There are many practical problems either extremely difficult or impossible to solve exactly by the conventional analytical methods. This may be due to the complexity of the composite nature of the materials, difficulties associated with the representation of the load and boundary conditions or some constitutive stress-strain relations.

The finite element method is a numerical technique in which the continuous system with an infinite number of degrees of freedom is represented by an assemblage of discrete members, which has a finite number of degrees of freedom. The assemblage is composed of connected elements of finite size. Adjacent finite elements are joined with each other by a number of nodes specified along their boundaries. The development in the finite



element method depends on the proper element properties and on the availability of an efficient means of solving the resulting system of linear or nonlinear simultaneous equations. For reinforced embankment, the nonlinear finite element analysis yields a wide range of useful information about displacements, strains, distribution of normal and shear stresses in embankment foundation system.

ANSYS (ANalysis SYStem) is a comprehensive general-purpose finite element computer program that contains over 100,000 lines of code and more than (180) different elements, has been used in this study to simulate road embankment foundation system with geotextiles reinforcement. One of the main advantages of ANSYS is the integration of the three phases of finite element analysis: pre-processing, solution and post-processing. Pre-processing routines in ANSYS define the model, boundary conditions, and loadings. Displays may be created interactively on a graphics terminal as the data are input to assist the model verification. Post-processing routines may be used to retrieve analysis results in a variety of ways. Plots of the structure's deformed shape and stress or strain contours can be obtained in the post-processing stage.

- Modeling of Reinforced Embankment

In the present study, the ANSYS program of version (5.4) was employed for analyzing embankment foundation system as well as the finite element modeling for geotextile reinforcement. A plane 42, 2-D structural solid has been adopted in this research. The element can be used as a plane element (plane strain or plane stress) or as an axisymmetric element. The element is defined by four nodes having two degrees of freedom at each node, translations and the nodal x and y directions. The element has plasticity, and large strain capability.

The embankment foundation soil modeled as elasto-plastic material (plane strain condition) based on Darger –Parger model with isotropic material therefore a stiffness elastic modulus

(E) and Poisson's ratio (ν), cohesion (C), angle of internal friction and angle of dilancy are used to represent their behavior. The load case studied is a rectangular domain representation with uniform distribution (static loading case) within the rectangular to simulate the traffic loading (20kN/m^2) as shown in Figure (3).

The cross section of road embankment used in this study of 18 m crest width and 1:2 side slopes are shown in Figure (2). The depth of the soft foundation soil is 20m finite element discretization of the problem is shown in Figure (3). Due to symmetry along the center line only half of the geometry was simulate.

In the present study, the geotextiles reinforcement was represented by the smeared model as shown in Figure (4) which assumes that the reinforcement is uniformly spread in a layer throughout the embankment soil element in a defined region of the finite element mesh. This model used for large scale model. The finite element program ANSYS version (5.4) is used to analyze the embankment and geotextiles theoretically using a plane 42, 2-D structural solid that has been adopted in this research. The element can be used as a plane element (plane strain or plane stress) element. The element is defined by four nodes having two degrees of freedom at each node, translations and the nodal x and y directions. The element has plasticity, and large strain capability.

- Analysis Results and Discussions

The geotextiles reinforcement was placed as layer of 0.5 m thickness working mat spread through the embankment and above the embankment foundation interface as shown in Figure (3).

The embankment foundation soil modeled as elasto-plastic material (plane strain condition) based on Darger –Parger model with isotropic material therefore a stiffness elastic modulus (E) and Poisson's ratio (ν), cohesion (C), angle on internal friction and Diletny angle are used to represent their

behavior. These parameters are used to characterize the elasto-plastic model for soft soil foundation and fill materials are listed in Table (1).

Figures (5) and (6) show the horizontal and vertical movement against vertical direction at the toe of embankment. And from these results, it would appear that the primary function of the geotextiles reinforcement was to reduce the horizontal displacement significantly. With the inclusions of reinforcement, the horizontal displacement reduced by about (81%), while the vertical displacement reduced by (32%). This shows that the reinforcement may be considered as important role in reducing horizontal and lateral movements.

The modulus and strength of geotextiles also appears to be of an important effect. Therefore its effect was studied and were shown in Figures (7) and (8) for horizontal and vertical displacement respectively. It's clear from these figures that the effect of geotextiles stiffness modulus on horizontal and displacement is quite significant. Even a very high modulus of geotextile will have relatively little effect on vertical displacement.

Figures (9) and (10) show the distribution of horizontal and vertical displacement with horizontal distance along the embankment surface from the toe of embankment. The maximum displacement occurred at the toe of embankment for both horizontal and vertical movement, then decrease gradually to a negligible value for the layer reinforced case. The contour lines for horizontal and vertical movements are also shown in Figures (11) to (14) for both cases studied.

Figures (15) and (16) show the shear stress developed in the embankment foundation system for both cases. It can be observed that the reinforcement reduce the shear stress developed in the foundation soil by 50%.

Figure (16) shows the deformation mesh of embankment foundation using the geotextiles reinforcements.

- CONCLUSIONS

The behavior of reinforced embankment with geotextiles have been investigated

using the ANSYS ver. (5.4) finite element program and the following conclusions can be drawn:

- With the inclusions of reinforcement, the horizontal displacement reduced by about (81%), while the vertical displacement reduced by (32%). This shows that the reinforcement may be considered as important role in reducing horizontal and lateral movements.
- The effect of geotextiles stiffness modulus on horizontal and displacement is quite significant. Higher values of geotextile modulus will have relatively little effect on vertical displacement.
- The maximum displacement occurred at the toe of embankment for both horizontal and vertical movement, then decrease gradually to a negligible value for the layer reinforced case.
- The reinforcement reduces the shear stress developed in the foundation soil by 50%.

REFERENCES:

- "ANSYS Manual", Version (5.4), USA, 1996.
- "ASTM" Annual Book of ASTM Standard, Section 4, Volume 04.03, 1987.
- Andrawes, K.Z., McGowna, A., Mashhoumr, M. M., and Wilson-Fahmy, R. F. (1980): "Tension Resistant Inclusions in Soils". ASCE Journal of the Geotechnical Engineering Division, 106(GT12), pp. 1313-1326.
- Bell, J. R., Greenwayd, D. R., and Vischerw, W. (1977): "Construction and Analysis of a Fabric Reinforced Low Embankment on Muskeg". Proceedings, 1st International Conference on the Use of Fabrics and Geotechnics, Paris, France, pp. 71-76.



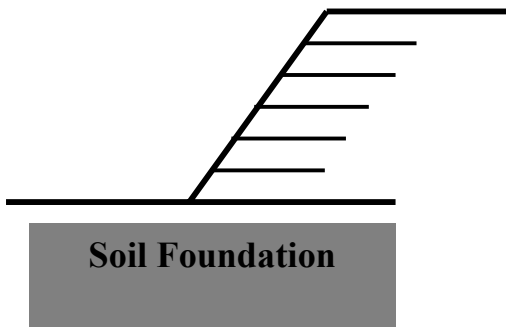
- Fowler, J. (1982): **“Theoretical Design Considerations for Fabric Reinforced Embankments”**. Proceedings, 2nd International Conference on Geotextiles, Las Vegas, Vol.2, pp: 665- 670.
- Haliburtan, T. A. (1981): **“Use of Engineering Fabric in Road and Embankment Construction”**. Seminar on the Use of Synthetic Fabrics in Civil Engineering, Toronto, pp. 66-94.
- Jewell, R. A. (1982): **“A Limit Equilibrium Design Method for Reinforced Embankments on Soft Foundations”**. Proceedings, 2nd International Conference on Geotextiles, Las Vegas, Vol. 2, pp. 671-676.
- Kamal, A. A., Pauleen, A. L., and Heshmati, A. R. (2005): **“Parametric Study of Reinforced and Unreinforced Embankment on Soft Soil”**. 13th ACME Conference: University of Sheffield March 21-22 2005.
- Neher, H., and Cudny, M. (2003): **“Numerical Analysis of Test Embankment on Soft Ground using An anistropic Model with Destructuration”**. Institute of Geotechnical Engineering, University of Stuttgart, Germany.
- Rowe, R. K., Macleanm, M. D., and Barsvaray, A. K. (1984): **“The Observed Behaviour of a Geotextile-Reinforced Embankment Constructed on Peat”**. Canadian Geotechnical Journal, 21, pp. 289-304.

Table (1): Polymer used in Manufacture of Geotextile.

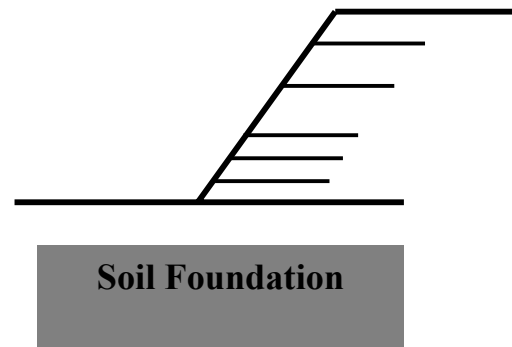
Polymer Composition of Geotextile			
Polypropylene (65%)	Polyester (32%)	Poly Amide (2%)	Polyethylene (1%)

Table (2): Input Parameter for F.E. Program Analysis (*Neher and Cudny, 2003*).

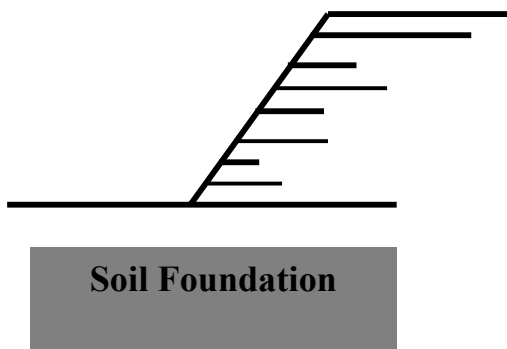
Material	Embankment Soil (fill materials)	Foundation Soil
E (MPa)	50	20
Poisons Ratio (ν)	.15	.2
Friction Angle ($^{\circ}$)	35	25
Cohesion (kPa)	3.0	5.7
Unit weight (kN/m^3)	21	15
Diltency Angle ($^{\circ}$)	0	0



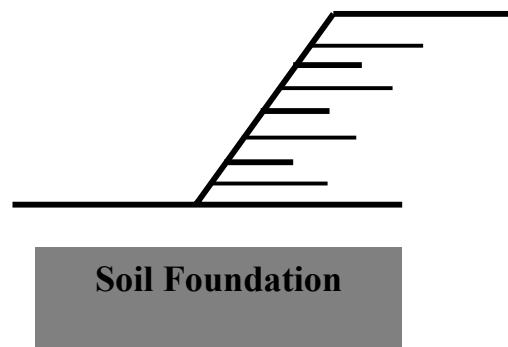
a) Even space - even length.



b) Uneven space- even length.



c) Even space – Uneven length with short facing



d) Uneven space –Uneven length with short facing layers.

Figure (1): Common Scheme use in designing the Reinforcement Layers.

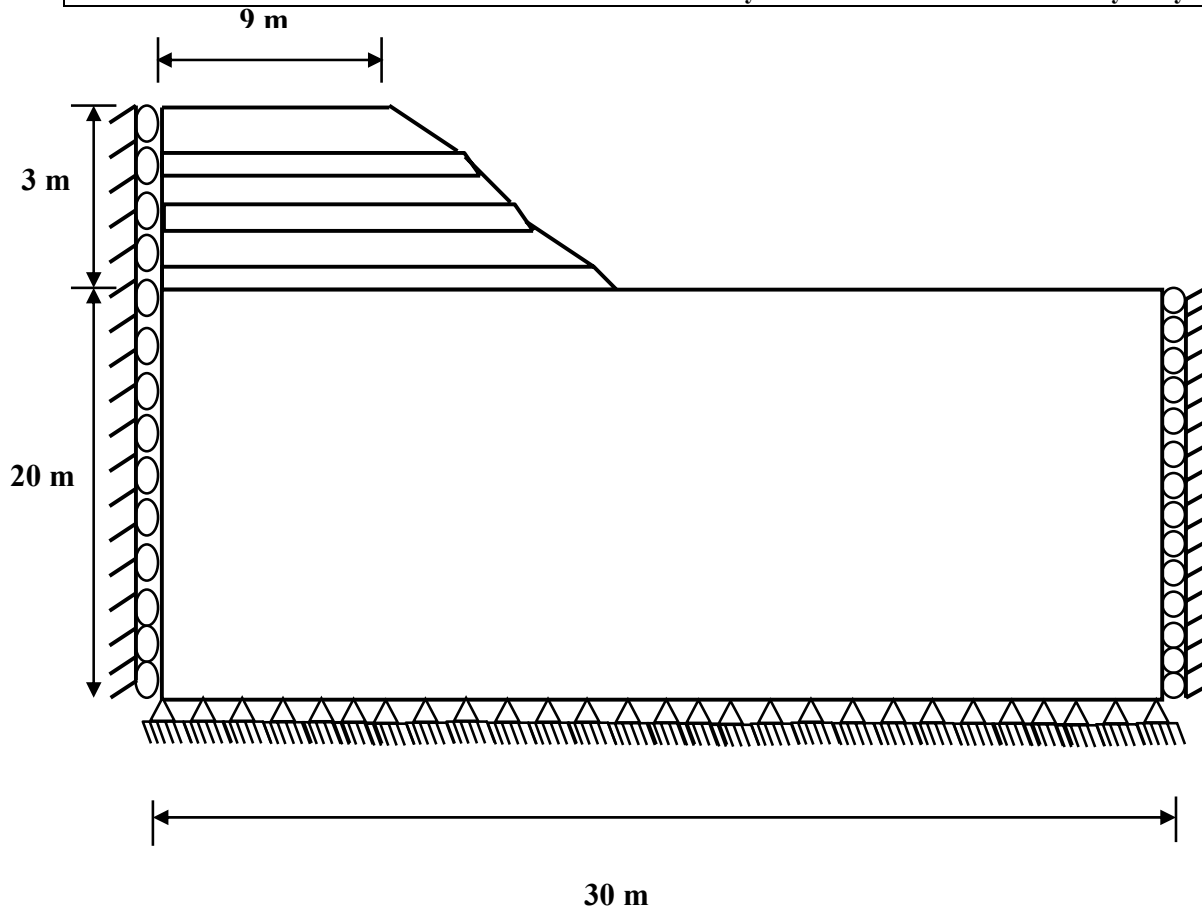


Figure (2): The Cross Section of Embankment Foundation System with Geotextiles Reinforcement.

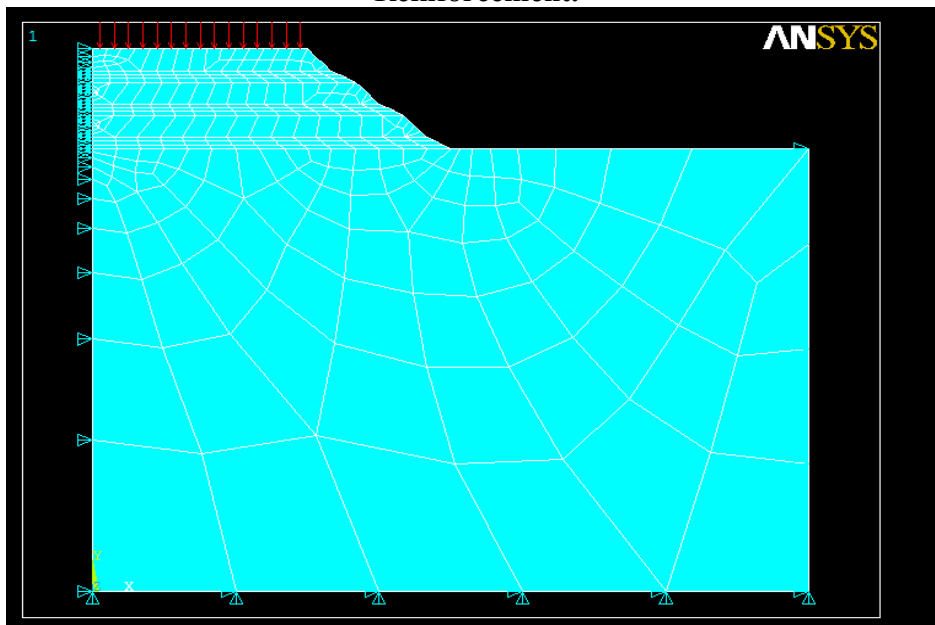


Figure (3): Finite Element Mesh of Embankment Foundation System.

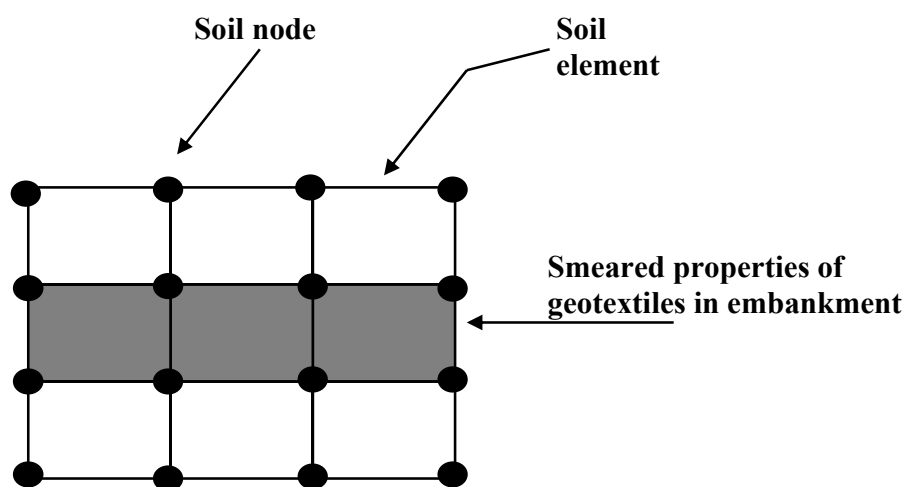


Figure (4): Model for Geotextiles Reinforcement in Embankment Foundation System.

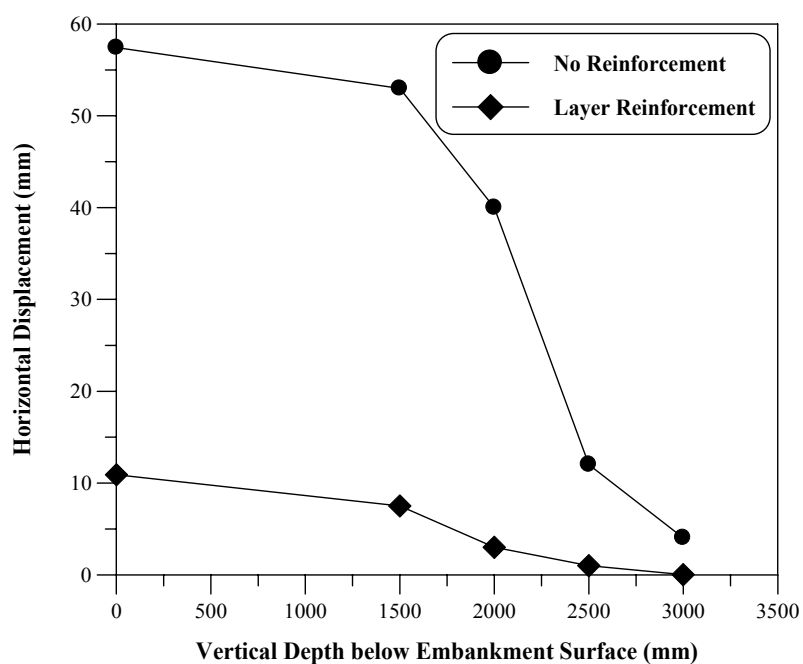


Figure (5): Variation of Horizontal Displacement with Vertical Depth below Embankment Surface.

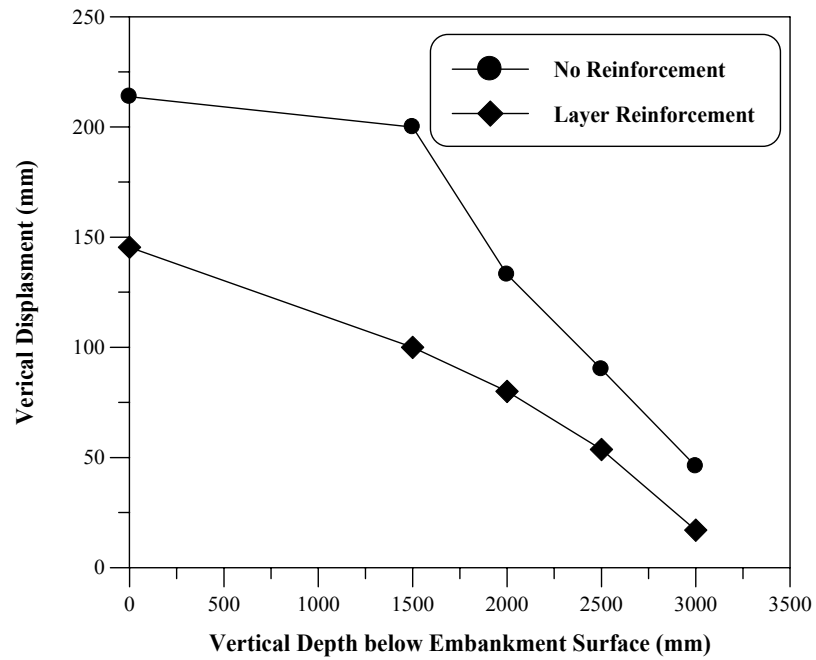


Figure (6): Variation of Vertical Displacement with Vertical Depth below Embankment Surface.

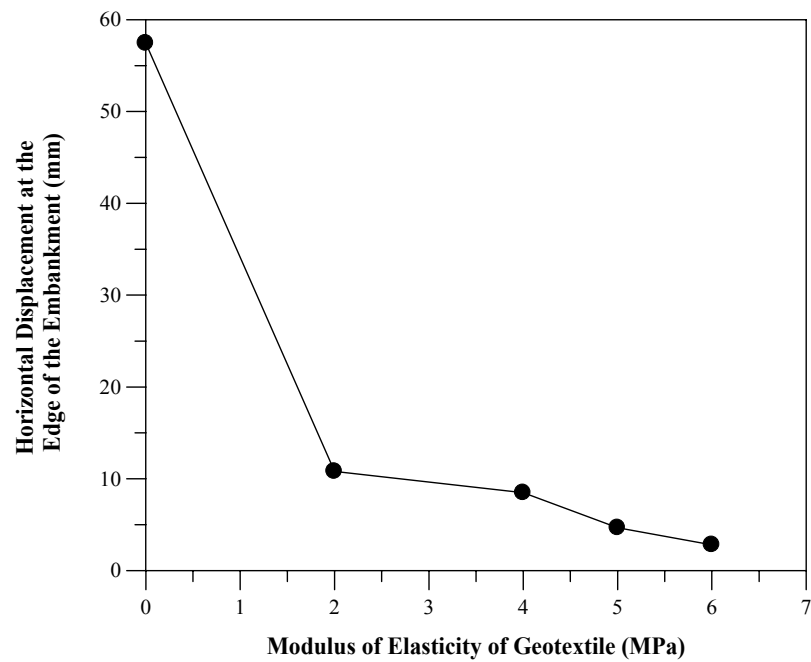


Figure (7): Effect of Elastic Modulus of Geotextile on Horizontal Displacement.

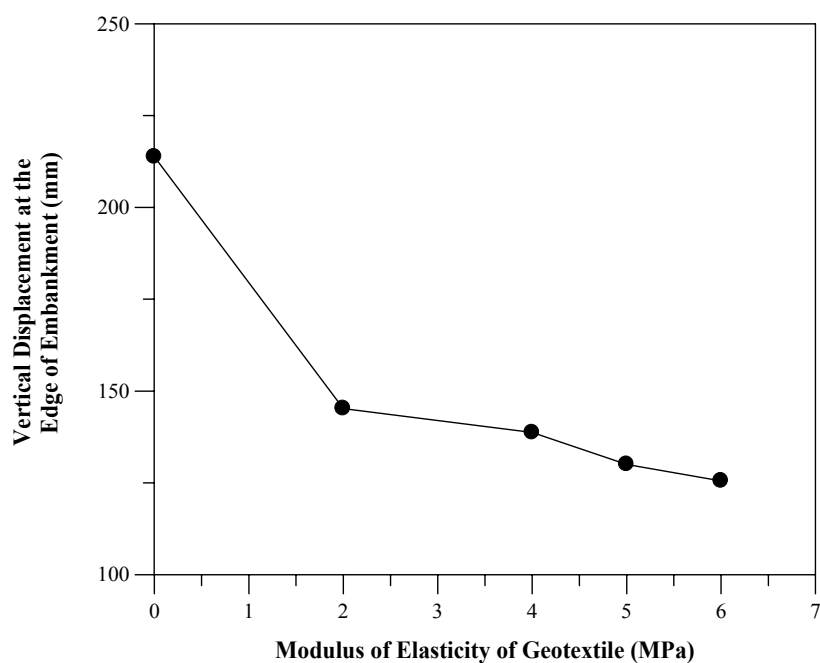


Figure (8): Effect of Elastic Modulus of Geotextile on Vertical Displacement.

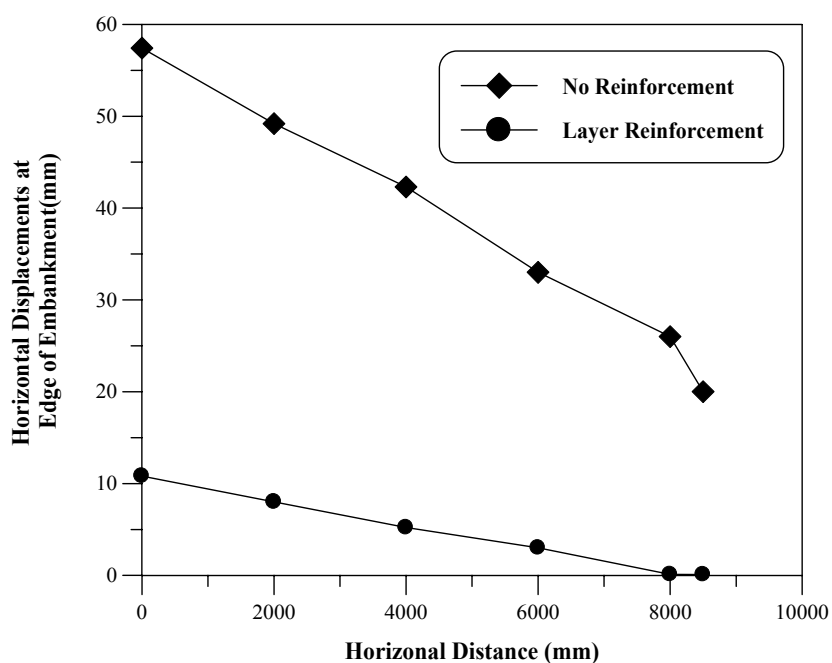


Figure (9): Variation of Horizontal Displacements with Horizontal Direction along Ground Surface.

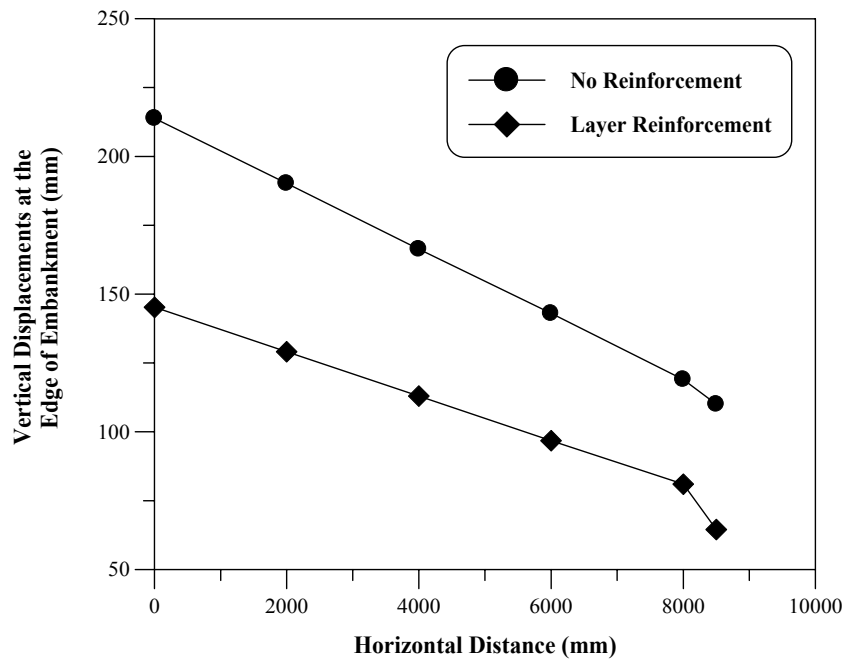


Figure (10): Variation of Vertical Displacements with Horizontal Direction along Ground Surface.

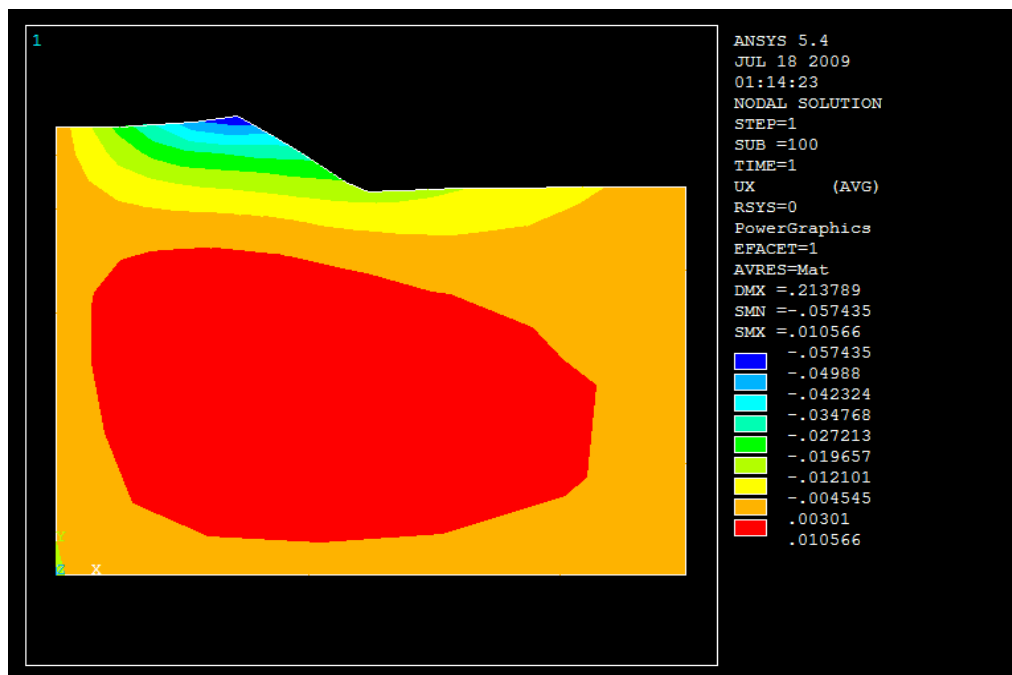


Figure (11): Horizontal Displacements Distribution in Embankments Foundation without Geotextiles Reinforcements.

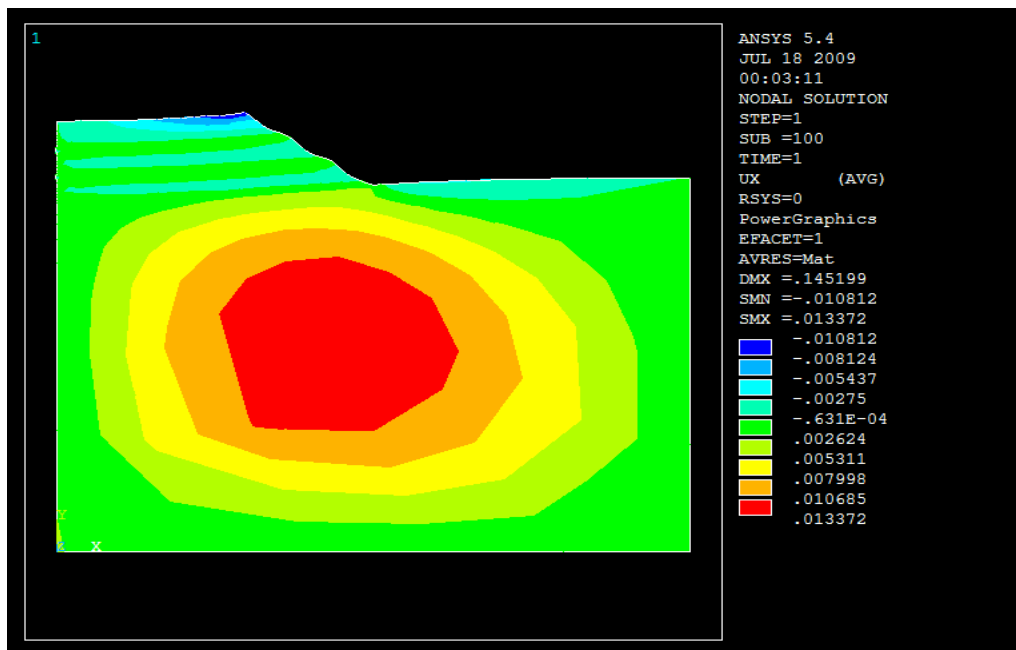


Figure (12): Horizontal Displacement Distribution in Embankments Foundation with Geotextiles Reinforcements.

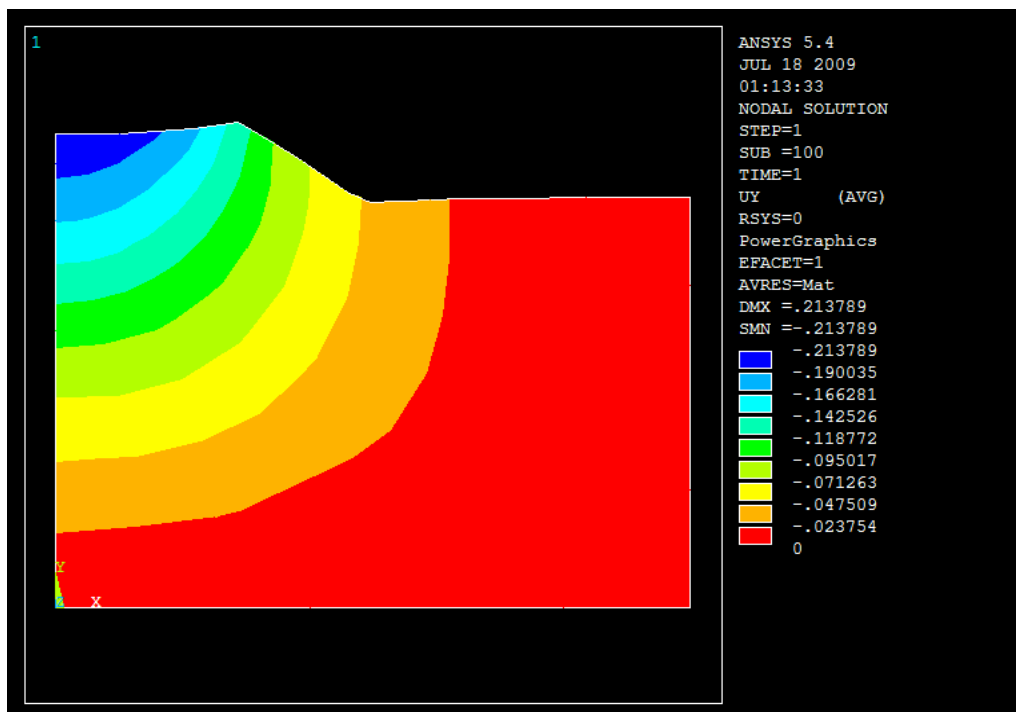


Figure (13): Vertical Displacements Distribution in Embankments Foundation without Geotextiles Reinforcement.

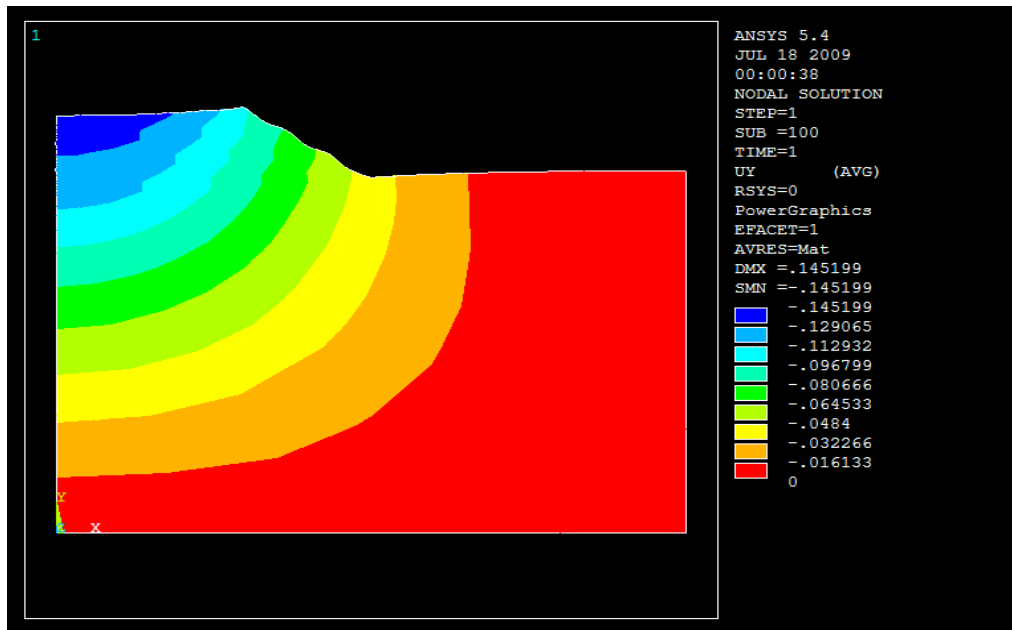


Figure (14): Vertical Displacements Distribution in Embankments Foundation with Geotextiles Reinforcement.

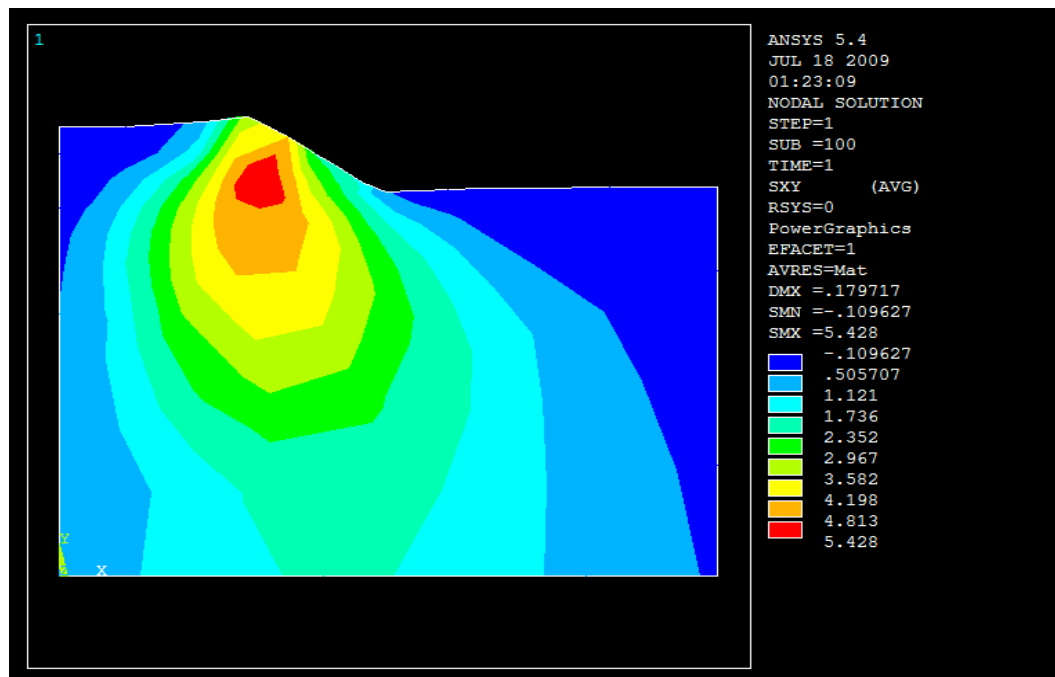


Figure (15): Shear Stress Distribution without Geotextiles Reinforcements.

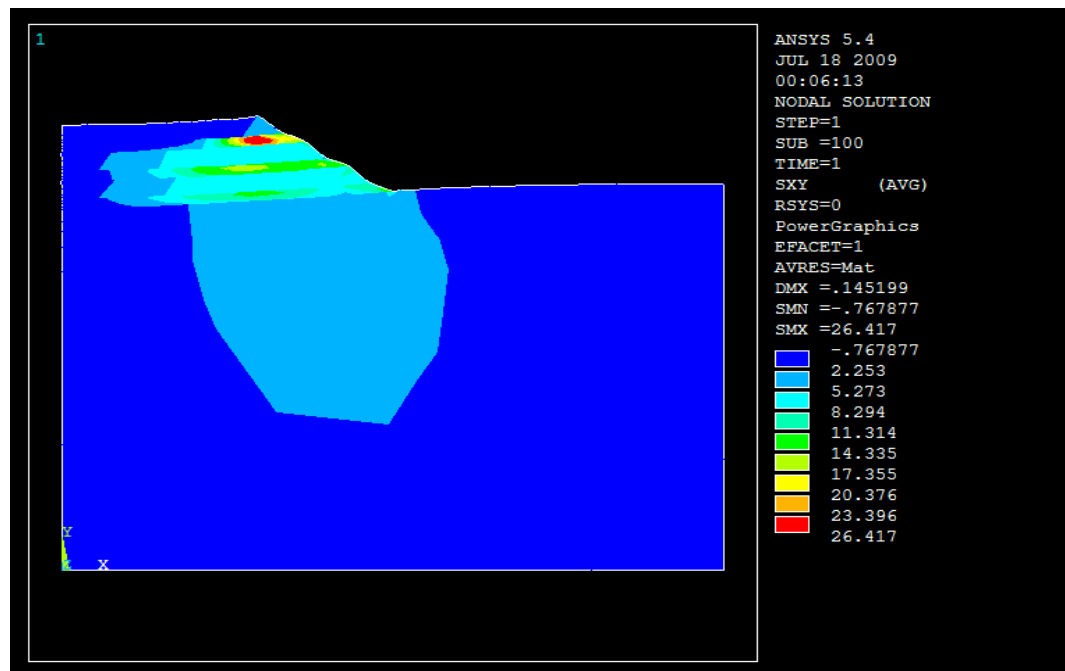


Figure (16): Shear Stress Distribution with Geotextiles Reinforcements.

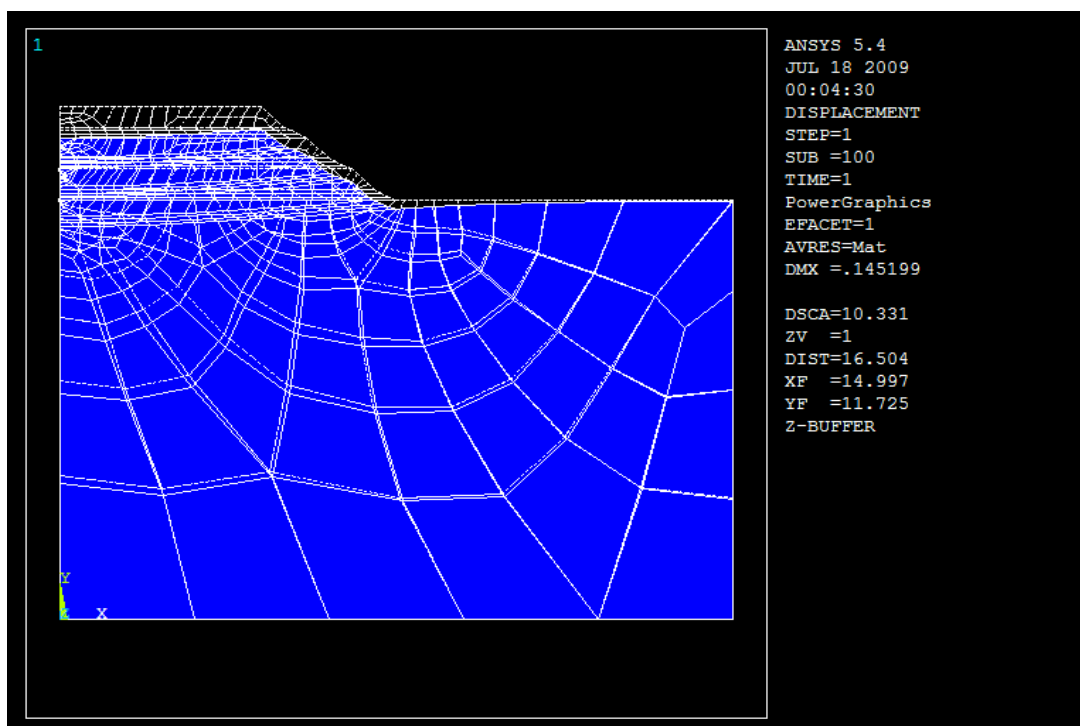


Figure (17): Deformation of Embankment Foundation with Geotextiles Reinforcements.



MIXED CONVECTION PHENOMINA AFFECTED BY RADIATION IN A HORIZONTAL RECTANGULAR DUCT WITH COCENTRIC AND ECCENTRIC CIRCULAR CORE

Manal H. AL-Hafidh

Raed Gatie Sayhood

Ass. Prof. /University of Baghdad

Mechanical Engineer

ABSTRACT

The numerical investigation has been performed to study the radiation affected steady state laminar mixed convection induced by a hot inner varied positions circular core in a horizontal rectangular channel for a fully developed flow. To examine the effects of thermal radiation on thermo fluid dynamics behavior in the eccentric geometry channel, the generalized body fitted co-ordinate system is introduced while the finite difference method is used for solving the radiative transport equation. The governing equations which used are continuity, momentum and energy equations. These equations are normalized and solved using the Vorticity-Stream function. After validating numerical results for the case without radiation, the detailed radiation effect is discussed. From the parametric study, the Nusselt number (Nu) distributions in steady state were obtained for Aspect Ratio AR (0.55-1) and Geometry Ratio GR (0.1-0.9). The fluid Prandtl number is 0.7, Rayleigh number ($0 \leq Ra \leq 10^4$), Reynolds number Re (1-2000), Optical Thickness ($0 \leq t \leq 10$), Conduction-Radiation parameter ($0 \leq N \leq 100$) for the range of parameters considered. It is indicated in the results that heat transfer from the surface of the circular core exceeds that of the rectangle duct and when circular core is lower than the center of the channel, the rate of heat transfer decreased. The correlation equations are concluded to describe the radiation effect.

:

-

.

.()

-

(0.1-0.9)

Re (1-

$(0 \leq Ra \leq 10^4)$

(Pr = 0.7)

(0.55-1)

$(0 \leq N \leq 100)$

-

$(0 \leq t \leq 10)$

1000)

KEY WORDS: mixed convection, radiation, rectangular duct, circular core, laminar flow.

INTRODUCTION:

Fully developed mixed convection laminar flow phenomena occur in a wide range of engineering applications as heat exchangers, solar collector, electronic equipment and similar devices. For this purpose various investigations have been performed in the literature under different boundary and operating conditions in order to maximize the heat transfer under optimum channel geometries.

Initial investigations on the heat transfer in channels neglected natural convection effects and only studied forced convection. In low Reynolds number flow conditions, both heat transfer mechanisms play a vital role and both have to be accounted for in which the heat transfer is being considered as mixed convection. [Pu et al, 1991] reported experimental results of mixed convection heat transfer in a vertical packed channel with asymmetric heating of opposing walls. The experiments were carried in the range of ($2 < Pe < 2200$) and ($700 < Ra < 1500$). The measured temperature distribution indicates the existence of secondary convection cell inside the vertical packed channel in the mixed convection regime.

Transfer of heat by simultaneous convective and radiative transfer at high temperature and high heat fluxes has become increasingly important in the analysis and design of high temperature gas – cooled nuclear reactors, advanced energy conversion devices, furnaces, combustors etc. these and many other applications have provided the impetus for research on combined convection radiation in participating media. [Larson and Viskanta, 1976] studied the transient laminar free convection and radiation in a rectangular enclosure. The effects of non participating radiation, wall heat conduction and laminar natural convection were examined. The results indicate that radiation dominates the heat transfer in the

enclosure and alters the convective flow patterns significantly.

[Kim and Viskanta, 1984] studied the effects of wall conduction and radiation heat exchanger among surfaces on laminar free convection heat transfer in a two – dimensional rectangular cavity modeling a cellular structure. The local and average Nusselt numbers were reported along the cavity walls for a range of physical interest. The local heat transfer rate was found to depend not only on the natural convection in the cavity but also on the wall conductance and radiation parameters. The results indicate that natural convection heat transfer in the cavity is reduced by heat conduction in the walls and radiation exchanger among surfaces.

[Bahlaoui, Raji, and Hasnoui, 2005] studied numerically a mixed convection coupled with radiation in an inclined channel with constant aspect ratio and locally heated from one side. The convective radiative and total Nusselt numbers were evaluated on the cold surface and at the exit of the channel and for different combinations of the governing parameters. The results obtained show that the flow structure is significantly altered by radiation which contributes to reduce or to enhance the number of the solutions obtained.

[Gururaja Rao, 2004] reported the results of an exhaustive numerical investigation into the problem of multi – mode heat transfer from a vertical channel for the twin cases of (i) uniform and (ii) discrete wall heat generation. Two –dimensional, steady state, incompressible, conjugate, laminar mixed convection with surface radiation is considered in both cases. The effects of parameters, such as surface emissivity, aspect ratio, modified Richardson number and discrete heat source position on the fluid flow and heat transfer characteristics are clearly brought out.

In the present investigation, the fully developed laminar mixed convective and radiative heat transfer will be investigated in an horizontal rectangular channel with interior circular core. The channel is fixed and the effect of heat generation is studied for thermal boundary condition of constant wall temperature and for $(0.1 \leq GR \leq 0.9)$, $(0.55 \leq AR \leq 1)$, $(1 \leq Re \leq 2000)$, $(0 \leq Ra \leq 10^4)$, $(0 \leq N \leq 100)$

MATHEMATICAL MODEL

Consider the steady state flow in an annulus of a rectangular channel with varied positions circular core as shown in **Fig. (1)**. This annulus is symmetrical about Y-axis ($\partial/\partial x = 0$). The flow is hydro dynamically and thermally fully developed laminar flow. The working fluid is assumed absorbing, emitting and the fluid properties are assumed constant except for density variation with temperature resulting in the secondary flows generated by the buoyancy forces. The axial (z) direction shown in **Fig. (1)** is the predominant direction for the fluid flow. The flow is laminar, and viscous dissipation effects are neglected. Axial conduction and radiation are assumed negligible following [Yang and Ebadian, 1991].

Governing Equations:

Assuming two – dimensional flow with constant properties, the governing equations for the vorticity – stream function and the temperature at steady state conditions are:

Stream Function Equation

$$-\omega = \frac{\partial^2 \psi}{\partial X^2} + \frac{\partial^2 \psi}{\partial Y^2} \quad (1)$$

Axial Momentum Equation

$$\frac{\partial \psi}{\partial Y} \frac{\partial W}{\partial X} - \frac{\partial \psi}{\partial X} \frac{\partial W}{\partial Y} = \left(\frac{\partial^2 W}{\partial X^2} + \frac{\partial^2 W}{\partial Y^2} \right) + 4 Re - \frac{Ra \sin \lambda}{Pr} (1 - \theta) \quad (2)$$

Dimensionless Energy Equation

$$\frac{\partial \psi}{\partial Y} \frac{\partial \theta}{\partial X} - \frac{\partial \psi}{\partial X} \frac{\partial \theta}{\partial Y} = \frac{1}{Pr} \left(\frac{\partial^2 \theta}{\partial X^2} + \frac{\partial^2 \theta}{\partial Y^2} \right) - \frac{W}{Pr} + \frac{N t^2}{4 Pr} (1 - \theta^4) \quad (3)$$

Where the stream function ψ is defined in terms of the axial and radial velocities as follows respectively:

$$U = \frac{\partial \psi}{\partial Y}, \quad V = -\frac{\partial \psi}{\partial X} \quad (4)$$

The last term of eq. (3) represents the radiation absorption term.

Normalization Parameters

The variables in the governing equations and boundary conditions were transformed to dimensionless formula by employing the following transformation parameters:

$$X = \frac{x}{d}, \quad Y = \frac{y}{d}, \quad Z = \frac{z}{d}$$

$$U = \frac{ud}{\nu}, \quad V = \frac{vd}{\nu}, \quad W = \frac{wd}{\nu}$$

$$\theta = \frac{T}{T_w}, \quad \frac{\partial p}{\partial z} = -\frac{4\rho\nu^2}{d^3} Re, \quad \frac{\partial T}{\partial z} = \frac{T_w}{Pr d},$$

$$Pr = \frac{\nu}{\alpha}$$

$$N = \frac{4\sigma\epsilon T_w^3}{K_R k}, \quad t = K_R d, \quad U = \frac{\partial \psi}{\partial Y},$$

$$V = -\frac{\partial \psi}{\partial X}$$

The boundary conditions applicable to these equations are:

(1) At the inlet of the duct ($Z = 0$):

$$U = V = \psi = \omega = 0,$$

$$\theta = 0.5, \quad W = \frac{Re}{\nu d}$$

(2) At the walls:

$$U = V = W = \psi = 0, \quad \theta = 1$$

$$\frac{\partial \theta}{\partial X} = \frac{\partial \psi}{\partial X} = \frac{\partial \omega}{\partial X} = \frac{\partial W}{\partial X} = 0 \quad (\text{at symmetry line})$$

NUMERICAL METHODS

The elliptic transformation technique which was originally proposed by [Fletcher, 1988] is applied to generate the curvilinear grid for dealing with the irregular cross sections. The transformation functions $\xi = \xi(X, Y)$ and $\eta = \eta(X, Y)$ are obtained to accommodate the irregular shape. Using the curvilinear grid obtained the governing eq. (1) to (3) and the boundary conditions are then discretized and solved in the computation domain (ξ, η) . In this work, an (81 X 61) grid in the transformed domain (ξ, η) is adopted. The grid systems have been properly adjusted to be orthogonal locally at the boundaries. The grid generation technique used is standard and well accepted. Therefore, further description about this technique would not give here.

By using this method, the following general equation can be used to generate all the governing equations (1-3) in computational co ordinate's formula:

$$J\Gamma(\psi_\eta \phi_\xi - \psi_\xi \phi_\eta) = (\tau\phi_\xi + \varpi\phi_\eta + \alpha_1\phi_{\xi\xi} - 2\beta_1\phi_{\xi\eta} + \gamma\phi_{\eta\eta}) + suJ^2 \quad (5)$$

Where ϕ represent the general variable which may be ω , W or θ and su is the source term. Where $\Gamma = 1$ for vorticity transport and axial momentum equations and $\Gamma = \text{Pr}$ for energy equation.

Finite Difference Formulation:

The three-point central difference formula is applied to all the derivatives. Each of

the governing equations can be rewritten in a general form as:

$$ap_{(i,j)}\phi_{(i,j)} = ae_{(i,j)}\phi_{(i+1,j)} + aw_{(i,j)}\phi_{(i-1,j)} + an_{(i,j)}\phi_{(i,j+1)} + as_{(i,j)}\phi_{(i,j-1)} + SU_{(I,J)}J_{(I,J)} \quad (6)$$

Where:

$$ap_{(i,j)} = 2(\alpha_{1(i,j)} + \gamma_{(i,j)})$$

$$ae_{(i,j)} = \alpha_{1(i,j)} - B$$

$$aw_{(i,j)} = \alpha_{1(i,j)} + B$$

$$an_{(i,j)} = \gamma_{(i,j)} - C$$

$$as_{(i,j)} = \gamma_{(i,j)} + C$$

$$B = \left(J_{(i,j)} \Gamma \frac{\psi_{(i+1,j)} - \psi_{(i-1,j)}}{2} - \tau_{(i,j)} \right) / 2$$

$$C = \left(-J_{(i,j)} \Gamma \frac{\psi_{(i,j+1)} - \psi_{(i,j-1)}}{2} - \varpi_{(i,j)} \right) / 2$$

$$SU_{(I,J)} =$$

$$- \frac{\beta_{1(i,j)}}{2J_{(i,j)}} (\phi_{(i+1,j+1)} - \phi_{(i+1,j-1)} - \phi_{(i-1,j+1)} + \phi_{(i-1,j-1)}) + su_{(i,j)}J_{(i,j)}$$

In the equations above i and j indicate to the points of the grid in the generalized coordinates ξ and η respectively.

As pointed out in [Anderson et al, 1984] the Relaxation method can be employed for the numerical solution of eq. (1). For this investigation, the Line Successive Over Relaxation (LSOR) method [Fletcher, 1988] and [Anderson et al, 1984] is used to solve equations (2 and 3). A computer program (Fortran 90) is built to calculate Nu . The convergence criterion for the inner iteration (Error_{in}) of ψ is 10^{-4} and for the outer iteration (Error_{out}) of θ_b is 10^{-10} , where:

$$Error_{in} = 2(\alpha_{1(i,j)} + \gamma_{(i,j)})\Delta\psi_{(i,j)} \quad (7)$$

$$\Delta\psi_{(i,j)} = \frac{\psi_{(i,j)}^{it+1} - \psi_{(i,j)}^{it}}{RP} \quad (8)$$

Where RP is the Relaxation Parameter and equal 1.1 and represent the number of iterations. The outer iteration is checked only for θ_b as follow:

$$Error_{out} = \frac{\theta_b^{it+1} - \theta_b^{it}}{\theta_b^{it}} \leq 10^{-10} \quad (9)$$

EVALUATION OF HEAT TRANSFER:

The peripheral heat transfer is defined through the conduction referenced Nusselt number as:

Local Nusselt number

The peripheral local Nusselt number on the walls of the channel is computed from:

$$Nu_L = \frac{-\frac{\partial\theta}{\partial n}\big|_w}{(1-\theta_b)} \quad (10)$$

Where n represent the dimensionless normal outward direction.

The mean Nusselt number on the wall of the rectangular duct and circular core is obtained by using Simpson's rule:

$$Nu_{c,r} = \frac{1}{s} \int_s Nu_L ds \quad (11)$$

Where s is represents the length of the wetted perimeter in the rectangular duct and circular core.

The mean Nusselt number (Nu) is a measure of the average heat transfer over the internal surface of the rectangular duct and the outer surface of the circular configuration. It is computed from the following equation:

$$Nu = C_c Nu_c + C_r Nu_r \quad (12)$$

Where, $C_c Nu_c$ is a measure of average heat transfer from the outer surface of the circular core while $C_r Nu_r$ corresponds to heat transfer from of the internal surface of the rectangular duct. C_c and C_r are the perimetric ratios for the heat transfer and are defined as:

$$C_c = \frac{\pi R}{H + L + \pi R}$$

$$C_r = \frac{H + L}{H + L + \pi R}$$

RESULTS AND DISSCUSION:

Effect of Circular Core Position:

The heat transfer process through the channel suffers from many changes in the heat transfer process because of the layer of the still air in the corners as shown in **Fig. (2)**. This layer cause to increase the thermal resistance and that lead to decrease the rate of heat transfer. The heat transfer rate through the wall of the circular core is uniform and greater than that on the walls of the rectangular duct. The direction of the heat transfer from the walls towards the core of the channel is shown by the isotherm lines.

The effect of the circular core position on the isotherms and streamlines for air is shown in **Fig. (2-6)**. It is shown when the circular core is lower than the center of the channel, the volume and intensity of the upper cell will be increased, while, for the lower cell its volume and intensity will be decreased until it is vanished because of increasing the cross section area above the circular core. But the lower area is decreased when the circular core is get down. This decreasing in the volume and intensity of the cells under the circular core will be lead to decrease the rate of heat transfer then decrease Nu as shown in **Fig (7)**.

Effect of GR:

. The bulk temperature of air increased with increasing in geometry ratio value as shown in **Fig. (8)** and that because of increasing in the surface area which participating in the heat transfer process

and that result to increase the rate of heat transfer.

Fig. (9) illustrates the variation of mean Nusselt number Nu through the channel with GR value. It is shown that when GR increased Nu increased and that resulting from increasing in the surface area of the circular wall. This increasing of the surface area will lead to increase the rate of heat transfer. The radiation effect is very small for the small values of GR. This effect increased with increasing in GR value because of increasing the heat gain by air with decreasing in the air quantity.

Fig (10) illustrates the change in the value of Nu_L along the wall of the circumference of the circular core with GR value. The value of Nu_L is approximately uniform and equally at small value of GR. For $GR > 0.4$, the value of Nu_L will be changed. and will be decreased in the throat regions because of impended of the wall to the vorticity and that lead to decrease the rate of heat transfer, while, in the other regions Nu_L will be increased because of increasing the intensity of vorticity and its center, and that results to increase the rate of heat transfer. But when GR reached 0.9, the value of Nu_L will be the maximum in the throat regions, this is resulted from the distance between the walls which is very small, and that lead to increase the rate of heat transfer.

Nu_{Lr} on the walls of the rectangular duct decreased with increasing in GR value in the throat regions as shown in **Fig (11)**, while, in the other regions the value of Nu_{Lr} increased when GR increased. The minimum value is approximately equal zero in the right corners of the rectangular duct, and that because of the decreasing in the rate of heat transfer resulting from increasing the thermal resistance of the semi-still air which is generated in these corners. The heat transfer rate through the wall of the circular core is uniform and greater than that on the walls of the rectangular duct.

Effect of Re:

Fig. (12-14) illustrate the isotherms and streamlines for different values of Re. These figures show that the increase in Re will not change the behavior of the stream function and the temperature distribution, but, it will be increase the intensity and the value of stream function and the temperature of the air.

The effect of Re on the value of Nu is shown in **Fig. (15)**, where it is shown that the value of Nu is decreased with increasing Re until it is reached the minimum value at $Re = 350$. But, Nu value will be something increased when Re is increased from 350. When $Re = 1$, the convection process is only natural convection, where the effect of the buoyancy force and the secondary flow had a vital role in the heat transfer process, and that lead to turn the streams of air widely through the cross section area of the channel. So, the increasing in Re is effected negatively on the heat transfer process, where it lead to increase the axial velocity of the flow and implement the vorticity of the air, but it is lower than the case of the natural convection. Also, the radiation effect is very small for the low values of Re, but its effect will be increased with increasing in Re value.

In **Fig. (16)** the effect of Ra on Nu value is shown with the variation in Re. This effect is approximately constant with the variation of Re value.

Radiation Effect:

The correlation equations for the plotted curves are done to know the radiation effect on the rate of heat transfer. These equations are made by using the curve fitting method.

$$Nu = 6.5677 + 39.176 GR^{2.887}$$

$$Nu = 13.0733 + 0.03231 AR^{-9.0938}$$

(Without radiation)

$$Nu = 7.577 + 44.648 GR^{3.1}$$

$$Nu = 12.117 + 0.58597 AR^{-4.55}$$

(With radiation)

For the bulk temperature, the effect of radiation will be written as follow:

$$\theta_b = -12.287 + 13.304 GR^{6.2 \times 10^{-3}}$$

(With Radiation)

$$\theta_b = -15.747 + 16.763 GR^{5.4 \times 10^{-3}}$$

(Without Radiation)

CONCLUSIOS:

- From the present work results and for the channel that described previously, the following conclusions can be obtained:
- When the circular core is lower than the center of the channel, the volume and intensity of the upper cell will be increased, while, for the lower cell its volume and intensity will be decreased.
- The decrease in the volume and intensity of the cells under the circular core lead to decrease the rate of heat transfer
- The bulk temperature of air increased with increasing in geometry ratio. When GR increased Nu increased and that resulting from increasing in the surface area of the circular wall. The value of Nu_L is approximately uniform and constant at small value of GR. For $GR > 0.4$, the value of Nu_L will be changed, and will be decreased in the throat regions but when GR reached 0.9, the value of Nu_L will be the maximum in the throat regions. Nu_{Lr} on the walls of the rectangular duct decreased with increasing in GR value in the throat regions, while, in the other regions the value of Nu_{Lr} increased when GR increased. The minimum value is approximately equal zero in the right corners of the rectangular duct
- The increases in Re will not change the behavior of the stream function and the temperature distribution, but, it will be increase the intensity and the value of stream function and the temperature of the air.
- Nu decrease by 33% with increasing in Re and at $Ra = 400$, while it is increased by 1% with increasing in Ra and at $Re = 100$.
- The radiation effect is very small for the low values of Re, but its effect will be increased with increasing in Re value.
- The radiation effect on the heat transfer coefficient is known by making a correlation equations and this effect show that Nu will be increased.

REFERENCES

- Anderson A., Tannehill C. and Pletcher H. (1984), "Computational Fluid Mechanics and Heat Transfer", McGr
- Bahlaoui A., Raji A., and Hasnoui M., (2005), "Multiple Steady State Solutions Resulting From Coupling Between Mixed Convection and Radiation In An Inclined Rectangular Channel", Int. J. of Mass Heat Transfer
- (<http://www.springerlink.com/content/rv03480249507w41/>).
- Fletcher C. A. J., (1988), "Computational Fluid Techniques for Fluid Dynamics 2", Springer-Verlag.
- Gururaja Rao C., (2004), "Numerical Investigation into Multi-Mode Heat Transfer from a Vertical Channel with Uniform and Discrete Wall Heat Generation", HPC 2004-3th International Conference on Heat Powered Cycles.
- Kim D. M. and Viskanta R., (1984), "Heat Transfer by Conduction, Natural Convection and Radiation across a Rectangular Cellular Structure", Int. J. of Heat and Fluid Flow, Vol.5, No.4, PP.205-213
- (www.springerlink.com/index/6R7T68Q705W73311.pdf).
- Larson D. W. and Viskanta R., (1976), "Transient Combined Laminar Free Convection and Radiation in a Rectangular Enclosure", J. Fluid Mechanics, Vol.78, Part 1, PP.65-85.
- Pu W. L., Cheng P. and Zho T. S., (1991), "An Experimental Study of Mixed Convection Heat Transfer in Vertical Packed Channel", AIAA, J. of Thermophysics and Heat Transfer, Vol.13, No.4, PP.517-521.
- Yang G. and Ebadian M. A., (1991), "Thermal Radiation and Laminar Forced Convection in the Entrance of a Pipe With Axial Conduction and Radiation", Int. J. Heat Fluid Flow, Vol.12, no. 3, pp. 202-209.

NOMENCLATURE

Symbol	Description	Units
AR	Aspect ratio ($AR = L / H$)	-
D	The diameter of circular core	m
d	The hydraulic diameter of the channel	m
H	The height of the rectangular duct	m



J	Jacobean of direct transformation	-
Symbol	Description	Units
k	Thermal conductivity of the air	W/m.°C
K_R	Volumetric absorption coefficient	m^{-1}
L	The width of the rectangular duct	m
N	Conduction-radiation parameter($4\sigma\epsilon T_w^3/K_R k$)	-
Nu	The mean Nusselt number	-
Nu_{LC}, Nu_{Lr}	The local Nusselt number in the circular and rectangular walls respectively	-
P_c, P_r	Wetted perimeter for the circular and rectangular walls respectively	m
Pr	Prandtl number ($Pr = \nu/\alpha$)	-
R	The circular core radius	m
Ra	Rayleigh number ($Ra = \beta g d^3 T_w / \alpha \nu$)	-
Re	Reynolds number [$Re = (-d^3/4\rho\nu)(\partial P/\partial z)$]	-
GR	Geometry ratio ($GR = D/H$)	-
T	Air temperature	°C
t	Optical thickness($t = K_R D_h$)	-
T_w	Wall temperature	°C
u, v, w	The velocity components in x, y and z direction respectively	m/s
U, V, W	The normalized velocity components in x, y and z direction respectively	-
x, y, z	The physical coordinates of the channel	m

X, Y, Z	The dimensionless physical coordinates of the channel	-
---------	---	---

GREEK SYMBOLS

Symbol	Description	Units
α	Thermal diffusivity	m ² /s
$\alpha_1, \beta_1, \gamma, \omega, \tau$	The coefficient of transformation of BFC	-
β	Coefficient of thermal expansion	1/K
ε	Emissivity	-
ξ, η	Coordinates in the transformed domain	m
θ	Dimensionless air temperature	-
θ_b	Dimensionless bulk temperature	-
θ_c, θ_r	Dimensionless temperature of the circular core and rectangular duct walls respectively	-
θ_w	Dimensionless wall temperature	-
ν	Kinematics' viscosity of air	m ² /s
ρ	Air density	kg/m ³
σ	Stefan Boltzmann constant	W/m ² K ⁴
ψ	Dimensionless air stream function	-
ω	Dimensionless air vorticity	-

SUPERSCRIPTS AND SUBSCRIPTS

Symbol	Description	Units
b	Bulk	-
C	Circular core	-
g	Generation	-
(i, j)	Grid nodes in X and Y directions	-
L	Local	-
<i>r</i>	<i>rectangular duct</i>	-
<i>w</i>	<i>Wall</i>	-
Symbol	Description	Units
°	<i>Degree</i>	-
-	<i>Average</i>	-

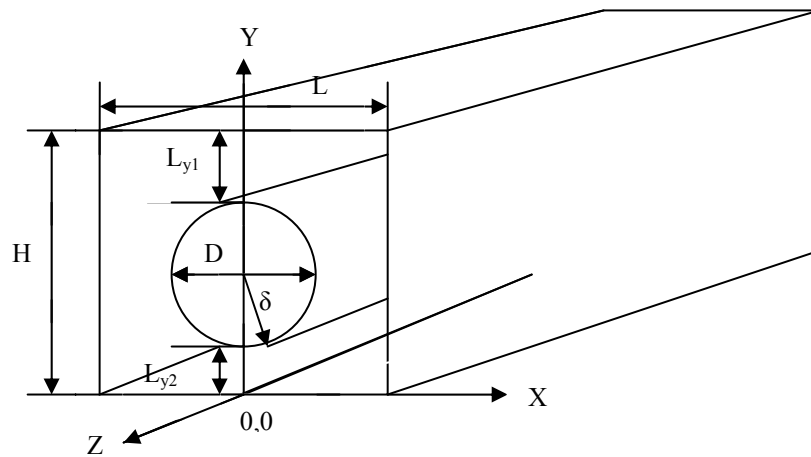


Fig.(1) Schematic of the Problem Geometry

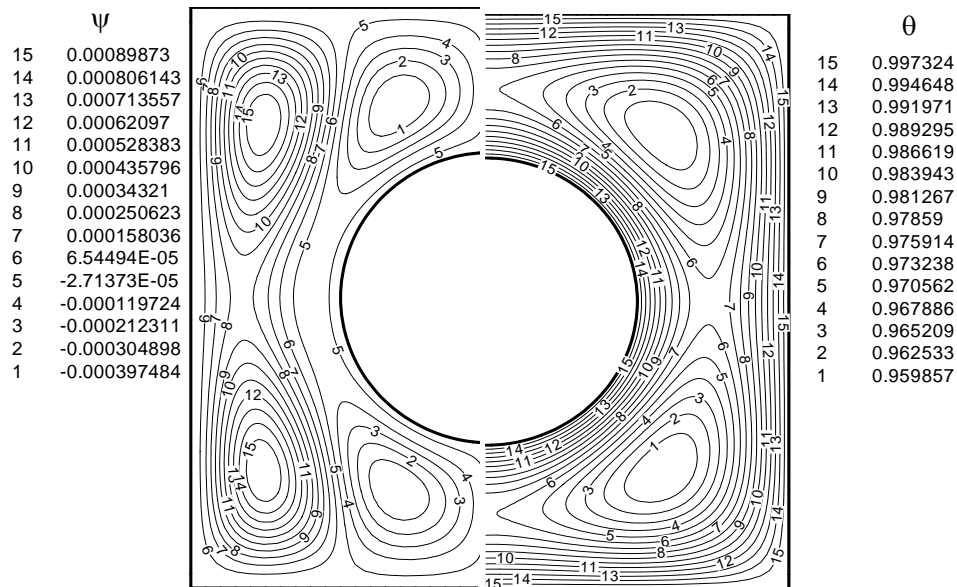


Fig. (2) Streamlines and Isotherms for Concentric Core and for GR = 0.5

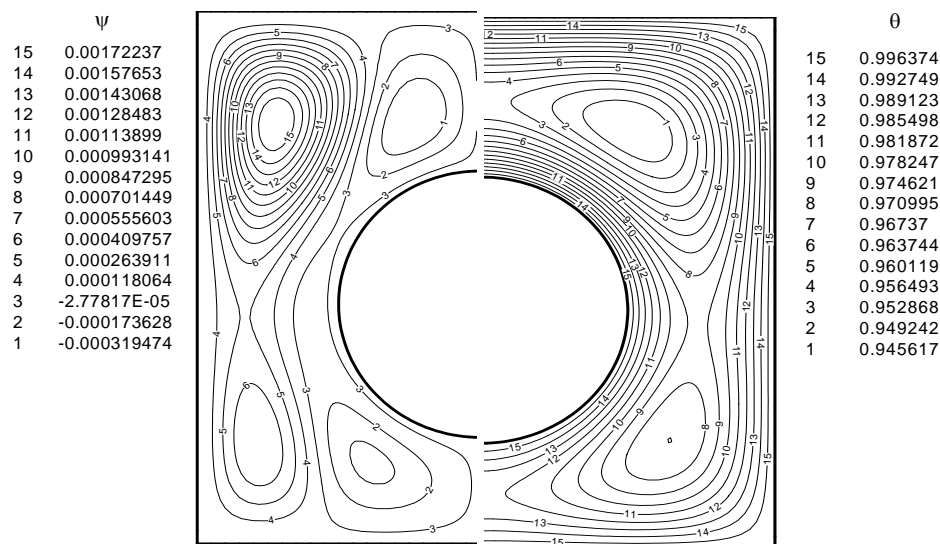


Fig. (3) Streamlines and Isotherms for $Ly_2 = 0.3$

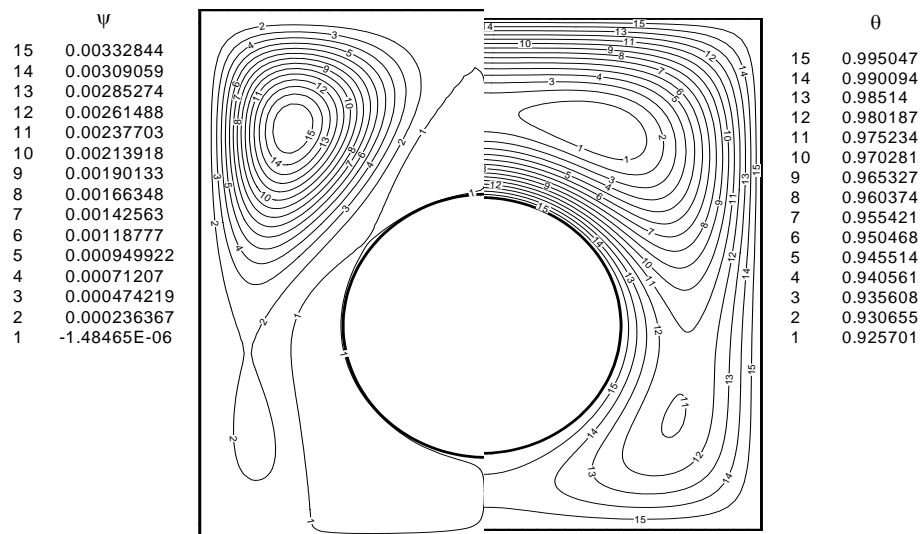


Fig. (4) Streamlines and Isotherms for $Ly_2 = 0.35$

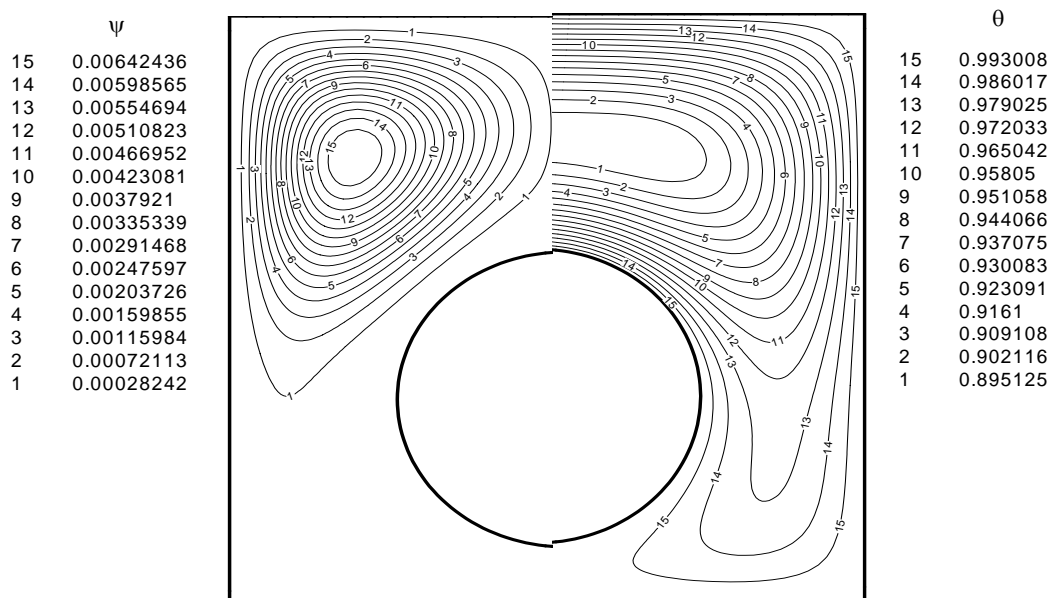


Fig. (5) Streamlines and Isotherms for $Ly_2 = 0.4$

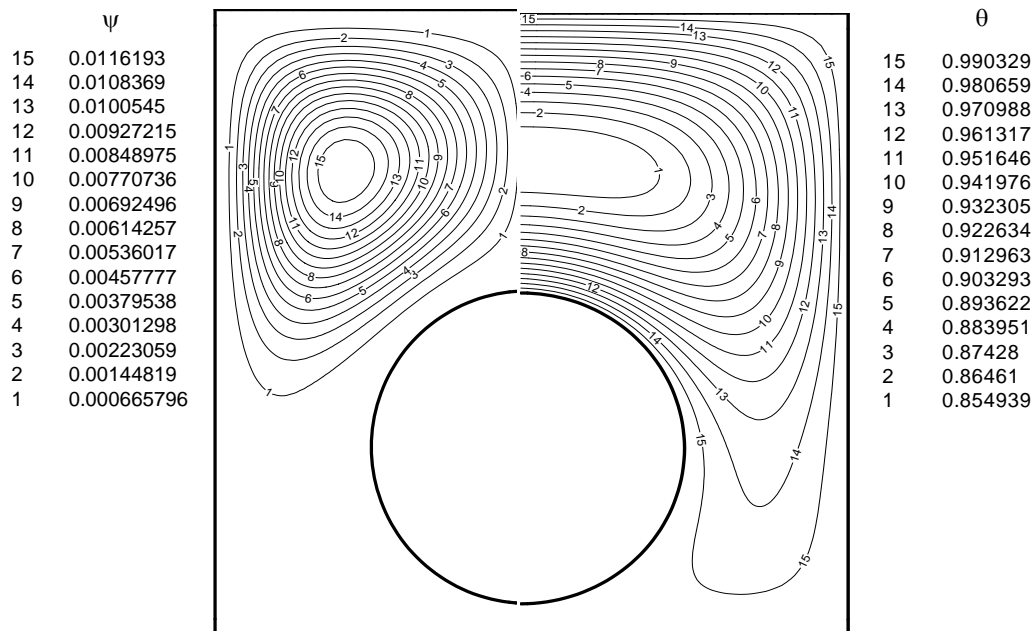


Fig. (6) Streamlines and Isotherms for $Ly_2=0.45$

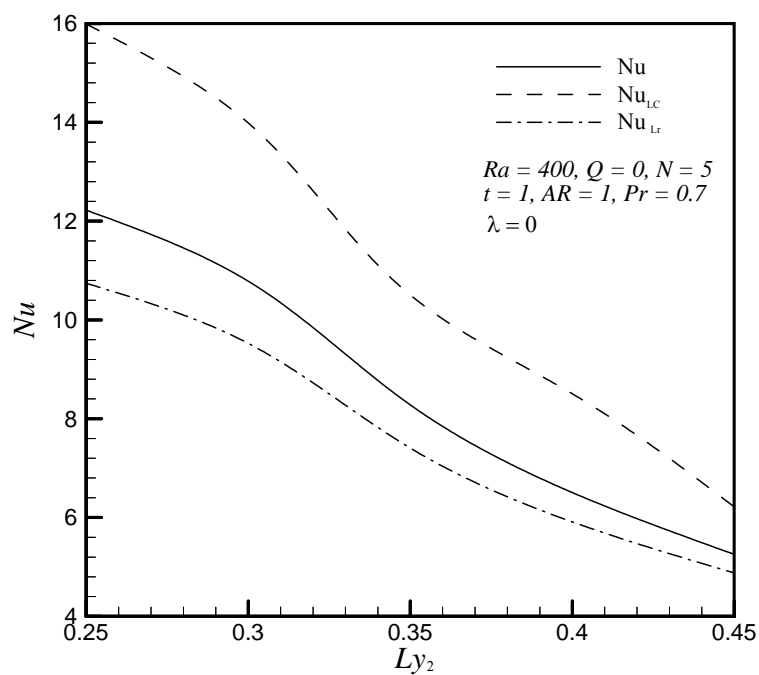


Fig. (7) The Effect of Circular Core Positions

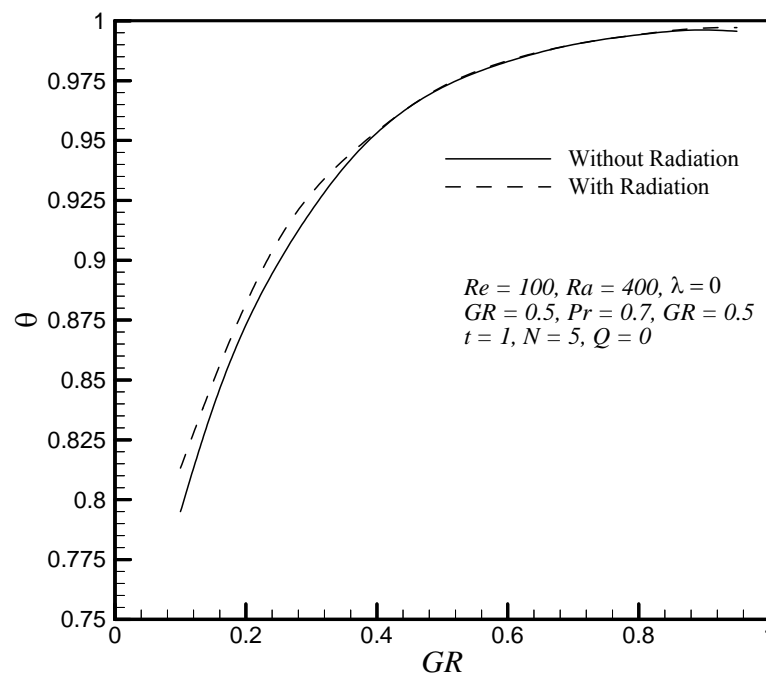


Fig. (8) The Effect of Geometry Ratio on the Bulk Temperature

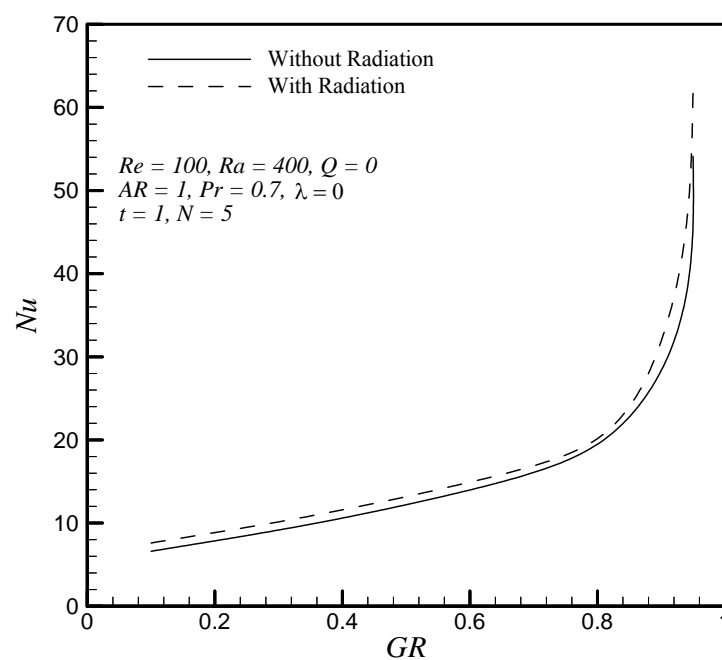


Fig. (9) The Variation of the Mean Nusselt Number with Geometry Ratio

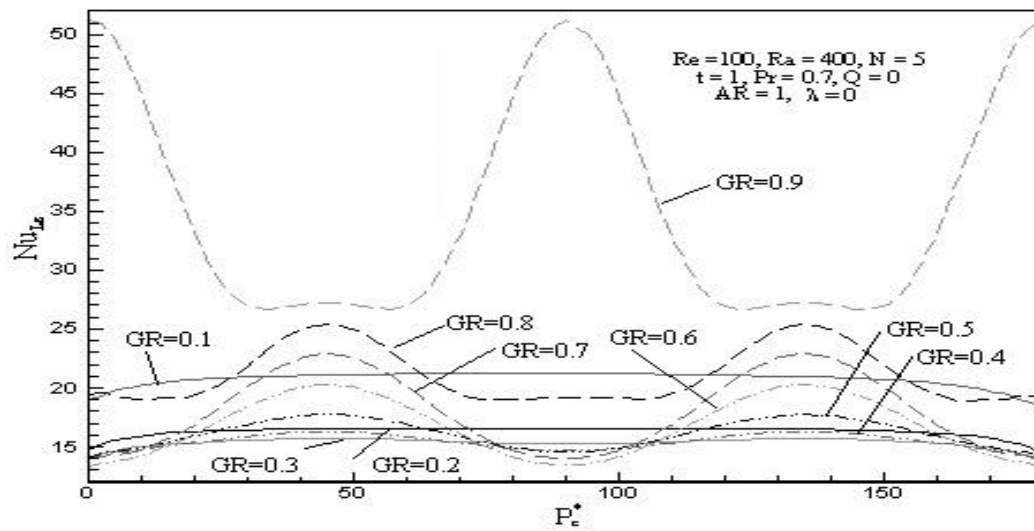


Fig. (10) The Variation of the Local Nusselt Number with P_c^*

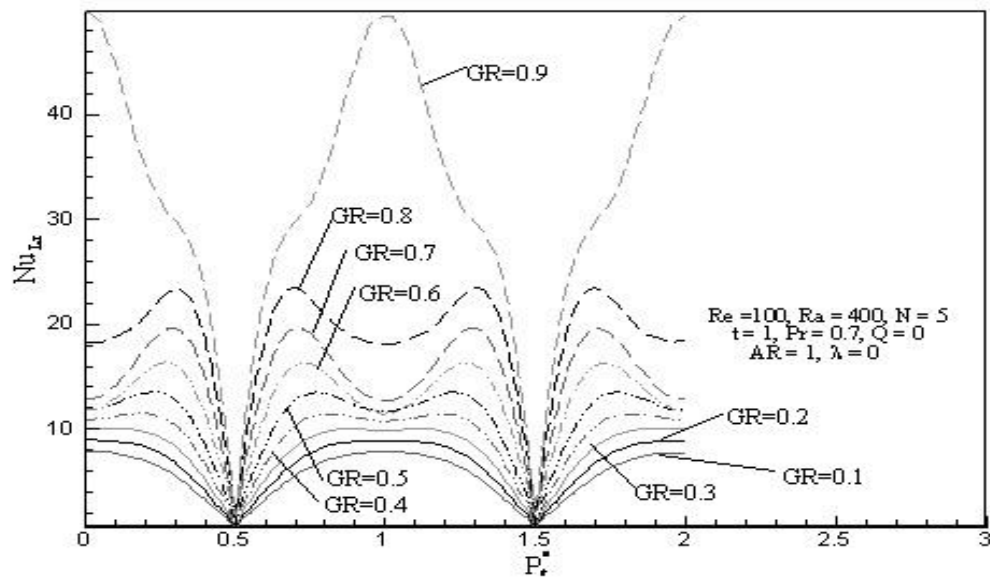


Fig. (11) The Variation of the Local Nusselt Number with P_r^*

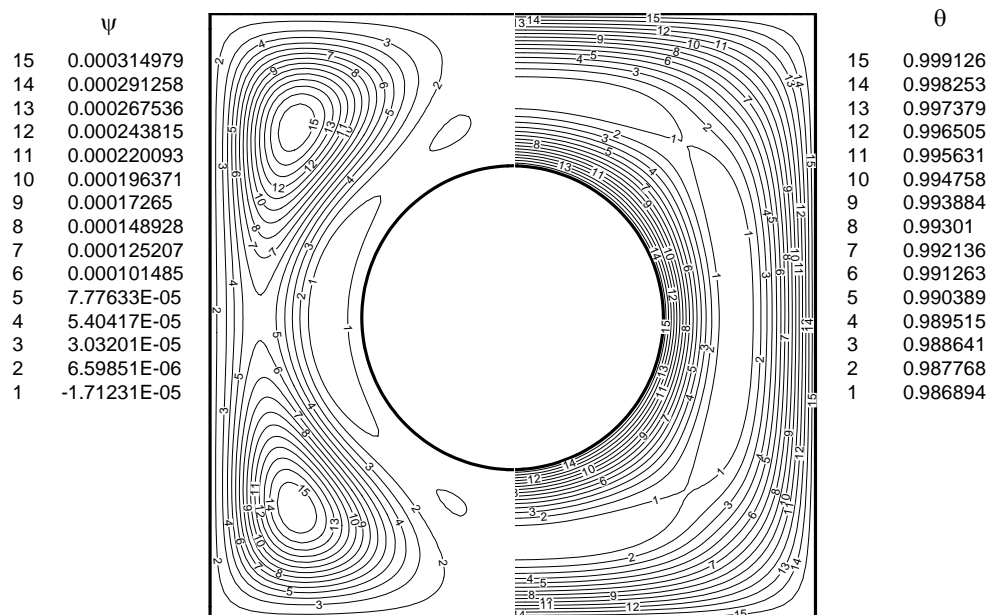


Fig. (12) Streamlines and Isotherms for $Re = 1$

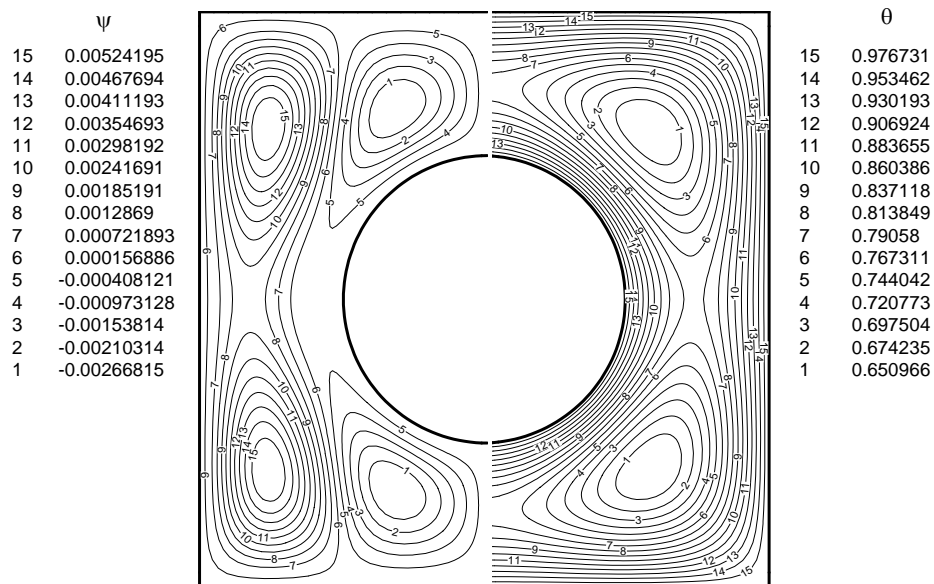


Fig. (13) Streamlines and Isotherms for $Re = 1000$

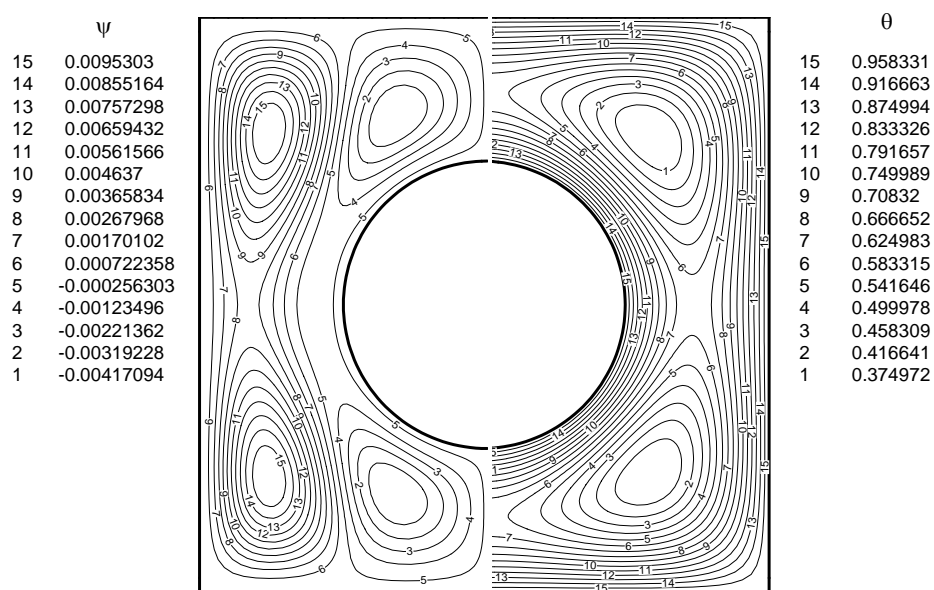


Fig. (14) Streamlines and Isotherms for $Re = 2000$

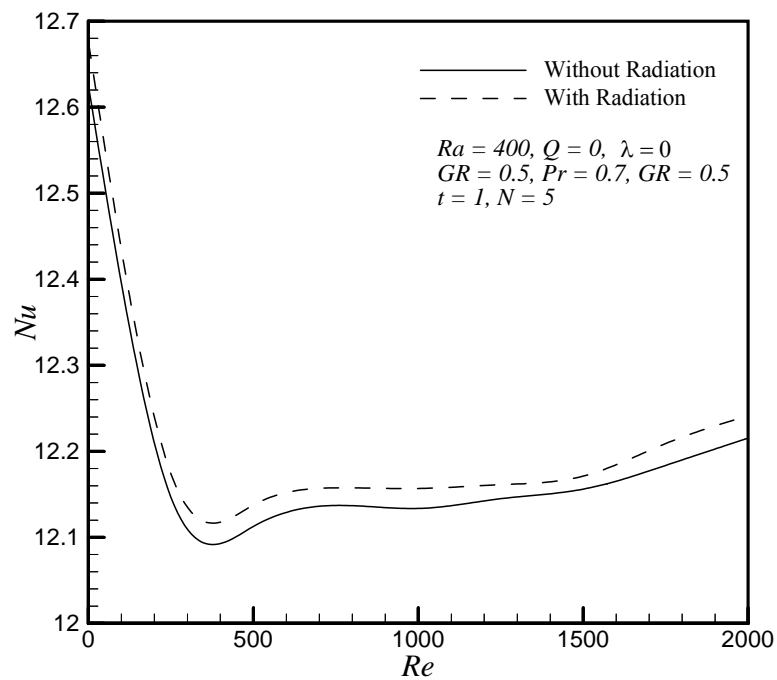


Fig. (15) The Variation of the Mean Nusselt Number with Reynolds Number

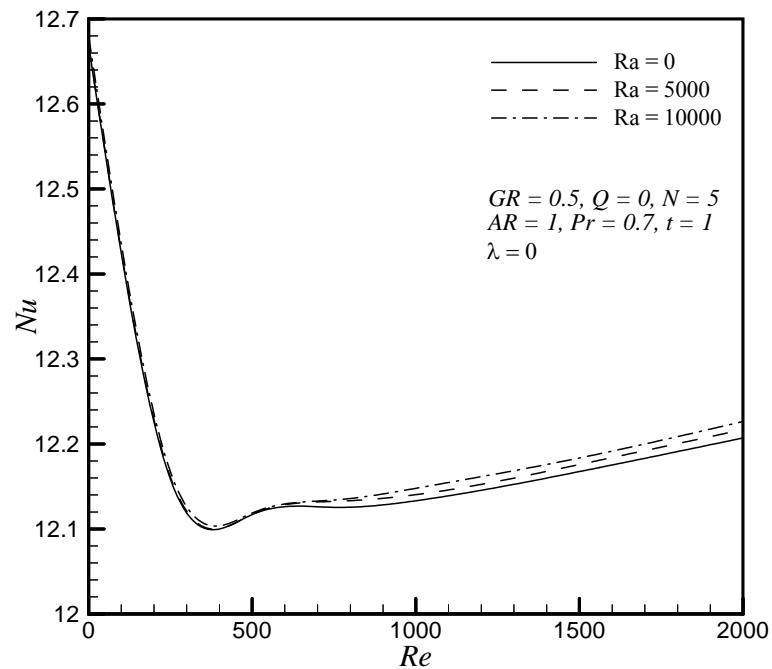


Fig. (16) The Variation of Nusselt Number with Re for Different Values of Ra

BEHAVIOR OF CONCRETE BEAMS REINFORCED IN SHEAR WITH CARBON FIBER REINFORCED POLYMER

Dr. Abdul-Muttalib I. Said Al-Mussaue
Ass. Prof
University of Baghdad
College of Engineering

Mr. Amjad H. Abdul-Razaq Al-Modhafer
Ass. Lecturer
University of Kufa
College of Engineering

ABSTRACT

Carbon fiber reinforced polymers (CFRP) were widely used in strengthening reinforced concrete members in the last few years, these fibers consist mainly of high strength fibers which increase the member capacity in addition to changing the mode of failure of the reinforced concrete beams. Experimental and theoretical investigations were carried to find the behavior of reinforced concrete beams strengthened by CFRP in shear and bending. The experimental work included testing of 12 beams divided into 4 groups; each group contains 3 beams. The following parameters were taken into consideration:

- Concrete crushing strength.
- CFRP strengthening location (shear strengthening and both shear and flexure strengthening).

Reinforced beams were simply supported subjected to two point loads. Each group consists of three beams; the first beam without CFRP, the second one, is strengthened with CFRP in shear and the third is strengthened with CFRP in both flexure and shear. Four groups with different crushing strength of (12, 20, 30 and 39 MPa). The CFRP sheets are attached externally.

It was found that in beam with low crushing strength loads transfer to the CFRP at early stages while in those of high crushing strength, CFRP contribution only starts when full strength of the beam is fulfilled. A full bond between CFRP sheets and the concrete is assumed in the theoretical analysis. Comparison between the theoretical and the experimental results revealed the validity of the numerical analysis and the developed methods such that there was a difference of 13% in the ultimate strength for the tested and analyzed beams.

خلاصة:

استعملت العناصر الإنشائية الخرسانية المسلحة المقواة بألياف البوليمر الكربونية في السنوات الحديثة ، تتألف ألياف التقوية البوليمرية بصورة أساسية من ألياف (عالية المقاومة) حيث تزيد سعة التحمل بالإضافة إلى تغيير أسلوب الفشل للعتبات الخرسانية المسلحة. أجريت تحريات عملية ونظرية لسلوك العتبات الخرسانية المسلحة، لحالتى تقوية العتبات في مناطق فشل القص والانثناء المقواة باستخدام CFRP حيث يتكون البرنامج العملي من 12 عتبة فحص قسمت إلى أربعة مجاميع ،كل مجموعة تضم 3 عتبات. الدراسة أخذت بنظر الاعتبار مقاومة الانضغاط للخرسانة و حالة التقوية ، استعملت مرة للتقوية في منطقة القص وأخرى في منطقتي القص والانثناء معاً لكل العتبات تم فحصها في فضاء بسيط الإسناد ومتعرض لنقطتي تحميل بينما المتغير الرئيس يمثل مقاومة الانضغاط للخرسانة و موقع CFRP. كل مجموعة تتكون من ثلاثة عتبات الأول وهو النموذج المرجعي وهو خالي من CFRP و الثاني يحتوي على CFRP في منطقة القص و هي عبارة عن سبعة شرائح مائلة بزاوية 45 درجة و الثالث يحتوي على CFRP في منطقتي القص والانثناء.

كل مجموعة لها مقاومة انضغاط مختلفة عن الأخرى وهي (12-20-30-39 MPa). استعمل CFRP كمقوي خارجي. أن استعمال CFRP له تأثير على نتائج الحمل الأقصى، شكل التشقق، الهطول. تم اكتشاف أن CFRP يشارك الخرسانة الضعيفة في أوقات مبكرة من الحمل بعكس الخرسانة التي لها قوة انضغاط عالية حيث تتحمل أولاً هي لوحدها جميع الاجتهادات ثم تشاركها شرائح CFRP في التحمل. إن أفضل استخدام لشرائح CFRP في منطقة القص بسبب تحول القوى بصورة مباشرة إلى شد على هذه الشرائح.

تم استعمال التحليل اللاخطي بواسطة العناصر ثلاثية الأبعاد لتحري أداء العتبات الخرسانية المسلحة المقواة ب CFRP ، حيث تم استخدام البرنامج الحاسوبي ANSYS.

اعتبرنا هنالك تماس تام بين شرائح CFRP والخرسانة. وتم الحصول على تنبؤ جيد لسلوك ما بعد التصدع. المقارنة بين النتائج النظرية والعملية أكدت صلاحية التحليل العددي و حيث كانت أكبر نسبة فرق في المقاومة القصوى أقل من 13 % لكل العتبات المفحوصة.

Keywords: Crushing strength, CFRP, Shear, Inclined strips, flexure, strengthening

INTRODUCTION:

A carbon fiber sheet is formed by laying out fibers in single or multiple directions and embedding in a protective epoxy resin. A carbon fiber sheet receives particular attention due to its higher strength, stiffness, corrosion and fatigue resistance with reasonable cost. One advantage of using a fiber composite material is the negligible increase in dead load due to its light weight; in addition, it can be easily carried to construction site in rolls. Because the reinforcing technique is much simpler with fiber composite, strengthening/retrofitting work is more convenient in a limited workspace and no specific work experience and heavy construction equipment are required at the site.

Carbon fiber sheet has a very high unidirectional tensile strength but has stiffness close to that of steel. Typical values are between 2500-4600 MPa for tensile strength and 235-269 GPa for Young's modulus. The behavior is essentially linearly elastic up to the tensile strength limit. Once it reaches its tensile strength, it fails in a perfectly brittle model, **Figure 1**. Fibers are assumed to have strength and stiffness only in the fiber direction and no resistance perpendicular to the fiber direction is considered. Because of its negligible thickness, carbon fiber sheet exhibit no effective compression or bending stiffness. Taking the above characteristics into account, a finite element with only axial stiffness is used to represent carbon fiber in structural analysis.

Fiber materials commonly used are carbon, glass or aramid. The different FRP materials and systems have varying properties and behavior. A qualitative comparison of the performance of carbon, glass, and aramid composites is presented in **Table 1**.

This carbon fiber used to manufacture an unidirectional tow sheet that has a width off 330 mm and is suitable for applications requiring a wet lay-up process to conform to the surface configuration of the structure as shown in **Figure 2**.

EXPERIMENTAL WORK:

The experimental program consisted of testing twelve simply supported beams. Beams with rectangular cross sections of 150 mm width by 280 mm height and 3350 mm length. A span between supports of 3200 mm and distance between loads of 1200 mm. The longitudinal reinforcement consists of three No.16 bars (16-mm-dia.) in tension and two No. 10 bars (10-mm-dia.) in compression, equivalent to reinforcement ratios of $\rho=0.0157$ and $\rho'=0.0041$, respectively.

Figures 3 and 4 show specimen dimensions, reinforcement details, support locations, and location of loading points.

No shear reinforcement in tested beam to ensure that shear failure in happen before bending failure.

In order to identify the test specimens with different strengthening schemes and different concrete strengths, the following designation system is used as list in **Table 2**:

Figures (4), show the reinforced concrete beams with CFRP in shear and flexure zone (side and bottom view).

TESTING PROCEDURE:

All beams were tested in a universal testing machine, with maximum capacity of 2000 kN. Beam was loaded directly at the top face with two equal concentrated loads. The ends of all beams were extended 125mm beyond the supports centerline to provide adequate anchorage for the longitudinal steel. 60mm x150mm bearing plates were used at loading points and at supports to avoid local crushing of concrete. The beams were tested under static loads, loaded in successive increments up to failure. For each increment, the load was kept constant until the required readings were recorded.

Demec points were used for each tested beam at mid-span on concrete surface and CFRP shown in **Figures 5** and the initial distance between each two horizontal Demec points were calibrated using an accompanying special ruler.

TEST RESULTS

The ultimate load and mid span deflections at cracking and ultimate stages are shown in **Table 4**. The same mode failure occurred for all beams. This mode was a diagonal shear crack causes rupture of all CFRP sheets located in the shear zone at ultimate load level. Discussion of results obtained for each group is presented in the following sections. The beams before tested are shown in **Figures 6**.

CRACK PATTERNS AND FAILURE MODE:

The loads are applied gradually up to failure. **Figure 7** shows crack patterns of all tested beams.

The sketch the map of cracks of *BC1*, *BC2*, *BC3* and *BC4* shown in **Figures 8**.

LOAD AGAINST MID-SPAN DEFLECTION:

From the load deflection curves of the tested beams it can be observed that the load against mid-span deflection response can be divided into three stages of behavior. In the first stage, a linear behavior of the load deflection response is observed. In the second stage, a nonlinear behavior of the load deflection response is noticed. Finally in third stage, as the applied load reaches near its ultimate value, the rate of increase in deflection is substantially exceeding the rate of increase in the value of the applied loads. **Figure 9**, shows the load-deflection for beams having same crushing strength at $f'_c=12, 20, 30$ and 39 MPa respectively.

FINITE ELEMENT MODEL:

The tested beams where analyzed using **ANSYS** program (**ANSYS** 2005 version 10). Four different materials are involved concrete, reinforcement, steel plates, and CFRP strips.

Concrete: the solid 65, 3-D reinforced concrete solid element was used to represent concrete in the models. The element using a $2 \times 2 \times 2$ Gaussian set of integration points is defined by eight nodes having three degrees of freedom at each node: translations in the nodal *x*, *y*, and *z* directions. This element is capable of cracking in tension and crushing in compression.

Steel: the solid 45 is used for the 3-D modeling of structural members steel bearing plates located at supports and under the applied loads.

Reinforcement: The link 8 element is a uniaxial tension-compression element with three degrees of freedom at each node, translations in the nodal *x*, *y*, and *z* directions. This element is used to represent the steel bars.

CFRP Sheets: Solid 46 is a layered version of the 8-node structural solid designed to model layered thick shells or solids. The element allows up to 250 different material layers. In present study, this element is used to represent CFRP strips.

Tested beams are $150 \text{ mm} \times 280 \text{ mm} \times 3350 \text{ mm}$; with a span between supports of 3200 mm . **Figure 10**, illustrates typical dimensions for all four beams before CFRP reinforcing. By taking advantage of the symmetry of the beams, a quarter of the full beam was used for modeling. This approach reduced computational time and computer disk space requirements significantly. A quarter of the beam model is shown in **Figure 11**.

Figure 12 shows typical steel reinforcement for a quarter beam model.

Ideally, the bond strength between the concrete and steel reinforcement should be considered. However, in this study, perfect bond between materials was assumed. To provide the perfect bond, the link element for the steel reinforcing was connected between nodes of each adjacent concrete solid element, so the two materials shared the same nodes. The same approach was adopted for CFRP composites. The high strength of the epoxy used to attach CFRP sheets to the beams supported the perfect bond assumption.

ANALYTICAL RESULTS:

The accuracy of the finite element modeling is determined by ensuring that the ultimate load is reasonably predicted in comparison with the experimental results, and the load-deflection curves are close to the experimental curves as well as the crack patterns are similar to that obtained from experimental test.

Comparison of the load-deflection curves, cracking loads, ultimate load carrying capacity and crack pattern by the finite element analysis and the laboratory tests is made.

The ratios of the predicted finite element ultimate loads to the corresponding experimental ultimate loads of the analyzed beams are listed in **Table 5**.

NUMERICAL LOAD VERSUS MID-SPAN DEFLECTION:

Figures 13 shows the load versus mid-span deflection curves for the finite element analyses and experimental results for beams.

Several conclusions are drawn from may be notice from comparison between experimental and analytical case studies.

- The theoretical results are nearby the experimental results as the appears of beam at the mid span deflection whereas the basic splits
- The failure load predicted is very close to the failure load measured during experimental testing.
- Established the beam in analytical analysis carried load greater than from experiential results due to technique of presented of model in ANSYS are it ideal and it not afforded to any outside factors corresponding to the experimental results.
- The theoretical solution gives a good impression in the reinforced concrete beam strengthened by CFRP, and it is possible to dispense of experimental work.

CONCLUSIONS:

- From test results and observations, the following conclusions can be drawn:
- Using of CFRP as an external strengthening technique results in a noticeable effect on ultimate load, crack pattern, deflections and as described below:
 - Increasing the ultimate load and the capacity of the beams.
 - Delaying the crack appearance and reducing the crack width.
- The location of CFRP sheets has a major effect; attaching CFRP in bottom face in addition to side face has more effect than when attaching the same quantity of CFRP to the side faces of beams.
- In all cases in the present work, the failure in strengthened beams is caused by shear failure followed by CFRP rupture.
- The presence of external CFRP bonded to concrete beams increases the ultimate load at failure to a significant value. The maximum increase in the ultimate strength of externally strengthened beams by CFRP depends on the amount of the area and configuration of the external CFRP sheet added.

- In this study, it is observed that the use of external CFRP sheet connected to the tension sides of beams could enhance the ultimate load capacity by (58%) over the capacity of the identical unstrengthened control beam.
- Using CFRP for strengthening beams at shear zone by CFRP sheet is found successful.
- 10. The beam strengthening by shear at any compressive strength of concrete are more load capacities less than from the beam strengthening for shear and flexure.
- 11. The three-dimensional finite element model used in the present work is able to simulate the behavior of externally strengthened reinforced concrete beams by CFRP in shear and flexural groups.
- 12. The comparison between the numerical and the experimental results declared the validity of the numerical analysis and the methodology developed here where the maximum difference ratio in ultimate load was less than 13% for all the tested and analyzed beams.
- 13. The general behavior of the finite element models represented by the center span load deflection curve shows good agreement with the test results from the experimentally tested beams.

NOTATION

ACI= American Concrete Institute

ANSYS=Finite Element Computer Program

CFRP=Carbon Fiber Reinforced Polymer

REFERENCES

- ACI Committee 318, 2002, "PCA Notes on ACI 318-02 Building Code Requirement for Structural Concrete," American Concrete Institute.
- ACI Committee 318, 2008, "Building Code Requirement for Structural Concrete (ACI 318-08) and Commentary," American Concrete Institute, Farmington Hills.
- ACI Committee 440, 2002, "Guide for the design and construction of externally bonded FRP systems for strengthening of concrete structures," American Concrete Institute, Michigan, USA.

- Al-Mahaidi, R., Lee, K., and Taplin, G., "Behavior and Analysis of RC T-Beams Partially Damaged in Shear and Repaired with CFRP Laminates", Monash University, Australia; 2001, al-mahaidi@eng.monash.edu.au
- ANSYS, 2005, "ANSYS Help," Release 10.
- Kachlakev, D., Miller, T., "Finite Element Modeling of Reinforced Concrete Structures Strengthened With FRP Laminates", Final Report, Oregon Department of Transportation, May, 2001.

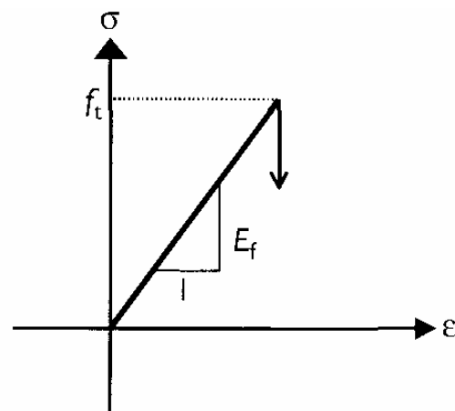


FIGURE 1, Carbon Fiber Sheet Modeling in Finite Element analysis

Table 1, Qualitative Comparison of Different Fibers Used in Composites.

Condition	Type of fibers used in composite		
	Carbon Fibers	Glass Fibers	Aramid Fibers
Tensile Strength	Very good	Very good	Very good
Young's Modulus	Very good	Good	Adequate
Long-term behavior	Very good	Good	Adequate
Fatigue behavior	Excellent	Good	Adequate
Bulk density	Good	Excellent	Adequate
Alkaline resistance	Very good	Good	Inadequate
Price	Adequate	Adequate	Very good



FIGURE 2, Carbon Fiber Sheet

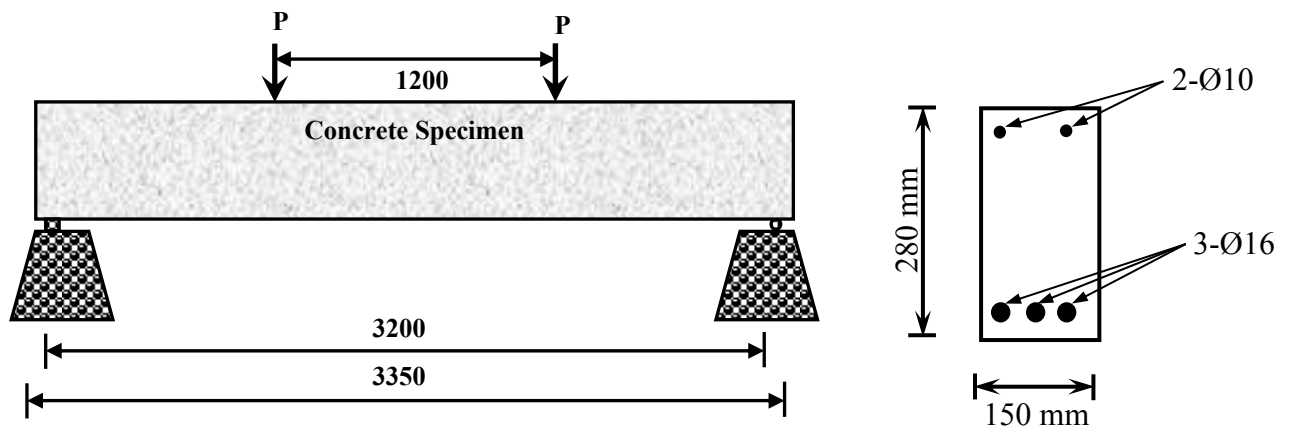


FIGURE 3, Geometry of Laboratory Specimens

Table 2, Classifications of Beams

No.	The Symbol	The Name
1	BC1	Beam Control at compressive strength equal 12 MPa
2	BS1	Beam Strengthened for shear at compressive strength equal 12 MPa
3	BF1	Beam Strengthened for shear and flexure at compressive strength equal 12 MPa
4	BC2	Beam Control at compressive strength equal 20 MPa
5	BS2	Beam Strengthened for shear at compressive strength equal 20 MPa
6	BF2	Beam Strengthened for shear and flexure at compressive strength equal 20 MPa
7	BC3	Beam Control at compressive strength equal 30 MPa
8	BS3	Beam Strengthened for shear at compressive strength equal 30 MPa
9	BF3	Beam Strengthened for shear and flexure at compressive strength equal 30 MPa
10	BC4	Beam Control at compressive strength equal 39 MPa
11	BS4	Beam Strengthened for shear at compressive strength equal 39 MPa
12	BF4	Beam Strengthened for shear and flexure at compressive strength equal 39 MPa

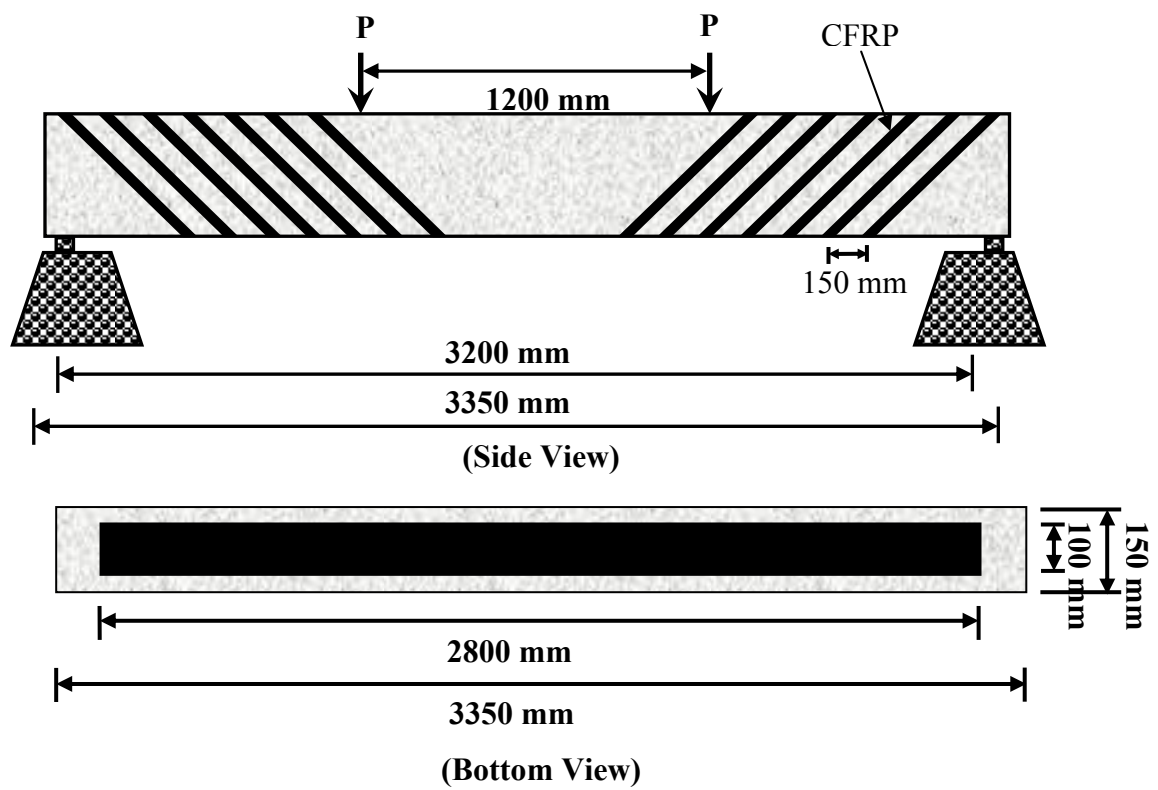


FIGURE 4, Specimens with CFRP in Flexure Zone



FIGURE 5, Demec Points in Concrete and CFRP

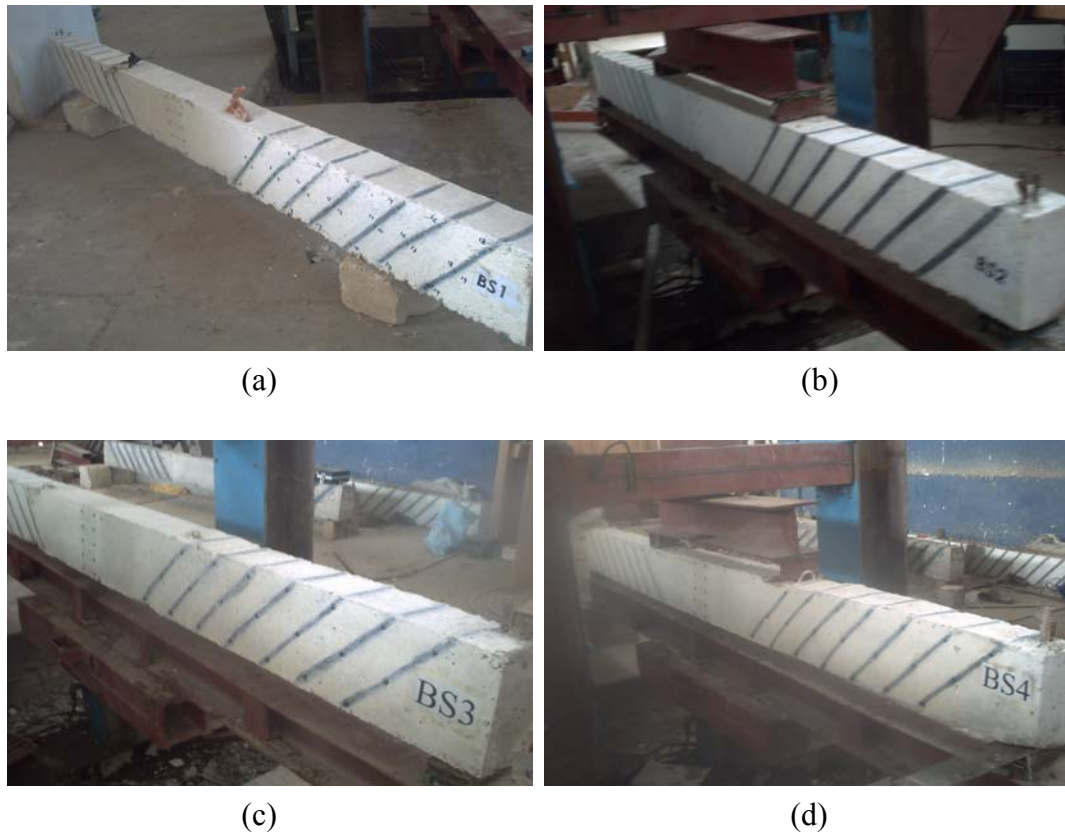


FIGURE 6, Beams Strengthened for Shear ($f'_c=12, 20, 30$ and 39 MPa)

Table 4, Experimental results of the tested beams.

Group no	Beam designation	crushing strengths (MPa)	Total applied load (KN)	Mid-span deflection (mm)	Percentage increase in ultimate load with respect to reference beam %	Percentage increase in ultimate deflection with respect to reference beam %
			P_u	u		
1	BC1	12	45	9.229	-----	-----
	BS1	12	65	22.625	44.4	145.2
	BF1	12	70	29.445	55.5	219
2	BC2	20	58	13.348	-----	-----
	BS2	20	69	21.679	19	62.4
	BF2	20	80	27.81	37.9	108.3
3	BC3	30	60	14.498	-----	-----
	BS3	30	71	19.702	18.3	35.9
	BF3	30	95	31.236	58.3	115.5
4	BC4	39	80	15.41	-----	-----
	BS4	39	95	23.318	18.8	51.33
	BF4	39	104	32.1	30	108.3

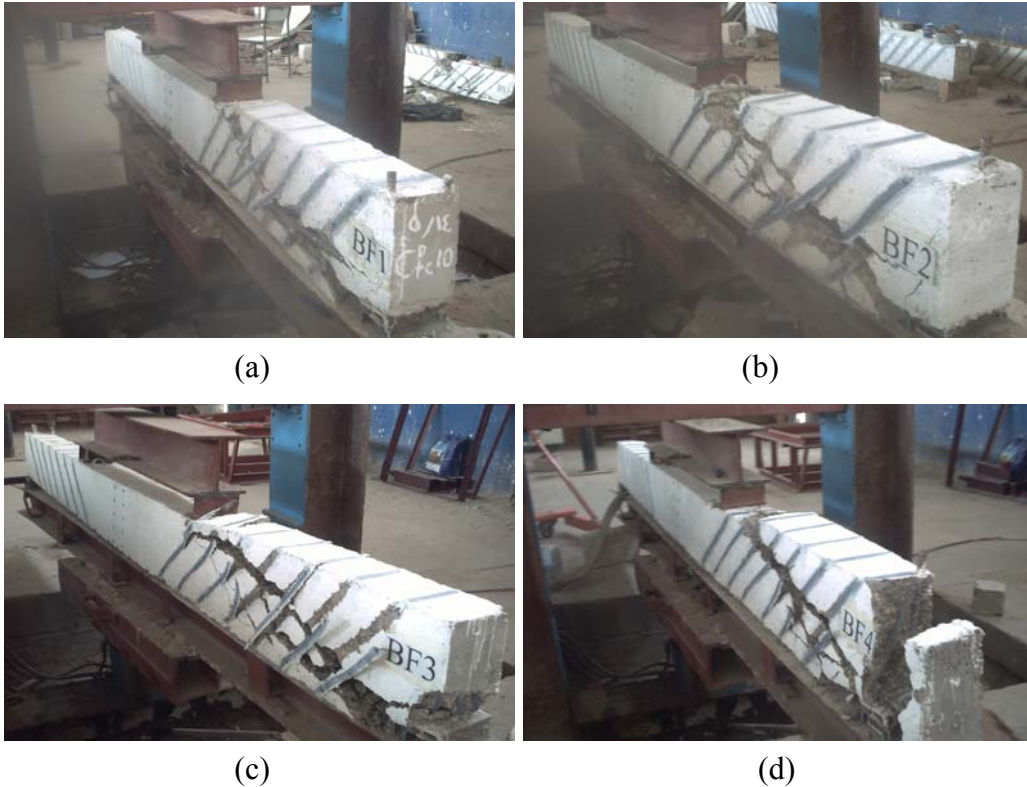
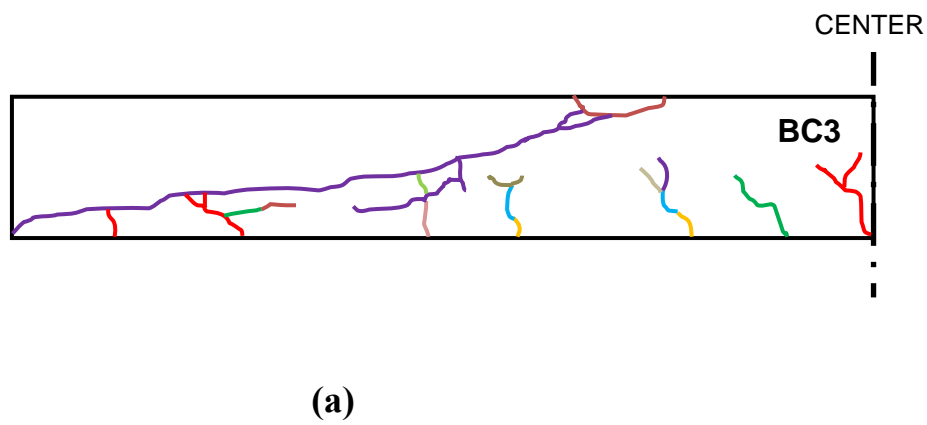
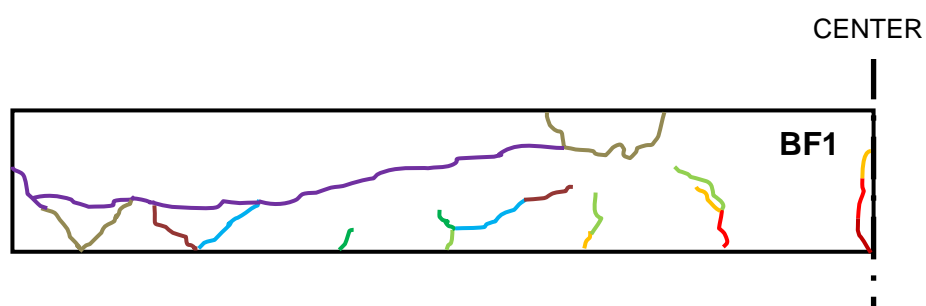


FIGURE 13, BF1, BF2, BF3 and BF4 After Tested

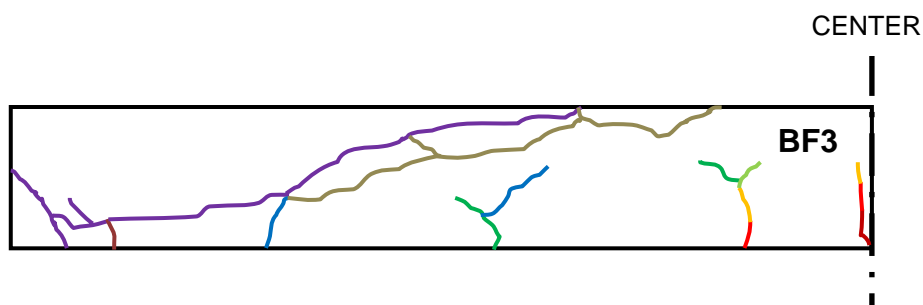


color	Load (kN)
	10
	20
	25
	35
	40
	45
	50
	55



(b)

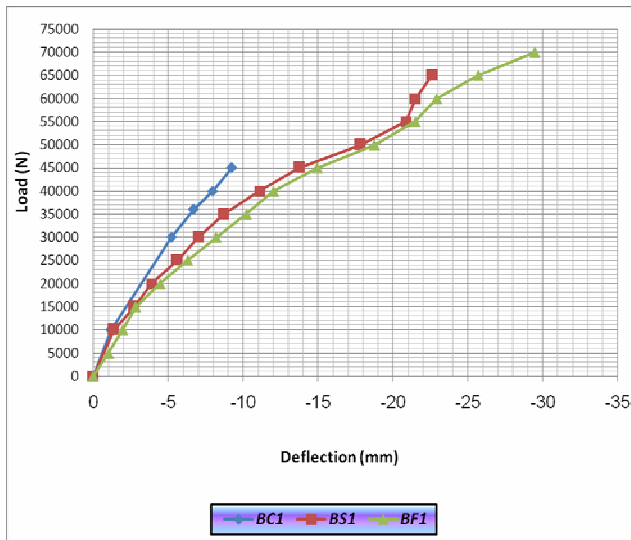
color	Load (kN)
	15
	20
	30
	40
	50
	60
	70
	73



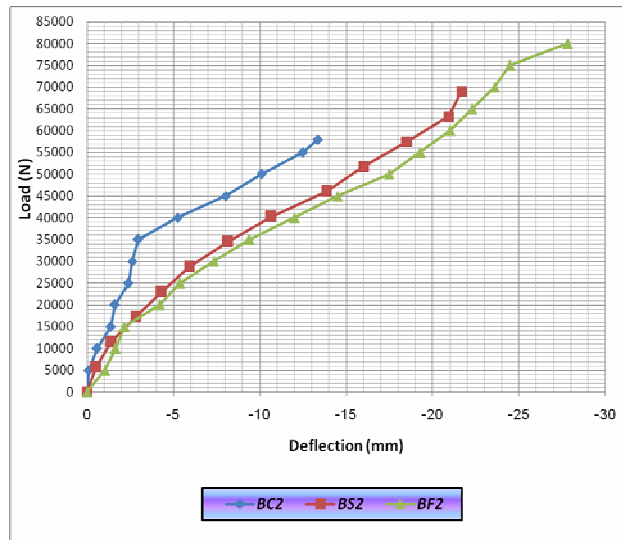
(c)

color	Load (kN)
	20
	30
	40
	50
	60
	70
	80
	85
	95

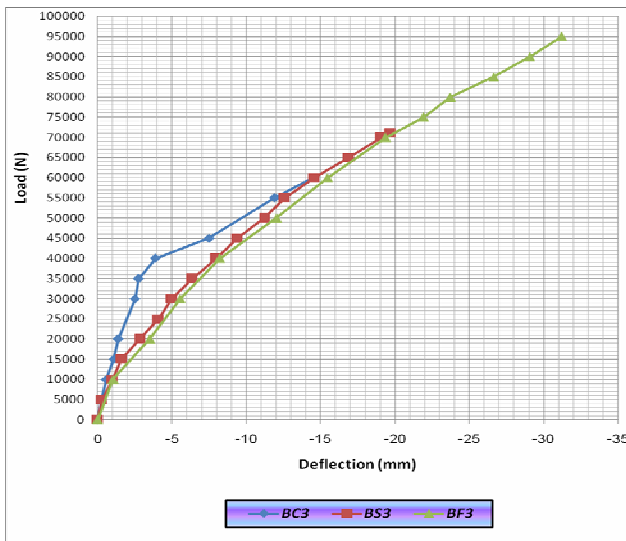
FIGURE 8, Crack Patterns for BC3, BS3 and BF3 respectively



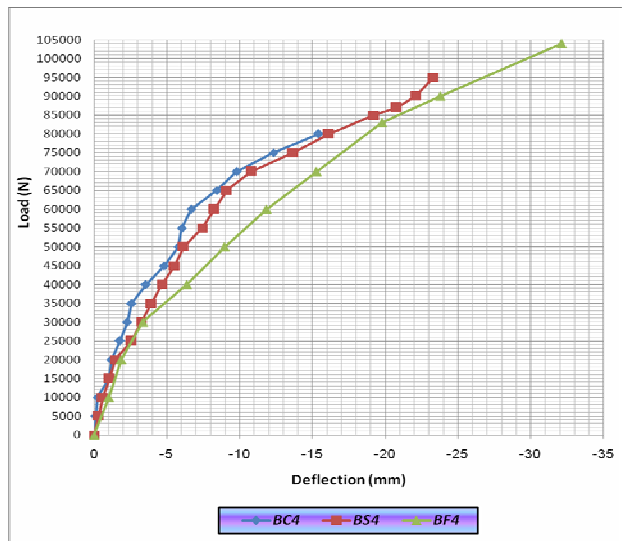
(a)



(b)



(c)



(d)

FIGURE 9, Load-Deflection Curves for Beams having between Beams at $f'_c=12, 20, 30$ and 39 MPa respectively

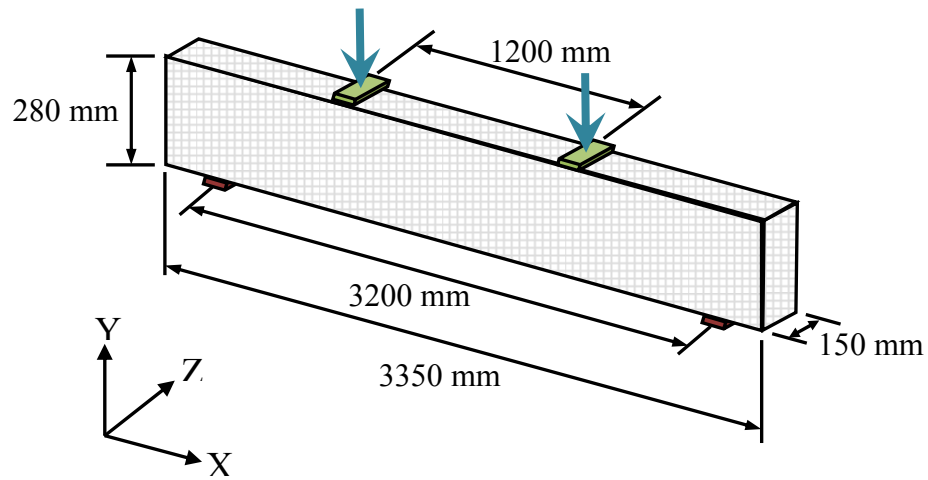


FIGURE 10, Typical Beam Dimensions (Not to Scale)

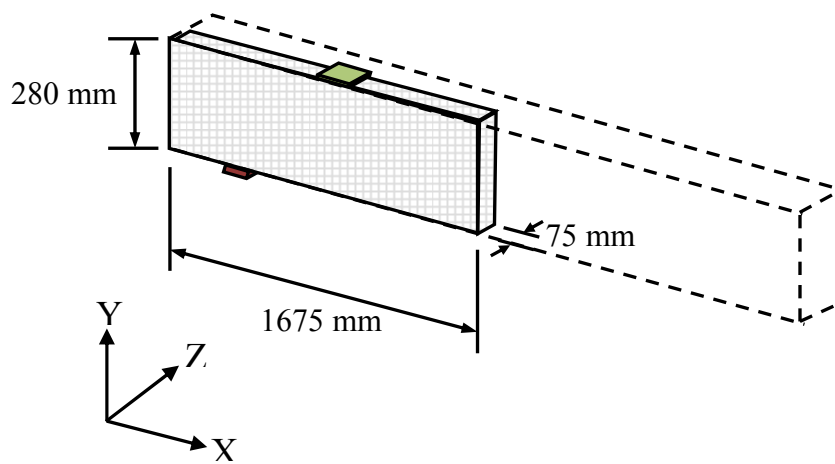


FIGURE 11, Use of A Quarter Beam Model (Not to Scale)

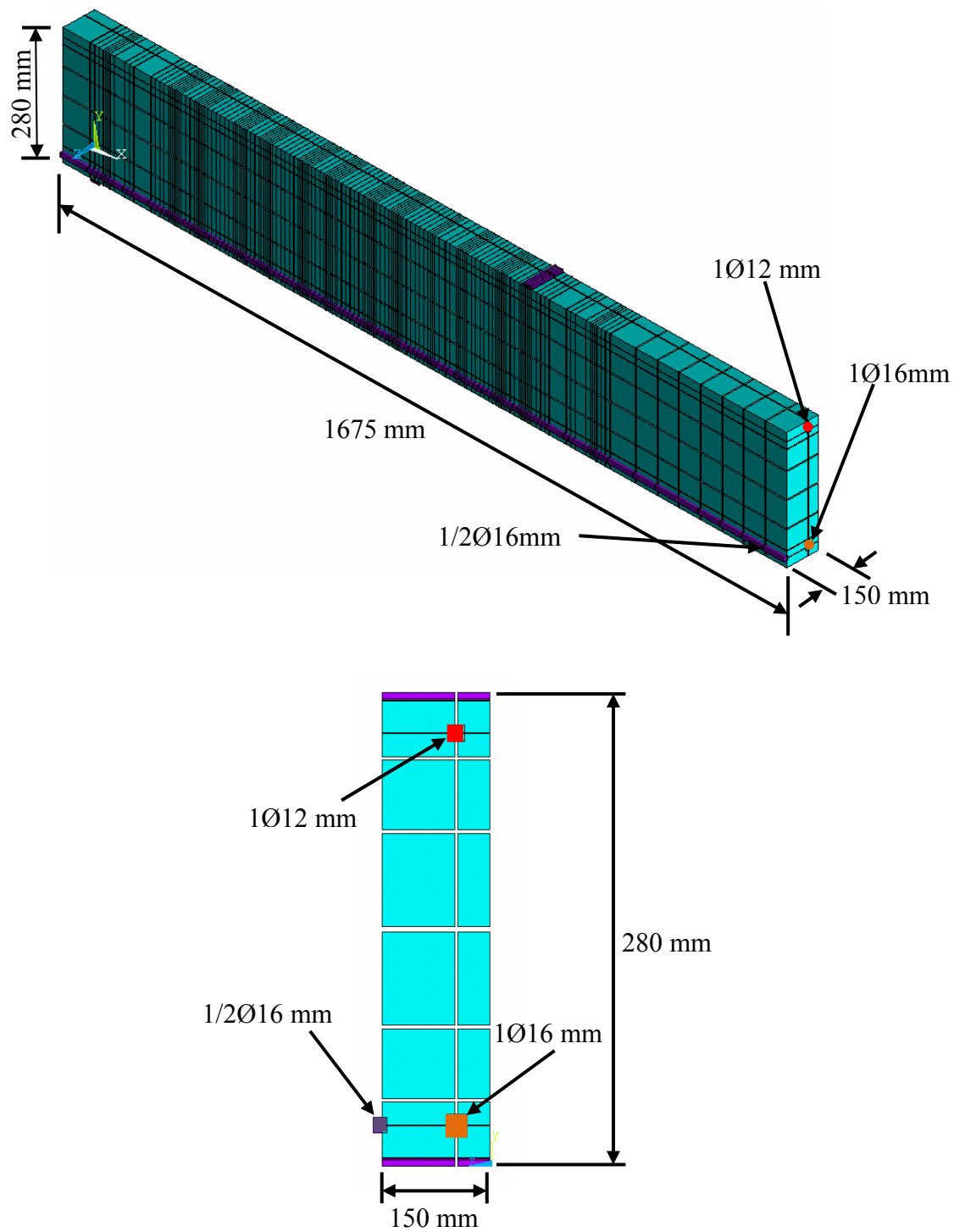
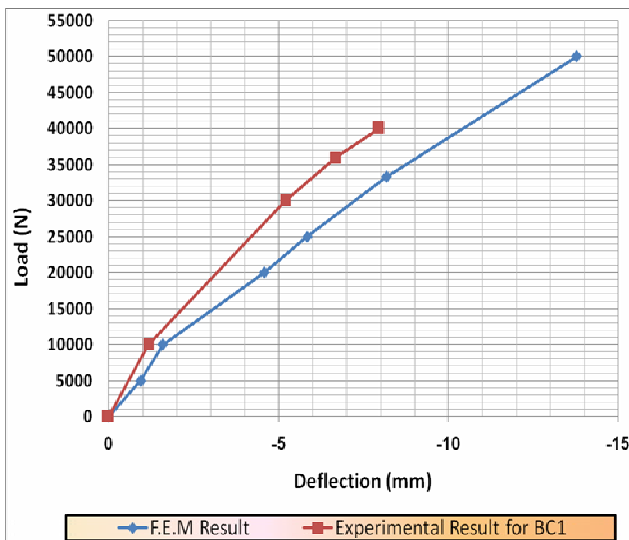


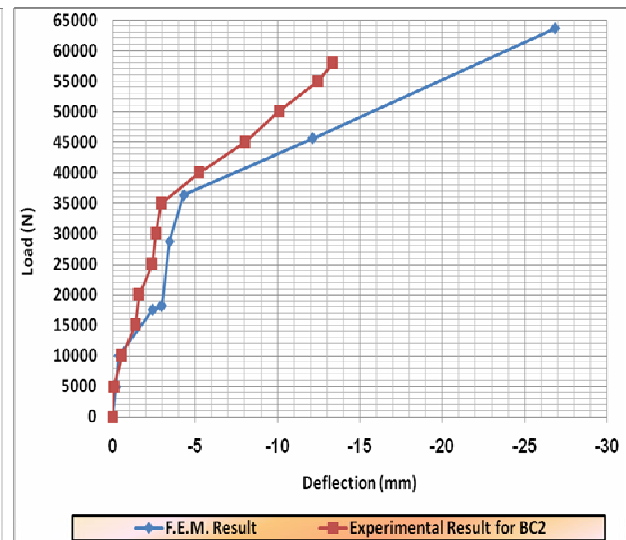
FIGURE 12, Typical Steel Reinforcement for A Quarter Beam Model (Not to Scale)

Table 5, Comparisons between experimental and numerical ultimate loads

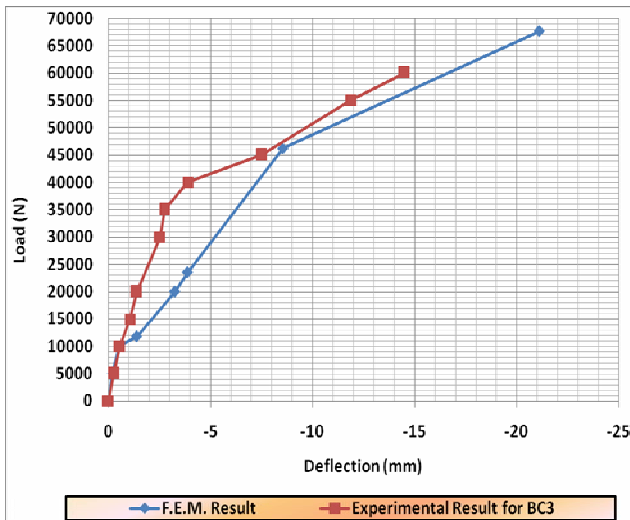
Beam designation	Numerical ultimate load (kN)	Experimental ultimate load (kN)	$\frac{P_{num}}{P_{ex}}$
<i>BC1</i>	50.0	45	1.11
<i>BS1</i>	70.0	65.0	1.08
<i>BF1</i>	74.7	70.0	1.07
<i>BC2</i>	63.6	58.0	1.09
<i>BS2</i>	66.7	69.0	0.97
<i>BF2</i>	80.0	80.0	1.00
<i>BC3</i>	67.6	60.0	1.13
<i>BS3</i>	77.8	71.0	1.10
<i>BF3</i>	90.0	95.0	0.95
<i>BC4</i>	88.5	80.0	1.11
<i>BS4</i>	100.0	95.0	1.05
<i>BF4</i>	106.0	104.0	1.02



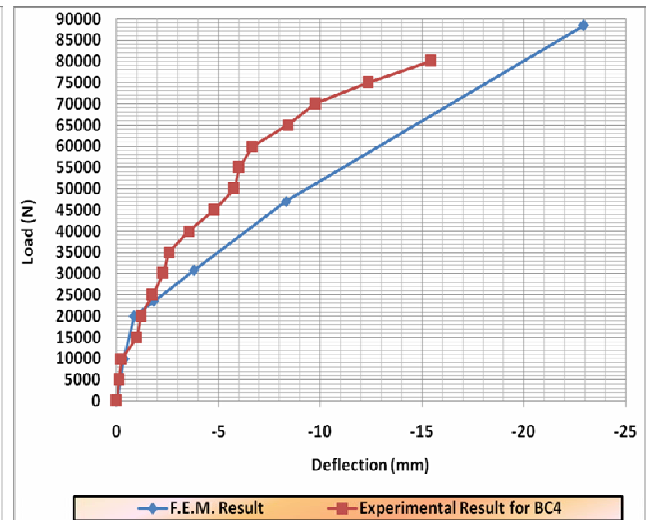
(a)



(d)

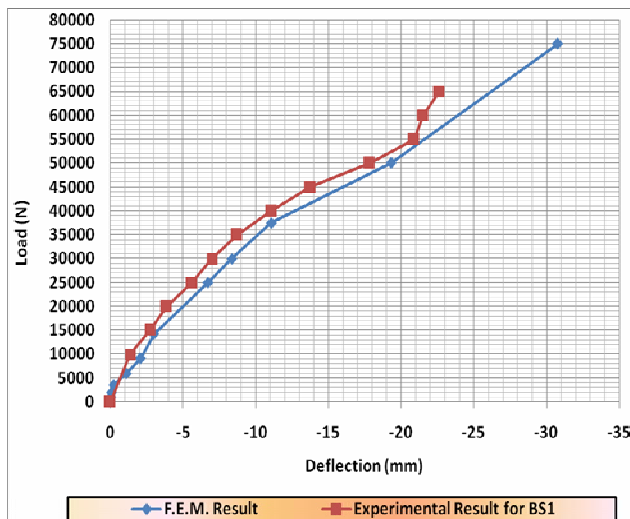


(c)

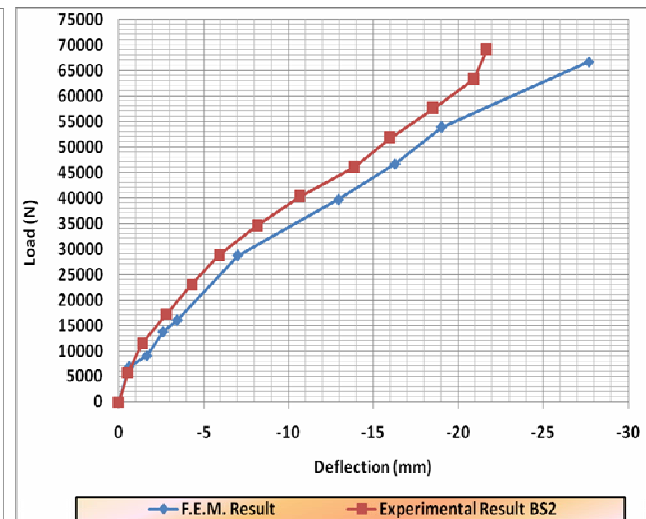


(d)

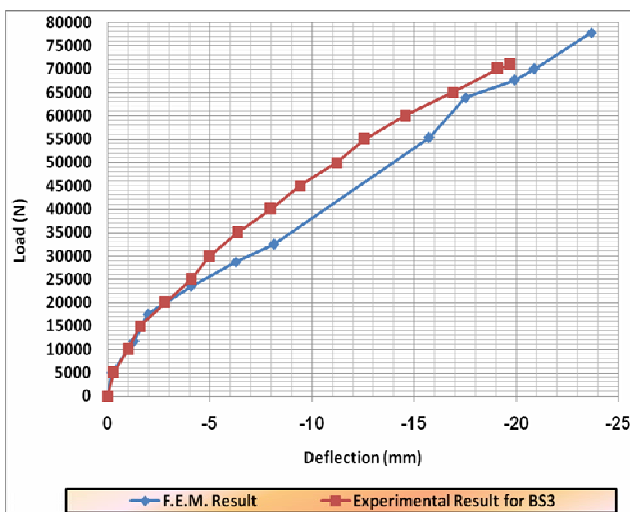
FIGURE 31, Load-Deflection Curve BC1, BC2, BC3 and BC4 respectively



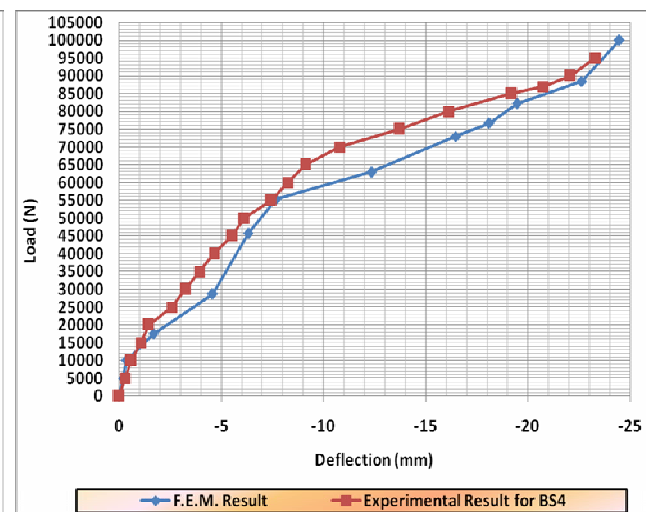
(a)



(b)

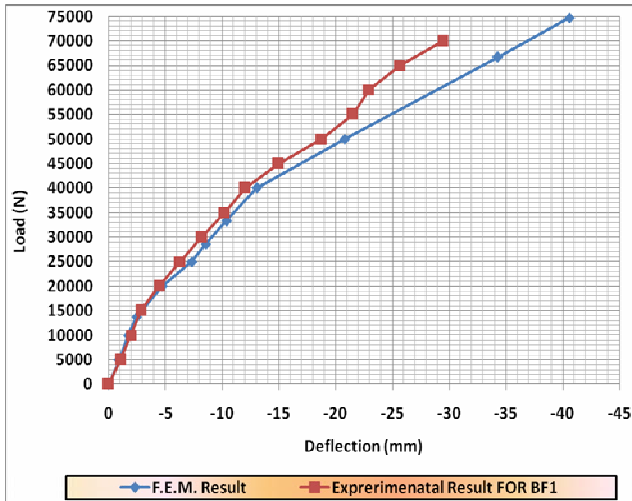


(c)

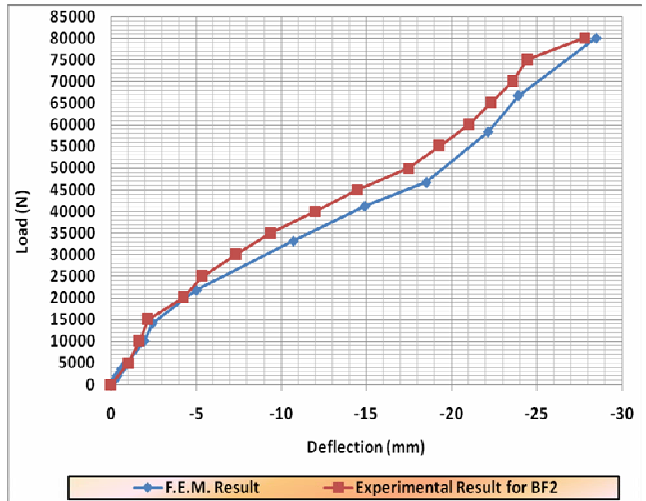


(d)

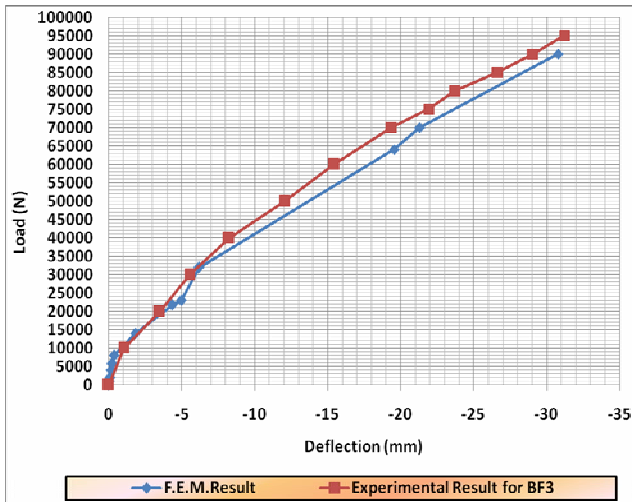
FIGURE 32, Load-Deflection Curve BS1, BS2, BS3 and BS4 respectively



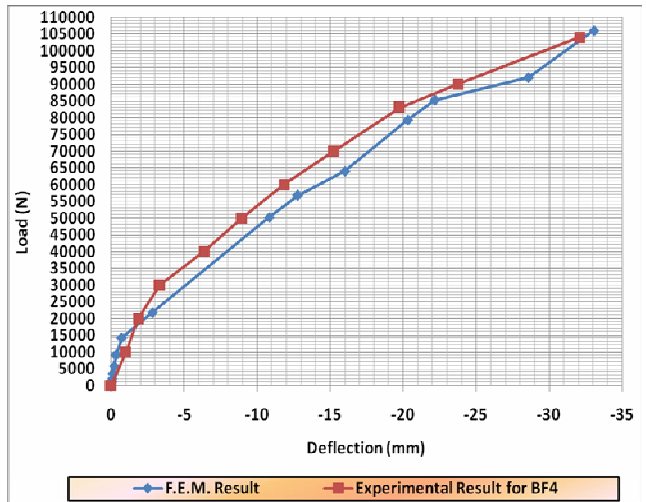
(a)



(b)



(c)



(d)

FIGURE 33, Load-Deflection Curve BF1, BF2, BF3 and BF4 respectively



THE EFFECTS OF BLOOD RHEOLOGICAL ON THE FLOW THROUGH AN AXISYMMETRIC ARTERIAL STENOSIS

Dr. Jafar M. Hassan
Assistant Professor
Department of Mechanical Engineering
University of Technology

ABSTRACT

The prediction of the blood flow through an axisymmetric arterial stenosis is one of the most important aspects to be considered during the Atherosclerosis. Since the blood is specified as a non-Newtonian flow, therefore the effect of fluid types and effect of rheological properties of non-Newtonian fluid on the degree of stenosis have been studied. The motion equations are written in vorticity-stream function formulation and solved numerically. A comparison is made between a Newtonian and non-Newtonian fluid for blood flow at different velocities, viscosity and Reynolds number were solved also. It is found that the properties of blood must be at a certain range to preventing atherosclerosis

الخلاصة

أن عملية تدفق الدم خلال تضيق الشريان المتناظر يعد واحد من أهم الظواهر التي تؤخذ بنظر الاعتبار خلال تصلب الشرايين. وبما ان الدم يصنف من الموائع الغير نيوتينية لذلك تمت دراسة أنواع الموائع وتأثير خواص الدم الغير نيوتيني على درجة تضيق الشريان. كتبت معادلة الجريان بصيغة المسار الدوامي وتم تحليلها عددياً، تمت مقارنة بين المائع النيوتيني و الغير النيوتيني لسرع جريان ولزوجة ومديات رقم رينولد مختلفة . لقد تبين ان خصائص الدم يجب أن تكون ضمن حدود محدودة لغرض منع حدوث حالة تصلب الشريان.

Nomenclature

A_1	Rate of deformation tensor	—
I	Unit tensor	—
J	Jacobian of direct transformation	—
K	Keulegan-Carpenter number	—
n	Power index	—
p	Pressure	N/m^2
Q	Flow rate	m^3/s
R	Radius of the tube at region concerned	m
Re	Reynolds Number	—
R_{min}	Radius of the tube at the throat	m
R_o	Radius of the tube	m

τ	Period of the imposed flow	s
T	Cauchy `tensor stress	N/ m ²
t	Time	s
$t+\Delta t$	Time step	s
u,v	Velocity components in x and r directions	m/s
x,r,t,v,u,p,Λ	Dimensionless variables	—
U_o	Averaged velocity over the section of radius R_o	m/s
Greek Symbols		
$\eta_o - \eta_\infty$	Asymptotic apparent viscosities	N.s/m ²
$\dot{\gamma}$	Shear rate	1/s
ψ	Stream function	m ³ /s
ω	Vorticity	1/s
ρ	Density of the fluid	kg/m ³
Λ	Material parameter	—
λ	Non-dimensional viscosity	—
α	Womersley number	—
ζ, η	Coordinate in the transformed domain	—
α, β, γ	Transformation parameter grid generation	—
δ, σ	Geometrical parameters	m
χ	Dimensional generalized viscosity	N.s/m ²
(x,r,θ)	Cylindrical coordinates system	m
μ	Viscosity of the fluid	N.s/m ²
RF	Relaxation Factor	—
r.h.s	Right Hand Solution	—
S.O.R.	Successive Over Relaxation	—
WBC	Wight Blood Cell	—

INTRODUCTION

The work is concerned with the effect of the Newtonian and non-Newtonian behavior of fluids. Basically, fluid is called non-Newtonian if its viscosity depends on the force that is applied to it. Viscosity is a measure of how easily a fluid flows (the higher the viscosity, the harder it would be to stir a bowl full of it). For example, water has lower viscosity than syrup. For an ordinary fluid (like water) the viscosity wouldn't depend on how fast you were stirring it, but for a non-Newtonian fluid it would. The average velocity in the aorta is about 30 cm/sec that in a capillary is only about 1 mm/sec. It is in the capillaries that exchange of O₂ and CO₂ take place, and this low velocity allows time for diffusion of the gases to occur [John, 1987]. There is no direct proportionality between shear stress

and shear rate for these fluids, there are a large number of rheological equations which describe the flow behavior of these fluids, but there is no single equation which exactly describes the shear stress-shear rate relationship of all these fluids over all ranges of shear rates [William, 1978]. The previous is a part of general science of Rheology, rheology as a science is concerned with the study of material that cannot be described by the classical law of Hooke for solids or Newton's law for liquids. That means; it is the science that studies the intermediate material between the above laws.

[Obaid, 1996] stated both Newtonian and non-Newtonian fluid flow cases were investigated for downstream facing step problem. The governing equations solved using a numerical finite element technique. The results are presented for different



Reynolds numbers and for some values of fluids parameter. He found that the length of the separated region grows consistently with Reynolds numbers. Also, the separated region grows slightly with increasing power index (n) when a certain Reynolds numbers have been considered.

[Pontrelil, 2001] presented a differential model of blood flow through a compliant vessel. A nonlinear, viscoelastic, constitutive equation for the wall is coupled with the one-dimensional, averaged fluid momentum equation to describe wave propagation disturbances due to prosthetic implantations, the geometrical, physical and biomechanical parameters need to be carefully identified with reference to a specific flow problem.

The purpose of this work is to study the blood flow over different degree of arterials stenosis, viscosity and Reynolds number.

A computer program using FORTRAN 90 developed to solve the governing equation using finite difference approximation method.

MATHEMATICAL MODEL FOR BLOOD FLOW

While the non-Newtonian approximation for blood flow is acceptable in modeling flow in large arteries and in the propagation of a pressure pulse, a nonlinear constitutive equation has to be used to describe flow in small vessels or at low shear rates, since the average shear rate at the wall of arteries is larger than this value.

Nevertheless, near the center of the vessels, or in separated regions of recirculating flow such as the downstream side of stenosis due to atherosclerosis, the average value of shear rate will be small. Non-Newtonian models take into account the effect of a shear-rate dependent viscosity in some range and reduce Navier-Stokes fluid in some other ranges.

While the plasma is a fluid with no significant departure from Newtonian behavior, when red cells are considered, the viscosity of the whole mixture increases noticeably. Marked Non-Newtonian properties are evidenced for concentrations greater than 10% [Chien, 1984]. It is experimentally shown that the blood apparent viscosity decreases as the shear rate increases. In the past years, many constitution equations have been proposed for the blood to model this shear-thinning property [Mann, 1990], [Phillips, 1975], [Oiknine, 1983]. Some of them depend on a large number of parameters, while some others are not completely satisfactory in all deformation ranges and for all flows.

Most of such models are based on the following stress – strain rate relationship:

$$\mathbf{T} = -\rho \mathbf{I} + \mu(\dot{\gamma}) \mathbf{A}_1 \quad (1)$$

Where \mathbf{T} is Cauchy's tensor stress. With :

$$\mathbf{A}_1 = \text{grad } \mathbf{v} + (\text{grad } \mathbf{v})^T$$

The rate of deformation tensor and its magnitude (i.e. the shear rate):

$$\dot{\gamma} = \left[\frac{1}{2} \text{tr}(\mathbf{A}_1^2) \right]^{1/2}$$

In the following expression for the blood viscosity function $\mu(\dot{\gamma})$ is suggested [Oiknine, 1983]:

$$\mu(\dot{\gamma}) = \eta_{\infty} + (\eta_0 - \eta_{\infty}) \left[\frac{1 + \log_e (1 + \Lambda \dot{\gamma})}{1 + \Lambda \dot{\gamma}} \right] \quad (2)$$

Where η_0 and η_{∞} ($\eta_0 \geq \eta_{\infty}$) are the asymptotic apparent viscosities as ($\dot{\gamma} \rightarrow 0$ and ∞) respectively, and ($\Lambda \geq 0$) is a material constant with the dimension of time representing the degree of shear-thinning (for $\eta_0 = \eta_{\infty}$, $\mu(\dot{\gamma}) = \text{constant}$ and the model reduces to the Newtonian one)

The complex nature of blood is approximated here with a three-parameter shear-thinning model, the apparent viscosity μ and the shear rate $\dot{\gamma}$. The apparent viscosity is expressed as a decreasing function of the shear rate $\dot{\gamma}$. Note that, at low shear rates, the apparent viscosity increases considerably. The asymptotic values η_0 are common in many other inelastic shear-thinning models and they are calibrated by best fitting experimental data, while the value of Λ is found by nonlinear regression analysis of viscometric data [Yeleswarapu, 1996].

The Equations of Motion

Blood is assumed to be anisotropic, homogeneous and incompressible continuum, having constant density ρ , and the vessel walls are considered rigid and impermeable. Its viscosity has the expression given by the equation (2).

The equation of motion is :

$$\rho \left(\frac{\partial V}{\partial t} + V \cdot \nabla V \right) = \text{div} T \quad (3)$$

where V is the velocity vector and the body forces are supposed negligible.

Let us now consider a cylindrical coordinate system (x, r, θ) having the x – axis coincident with the pipe axis. Because of an axisymmetric two-dimension solution, all variables are assumed independent of θ and the peripheral component of V vanishes.

The pipe has a circular cross section whose radius is R_0 in every where except in a small region centered at $(x = 0)$ with a mild smooth axisymmetric contraction (stenosis), as described by the following function [Yeleswarapu, 1996]:

$$R = R_0 \left(1 - \text{ST} \left(\frac{1 - \cos(\pi x / D)}{2} \right)^2 \right), \quad 0 \leq x \leq 2D \quad (4)$$

Where ST is the degree of the stenosis defined by:

$$\text{ST} = \left(\frac{R_0 - R_{\min}}{R_0} \right) 100\%$$

and R_{\min} is the radius of the tube at the throat of the constriction.

The vector equation (3) can be written in scalar form:

$$\rho \left(\frac{\partial u}{\partial t} + u \frac{\partial u}{\partial r} + v \frac{\partial u}{\partial x} \right) = - \frac{\partial p}{\partial r} \quad (5)$$

$$+ \mu(\dot{\gamma}) \left[\frac{\partial^2 u}{\partial r^2} + \frac{1}{r} \frac{\partial^2 u}{\partial x^2} - \frac{u}{r^2} \right] + 2 \frac{\partial \mu}{\partial t} \frac{\partial u}{\partial t} + \frac{\partial \mu}{\partial x} \left(\frac{\partial u}{\partial x} + \frac{\partial v}{\partial r} \right)$$

$$\rho \left(\frac{\partial v}{\partial t} + u \frac{\partial v}{\partial r} + v \frac{\partial v}{\partial x} \right) = - \frac{\partial p}{\partial x} + \mu(\dot{\gamma}) \left[\frac{\partial^2 v}{\partial r^2} + \frac{1}{r} \frac{\partial v}{\partial r} - \frac{\partial^2 v}{\partial x^2} \right] \quad (6)$$

$$+ \frac{\partial \mu}{\partial r} \left(\frac{\partial u}{\partial x} + \frac{\partial v}{\partial r} \right) + 2 \frac{\partial \mu}{\partial x} + \frac{\partial v}{\partial x}$$

Where (u, v) are the components of V in x and r directions respectively.

Let us now introduce a set of nondimensional variables:



$$\begin{aligned}
\mathbf{x} &\rightarrow \frac{x}{R_0} & \mathbf{r} &\rightarrow \frac{r}{R_0} \\
\mathbf{t} &\rightarrow \frac{t U_0}{R_0} & \mathbf{u} &\rightarrow \frac{u}{U_0} \\
\mathbf{v} &\rightarrow \frac{v}{U_0} & \mathbf{p} &\rightarrow \frac{p}{\rho U_0^2} \\
\Lambda &\rightarrow \frac{\Lambda U_0}{R_0} & \lambda &= \frac{\eta_0}{\eta_\infty}
\end{aligned}$$

With U_0 the velocity averaged over the inlet section of radius R_0 .
Moreover, two characteristic nondimensional numbers:

$$\alpha = R_0 \sqrt{\frac{\rho}{\eta_\infty \tau}} \quad K = \frac{U_0 \tau}{R_0} \quad (7)$$

Are introduced in unsteady flows and are defined as the Womersley and the Keulegan-Carpenter numbers respectively (typically, the characteristic time τ is the period of an imposed flow rate)

In the study case τ is the unit time and equal to R_0/U_0 for ($K=1$), and $\alpha^2 = \frac{\rho R_0 U_0}{\eta_\infty}$ is the

Reynolds number. The nondimensional counterparts of equations (5)-(6) are cross differentiated and subtracted, to obtain the vorticity – stream function formulation with ω the azimuthal vorticity and ψ the Stokes stream function :

$$\begin{aligned}
&\frac{\partial \omega}{\partial \mathbf{t}} + \left(\frac{1}{\mathbf{r}} \frac{\partial \psi}{\partial \mathbf{r}} \frac{\partial \omega}{\partial \mathbf{x}} - \frac{1}{\mathbf{r}} \frac{\partial \psi}{\partial \mathbf{x}} \frac{\partial \omega}{\partial \mathbf{r}} \right) + \frac{\omega}{\mathbf{r}^2} \frac{\partial \psi}{\partial \mathbf{x}} = \\
&\frac{1}{\alpha^2} \left[\chi \left(\frac{\partial^2 \omega}{\partial \mathbf{x}^2} + \frac{\partial^2 \omega}{\partial \mathbf{r}^2} + \frac{1}{\mathbf{r}} \frac{\partial \omega}{\partial \mathbf{r}} - \frac{\omega}{\mathbf{r}^2} \right) + 2 \frac{\partial \chi}{\partial \mathbf{x}} \frac{\partial \omega}{\partial \mathbf{x}} \right. \\
&+ \frac{\partial \chi}{\partial \mathbf{r}} \left(2 \frac{\partial \omega}{\partial \mathbf{r}} + \frac{\omega}{\mathbf{r}} \right) + 2 \frac{\partial^2 \chi}{\partial \mathbf{r} \partial \mathbf{x}} \left(\frac{1}{\mathbf{r}^2} \frac{\partial \psi}{\partial \mathbf{x}} - \frac{2}{\mathbf{r}} \frac{\partial^2 \psi}{\partial \mathbf{r} \partial \mathbf{x}} \right) \\
&\left. + \left(\frac{\partial^2 \chi}{\partial \mathbf{x}^2} - \frac{\partial^2 \chi}{\partial \mathbf{r}^2} \right) \left(\frac{1}{\mathbf{r}} \frac{\partial^2 \psi}{\partial \mathbf{r}^2} - \frac{1}{\mathbf{r}} \frac{\partial^2 \psi}{\partial \mathbf{x}^2} - \frac{1}{\mathbf{r}^2} \frac{\partial \psi}{\partial \mathbf{r}} \right) \right] \quad (8)
\end{aligned}$$

Where

$$\chi(\dot{\gamma}) = 1 + (\lambda - 1) \frac{1 + \log_e(1 + \Lambda \dot{\gamma})}{1 + \Lambda \dot{\gamma}} \quad (9)$$

$$\begin{aligned}
\dot{\gamma}^2 = \frac{4}{\mathbf{r}^2} &\left[\frac{1}{\mathbf{r}^2} \left(\frac{\partial \psi}{\partial \mathbf{x}} \right)^2 + \left(\frac{\partial^2 \psi}{\partial \mathbf{r} \partial \mathbf{x}} \right)^2 - \frac{1}{\mathbf{r}} \frac{\partial \psi}{\partial \mathbf{x}} \frac{\partial^2 \psi}{\partial \mathbf{r} \partial \mathbf{x}} \right] \\
&+ \frac{1}{\mathbf{r}^2} \left(\frac{\partial^2 \psi}{\partial \mathbf{r}^2} - \frac{1}{\mathbf{r}} \frac{\partial \psi}{\partial \mathbf{r}} - \frac{\partial^2 \psi}{\partial \mathbf{x}^2} \right)^2 \quad (10)
\end{aligned}$$

Are the dimensionless generalized viscosity and the squared shear rate, respectively.

The following relation between velocity components, vorticity and stream function holds:

$$\omega = \frac{\partial \mathbf{u}}{\partial \mathbf{x}} - \frac{\partial \mathbf{v}}{\partial \mathbf{r}}$$

$$\begin{aligned} \mathbf{u} &= -\frac{1}{\mathbf{r}} \frac{\partial \psi}{\partial x} \\ \mathbf{v} &= \frac{1}{\mathbf{r}} \frac{\partial \psi}{\partial \mathbf{r}} \end{aligned} \quad (11)$$

And the equations above to be solved for $0 \leq \mathbf{r} \leq 1$.

It is worth noting that the r.h.s. of Eqn. (8) is made up of many terms of different physical significance due to the variable viscosity and express a transport and diffusion of vorticity from the boundary to the main stream. The combined nonlinear effect of these components enters in the dynamics of the vorticity and is important for understanding the formation, the development and the separation of boundary layer. Note that in a fluid with constant viscosity, all the terms in square brackets except the first one disappear.

Vorticity and stream function are related by the Poisson equation:

$$-\omega \mathbf{r} = \frac{\partial^2 \psi}{\partial \mathbf{x}^2} + \frac{\partial^2 \psi}{\partial \mathbf{r}^2} - \frac{1}{\mathbf{r}} \frac{\partial \psi}{\partial \mathbf{r}} \quad (12)$$

The velocity field, automatically satisfying the continuity equation, can be computed from the stream function. The boundary conditions are required for all boundaries of computational domain since the governing equations are elliptic in partial coordinates. In general, along the boundary of the lower symmetric plane, the stream function is respectively set equal to zero and to a constant value, which is equivalent to one half of the mean mass flow rate through the pipe. The vorticity is zero along the symmetry. On the wall pipe the value of the stream function is uniform, corresponding to an impermeable wall. The value of vorticity on the pipe wall is unknown and must be solved as a part of solution. The inlet boundary condition is uniform flow (\mathbf{u} =uniform velocity, \mathbf{v} =0) and the outlet boundary of stream and vorticity which is located three periods down stream is imposed to be the same in the stream wise direction. The initial boundary conditions for all variables are zero Fig. (1).

NUMERICAL METHOD

The essence of computational fluid mechanics is the representation of the governing equation in algebraic form suitable for solution by available mathematical techniques. Adopting the finite difference approach, the governing equations that are expressed in the form of differential equations can be represented as finite differences and converted to algebraic equations.

In this part, the vorticity-transport equation ω , stream function equation ψ and the shear rate equation are discretized using the finite difference method with "Time Marching" because it attempts to follow the time evaluation of the flow, in arriving to the steady-state solution.

The approximations for the time derivative in the vorticity equation (8), the numerator is a forward difference for vorticity change occurring at (m,n), from time (t) to (t + Δt).

$$\frac{\partial \omega}{\partial t} = \frac{\omega_{(m,n)}^{i+1} - \omega_{(m,n)}^i}{\Delta t} \quad (13)$$

Where the ($\omega_{(m,n)}^{i+1}$) is the vorticity at time (t + Δt) and the ($\omega_{(m,n)}^i$) is the vorticity at (t).

The central finite difference approximations are used for convection terms in the vorticity equations as follows:



$$\frac{1}{\mathbf{r}} \left(\frac{\partial \psi}{\partial \mathbf{r}} \frac{\partial \omega}{\partial \mathbf{x}} \right) - \frac{1}{\mathbf{r}} \left(\frac{\partial \psi}{\partial \mathbf{x}} \frac{\partial \omega}{\partial \mathbf{r}} \right) =$$

$$\frac{1}{\mathbf{r}_{(m,n)}} \left[\frac{\psi_{(m,n+1)} - \psi_{(m,n-1)}}{2 \Delta \eta} \frac{\omega_{(m+1,n)}^i - \omega_{(m-1,n)}^i}{2 \Delta \zeta} \right.$$

$$\left. - \frac{\psi_{(m+1,n)} - \psi_{(m-1,n)}}{2 \Delta \zeta} \frac{\omega_{(m,n+1)}^i - \omega_{(m,n-1)}^i}{2 \Delta \eta} \right] / J(m,n)$$

(14)

$$\frac{\omega}{\mathbf{r}^2} \frac{\partial \psi}{\partial \mathbf{x}} = \frac{\omega_{(m,n)}^i}{\mathbf{r}(m,n)^2} \left[\frac{\psi_{(m+1,n)} - \psi_{(m-1,n)}}{2 \Delta \zeta} \mathbf{r}_\eta(m,n) \right.$$

$$\left. - \frac{\psi_{(m,n+1)} - \psi_{(m,n-1)}}{2 \Delta \eta} \mathbf{r}_\zeta(m,n) \right] / J(m,n)$$

(15)

$$(\alpha \omega_{\zeta\zeta} - 2 \beta \omega_{\zeta\eta} + \gamma \omega_{\eta\eta}) / J^2 =$$

$$\alpha_{(m,n)} \left(\frac{\omega_{(m+1,n)}^i - 2 \omega_{(m,n)}^i + \omega_{(m-1,n)}^i}{2 \Delta \zeta^2} \right)$$

$$- 2 \beta_{(m,n)} \left(\frac{\omega_{(m+1,n+1)}^i - \omega_{(m+1,n-1)}^i - \omega_{(m-1,n+1)}^i + \omega_{(m-1,n-1)}^i}{4 \Delta \zeta \Delta \eta} \right)$$

$$+ \gamma_{(m,n)} \left(\frac{\omega_{(m,n+1)}^i - 2 \omega_{(m,n)}^i + \omega_{(m,n-1)}^i}{\Delta \eta^2} \right) / J_{(m,n)}^2$$

(16)

$$\frac{1}{\mathbf{r}} (\omega_\eta \mathbf{x}_\zeta - \omega_\zeta \mathbf{x}_\eta) / J - \frac{\omega}{\mathbf{r}^2} =$$

$$\frac{1}{\mathbf{r}(m,n)} \left[\frac{\omega_{(m,n+1)}^i - \omega_{(m,n-1)}^i}{2 \Delta \eta} \mathbf{x}_z(m,n) \right.$$

$$\left. - \frac{\omega_{(m+1,n)}^i - \omega_{(m-1,n)}^i}{2 \Delta \zeta} \mathbf{x}_e(m,n) \right] / J_{(m,n)} - \frac{\omega_{(m,n)}^i}{\mathbf{r}_{(m,n)}^2}$$

(17)

$$2(\chi_\zeta \mathbf{r}_\eta - \chi_\eta \mathbf{r}_\zeta)(\omega_\zeta \mathbf{r}_\eta - \omega_\eta \mathbf{r}_\zeta) / J^2 =$$

$$2 \left(\frac{\chi_{(m+1,n)} - \chi_{(m-1,n)}}{2 \Delta \zeta} \mathbf{r}_e(m,n) \right)$$

$$\left(\frac{\chi_{(m,n+1)} - \chi_{(m,n-1)}}{2\Delta\eta} \mathbf{r}_z(m,n) \right) \left(\frac{\omega_{(m+1,n)}^i - \omega_{(m-1,n)}^i}{2\Delta\zeta} \mathbf{r}_e(m,n) - \frac{\omega_{(m,n+1)}^i - \omega_{(m,n-1)}^i}{2\Delta\zeta} \mathbf{r}_z(m,n) \right) \Bigg/ J_{(m,n)}^2 \quad (18)$$

$$\left(\chi_\eta \mathbf{x}_\zeta - \chi_\zeta \mathbf{x}_\eta \right) / J \left(2 \left(\omega_\eta \mathbf{x}_\zeta - \omega_\zeta \mathbf{x}_\eta \right) / J \right) + \frac{\omega}{\mathbf{r}} = \left(\frac{\chi_{(m,n+1)} - \chi_{(m,n-1)}}{2\Delta\eta} \mathbf{x}_z(m,n) - \frac{\chi_{(m+1,n)} - \chi_{(m-1,n)}}{2\Delta\zeta} \mathbf{x}_e(m,n) \right) \Bigg/ J(m,n) * \left[2 \left(\frac{\omega_{(m,n+1)}^i - \omega_{(m,n-1)}^i}{2\Delta\eta} \mathbf{x}_z(m,n) - \frac{\omega_{(m+1,n)}^i - \omega_{(m-1,n)}^i}{2\Delta\zeta} \mathbf{x}_e \right) \Bigg/ J(m,n) \right] + \frac{\omega_{(m,n)}^i}{\mathbf{r}_{(m,n)}} \quad (19)$$

$$2 \left(\chi_{\zeta\eta} (\mathbf{r}_\eta \mathbf{x}_\zeta - \mathbf{r}_\zeta \mathbf{x}_\eta) - \chi_{\zeta\zeta} (\mathbf{r}_\eta \mathbf{x}_\eta) - \chi_{\eta\eta} (\mathbf{r}_\zeta \mathbf{x}_\zeta) \right) / J^2 = 2 \left(\frac{\chi_{(m+1,n-1)} - \chi_{(m+1,n-1)} - \chi_{(m-1,n-1)} + \chi_{(m-1,n-1)}}{4\Delta\zeta\eta} (\mathbf{r}_e(m,n) \mathbf{x}_z(m,n) - \mathbf{r}_z(m,n) \mathbf{x}_e(m,n)) - \frac{\chi_{(m+1,n)} - 2\chi_{(m,n)} + \chi_{(m-1,n)}}{\Delta\zeta^2} (\mathbf{r}_e(m,n) \mathbf{x}_e(m,n)) - \frac{\chi_{(m,n+1)} - 2\chi_{(m,n)} + \chi_{(m,n-1)}}{\Delta\eta^2} (\mathbf{r}_z(m,n) \mathbf{x}_z(m,n)) \right) \Bigg/ J_{(m,n)}^2 \quad (20)$$

$$\frac{1}{\mathbf{r}^2} (\psi_\zeta \mathbf{r}_\eta - \psi_\eta \mathbf{r}_\zeta) / J = \frac{1}{\mathbf{r}_{(m,n)}^2} \left[\frac{\psi_{(m+1,n)} - \psi_{(m-1,n)}}{2\Delta\zeta} \mathbf{r}_e(m,n) - \frac{\psi_{(m,n+1)} - \psi_{(m,n-1)}}{2\Delta\eta} \mathbf{r}_z(m,n) \right] \Bigg/ J(m,n) \quad (21)$$

$$\frac{2}{\mathbf{r}} (\psi_{\zeta\eta} (\mathbf{r}_\eta \mathbf{x}_\zeta - \mathbf{r}_\zeta \mathbf{x}_\eta) - \psi_{\zeta\zeta} (\mathbf{r}_\eta \mathbf{x}_\eta) - \psi_{\eta\eta} (\mathbf{r}_\zeta \mathbf{x}_\zeta)) / J^2 = \frac{2}{\mathbf{r}_{(m,n)}} \left(\frac{\psi_{(m+1,n+1)} - \psi_{(m+1,n+1)} - \psi_{(m-1,n+1)} + \psi_{(m-1,n+1)}}{4\Delta\zeta\Delta\eta} (\mathbf{r}_e(m,n) \mathbf{x}_z(m,n) - \mathbf{r}_z(m,n) \mathbf{x}_e(m,n)) - \frac{\psi_{(m+1,n)} - 2\psi_{(m,n)} + \psi_{(m-1,n)}}{\Delta\zeta^2} \mathbf{r}_e(m,n) \mathbf{x}_e(m,n) - \frac{\psi_{(m,n+1)} - 2\psi_{(m,n)} + \psi_{(m,n-1)}}{\Delta\eta^2} \mathbf{r}_z(m,n) \mathbf{x}_z(m,n) \right) \Bigg/ J_{(m,n)}^2 \quad (22)$$

$$(\alpha_x \chi_{\zeta\zeta} - 2\beta_x \chi_{\zeta\eta} + \gamma_x \chi_{\eta\eta}) / J^2 = \left(\alpha_x(m,n) \frac{\chi_{(m+1,n)} - 2\chi_{(m,n)} + \chi_{(m-1,n)}}{\Delta\zeta^2} - 2\beta_x(m,n) * \frac{\chi_{(m+1,n+1)} - \chi_{(m+1,n-1)} - \chi_{(m-1,n+1)} + \chi_{(m-1,n-1)}}{4\Delta\zeta\Delta\eta} \right)$$



$$+ \gamma_x(m, n) * \frac{\chi_{(m, n+1)} - 2\chi_{(m, n)} + \chi_{(m, n-1)}}{\Delta\eta^2} \bigg) / J_{(m, n)}^2 \quad (23)$$

$$\begin{aligned} & \frac{1}{\mathbf{r}} (\alpha_R \psi_{\zeta\zeta} - 2\beta_R \psi_{\zeta\eta} + \gamma_R \psi_{\eta\eta}) / J^2 \\ & - \frac{1}{\mathbf{r}^2} (\psi_\eta \mathbf{x}_\zeta - \psi_\zeta \mathbf{x}_\eta) / J = \\ & \frac{1}{\mathbf{r}_{(m, n)}} \left(\alpha_R(m, n) \frac{\psi_{(m+1, n)} - 2\psi_{(m, n)} + \psi_{(m-1, n)}}{\Delta\zeta^2} \right. \\ & - 2\beta_R(m, n) \frac{\psi_{(m+1, n+1)} - \psi_{(m+1, n-1)} - \psi_{(m-1, n+1)} + \psi_{(m-1, n-1)}}{4\Delta\zeta\Delta\eta} \\ & \left. + \gamma_R(m, n) \frac{\psi_{(m, n+1)} - 2\psi_{(m, n)} + \psi_{(m, n-1)}}{\Delta\eta^2} \right) / J_{(m, n)}^2 \\ & - \frac{1}{\mathbf{r}_{(m, n)}^2} \left(\frac{\psi_{(m, n+1)} - \psi_{(m, n-1)}}{2\Delta\eta} \mathbf{x}_Z(m, n) - \frac{\psi_{(m+1, n)} - \psi_{(m-1, n)}}{2\Delta\zeta} \mathbf{x}_e(m, n) \right) / J(m, n) \end{aligned} \quad (24)$$

Where α , β and γ are transformation coefficients

$$\begin{aligned} \alpha &= \mathbf{x}_\eta^2 + \mathbf{r}_\eta^2 \\ \beta &= \mathbf{x}_\zeta \mathbf{x}_\eta + \mathbf{r}_\zeta \mathbf{r}_\eta \\ \gamma &= \mathbf{x}_\zeta^2 + \mathbf{r}_\zeta^2 \end{aligned} \quad (25)$$

And J denotes the Jacobain of the transformation

$$J = \frac{\partial(\mathbf{x}, \mathbf{r})}{\partial(\zeta, \eta)} = \mathbf{x}_\zeta \mathbf{r}_\eta - \mathbf{x}_\eta \mathbf{r}_\zeta \quad (26)$$

The constant ζ ($\zeta = \zeta(\mathbf{x}, \mathbf{r})$) lines and constant η ($\eta = \eta(\mathbf{x}, \mathbf{r})$) lines can be spaced as desired around the boundaries in the physical domain, since the assignment of the (ζ, η) values to (\mathbf{x}, \mathbf{r}) boundary points via (\mathbf{x}_i) and (\mathbf{r}_i) functions are arbitrary, if the shapes of the boundaries shown in Fig. (1) are described.

A computer program developed to solve the above equations. The flow charts shown in figs. (2 and 3).

Results and Discussion

The primary advantages of grids generated by the solution of partial differential equations are smoothness and better control of grid orthogonally at boundary, but the disadvantages are increased computational cost and complexity. So four-grid generation has been generated for four stenosis. Figure (4) shows the grid generation for (0.0), (0.2), (0.5) and (0.8) degree of stenosis.

The parameters that the problem depends on range around some typical values to obtain results of biomechanical interest. They are chosen equal to Newtonian and non-Newtonian fluids to allow a comparison of the two cases. The following physical parameters are assigned in equation (7): $K=1$ and $\alpha^2=10$. Therefore,

Reynolds number $Re = K * \alpha^2 = 10$ is within the physiological range of blood flow in small vessels and rheological parameters (λ, Λ) are (40, 50) [Chien, 1984].

The differences between Newtonian and non-Newtonian flows become significant as shown in Figure (5), the shear rate of Newtonian flow is greater than that of non-Newtonian flow it is positive at the stenosis which the non-Newtonian because a negative at the stenosis due to the effect of viscosity which related to a vortices at the outlet of the stenosis. The effect of dimensionless viscosity (λ) shown in Figure (6) increasing λ the shear rate increases because the viscosity of blood depends on the Hematocrit. Where, the Hematocrit is a centrifuge or a device for separating the cells and on other particulate elements of the blood from the plasma.

Figure (7) shows the velocity profiles for non-Newtonian fluid of $Re=10, 20, 50$ and 300 for 0.8 degree of stenosis. Figure (8) shows the shear stress for non-Newtonian fluid at $Re (10, 20, 50$ and $300)$ for 0.8 degree of stenosis. The shear increases with decrease in the degree of stenosis. From Figures (7 and 8) it is found that the flow rates, and the different properties which affect the blood flow such as pressure drop, viscosity, length and radius of the vessel, which are the main parameters that cause the atherosclerosis. The heart tries to increase the velocity of blood and this velocity is periodic (pulsating), to try to open the stenosis so the recirculation is greater at 0.8 degree of stenosis. The flows of non-Newtonian fluid of $Re=50$ and degrees of stenosis equal to $0.2, 0.5$, and 0.8 are simulated. The streamline of $Re=50$ for the three stenosis is shown in Figure (9) the marked effects that the degree of stenosis has on the flow field. Whereas for 0.2 degree of stenosis there is no vortex formed and even for 0.5 degree of stenosis there is a small recirculation zone, for 0.8 degree of stenosis the recirculation zone is dominant in the flow field.

The shear rate for non-Newtonian fluid of $Re=50$ and degree of stenosis equal to $0.2, 0.5$ and 0.8 is shown in Figure (10) the shear rate increases when the degree of stenosis decreases, which leads to adverse pressure gradient.

Figures (11 and 12) shows that increasing the viscosity will lead to decrease the velocity at the wall even for constant diameter which leads to thromboses. The increasing in the viscosity called the polycythaemia. This increase is due to decreases in the total volume of plasma or increase the total volume of the red cells. That cause deficiency of oxygen to the tissue. The symptoms for this case, headache, thromboses, cyanosis and itching. It is treated by blood letting which lead to regenerating the red cell and therefore the viscosity of blood will reduce.

CONCLUSIONS

Mathematical models and numerical simulations offer an alternative and non-invasive tool for obtaining detailed and realistic descriptions of complex arterial flows.

A simulation of the blood flow through a stenotic arterial segment has been carried out. Although the important effect of unsteadiness is disregarded, this work shows the combined role played by the geometry and the material nonlinearity on the flow field.

The results demonstrate that the non-Newtonian character of the blood, in some typical regions, modify the flow pattern, even beyond the contracted region, reduce the shear stress at the wall a cross the tenosis. Therefore the presented model is able to predict the main characteristics of the physical flows and may have some interest in biomedical applications. An estimate of the characteristic parameters should be addressed on the basis of existing measurements.

The flow field and wall shear-stress distributions that each model induce for different Reynold number and degree of stenosis is investigated and results show that there are marked differences between simulating the blood as Newtonian and as non-Newtonian fluid. The rheological parameters in non-Newtonian fluid (blood) have the normal medical cases where increasing or decreasing these parameters, will leads to up normal in medical cases.



ACKNOWLEDGMENT

I would like to express my faithful gratitude to Dr. Taha Al-Ani specialist in Medicine and Dr. Ayad M. Al-Rawi in Al-Kerama Hospital for their co-operation.

REFERENCES

- Chien, S., Usami, S., Skalak, R., blood flow in small tube, in Hand book of physiology, Sec.2. The Cardiovascular System, Vol. 4, M. renkins, C.C. Michel Eds, American Physiology Society. Bethesda, PP. 217-249, (1984).
- John R. Cameron and James G. Skofronick "Medical Physics", Awiley-Interscience Publication, New York, 1987.
- Mann, D.E., Tarbell, J. M., "Flow of non-Newtonian blood analog fluids in grid curved straight artery modeles", Biorheology, Vol. 27, Pp. 7711-733, (1990).
- Obiad T. A. S., "A finite Element Method for Generatized Newtonian Flow", University of Basrah. Eng. & Technology Vol. 15, No. 5, Pp. 30-40, (1996).
- Oiknine C., "Rheology of the human blood", in Adv. Cardiovasc. Phys., Vol. 5, Part 1, PP. 1-25, Karger. Based, (1983).
- Phillips, W. M., Deutsch, S., Toward a constitutive equation for blood, Biorhology, Vol. 12, PP. 383-389, (1975).
- Pontrell G., "modeling the fluid-wall interaction in a blood vessel", Instituto Perle Applicazionidelcalcolo- CNR, Roma, Italy, June, (2001).
- William R. Schowalter, "Mechanics of non-Newtonian Fluid", Princeton University, U.S.A., (1978).
- Yeleswarapu, K. K., Evaluation of continuum models for Characterizing the constitutive behavior of blood, Ph. D. thesis, University of Pittsburgh, (1996).

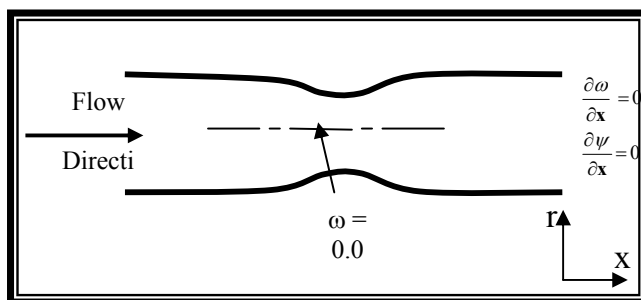


Figure (1) Boundary condition

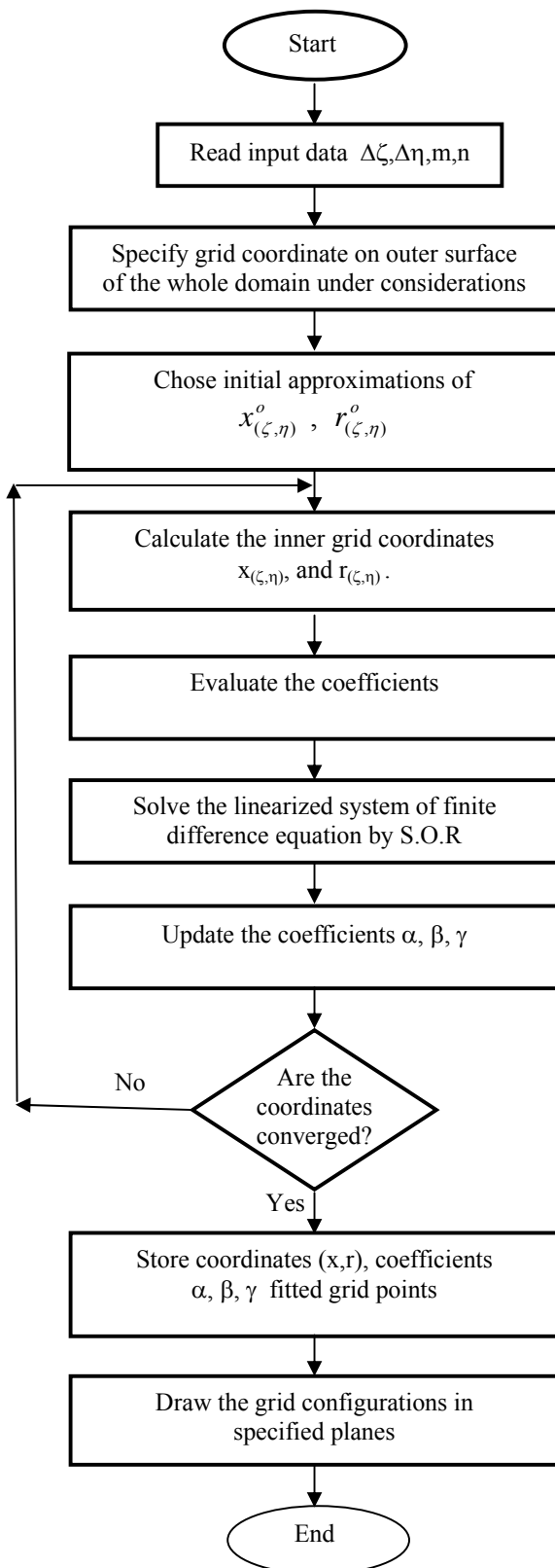


Figure (2) Flowchart for program to create the node grids

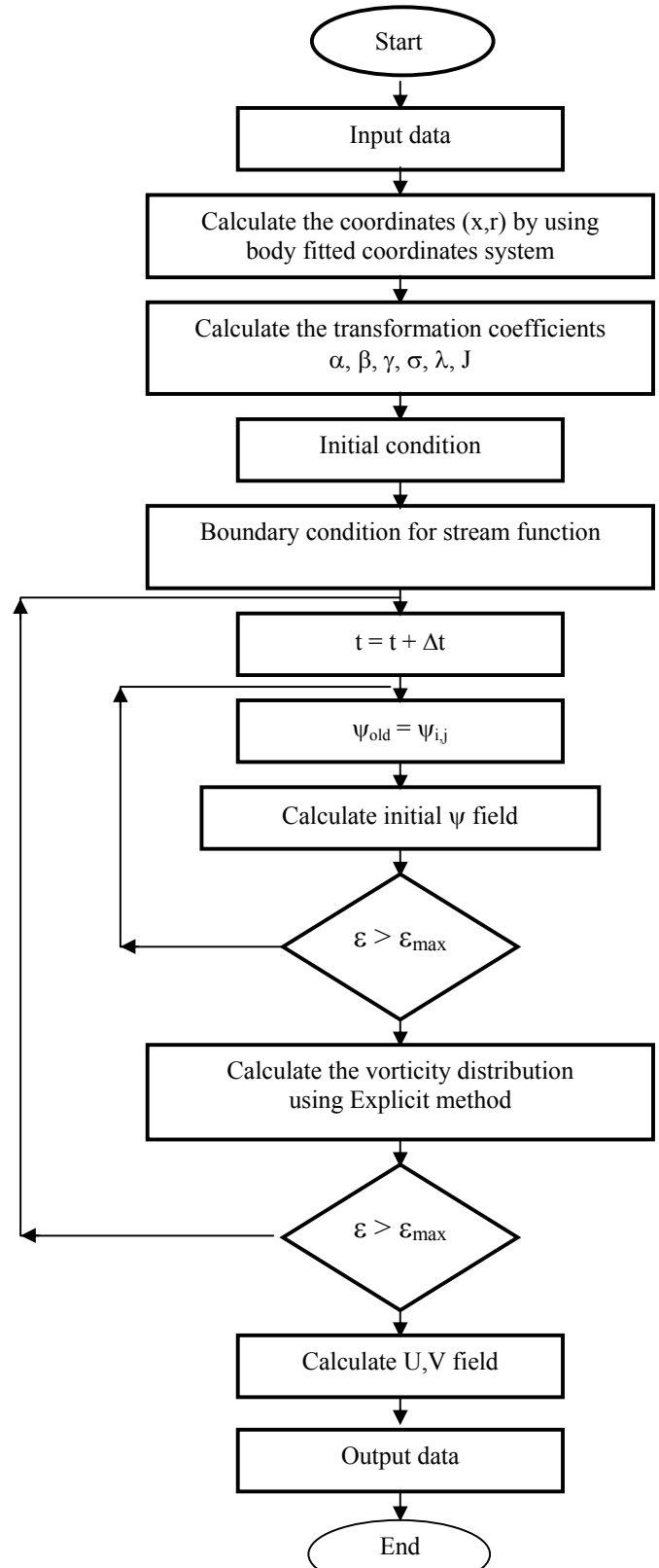


Figure (3) Flowchart for program used to solve the problem

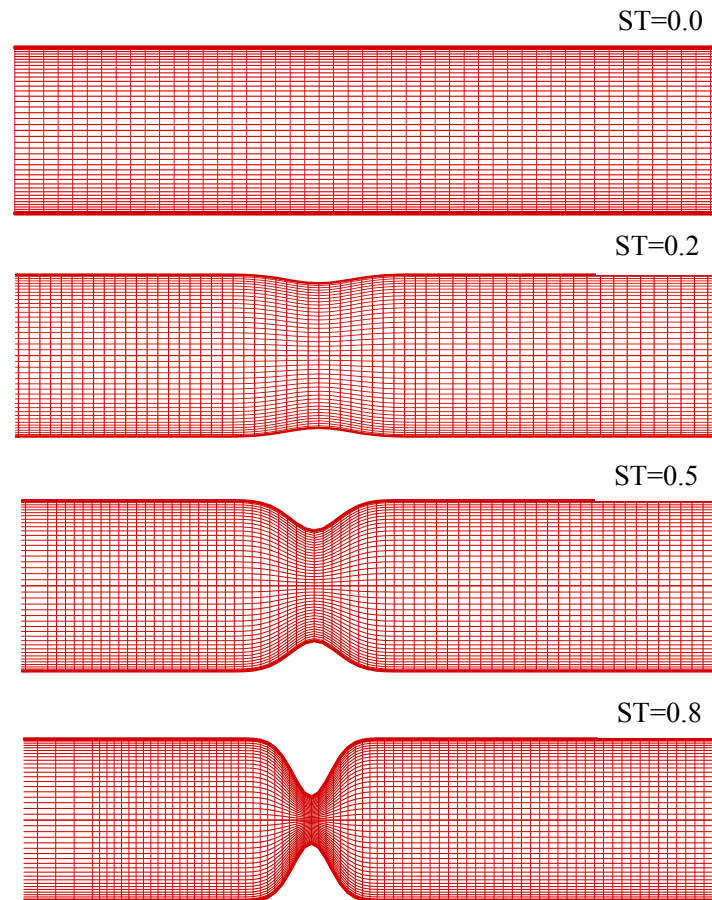


Figure (4) The grid generation for the section of stenosis (0.0),(0.2), (0.5) and (0.8).

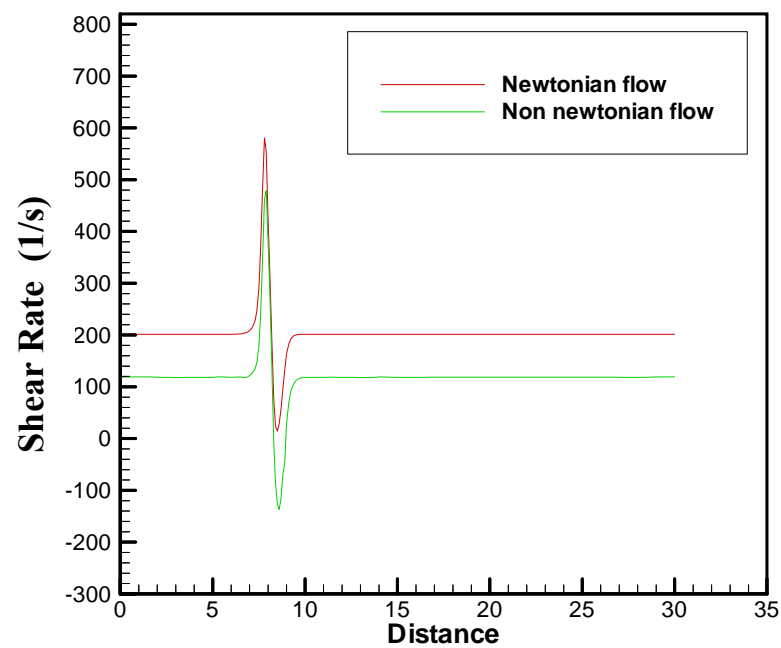


Figure (5) Shear Rate at the wall for $Re = 10$ (comparison between Newtonian and non-Newtonian)

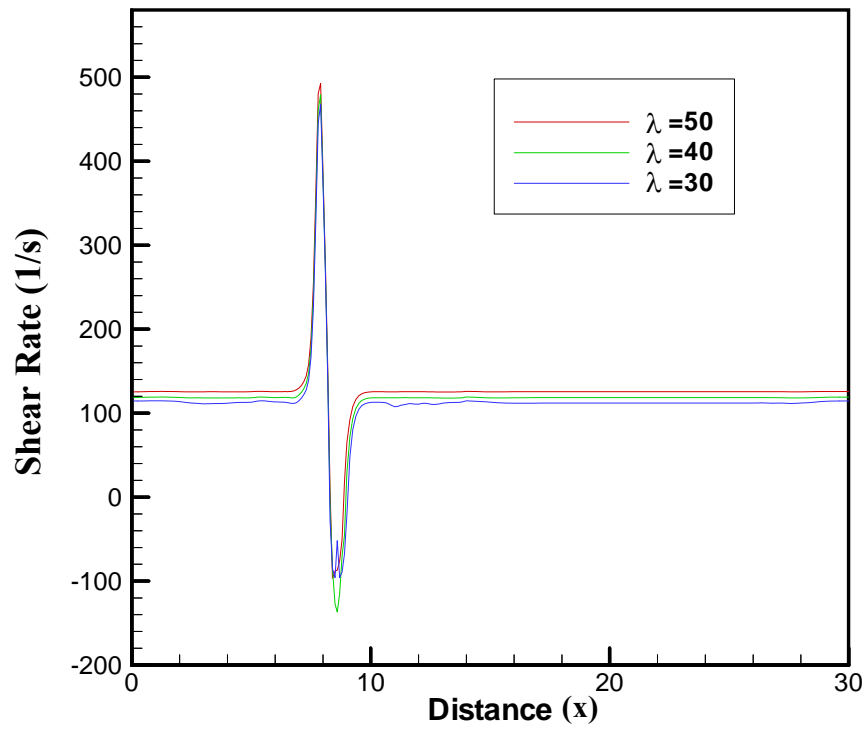
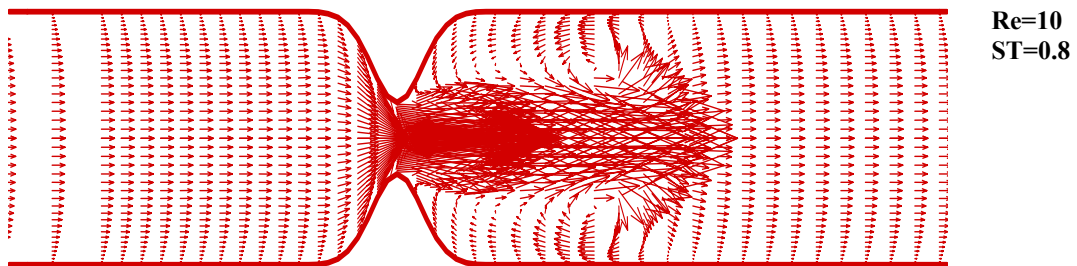
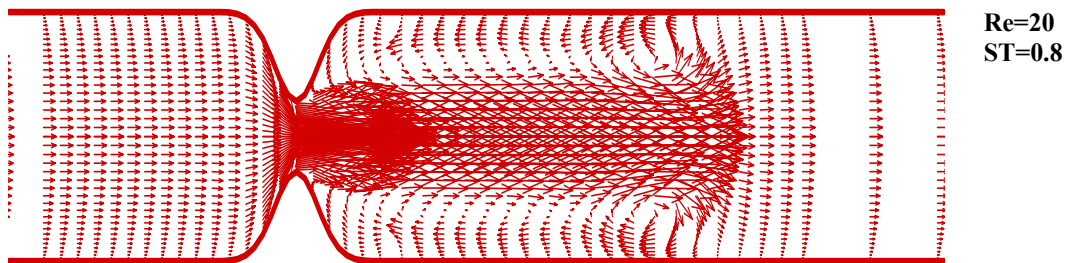


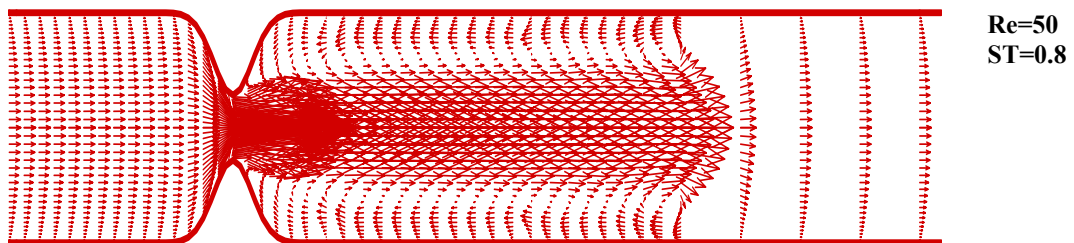
Figure (6) Shear Rate at the wall for $Re = 10$ and degree of stenosis equal to 0.5 for difference non dimensional viscosities $\lambda = (50, 40, 30)$.



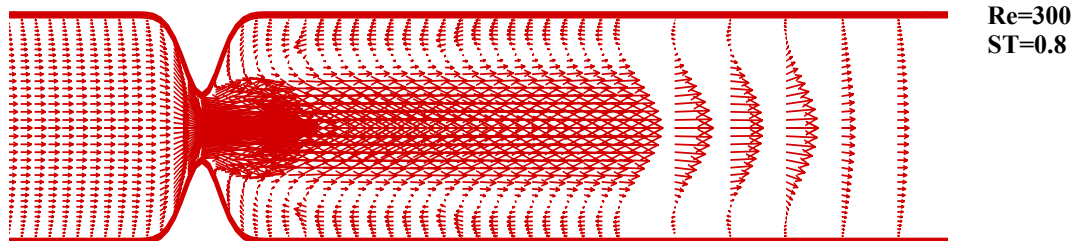
(a)



(b)



(c)



(d)

**Figure (7) The velocity profiles for non-Newtonian flow for:
(a) $Re = 10$; (b) $Re = 20$; (c) $Re = 50$; (d) $Re = 300$
and for 0.8 single degree of stenosis.**

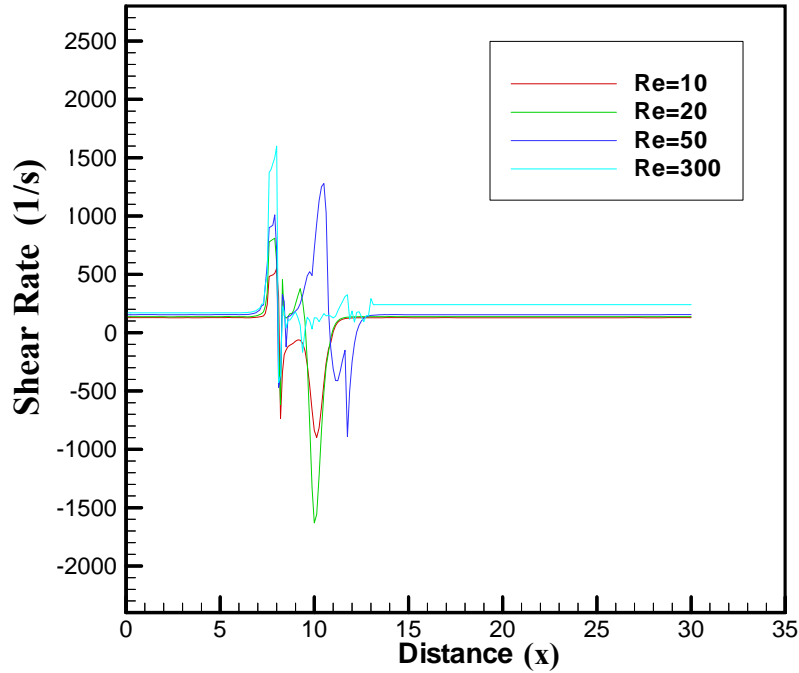


Figure (8) Shear Rate at the wall for $Re = 10, 20, 50$ and 300 and single degree of stenosis equal to 0.8

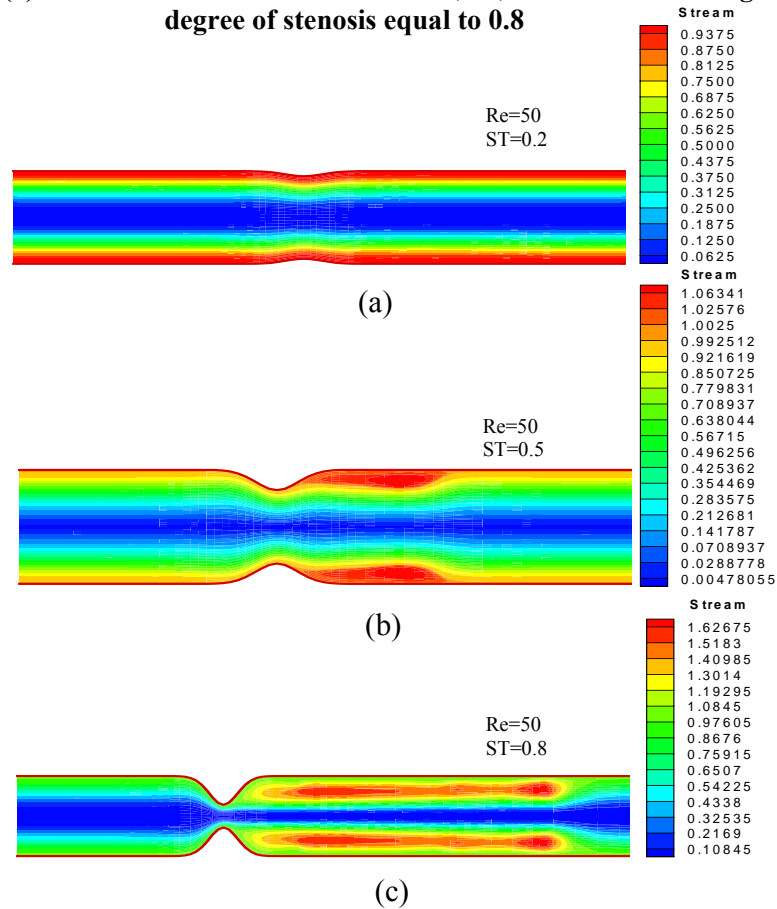


Figure (9) Streamline for non-Newtonian for $Re = 50$ and for different degrees of Stenosis: (a) 0.2 ; (b) 0.5 ; (c) 0.8 .

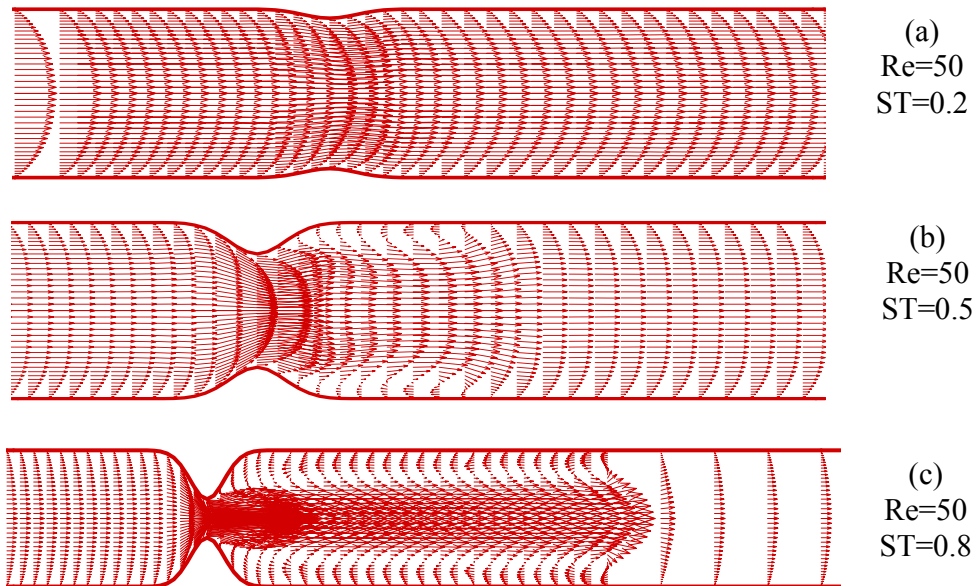


Figure (10) The velocity profile for non-Newtonian flow for $Re = 50$ and for different degrees of stenosis (a) 0.2 ; (b) 0.5 ; (c) 0.8

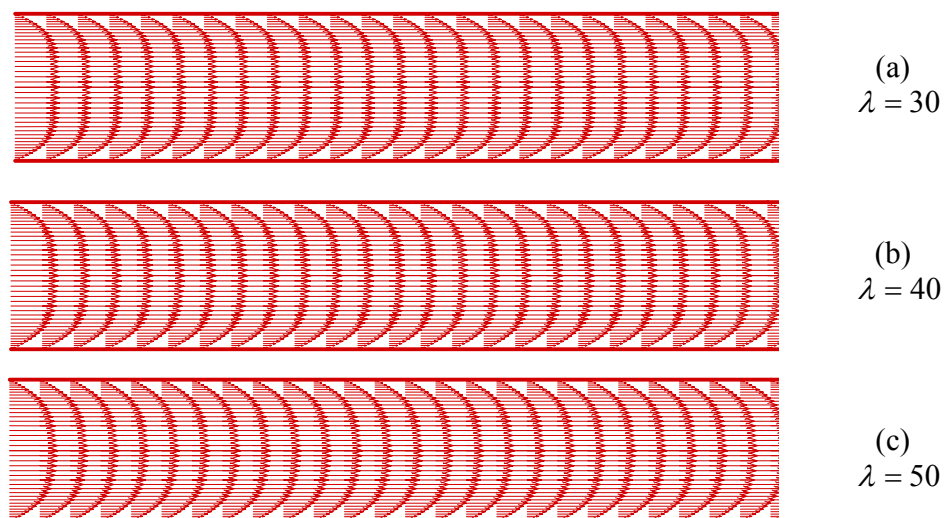


Figure (11) The velocity profile for non-Newtonian flow for $Re=300$, $ST=0.0$

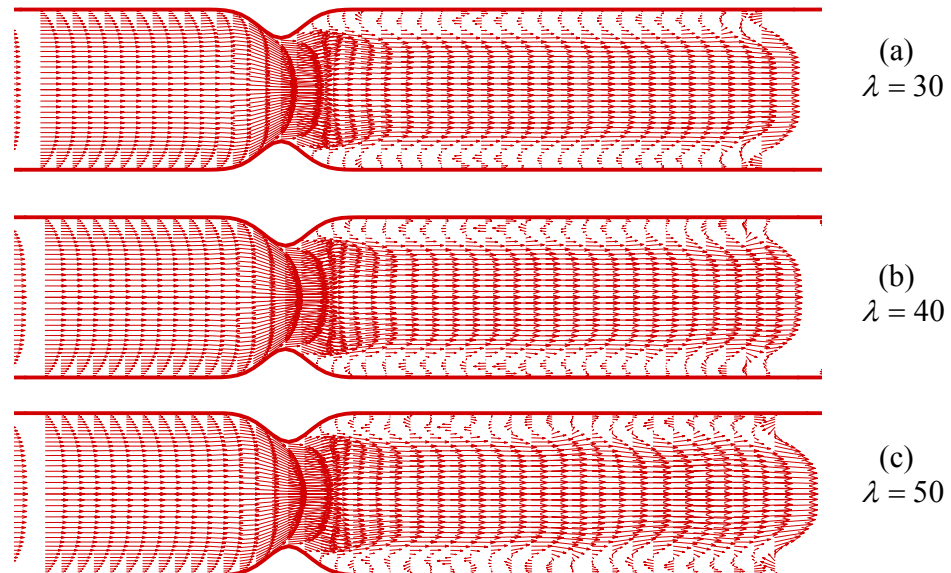


Figure (12) The velocity profile for non-Newtonian flow for $Re=300$, $ST=0.5$



FINITE ELEMENT ANALYSIS OF STRIP FOOTING RESTING ON GIBSON-TYPE SOIL BY USING MATLAB

Ahmed Qasim Obaid¹ ; Firas Hussain Ali¹ ; and Adnan Qahtan Mohammed¹

¹ Assistant Lecturer, Department of Engineering Affairs, Baghdad University, Iraq.

ABSTRACT

This research presents a method of using MATLAB in analyzing a nonhomogeneous soil (Gibson-type) by estimating the displacements and stresses under the strip footing during applied incremental loading sequences. This paper presents a two-dimensional finite element method. In this method, the soil is divided into a number of triangle elements. A model soil (Gibson-type) with linearly increasing modulus of elasticity with depth is presented. The influences of modulus of elasticity, incremental loading, width of footing, and depth of footing are considered in this paper. The results are compared with authors' conclusions of previous studies.

(Gibson-type)

MATLAB

(Gibson-type)

KEYWORDS: nonhomogeneous soil, Gibson-type, MATLAB, finite element method, strip footing.

INTRODUCTION

In general, the magnitude and distribution of the displacements and stresses in soil are predicted by using solutions that model soil as a linearly elastic, homogeneous and isotropic continuum. From the standpoint of practical considerations in engineering, anisotropic soils are often modeled as orthotropic or isotropic medium. Besides, the effects of deposition, overburden, desiccation, etc., can lead geotechnical media, which exhibit both nonhomogeneity and anisotropic deformability characteristics.

The type of elastic nonhomogeneity is a useful approximation for modeling certain problems of geotechnical interest (Selvadurai, 1998).

In this work, an elastic static loading problem for a continuously nonhomogeneous isotropic medium with Young's modulus varying linearly with depth is relevant.

The solutions of displacements and stresses for various types of applied loads to homogeneous and nonhomogeneous isotropic/anisotropic full/half-spaces have played an important role in the design of foundations. However, it is well known that a strip load solution is the basis of complex loading problems for all constituted materials. A large body of the literature was devoted to the calculation of displacements and stresses in isotropic media with the Young's or shear modulus varying with depth according to the linear law, the power law, and the exponential law, etc. A more recent survey of the existing solutions for a nonhomogeneous isotropic is summarized in Table 1 (Wang et al., 2003).

A closed-form expression for a footing resting on a soil with stiffness linearly increasing with depth (Gibson, 1967) is given only for undrained loading ($\nu=0.5$). To resolve drained loading cases with $\nu<0.5$, finite element solutions were developed for estimating the displacements for nonhomogeneous cases (e.g. Carrier and Christian, 1973; and Boswell and Scott, 1975).

A numerical technique was used by Stark and Booker (1997) for the analysis of surface displacements of a non-homogeneous elastic half-space subjected to vertical and/or horizontal surface loads uniformly distributed over an arbitrarily shaped area.

In geotechnical engineering practice, it is usual to consider only the change in stresses ($\Delta\sigma$) when computing displacements.

In practice, most foundations are flexible. Even very thick ones deflect when loaded by the superstructure loads (Bowles, 1996).

- NONHOMOGENEOUS "GIBSON-TYPE" SOIL PROFILE

In natural soil deposits, the variation of soil modulus with depth may assume any of a number of possible scenarios which shown in Table 1. Since many soils exhibit stiffness increasing with depth because of the increase in overburden stress, the displacement and stress will be evaluated for a Gibson type soil. A footing resting on a nonhomogeneous elastic medium with modulus increasing with depth is a more generalized problem (Boswell and Scott, 1975; and Stark and Booker, 1997).

The variation of elastic modulus for a generalized Gibson soil (Gibson, 1967) is expressed by:

$$E_s = E_o + kz \quad (1)$$

where E_s = the elastic soil modulus increasing linearly with depth; E_o = Young's modulus of elasticity of soil directly underneath the foundation base; k = linear rate of increase of elastic modulus with depth (units of E per unit depth); and z = depth, (Figure 1) (Mayne and Poulos, 1999; and Das, 2002).

- FINITE ELEMENT ANALYSIS

The finite element method provides an extremely powerful method for the analysis of elastic materials. Many natural soil deposits can be considered to have been deposited in a sequence of horizontal layers and, thus, there is no variation of elastic properties in any horizontal plane.

One of the essential ingredients for a successful finite element analysis of a geotechnical problem is an appropriate soil constitutive model (Potts and Zdravkovic, 2001).

The advantage of an arbitrary triangular shape is to approximate to any boundary shape (Zienkiewicz and Taylor, 2000). So the triangular element shape is considered in this research.

A finite element computer program for a rigid circular plate resting on a non-homogeneous elastic half-space was presented by Carrier and Christian (1973).

Boswell and Scott (1975) presented a finite element solution for a flexible circular footing resting on a semi-infinite half space.

In the present study, 3-noded triangles elements with two degree of freedom at each node have been used to model soil. In each increment of the analyses, the stress-strain behavior of the soil is treated as being linear, and the relationship between stress and strain is assumed to be governed by the generalized Hooke's law of elastic deformations, which may be expressed as follows for conditions of plane strain case:

$$\begin{Bmatrix} \Delta\sigma_x \\ \Delta\sigma_y \\ \Delta\tau_{xy} \end{Bmatrix} = \frac{E_s(1-\nu)}{(1+\nu)(1-2\nu)} \begin{bmatrix} 1 & \frac{\nu}{1-\nu} & 0 \\ \frac{\nu}{1-\nu} & 1 & 0 \\ 0 & 0 & \frac{1-2\nu}{2(1-\nu)} \end{bmatrix} \begin{Bmatrix} \Delta\epsilon_x \\ \Delta\epsilon_y \\ \Delta\gamma_{xy} \end{Bmatrix} \quad (2)$$

where $\Delta\sigma_x$, $\Delta\sigma_y$ and $\Delta\tau_{xy}$ = the increments of stress during a step of analysis; $\Delta\epsilon_x$, $\Delta\epsilon_y$ and $\Delta\gamma_{xy}$ = the corresponding increments of strain; E_s = the value of Young's modulus; and ν = the value of Poisson's ratio.

About MATLAB

The MATLAB programming language is useful in illustrating how to program the finite element method due to the fact it allows one to very quickly code numerical methods and has a vast predefined mathematical library. A simple two dimensional finite element program in MATLAB need only be a few hundred lines of code whereas in Fortran or C++ one might need a few thousand (Chessa, 2002).

MATLAB can be very useful as a solution tool for the finite element method which Matrix and vector manipulations are essential parts in the method (Kwon and Bang, 1997).

- The Finite Element Computer Program by MATLAB

A computer program designed by the authors was used in the finite element analysis carried out during this research. The program allows for triangle type of elements to be used in

the finite element mesh in solving soil problems under plane conditions (strain or stress). The behavior of the soil can be approximated by Gibson model (Gibson, 1967). The model that is considered in this work is nonhomogeneous, isotropic on primary loading with a different modulus.

The sign convention for the stresses and the convention for numbering the nodes of elements are shown in Figure (2). The program presents the results of analysis as the displacements of the nodal points, and the value of stresses developed at the centre of each element at the end of each solution increment.

Figure (3) is a flowchart that illustrates the main features of the solution procedure adopted in the finite element computer program used.

Verification of the Computer Program

The authors have used this program in different problems (Figure 4) presented by another researchers (e.g. Brown, 1984; and Smith and Griffiths, 1988).

The results obtained by the program modified in this research were compared with results presented by Brown (1984); and Smith and Griffiths (1988). In all these comparisons, excellent agreement was found between the present work results and those published, as shown in Table 2.

- PROBLEM GEOMETRY

The case study is treated as plane strain two-dimensional problem for simplicity when analyzed by the finite element method. The shape of elements used is the triangular element because of its suitability to simulate the very important behavior of soils under strip footing.

The basic problem chosen for the parametric study shown in Figure (5.a), involves a soil stratum, 21.0 m thick and 28.0 m width, of a silty clay soil underlain by bedrock and loads by strip sequence loadings (80, 160, 240 kN/m²) with base width equal to 1.0 m.

The finite element mesh (Figure 5.b) used consists of 989 nodal points and 1848 triangular two-dimensional elements. The nodal points along

the bottom boundary of the mesh are assumed to be fixed both horizontally and vertically. The nodes on the right and left ends of the mesh are fixed in the horizontal direction while they are free to move in the vertical direction. All interior nodes are free to move horizontally and vertically.

- MATERIAL CHARACTERIZATION

The stratum is silty clay soil and the properties of the soil are reported in Table 3, (Das, 2002). The behavior of soil material is a nonhomogeneous elastic medium with modulus increasing linearly with depth.

- RESULTS AND DISCUSSIONS

In this study, a model of silty clay soil was analyzed under uniformly flexible strip loading with soil modulus increasing linearly with depth. In order to develop more knowledge about the behavior of soils under strip loading problems, a parametric study is performed by varying the basic problem parameters and comparing these results with the original basic problem results. The results of increasing the load, constant soil modulus with depth, and changing the footing depth (D_f) and width (B) are presented as follow:

For uniformly flexible strip loaded area the vertical displacement along the surface of the model is shown in Figure (6) and the contact settlement under the strip footing is shown in Figure (7). The settlement at the center is much larger than the settlement at the edge of the loaded area. These results agree with the results founded by Wu (1974) and Das (2002). Also the vertical displacement increases in direct proportion to the pressure of the loaded area, as shown in Figures (6) and (7), which agrees with that reported by Craig (1987).

The vertical stress contours throughout the soil to depth ($5B$) under the strip loadings (80, 160, 240 kN/m²) with base width (B) equal to 1.0 m are shown in Figure (8). It can be seen that the vertical stress values along the depth of the layer decrease throughout the layer for each increment and increase throughout the loading sequence stages.

From the settlements at depth ($4B$) from the top of model (Figure 9), it can be seen that the settlement for soil with modulus increasing linearly with depth is less than the settlement for

soil with constant modulus ($E_s = E_o = 9000$ kN/m²). The results agree with that mentioned by Terzaghi in Wu's book (Wu, 1974).

The immediate settlement at the center of the loaded area is reduced when the strip footing is placed at some depth ($D_f \leq B$) in the ground, depending on footing width (B), as shown in Figure (10). These results agree with that mentioned by Fox in Bowles' book (Bowles, 1996).

The vertical displacement (immediate settlement) increases in direct proportion to the width of the loaded area (size of the footing), as shown in Figure (11), which agrees with that reported by Wu (1974) and Craig (1987).

CONCLUSIONS

The results obtained from this study can lead that the computer program can simulate the analysis of the nonhomogeneous silty clay soil (Gibson-type), which had a soil modulus increasing linearly with depth and loaded with incremental strip loading.

This paper shows how the computer solutions may be used to improve the prediction of settlements and stresses beneath a strip footing resting on Gibson-type soil.

Displacements and stresses can be calculated with knowledge of soil stiffness beneath the footing, rate of increase of soil stiffness with depth, soil Poisson's ratio, depth to an incompressible layer, and footing width.

The immediate settlement at the center is much larger than the settlement at the edge of the strip loaded area. The immediate settlement increases in direct proportion to the pressure and the width of the strip loaded area. The vertical stress values (stress bulb) under the strip loaded area decrease throughout the layer for each increment and increase throughout the loading sequence stages. The vertical displacement for soil with modulus increasing linearly with depth (Gibson-type) is less than the vertical displacement for the same soil with constant modulus which leads to that the soil with (Gibson-type) modulus is more approximate simulation for soil modulus. The immediate settlement of the strip loaded area decreases when the depth of strip footing increases. The results compare favorably



with available published analytical and numerical solutions.

REFERENCES

- Boswell, L.F., and Scott, C.R., (1975), "A flexible circular plate on a heterogeneous elastic half-space: influence coefficients for contact stress and settlement", *Geotechnique*, Vol. 25, No. 3, pp. 604-610;
- Bowles, J. E., (1996), "Foundation analysis and design", 5th edition, McGraw-Hill Companies, Inc.;
- Brown D. K., (1984), "An introduction to the finite element method using BASIC programs", Taylor and Francis Group;
- Carrier, D.W., and Christian, J.T., (1973), "Rigid circular plate resting on a nonhomogeneous elastic half space", *Geotechnique*, Vol. 23, No. 1, pp. 67-84;
- Chessa J., (2002), "Programming the finite element method with MATLAB", Internet;
- Craig R. F., (1987), "Soil mechanics", 4th edition, Van Nostrand Reinhold (UK) Co. Ltd;
- Das, B. M. (2002), "principles of geotechnical engineering", 5th edition, Wadsworth Group;
- Gibson R. E., (1967), "Some results concerning displacements and stresses in a non-homogeneous elastic half-space", *Geotechnique*, 17, pp. 58-67;
- Kwon Y. W., and Bang H., (1997), "The finite element method using MATLAB", CRC Press;
- Mayne, P.W., and Poulos, H.G., (1999), "Approximate displacement influence factors for elastic shallow foundations", *J. Geotech. and Geoenviron. Eng., ASCE*, 125(6), pp. 453-460;
- Potts D. M., and Zdravkovic L., (2001), "Finite element analysis in geotechnical engineering: Application", Thomas Telford;
- Selvadurai, A. P. S., (1998), "Lan Q. Axisymmetric mixed boundary value problems for an elastic halfspace with a periodic nonhomogeneity", *Int. J. Solids Struct.*, 35, pp. 1813-1826;
- Smith I. M., and Griffiths D. V., (1988), "Programming the finite element method", 2nd edition, John Wiley & Sons Ltd;
- Stark, R.F., and Booker, J.R., (1997), "Surface displacements of a non-homogenous elastic half-space subjected to uniform surface tractions", *International Journal of Numerical and Analytical Methods in Geomechanics*, Vol. 21, No. 6, pp. 361-378;
- Wang C.D., Tzeng C.S., Pan E., and Liao J.J., (2003), "Displacements and stresses due to a vertical point load in an inhomogeneous transversely isotropic half-space", *International Journal of Rock Mechanics & Mining Sciences*, 40, pp. 667-685;
- Wu T. H., (1974), "Soil mechanics", 7th printing, Allyn and Bacon, Inc.;
- Zienkiewicz O. C., and Taylor R. L., (2000), "The Finite element method / volume 1: the basis", 5th edition, Butterworth-Heinemann.

Table 1. Existing analytical/numerical solutions for nonhomogeneous isotropic media, (Wang et al., 2003)

Types of nonhomogeneity	Author
$E = m_E z^\alpha$ or $G = m_G z^\alpha$ ($0 \leq \alpha \leq 1$)	Rostovtsev ; Lekhnitskii ; Popov ; Zaretsky and Tsytoich ; Kassir ; Rostovtsev and Khramevskaya ; Carrier and Christian ; Puro ; Popov ; Booker et al. ; Oner ; Booker ; Giannakopoulos and Suresh ; Stark and Booker ; Yue et al. ; Holzlochner .
$E = E_0(a + bz)^c$ or $G = G_0(a + bz)^c$	Plevako ; Chuaprasert and Kassir ; Kassir and Chuaprasert ; Dhaliwal and Singh ; Harnpattanapanich and Vardoulakis ; Rajapakse and Selvadurai ; Jeng and Lin .
$E = E_0 + \lambda z$ or $G = G_0 + \lambda z$	Gibson ; Gibson et al. ; Brown and Gibson ; Awojobi and Gibson ; Carrier and Christian ; Alexander ; Calladine and Greenwood ; Rajapakse ; Chow ; Rajapakse and Selvadurai ; Dempsey and Li ; Yue et al. .
$E = E_0 + E_1 e^{\xi z}$ or $G = G_0 + G_1 e^{\xi z}$	Ter-Mkrtych'ian ; Rowe and Booker ; Row and Booker ; Selvadurai et al. ; Vrettos ; Selvadurai ; Giannakopoulos and Suresh ; Jeng and Lin .
$G = G_0 e^{-\xi r}$	George .
$G = G_0 r^\alpha z^\beta$	Singh ; Dhaliwal and Singh .
$G = G_0 * h / (h - z)$	Awojobi .
$G = \text{constant}$	Gibson and Sills .

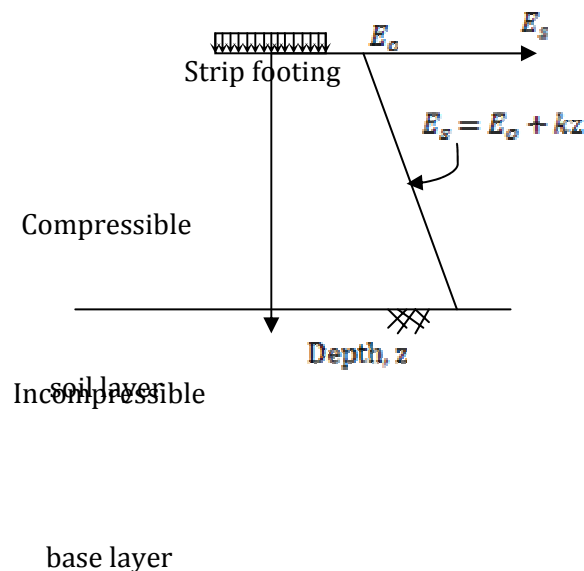


Fig. 1. Variation of soil modulus with depth



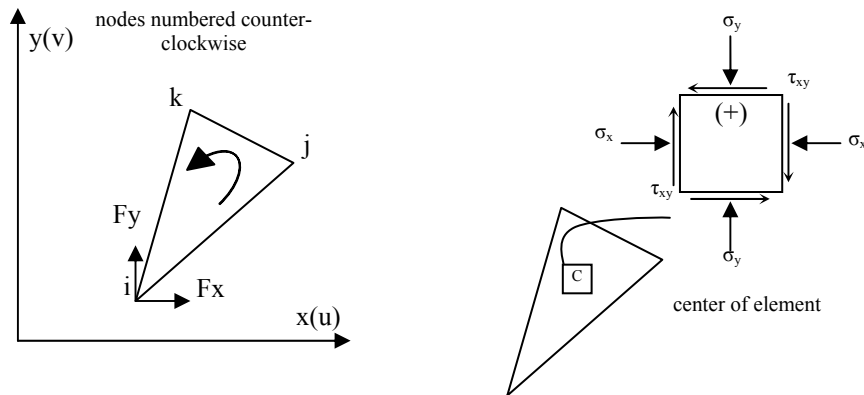


Fig. 2. Sign convention and element numbering

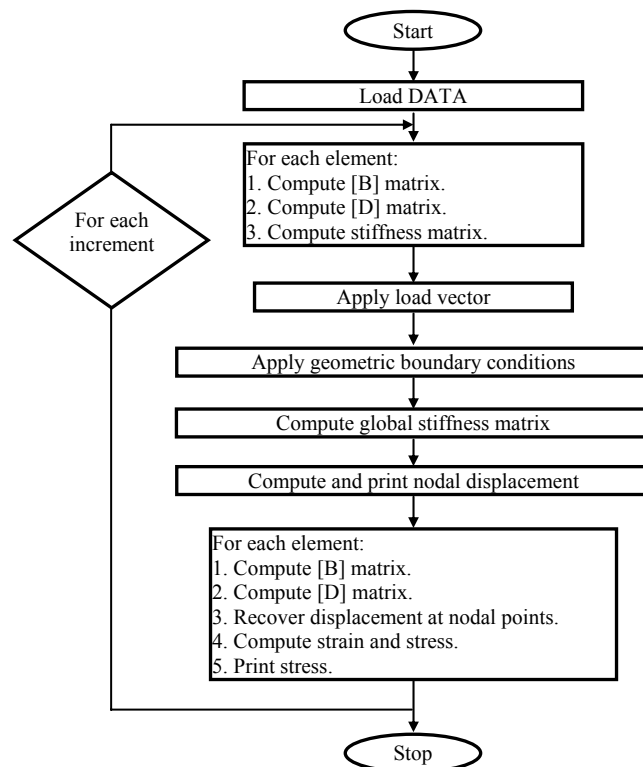
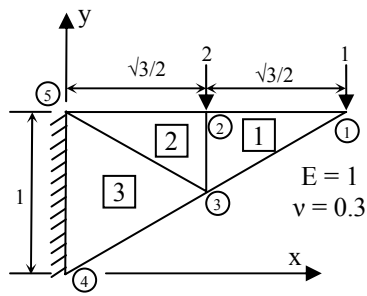
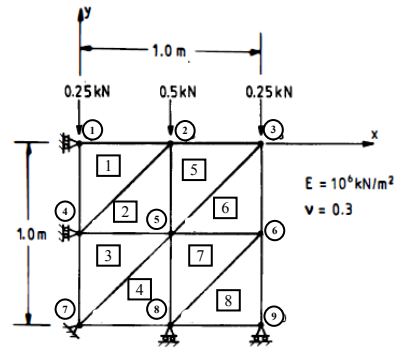


Fig. 3. Simplified flow chart of the finite element program



(a) after Brown (1984).



(b) after Smith and Griffiths (1988).

Fig. 4. Mesh and data for different problems

Table 2. Comparison with the theoretical results

Item considered	Brown results	Authors results
Hor. Disp. of node 1	7.712	7.7122134E+000
Ver. Disp. of node 3	-	-
	13.582	1.3583206E+001
Ver. Stress at elem. 2	-2.461	-
		2.4605374E+000
Hor. Stress at elem. 2	6.816	6.8155730E+000

Item considered	Smith and Griffiths results	Authors results
Ver. Disp. of node 2	-0.1000E-05	-1.000000E-006
Hor. Disp. of node 6	0.3000E-06	3.000000E-007
Ver. Stress at elem. 1	-0.1000E+01	-
		1.000000E+000
Shear Stress at elem. 8	0.0000E+00	0.000000E+000

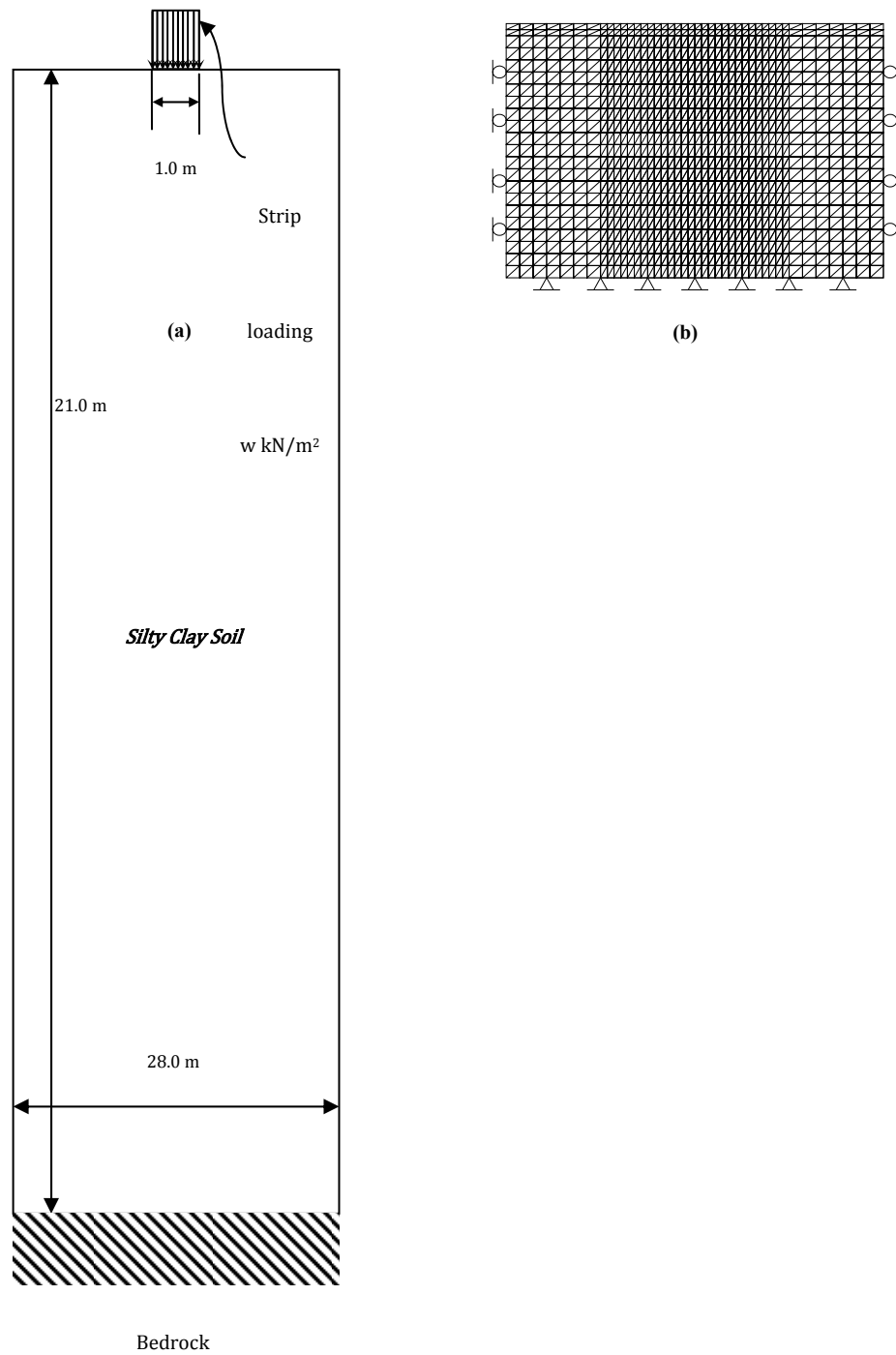


Fig. 5. The basic problem for the parametric study

Table 3. The soil properties

E_o	9000 kN/m ²
k	500 kN/m ² /m
ν	0.3

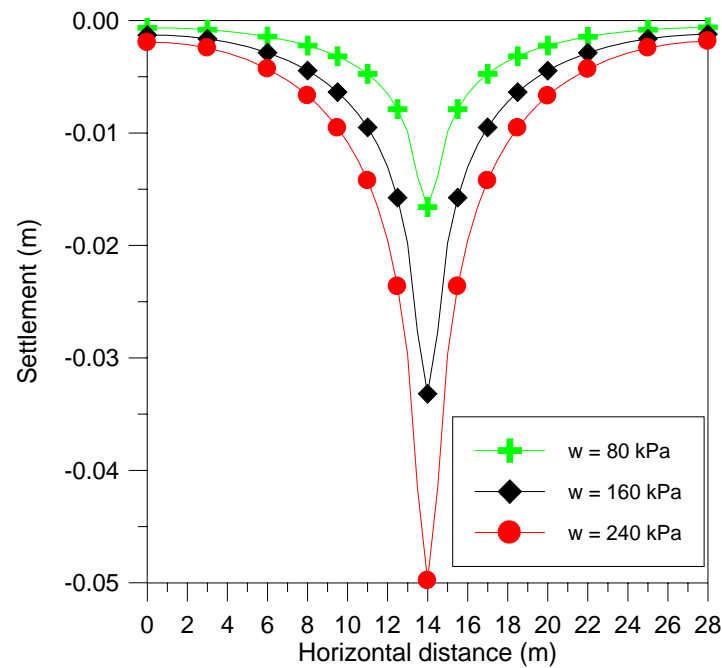


Fig. 6. Settlements along the surface of the model under the strip loadings (80, 160, 240 kN/m²) with base width equal to 1.0 m

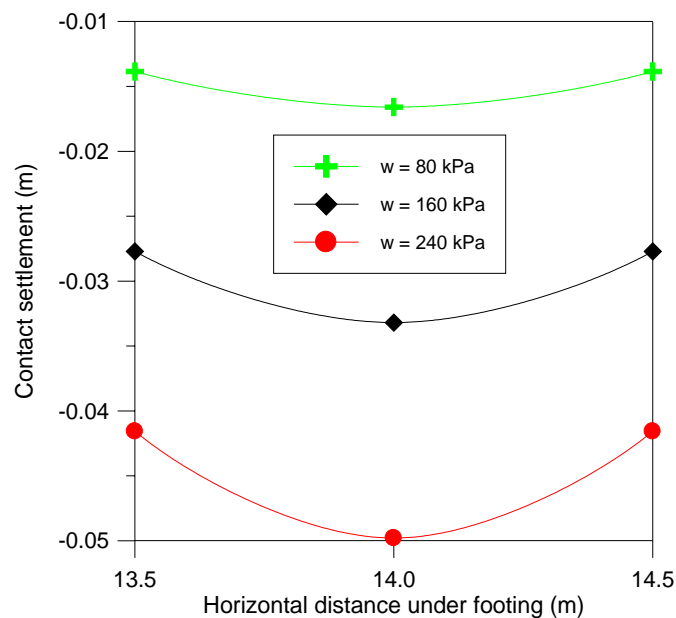


Fig. 7. Contact settlements under the strip loadings (80, 160, 240 kN/m²) with base width equal to 1.0 m

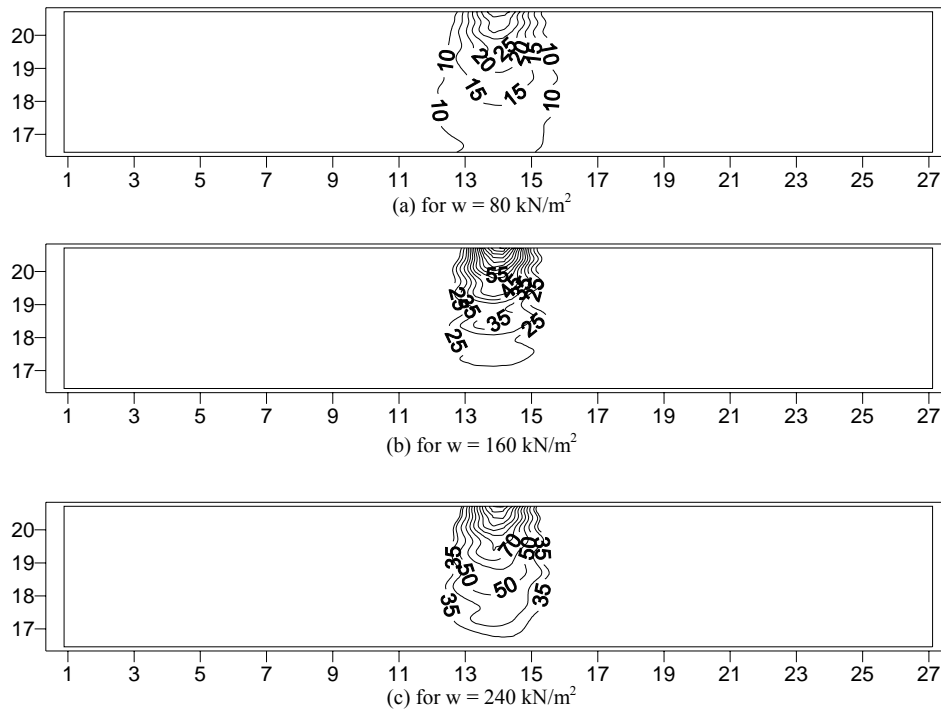


Fig. 8. Vertical stress contours for the soil model to depth (5B) throughout the loading sequences

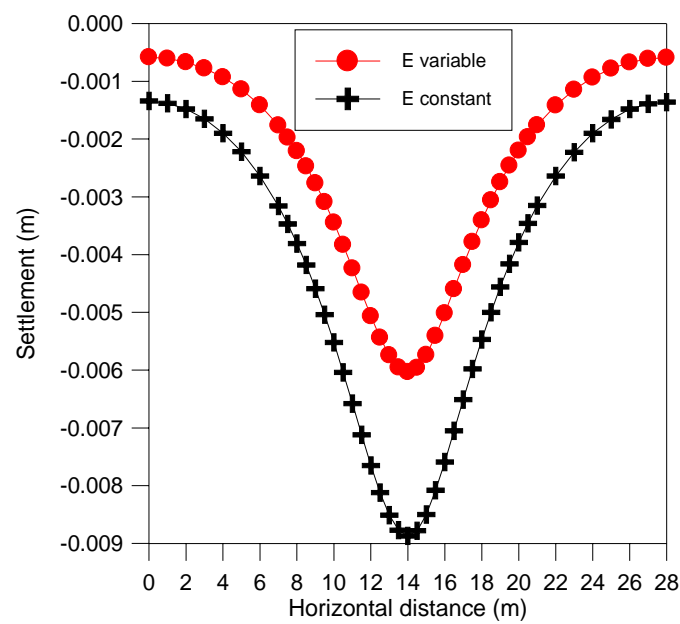


Fig. 9. Settlements along the horizontal distance at depth (4B) under strip loading (80 kN/m^2)

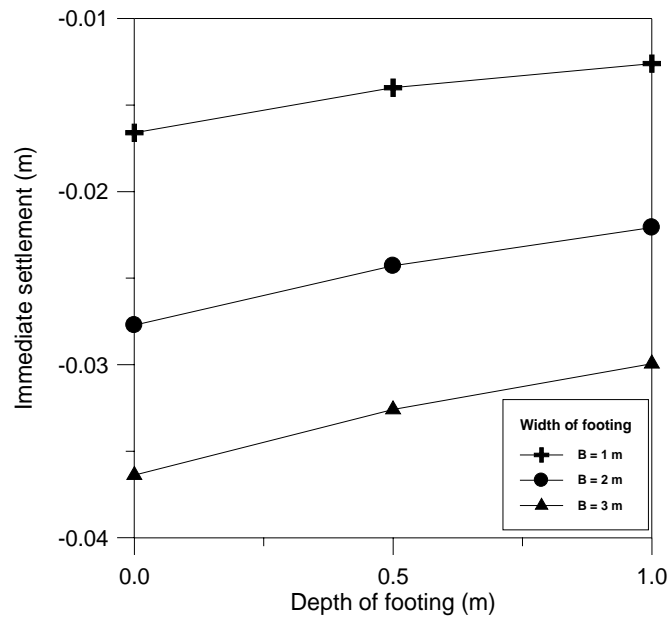


Fig. 10. Immediate settlements at the center of the strip loading (80 kN/m^2) with different width of footing according to depth of footing

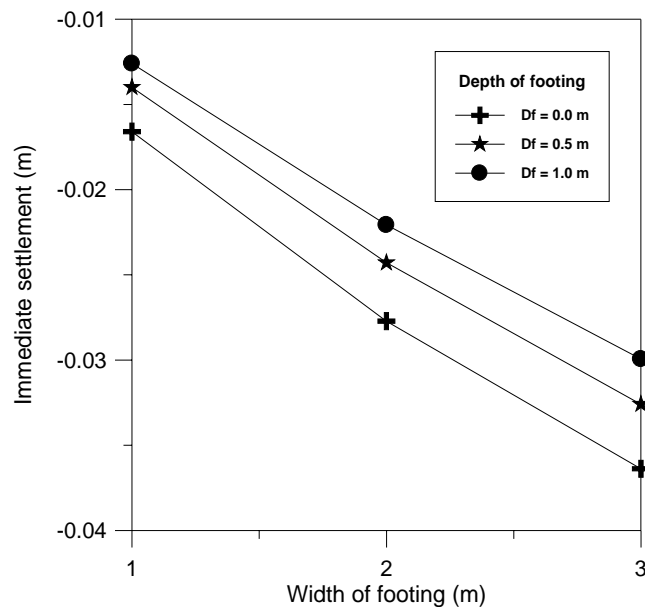


Fig. 11. Immediate settlements at the center of the strip loading (80 kN/m^2) with different depth of footing according to width of footing

HYDRODESULFURIZATION OF THIOPHENE OVER CO-MO/AL₂O₃ CATALYST USING FIXED- AND FLUIDIZED-BED REACTORS

Prof. Dr. Abdul Halim A-K Mohammed, Chemical Engineering Department, Baghdad University
Dr. Saad Hanash Ammar, Chemical Engineering Department, Nahrain University, 2009

ABSTRACT

The present work reports a direct experimental comparison of the catalytic hydrodesulfurization of thiophene over Co-Mo/Al₂O₃ in fixed- and fluidized-bed reactors under the same conditions. An experimental pilot plant scale was constructed in the laboratories of chemical engineering department, Baghdad University; fixed-bed unit (2.54 cm diameter, and 60cm length) and fluidized-bed unit (diameter of 2.54 cm and 40 cm long with a separation zone of 30 cm long and 12.7 cm diameter). The affecting variables studied in the two systems were reaction temperature of (308 – 460) °C, Liquid hourly space velocity of (2 – 5) hr⁻¹, and catalyst particle size of (0.075-0.5) mm. It was found in both operations that the conversion increases with increasing of reaction temperature, slightly decreases with increasing of liquid hourly space velocity and not affected by particle size. Also a kinetic analysis was performed for thiophene hydrodesulfurization reaction in fixed bed reactor and the results indicate that the reaction kinetics are not affected by pore and film diffusion limitations. The results of the comparison between the two reactors indicate that a low conversion was obtained in a fluidized bed than in fixed bed over the range of conditions studied. The lower conversion can be attributed to the gas that bypasses the bed in the form of bubbles or channels.

KEYWORDS: Thiophene, Hydrodesulfurization, Fixed- bed reactor, Fluidized-bed reactor.

تم في هذا البحث دراسة تفاعل هدرجة الثيوفين لازالة الكبريت بوجود عامل مساعد صلب وهو الكوبولت - موليبديوم المحمل على الالومينا. وذلك في نوعين من المفاعلات وهما المفاعل ذو الطبقة الثابتة والمفاعل ذو الطبقة المميعة. تم بناء منظومتين ريادية مكونة من مفاعل الطبقة الثابتة (ذو قطر 2,54 سم وطول 60 سم) ومفاعل الطبقة المميعة (ذو قطر 2,54 سم مطول 40 سم) الهدف من هذا الدراسة هو مقارنة اداء كل من هذين المفاعلين تحت نفس الظروف من درجة حرارة (308- 460) م° وسرعة حجمية (2-5) سا⁻¹، وحجم جسيمة العامل المساعد (استخدمت ثلاث مديات لحجم جسيمة العامل المساعد: (0,075 – 0,15) ملم، (0,3 – 0,5) ملم، بالإضافة للحجم الاصلي (1) × (2 – 5) ملم). اظهرت النتائج في تجارب المفاعل ذو الطبقة الثابتة تأثر التحول كثيرا بتغيير درجة حرارة التفاعل حيث يزداد التحول بزيادة درجة الحرارة ويتأثر قليلا بتغيير السرعة الحجمية ولا يتأثر بتغيير حجم جسيمة العامل المساعد. كذلك ظهرت نتائج مشابهة في تجارب المفاعل ذو الطبقة المميعة. استنتج من هذه النتائج ان حركية تفاعل هدرجة الثيوفين بوجود العامل المساعد الكوبولت - موليبديوم المحمل على الالومينا لا تتأثر بمقاومة الانتشار الداخلي لجسيمة العامل المساعد (داخل المسامات) وكذلك لا تتأثر بمقاومة الانتشار الخارجي للجسيمة (الانتشار الغشائي). بصورة عامة وبمقارنة الاداء بين المفاعلين، اظهرت النتائج حصول تحول اقل في المفاعل ذو الطبقة المميعة عنه في المفاعل ذو الطبقة الثابتة وذلك بسبب مرور قسم من الغاز المتفاعل الداخل خلال فقاعات او قنوات في طور الفقاعات ولا يمر على العامل المساعد في الطور المستحلب في المفاعل ذو الطبقة المميعة.

INTRODUCTION

Reactant fluid can be made to contact solid catalyst in many ways, and each has its specific advantages and disadvantages. The contacting patterns may be divided into two broad types, the fixed-bed reactors and the fluidized-bed reactors. The moving-bed reactor is an intermediate case which embodies some of the advantages and some of the disadvantages of fixed-bed and fluidized-bed reactors [1].

In comparison merits of these reactor types; in passing through fixed bed, fluid approximate plug flow. It is quite different with bubbling fluidized beds where the flow is complex and not well known, but certainly far from plug flow, and with considerable bypassing. This behavior is unsatisfactory from the standpoint of effective contacting and requires much more catalyst for high gas conversion, and greatly depresses the amount of intermediate which can be formed in series reactions. Hence, if efficient contacting in a reactor is of primary importance, then the fixed bed is favored [2].

Effective temperature control of large fixed beds can be difficult because such systems are characterized by a low heat conductivity. Thus in highly exothermic reactions hot spots or moving hot fronts are likely to develop which may ruin the catalyst. In contrast with this, the rapid mixing of solids due to bubbles and strong turbulent flow in fluidized beds allows easily and reliably controlled, practically isothermal, operations. So if operations are to be restricted within a narrow temperature range, either because of the explosive nature of the reaction or because of product distribution considerations, then the fluidized bed is favored. Fixed beds cannot use very small sizes of catalyst because of plugging and high-pressure drop, whereas fluidized beds are well able to use small-size particles. Thus for very fast reactions in which pore and film diffusion may influence the rate, the fluidized bed with its vigorous gas-solid contacting and small particles will allow a much more effective use of the catalyst [3].

If the catalyst has to be treated (regenerated) frequently because it deactivates rapidly, then the liquid-like fluidized state allows it to be pumped easily from unit to unit. This feature of fluidized contacting offers

overwhelming advantages over fixed bed operations for such solids [4].

AIM OF THE PRESENT WORK

The objective of the work presented in this paper can be summarized as follows:

- Investigating the effect of fluidization on HDS reaction and comparison between the performances of fixed- and fluidized-bed reactors.
- The effect of the variables temperature, 308 – 460 °C, liquid hourly space velocity (LHSV), 2 – 5, and catalyst particle size, were studied in both types of reactors on the HDS conversion.

EXPERIMENTAL

(I) MATERIALS

- Feed

Thiophene, C₄H₄S of 99.9% purity (supplied from Fluka AG, Chem. Company) was used as a raw material for catalytic hydrodesulfurization process (molecular weight, 84; density, 1.071 gm/cm³ at 16 °C; and boiling point, 84.1 °C).

-Catalyst

Cobalt Molybdenum supported on Alumina (**HR-306**), supplied from Middle Refineries Company, Baghdad was used as hydrodesulfurization catalyst. The physical and chemical properties of catalyst HR-306 are mentioned in Table (1). The catalyst was activated by heating in hydrogen to 350 °C and stabilized (sulfide) with thiophene and H₂ for about 2 hr.

- Gases

Hydrogen with purity of 99.9 % supplied from Middle-Electric General Company, Baghdad was used in Thiophene hydrodesulfurization process. High grade quality (purity 99.9 %) of nitrogen obtained from Al-Mansor

factory, Baghdad was also used in this investigation. Nitrogen was used in the beginning in order to ensure good temperature distribution in the reactor, to purge the air from the reactor and at the end of experiment to purge off the gases from all the system.

- UNITS AND PROCEDURE

-Fixed bed system

The series of fixed bed runs were made in a conventional continuous flow fixed bed catalytic reactor unit. Schematic flow diagram of the experimental system is given in Figures 1. The equipment can be divided functionally into five parts, liquid feed dosing pump, gases feed, evaporator/preheating, reactor system, and condensation/separation.

The fixed bed reactor consisted of a carbon steel tube (2.54 cm diameter, and 60cm length) which was charged for each experiment with about 22 gm (25.7 cm³) sample of catalyst and placed in the middle zone while the upper and lower zones were filled with inert glass balls and work as a preheaters. The reactor was heated by four steel- Jacket heaters. Temperatures in the reactor were measured by thermocouples at three positions. The thermocouples measured the temperature profile along full length of reactor.

Before each run a 10-min nitrogen pretreatment was employed to purge the air from the system and for catalyst conditioning. The reactor is heated to the desired reaction temperature, and after reaching that temperature, the nitrogen valve was closed. After catalyst pretreatment, liquid thiophene feed was pumped by a dosing pump to the evaporator at the prespecified rate. The evaporator consists of coil tube (10m long with 5mm i.d). The heat was supplied by using 6 kW electrical heaters to vaporize and heat the feed to the desired temperature controlled by voltage regulator.

Thiophene vapor feed was mixed with hydrogen and then passed through the upper preheater and in downflow through the reactor, distributed uniformly and reacted on

the catalyst. The vapor of product passed through the condenser and the condensates were collected. The reaction was allowed to proceed continuously for 30 min to permit the system to achieve a steady state conversion, pressure, and temperature. During this time the liquid product went to the waste-product receiver. After that liquid samples characterizing the run were taken over the next 20 min period. At the end of the sampling period the liquid product stream was switched to waste and the feed valves shut off.

Some gas product samples were analyzed by the gas chromatography analysis (Packard 438A located in Ibn-Sina State Company), thiophene was not detected in the gas product stream; it was present in liquid product stream only. Therefore, the percentage conversion of HDS reaction can be calculated simply from equation 1.

$$\text{Conversion (\%)} = \left(1 - \frac{V_A}{V_{Ao}}\right) * 100 \quad (1)$$

Where V_{Ao} is the liquid thiophene feed volume within (ml) and V_A is unreacted thiophene volume (ml) after the same period.

As preliminary experiments, the effect of duration time (time-on-stream) on catalyst activity was examined at temperature, 411 °C; LHSV 2 h⁻¹; catalyst particle size, 1* (2-5) mm and atmospheric pressure. The catalytic hydrodesulfurization reaction conditions employed in fixed-bed runs were reaction temperature of (308-460) °C, LHSV of (2 – 5) hr⁻¹, and Catalyst particle size ranges of 1* (2-5) mm, (0.5-0.3) mm, and (0.3-0.15) mm.

-Fluidized bed system

The fluidized runs were performed in an experimental fluidized bed reactor unit. Figure 2 shows the schematic flow diagram of the unit. The unit consisted of a thiophene storage tank, dosing pump, electrical evaporator, preheater to preheat the thiophene vapor and hydrogen mixture, fluidized bed reactor to contact the feed mixture and catalyst, condenser/separator to condensate and separate the unreacted

thiophene, and control and power supply box.

The fluidized bed reactor was made from stainless-steel with diameter of 2.54 cm and 40 cm long with a separation zone of 30 cm long and 12.7 cm diameter. The reactor was heated electrically and the temperature was measured using thermocouples at two positions.

Perforated plate made from stainless steel with 0.5 mm thickness was used as a distributor. The distributor plate designed so as to make a free area of flow of 4.18% of the total area. The number of holes equal to 27 hole, with a hole diameter of 1 mm. A layer of a fine mesh screen was placed on the distributor to prevent the plugging of the distributor holes by the solid particles.

Before a run was started, the desired amount of catalyst was placed in the reactor and the equipment heated while nitrogen was passed upflow through the reactor. The desired amount of liquid thiophene was pumped by dosing pump to the evaporator and the vapor of thiophene was mixed with hydrogen then the mixture was preheated and entered the reactor from the bottom through the distributor. The reaction was allowed to proceed continuously for about 30 min to permit the system to achieve a steady state operation. After that liquid samples characterizing the run were taken over the next 20 min period.

The experimental conditions of fluidized-bed runs were L/D ratio of (2 – 8), reaction temperature of (308-460) °C, LHSV of (2 – 5) hr⁻¹, and catalyst particle size ranges of (0.075-0.15) mm, (0.15-0.3) mm, and (0.3-0.5) mm. As a preliminary study, some experiments were performed to investigate the ratio of superficial gas velocity to minimum fluidization velocity (u_0/u_{mf}) on conversion by changing L/D ratio.

Minimum fluidizing velocity experiments were carried out in a Q.V.F. glass column of 2.54 cm diameter and 40 cm long with a separation zone of 30 cm long and 12.7 cm diameter.

RESULTS AND DISCUSSION

FIXED BED RUNS

Catalyst activity

The catalytic activity (time on stream study) of Co-Mo/Al₂O₃ catalyst for the HDS of thiophene was examined in fixed bed reactor at temperature of 411 °C, catalyst particle size of 1*(2-5) mm, H₂ / thiophene mole ratio of 10, and LHSV of 2 hr⁻¹. Figure 3 shows the relationship between the conversions and duration time.

At first the catalyst activity increases with time during the first hour of operation properly due to the enhancement in catalyst activity by sulfiding the surface of catalyst with H₂S produced by reaction. This trend in HDS activity clearly indicates that the surface of the catalyst evolves into a more active structure during the course of the reaction. This results permit to conclude that during the reaction there is a surface sulfiding which conducts to the formation of a more active phase. Following the activity is then decreases until about 2 hr because of the accumulation of carbonaceous deposits on the catalyst surface. Then steady state activities were obtained after 2 hour of operation and remain substantially constant over a long period of time.

The same results of catalyst activity for catalytic HDS of thiophene over Co-Mo/Al₂O₃ was also observed and stated in previous studies of Kolboe and Amberg [5] and Van Parijs and Fromen [6].

Effect of liquid hourly space velocity (LHSV)

The effect of LHSV on thiophene conversion was determined at different reaction temperatures (308 to 460 °C), catalyst particle size of 1*(2-5) mm, and H₂ / thiophene mole ratio of 10. As shown in figure 4 the results showed that the LHSV has small effect on the conversion. At LHSV of 2 h⁻¹ and temperature 308 °C, the conversion is 56.7% and at LHSV of 5 h⁻¹ and the same temperature the conversion decreases to 45%.

As the LHSV increases thiophene conversion slightly decreases which means that the film diffusion has no effect on the reaction

kinetics. These observations agree well with the results of Ghanbari et al. [7].

- Effect of Temperature

As shown in figure 5 the conversion increases as the temperature increases. At 308 °C and constant LHSV of 2 h⁻¹, the conversion is 56.7% while at 460 °C using the same LHSV the conversion reaches 78%. This is attributed to the increase of active sites that can be used for the reaction when the temperature increases. These observations agree well with the results of Kolboe and Amberg [5].

Effect of particle size

Three different particle size ranges of catalyst were used for investigation of pore diffusional limitation on the reaction kinetics of thiophene HDS. In this set of experiments the conversion of reaction was measured with different LHSV and at temperature of 360 °C. The results of these tests are shown in figure 6. As shown from this figure, the change in particle size range of catalyst is not affect the conversion. This indicates that the mass transfer resistance spring from pore diffusion has no effect on the reaction kinetics. This is the same observation of Ghanbari et al [7].

FLUIDIZED BED RUNS

The estimation of the minimum fluidization velocity

The pressure drop as a function of gas velocity was measured in order to obtain the values of minimum fluidization velocity for three particle sizes of catalyst, which differs from one size to another. Figures 7, 8, and 9 show the experimental determination of minimum fluidization velocity from the relation of bed pressure drop with air superficial velocity for the particle sizes of (0.075-0.15), (0.15-0.3) and (0.3-0.5) mm respectively. The values of minimum fluidization velocities become higher as the particle size increases, because of voidage increasing, which increases the quantities of the gas of necessary to fluidize these particles. Table 2 shows the experimental values of minimum fluidization velocity for the three particle sizes ranges.

Effect of superficial gas velocity

For investigation of the ratio of superficial gas velocity to minimum fluidization velocity (u_o/u_{mf}) on conversion, experiments were performed at different L/D ratio to vary the u_o/u_{mf} ratio at constant LHSV. The experimental conditions of these tests are LHSV of 2 hr⁻¹, reaction temperature of 360 °C, catalyst particle size range of (0.075-0.15) mm, and H₂/thiophene mole ratio of 10.

It is seen from figure 10 that conversion is slightly affected by the inlet gas velocity, even the u_o/u_{mf} ratio increases to eight times, the conversion has not varied significantly. Therefore one value of L/D ratio will be selected (L/D = 2) for the variation of LHSV experiments.

Effect of LHSV

The effect of LHSV on conversion in fluidized bed reactor was studied at different reaction temperature (308 to 460 °C), different particle size, L/D ratio of 2, and H₂/thiophene mole ratio of 10. Figures 11, 12, and 13 show the effect of LHSV on conversion at particle sizes of (0.075-0.15) mm, (0.15-0.3) mm, and (0.3-0.5) mm respectively. As shown in these figures, the conversion slightly decreases with increasing of LHSV. The same results were obtained in fixed bed operation and this means that the reaction rate is not affected by film diffusion step.

Effect of Temperature

Figure 14 shows the effect of temperature on conversion at different particle sizes and LHSV of 2 hr⁻¹. The conversion increases as the temperature increases. This may be attributed to the increase of active sites that can be used for the reaction when the temperature increases.

Effect of Particle size

Figure 15 shows the effect of catalyst particle size ranges on thiophene conversion. It is clear from this figure that the particle size of catalyst does not affect the thiophene conversion. The same results were obtained in fixed bed operation.

Comparison between the performances of fixed- and fluidized-bed operation

Figures 16, 17, 18, and 19 show the comparison between fixed- and fluidized-bed reactors at temperatures of 308, 360, 411, and 460 °C respectively. As shown in these figures the experimental results show that for HDS of thiophene over the range of conditions studied a lower conversion is obtained in a fluidized bed than in fixed bed. This is in agreement with the results of all workers [8-18] who also obtained lower conversion in their fluidized beds. The lower conversion can be attributed to the gas that bypasses the bed in the form of bubbles or channels and strong backmixing for both particles and gas [7, 11].

Anyway the experimental results indicate that there is indeed a range of gas velocity where there is a minimum deviation of fluidized- from fixed-bed conversion. Figures 16, 17, 18, and 19 show this phenomenon where the optimum velocity exists for the closest approach of the fluidized conversion to the fixed bed result, which is between 3 and 4 h⁻¹ LHSV for the system investigated.

At relatively low gas velocities (low LHSV), channeling may take place in all or part of the bed. When a bed is channeling most of the gas is blowing through holes in a settled or bridged layer of particles. Some of the gas may be flowing through this settled layer but there is no continual agitation of the particles. Continued increase in gas velocity brings a corrective action in the turbulent intermixing between the dense and bubble phases which limits the nonuniformity of gas and catalyst composition and thus tends to bring the conversion closer to that for the fixed bed operation [10, 11].

CONCLUSIONS

The following conclusions are deduced:

- In the time on stream study, the catalyst activity increases with time of operation properly due to the enhancement in catalyst activity by sulfiding the surface of catalyst with H₂S produced by reaction. Then the activity

decreases because of the accumulation of carbonaceous deposits on the catalyst surface. Finally, steady state activities were obtained after 2 hour of operation and remain substantially constant over a long period of time.

- In both reactor types, the conversion increases with increasing of reaction temperature, slightly decreases with increasing of liquid hourly space velocity (the hydrodesulfurization reaction of thiophene over Co-Mo/Al₂O₃ is not influenced by film diffusion limitation) and not affected by catalyst particle size (the reaction is not influenced by pore diffusion limitation).
- The results indicate that a low conversion was obtained in a fluidized bed than in fixed bed over the range of conditions studied. The lower conversion can be attributed to the gas that bypasses the bed in the form of bubbles or channels and strong backmixing for both particles and gas.

REFERENCES

- Davidson, J.F. and Harrison, D. "Fluidization", Academic Press, London, (1971).
- Kunii D. and Levenspiel O., "Fluidization Engineering", Krieger Publishing Co., New York, (1977).
- Smith J. M., "Chemical Engineering Kinetics", 3^{ed} ed., McGraw-HILL, London, (1981).
- Charles G. H., "An introduction to chemical engineering kinetics and reactor design", JOHN WILEY & SONS, New York, (1977).
- Kolboe S. and Amberg C. H., Canadian Journal of Chemistry. Volume 44 (1966).
- Van Parijs I. A. and Fromen G. F., Ind. Eng. Chem. Prod. Res. Dev., Vol. 25, No. 3, (1986).
- Ghanbari K. and et. al. Petroleum & Coal 48(2) 33-36 (2006)

Johnstone, H. F., Batchlor, J. D., Shen, C. Y., A.I.Ch.E. J., 1, 318 (1955).

- Shen, C. Y., Johnstone, H. F., A.I.Ch.E. Journal, 1, 349 (1955).
- Mathis J. F., Watson C. C., A.I.Ch.E. Journal, Vol. 2, No. 2, 518 (1956).
- Ishii, T., Osberg, G. L., A.I.Ch.E. J., 11, 279 (1965).
- Lewis W. K., Gilliland E. R., and Werner G., A.I.Ch.E. Journal, Vol. 5, No. 4 (1959)
- Gomezplata A. and Shuster W., A.I.Ch.E. Journal, 6, 454 (1960).
- Weekman V. W. and Donald M. N., A.I.Ch.E. Journal, Vol. 16 No. 3 (1970).

- Nace, D. M., Voltz, S. E., Weekman, V. W., Jr., Ind. Eng. Chem. Process Des. Develop, 10, 530 (1971).
- Benjamin G., Donald M., and Sterling E., Ind. Eng. Progress, Des. Develop, Vol. 13, No. 3, (1974).
- James H. Edwards, Ralph J. Tyler, and Stephen D. White, Energy & Fuels, Val. 4, No. 1, (1990).
- Wagialla K. M. and S Elnashaie S. E. H., Ind. Eng. Chem. Res., Vol. 30, No. 10, (1991).

Table 1: Properties of catalyst HR-306

Surface area (m ² /gm)	280
Pore volume (cc/gm)	0.55
Cobalt (wt %)	4
Molybdenum (wt %)	12
Density (g/cm ³)	0.6
Manufacturer	Procatalyse

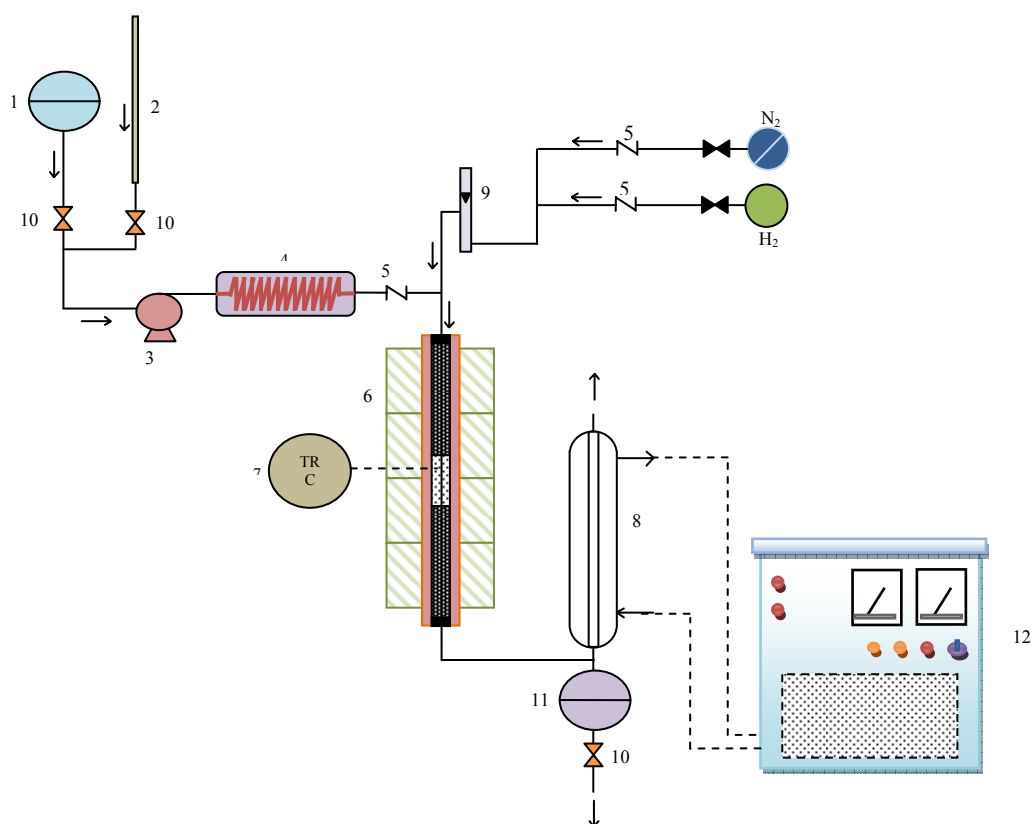


Fig. 1 Schematic flow diagram of the fixed bed reactor unit: (1) Feed reservoir; (2) Metering buret; (3) Dosing pump; (4) Evaporator; (5) One way valve; (6) Reactor system; (7) Temperature

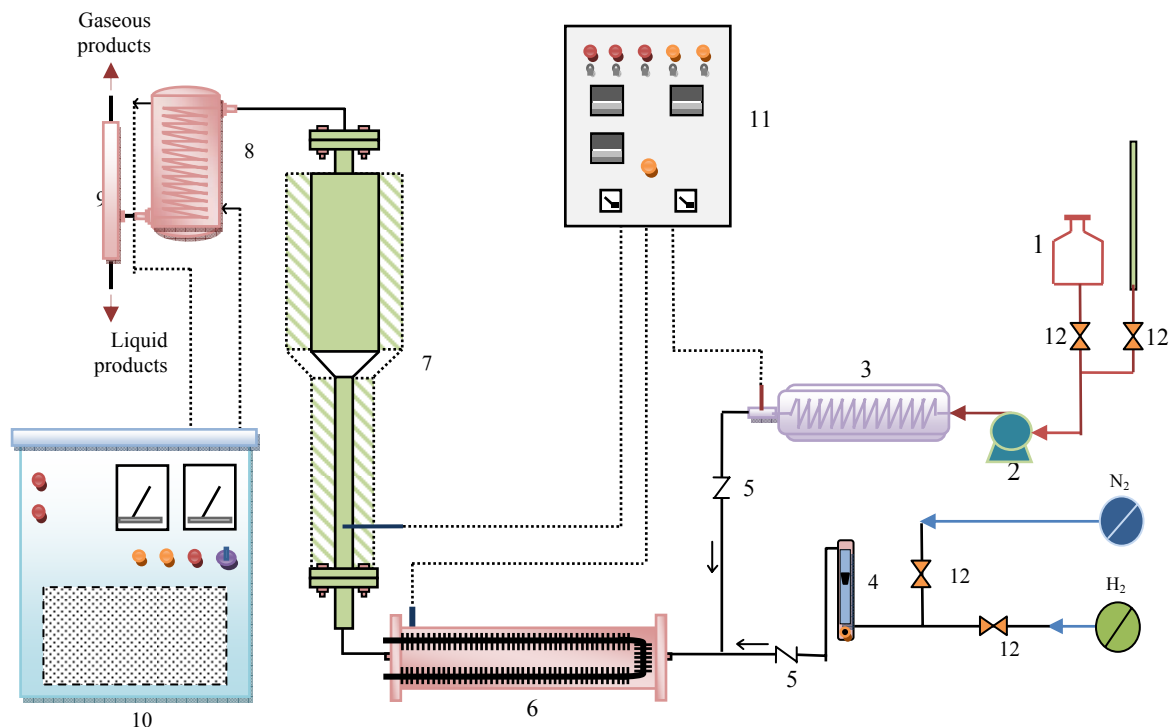


Fig. 2 Schematic flow diagram of the fluidized bed reactor unit: (1) Feeding tank; (2) Dosing pump; (3) Evaporator; (4) Gas flow meter; (5) One way valve; (6) Preheater; (7) Fluidized bed reactor; (8) Condenser; (9) Gas-liquid separator; (10) Chiller; (11) Control and power supply box; (12) Valve.

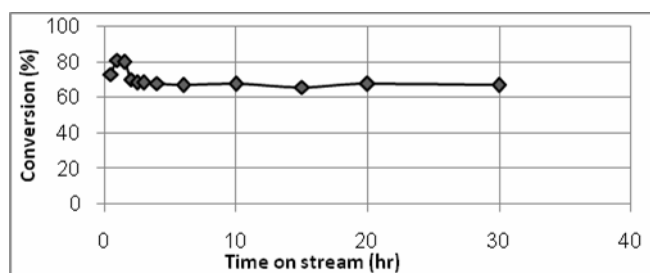


Fig. 3 Hydrodesulfurization of Thiophene over Co-Mo/Al₂O₃ at 411°C (fixed bed operation).

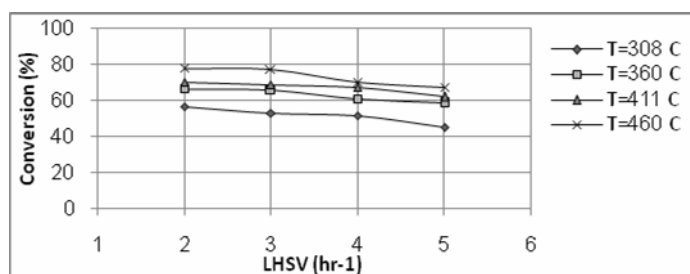


Fig. 4 Effect of LHSV on thiophene conversion at different temperatures (fixed bed operation)

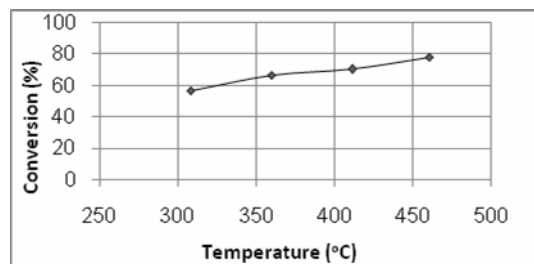


Fig. 5 Effect of Temperature on Thiophene Conversion at LHSV 2 hr⁻¹ (fixed bed operation).

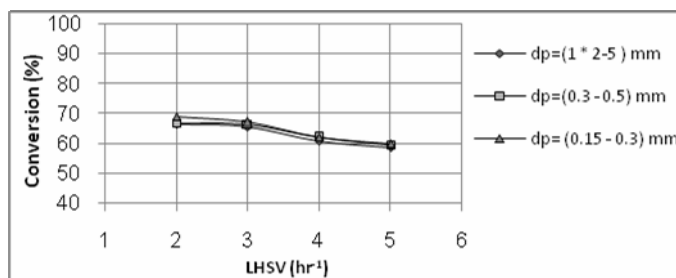


Fig. 6 Effect of Catalyst particle size on Thiophene Conversion at different LHSV and at temperature of 360 °C (fixed bed operation).

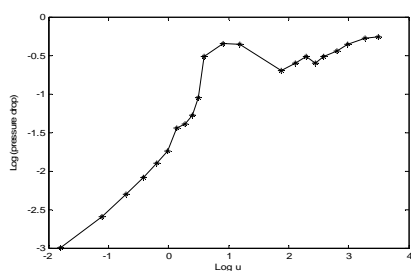


Fig. 7 Relationship between bed pressure drop and superficial velocity for particle size of (0.075-0.15) mm.

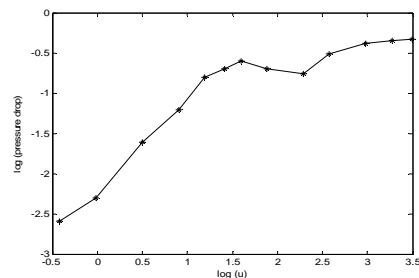


Fig. 8 Relationship between bed pressure drop and superficial velocity for particle size of (0.15-0.3) mm.

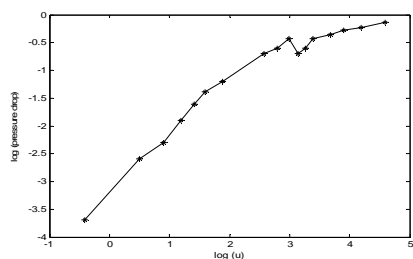


Fig. 9 Relationship between bed pressure drop and superficial velocity for particle size of (0.3-0.5) mm.

Table 2 Experimental values of minimum fluidization velocity

Particle size (mm)	u_{mf} (cm/s)
0.075-0.15	6.04
0.15-0.3	9.974
0.3-0.5	24.5

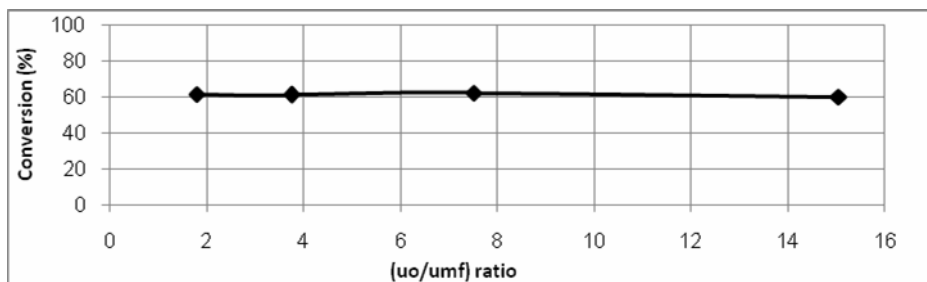


Fig. 10 Effect of u_o/u_{mf} ratio on conversion (fluidized bed operation).

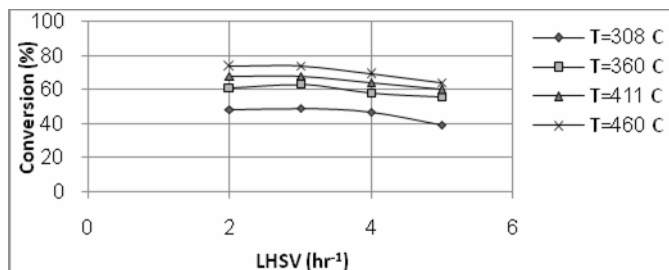


Fig. 11: Effect of LHSV on conversion at different temperatures and at particle size of (0.075-0.15) mm (fluidized bed operation).

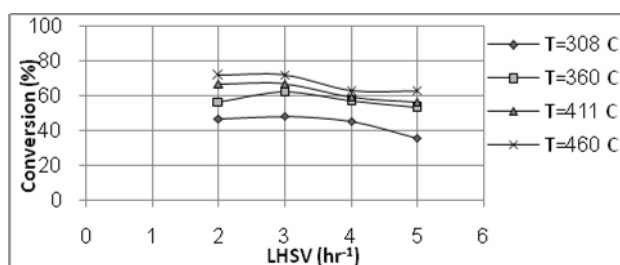


Fig. 12: Effect of LHSV on conversion at different temperatures and at particle size of (0.15-0.3) mm (fluidized bed operation).

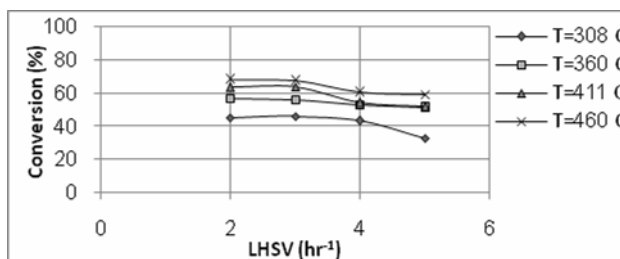


Fig. 13: Effect of LHSV on conversion at different temperatures and at particle size of (0.3-0.5) mm (fluidized bed operation).

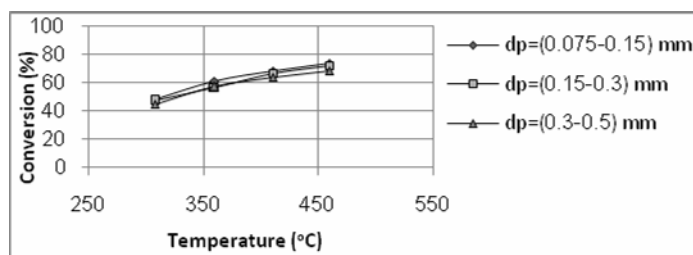


Fig. 14: Effect of temperature on conversion at different particle size and at LHSV of 2 hr⁻¹ (fluidized bed operation).

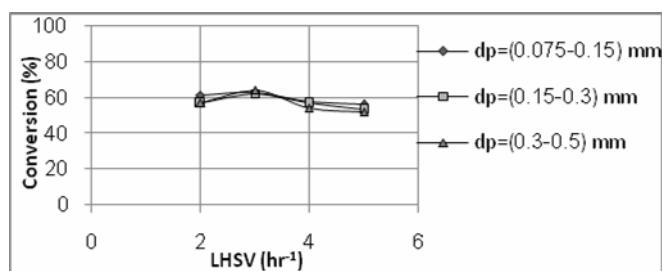


Fig. 15: Effect of particle size on conversion at different LHSV and at temperature of 360 °C (fluidized bed operation).

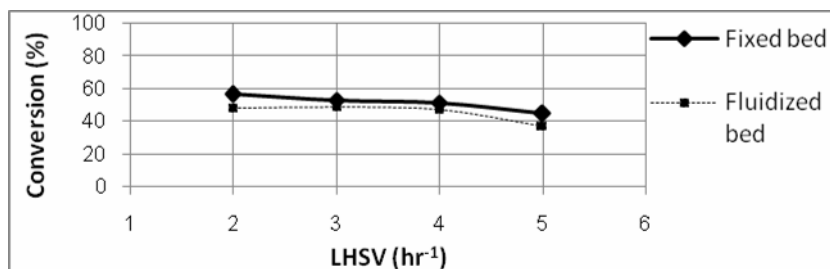


Fig. 16 Conversion as a function of LHSV for fluidized operation compared with fixed bed operation at temperature of 308 °C.

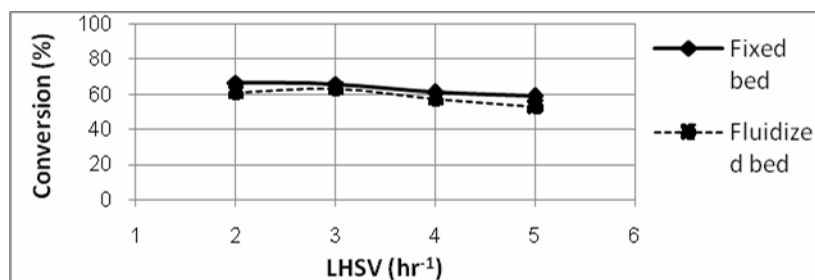


Fig.17 Conversion as a function of LHSV for fluidized operation compared with fixed bed operation at temperature of 360 °C.

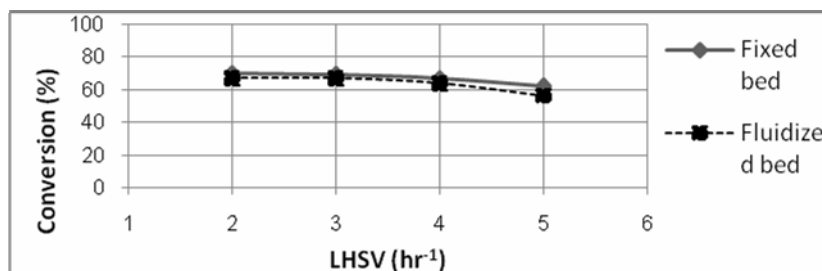


Fig. 18 Conversion as a function of LHSV for fluidized operation compared with fixed bed operation at temperature of 411 °C.

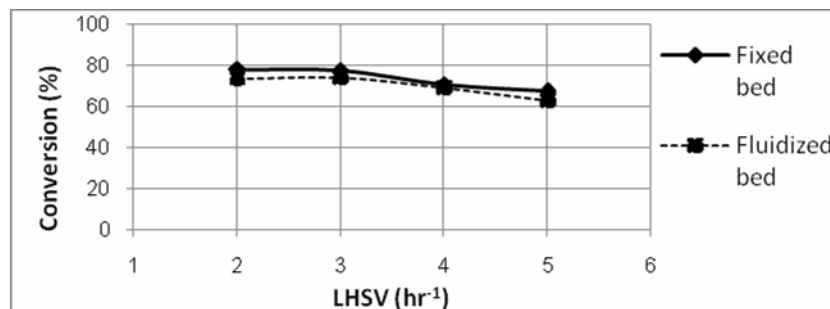


Fig.19 Conversion as a function of LHSV for fluidized operation compared with fixed bed operation at temperature of 460 °C.



TREATMENT OF A HIGH STRENGTH ACIDIC INDUSTRIAL CHEMICAL WASTEWATER USING EXPANDED BED ADSORBER

Sawsan A. M. Mohammed, Sarmad Foad and Haider Abbas Shanshool

Chemical Engineering Department – College of Engineering – University of Baghdad – Iraq

ABSTRACT

Treatment of a high strength acidic industrial wastewater was attempted by activated carbon adsorption to evaluate the feasibility of yielding effluents of reusable qualities. The experimental methods which were employed in this investigation included batch and column studies. The former was used to evaluate the rate and equilibrium of carbon adsorption, while the latter was used to determine treatment efficiencies and performance characteristics. Fixed bed and expanded bed adsorbers were constructed in the column studies.

In this study, the adsorption behavior of acetic acid onto activated carbon was examined as a function of the concentration of the adsorbate, contact time and adsorbent dosage. The adsorption data was modeled with Freundlich and Langmuir adsorption isotherms.

The amount of acetic acid adsorbed increased with the decrease in initial concentration of acetic acid and increased with the increase in contact time and adsorbent dose. The effects of various important and influencing parameters such as flow rate, bed height, inlet adsorbate concentration on breakthrough curve are studied in details in the column studies.

KEYWORDS: Acetic acid removal, expanded bed adsorber, wastewater treatment, adsorption on activated carbon.

الخلاصة:

تم في هذه الدراسة معالجة مياه التصريف العالية الحموضة بواسطة الامتزاز على الكربون المنشط واستخدمت طريقة الامتزاز ذو الدفعات وباستخدام الاعمدة الثابتة والممتدة. حيث استخدمت الاولى لايجاد معدل وعلاقة الامتزاز لحامض الخليك على الكربون المنشط بينما استخدمت الثانية لايجاد كفاءة عملية المعاملة وايجاد الاداء. المتغيرات التي تم دراستها هي تركيز المادة الممتزة والزمن وكمية المادة المازة. استخدمت علاقة فرويندليش ولنكمير لتمثيل النتائج. بينت النتائج بان كمية حامض الخليك الممتزة تزداد مع نقصان التركيز الابتدائي للحامض وتزداد مع زيادة زمن التماس وكمية المادة المازة. اما بالنسبة للدراسة باستخدام الاعمدة فان تأثير معدل الجريان وارتفاع الحشوة وتركيز المادة الممتزة على منحنى المقاومة تم دراستها بالتفصيل.

INTRODUCTION

Wastewater, containing organic compounds, causes great problems. Most of the organic compounds like phenols, amines and acids are classified as priority pollutants, which are to be removed from water and wastewater. A wide range of industrial effluents, especially from rubber, pharmaceutical, food processing, agro-chemical industries, municipal sewage, agricultural run-offs, decaying vegetables and animals are the major sources of organic carboxylic acid (Kannan and Xavier, 2001; Kannan, and Murugavel, 2008).

Carboxylic acids also applied in conservation and disinfections in the textile and tanning industries. During their use, a significant amount of these acids get into wastewater currents, finishing up in residual wastewaters (Alessandra et al., 2004).

Whereas the separation of acetic acid from water by conventional distillation is economic at concentrations exceeding 70 wt%, for low concentrations in water (below 5 wt %), adsorptive separations can provide a viable option (Ganguly and Goswami, 1996).

Activated carbon is the most well known and widely used commercial adsorbent in water purification. The adsorption on activated carbon posses some advantages over other technologies due to the possibility of recovering a pure, high removal efficiency at low concentration and low energy (Benkhedda et al., 2000).

The most common reason for using expanded bed adsorber in this study is to obtain vigorous agitation of the solids in contact with the fluid, leading to excellent contact of the solid and the fluid and the solid and the wall. This means that nearly uniform concentrations can be obtained (McCabe et al., 2001).

Both batch and column-type carbon adsorption operations were employed in this investigation. The batch test was conducted to evaluate the adsorption rate and capacity.

The column operations were conducted in two different manners, fixed-bed and expanded. A comparison of the treatment efficiency and performance characteristics between the two different modes of carbon adsorption was made.

EXPERIMENTAL PROCEDURE

The adsorbent used in this study was a granular activated carbon. The characteristics of this carbon are reported in Table 1.

ADSORPTION ISOTHERM MEASUREMENTS

A stock solution of acetic acid (0.2 N) was prepared and diluted to the required initial concentrations (C_0 range: 600-6000 ppm). Equilibrium studies were made at room temperatures by employing the batch adsorption technique. Weighed amounts of activated carbon (12-28 gm/l) were taken in conical flasks containing 50 ml of aqueous solutions of acetic acid of known concentration. The flasks were stoppered and attached to a mechanical shaker for a specified period of contact time (range: 5-45 min). After equilibrium, the aqueous phase was filtered and titrated with sodium hydroxide (0.25 N) to determine the equilibrium concentration of the acetic acid. The indicator used was phenolphthalein (0.5%).

COLUMN STUDIES

The schematic representation of experimental set-up is shown in Fig. (1); it consists of a glass column of 2.45 cm internal diameter and a height of 75 cm. The column was packed with activated carbon (0.5) mm in diameter, to a height of 8 cm. The activated carbon particles are supported by a wire mesh fitted at the column bottom. The liquid from the storage tank was pumped through a rotameter connected on the line.



The flow rate of wastewater was (50) l/hr. the effluents from the bed were analyzed for acetic acid content by titration with NaOH at chosen intervals of time until breakthrough occurs. The minimum fluidized velocity for particles (V_{mf}) had been estimated to be (5.17×10^{-4} m/s) using the following equation (Ramaswamy et al, 2008):

$$V_{mf} = \frac{\mu_l}{d_p \rho_l} \left[\sqrt{(33.7)^2 + 0.0408 \frac{d_p^3 \rho_l (\rho_p - \rho_l) g}{\mu_l^2}} - 33.7 \right] \quad (1)$$

Another set of experiments were made using closed circuit expanded bed in which liquid was continuously recycled through the system as shown in Fig. (2).

RESULTS AND DISCUSSION

Adsorption Isotherms

Among the many models of isotherms of adsorption found in the literature involving aqueous solutions, the experimental data of equilibrium of this study were correlated with Freundlich and Langmuir models described below in Eqs. (2) and (3) respectively, (Adamson, 1960; Alessendra, 2005)

Freundlich isotherm:

$$\log(q_e) = \log k + n \log C_e \quad (2)$$

Langmuir isotherm:

$$\frac{C_e}{q_e} = \frac{1}{ab} + \frac{C_e}{a} \quad (3)$$

Where, k and n are the constants of Freundlich related to the capacity and intensity of the adsorption; q_e is the amount of acid adsorbed per unit weight of the adsorbent, C_e is the equilibrium concentration of acid (ppm), a and b are the constants of the Langmuir model that represents the capacity and the energy of adsorption.

The values of k and n were obtained from the linear correlation of $\log q_e$ against $\log C_e$ and the Langmuir constants were also determined from the linear correlation of C_e/q_e

against C_e . The isotherm parameters along with the correlation coefficients are represented in Table 2. The observed linear relationships of Figs. (3) and (4) confirm that these two adsorption isotherms are applicable. The applicability of Langmuir isotherm model indicates the formation of monolayer coverage of adsorbate on outer surface of the adsorbent (Ghosh and Philip, 2005). Further, the essential characteristics of the Langmuir isotherm can be described by a separation factor R_L , which is defined by (Weber and Chakravorti, 1974):

$$R_L = \frac{1}{(1 + b C_0)} \quad (4)$$

The separation factor R_L indicates the isotherm's shape and the nature of the adsorption process as unfavorable ($R_L > 1$), linear ($R_L = 1$), favorable ($0 < R_L < 1$) and irreversible ($R_L = 0$). In the present study the value of R_L being 0.381 indicating that the sorption process is favorable.

EFFECT OF CONTACT TIME

In the adsorption systems contact time plays an important role. In order to study the kinetics and dynamics of adsorption of acetic acid by activated carbon, the adsorption experiments were conducted and the extent of removal of acetic acid was obtained by varying the contact time (range 5-45 min) at fixed concentration of acetic acid (600 ppm) with a fixed dose of adsorbent (20 g/l).

Fig. (5) indicates that the removal of acetic acid by activated carbon is rapid at the initial period and becomes slow, stagnant and then decreases with the increase in contact time. The relative increase in the extent of removal of acetic acid is very low after 30 min of contact time, which is fixed as the optimum contact time. This indicates that the rate of removal of acid is higher in initial stages, due to the availability of adequate surface area of the adsorbent, and with increase in contact time, due to decrease of surface area availability, the adsorption decreases. The decrease in the extent of removal of acid after 30 min of contact time maybe due to the desorption process. Similar

results have been reported for the removal of acids by Ramu et al, 1992.

EFFECT OF DOSE OF ADSORBENT

The percentage removal of acetic acid by adsorption was obtained with various doses of adsorbent (range: 12-28 g/l) with initial concentration of acetic acid (600 ppm) and contact time (30 min).

Fig. (6) shows that the amount removal of acid increases exponentially with increase in dose of adsorbent. This maybe due to the increase in availability of active sites due to the increase in the effective surface area resulting from increase in dose of adsorbent especially at higher adsorbent doses. Similar observation has been reported by McKay et al, 1983; Annadural and Krishnan, 1997 and Kannan and Xavier, 2001.

OPEN CIRCUIT EXPANDED BED BREAK-THROUGH CURVE

Successful design of a column adsorption process requires prediction of the concentration-time profile or breakthrough curve for the effluent. The maximum adsorption capacity of an adsorbent is also needed in design.

There are many factors that affect the adsorption capacity in the column such as flow rate, bed depth and influent concentration.

Effect of Inlet Concentration

The effect of inlet adsorbate concentration on effluent concentration is shown in Fig. (7).

The inlet adsorbate concentrations considered are 6000, 3000 and 1500 ppm. During these studies other parameters such as bed height and flow rate are kept constant. For higher feed concentration, steeper breakthrough curves are found, because of the lower mass-transfer flux from the bulk solution to the particle surface due to the weaker driving force. In addition, at high concentration, the isotherm gradient is

lower, yielding a higher driving force along the pores. Thus the equilibrium is attained faster for values of higher adsorbate concentration (Babu and Gupta, 2004).

Volesky and Prasetyo (1994) reported that the driving force for adsorption is the concentration difference between solute on the sorbent and the solute in the solution. So at high concentrations the activated carbon becomes more quickly saturated, thereby decreasing the breakthrough time.

EFFECT OF FLOW RATE

The results for different solution flow rates are plotted for a bed height of 8 cm and an inlet adsorbate concentration of 3000 ppm in Fig. (8). The flow rates considered are 50, 75 and 100 l/hr. Fig. (8) reveals that as the flow rate increases, the breakthrough curve becomes steeper. This is because of the residence time of the solute in the column, which is not long enough for adsorption equilibrium to be reached at high flow rates. So at high flow rate the adsorbate solution leaves the column before equilibrium occurs (Babu and Gupta, 2004).

EFFECT OF BED HEIGHT

The effect of bed height on the effluent adsorbate concentration is presented for flow rate 50 l/hr and inlet adsorbate concentration of 3000 ppm in Fig. (9). The bed heights considered are 8 and 12 cm. It is observed that at smaller bed height the effluent adsorbate concentration ratio increases more rapidly than for a higher bed height. Furthermore, the bed is saturated in less time for smaller bed heights. Smaller bed height corresponds to less amount of adsorbent, so the adsorbent gets saturated early (Huang and Hardie, 1971).

COMPARISON BETWEEN EXPANDED BED AND FIXED BED ADSORBERS

In order to compare the relative treatment between the expanded bed and fixed bed



adsorbers, the solution was forced downward through the fixed bed with a controllable flow rate

(50 l/hr) and initial concentration of 3000 ppm.

In a packed bed, the adsorbent particles are stationary and liquid flow through the bed approximates to plug flow. In contrast, due to the mixing of the adsorbent, a fluidized bed would be expected to show an inferior adsorption performance compared with the packed bed. The conclusion is already drawn from Fig. (10), which is in agreement with the work of Shahavi et al, (2008).

In addition, in up flow adsorption column, the contact between adsorbent and adsorbate are better compared to down flow mode-Up flow mode was selected to minimize the channeling effects inside the column.

CLOSED CIRCUIT EXPANDED BED

Effect of Inlet Concentration

Three initial concentrations of acetic acid in water were tested: 6000, 3000 and 1500 ppm, for a constant flow rate of 50 l/hr.

The closed circuit fluidized bed was adequately modeled as stirred batch adsorption equipment. The intense pump recycling rate produces similar mixing effects as those of a mechanical device, which supports this strategy. It is well established that adsorption rates are generally fast higher than other rates (e.g., diffusion of mass and heat) in such systems. Physical adsorption, the topic of this work, is particularly very fast. On this basis it will be assumed that at any time during adsorption, a condition close to equilibrium is established in the vicinity of the adsorbent surface (Corrêa et al., 2007)

Fig. 11 shows the time profile of acetic acid concentration in the circulating liquid of the closed circuit fluidized bed adsorption system developed in this work. Acetic acid concentration didn't change after around 900 s (15 min), suggesting that a condition near adsorption equilibrium was achieved in the system.

CONCLUSIONS

The following conclusions are drawn from the above-discussed results:

For batch studies:

- The adsorption data fit well with both Freundlich and Langmuir isotherms.
- The removal of acetic acid by activated carbon is rapid at the initial period and becomes slow, stagnant and then decreases with the increase in contact time.
- The amount removal of acid increases exponentially with increase in dose of adsorbent.

For open circuit expanded bed:

- For higher feed concentration, steeper breakthrough curves are obtained and break point time is achieved sooner.
- As the flow rate increased, the breakthrough curve becomes steeper. The break point time is obtained earlier and effluent adsorbate concentration ratio increases more rapidly.
- For smaller bed height, the effluent adsorbate concentration ratio increases more rapidly than for a higher bed height.
- A fluidized bed would be expected to show better adsorption performance compared with the packed bed.

In closed circuit expanded bed, a condition near adsorption equilibrium was achieved in the system.

NOMENCLATURE

a Monolayer (maximum) adsorption capacity (mg/ g)

b Langmuir constant related to energy of adsorption (l /mg)

C The concentration of acid at time t (ppm)

C₀ The concentration of acid at time zero (ppm)

C_e Equilibrium concentration of acid (ppm)

d_p Particle diameter (m)

g Acceleration due to gravity (m/s^2)
 k Adsorption capacity ($\text{g/l}^{1/n}$)
 L Column length (cm)
 n Order/intensity of adsorption (-)
 Q Flow rate (l/hr)
 q_e Amount of acid adsorbed per unit weight of adsorbent (mg/g)
 R_t Separation factor (-)
 t Time (s)
 V_{mf} Particle minimum fluidization velocity (m/s)

Greek letters

ρ_l Density of fluid (kg/m^3)
 ρ_p Density of particle (kg/m^3)
 μ_l Dynamic viscosity of fluid (kg/m.s)

REFERENCES

- Adamson A.W., 1960, Physical Chemistry of Surface, Inter Science Publ. Inc., New York, pp. 777.
- Alessandra F. Freitas, Bruno B. França, Marisa F. Mendes and Gerson L.V. Coelho, 2005 "Thermodynamic Studies of Acetic Acid Adsorption onto Activated Carbon" 2nd Mercosur Congress on Chemical Engineering, 4th Mercosur Congress on Process Systems Engineering, Brazil.
- Annadurai G and Krishnan M.R.V., 1996 "Adsorption of Basic Dye Using Chitin", Indian J. Environ. Protec., 16(6), pp.444-449.
- B.V. Babu, S. Gupta, 2004 "Modeling and Simulation for Dynamics of Packed Bed Adsorption", Proceedings of International Symposium & 57th Annual Session of IChE in association with AIChE, Mumbai, December 27-30.
- Benkhedda, J., Jaubert, J.N., Barth, D., Perrin, L., Baily, M., 2000 "Adsorption Isotherms of m-Xylene on Activated Carbon: Measurements and Correlation with Different Models", J. Chem. Thermodynamics, 32, pp. 401-411.
- Ganguly S. K. and Goswami A. N., 1996, "Surface Diffusion Kinetics in the Adsorption of Acetic Acid on Activated Carbon", Separation Science and Technology, Vol. 31, Issue 9, pp. 1267 – 1278.
- Ju-Cbang Huang and Michael G. Hardie, 1971 "Water Reclamation by Physiochemical Treatment of Wastewater", Water Resources Bulletin, Vol. 7, No. 1, pp.148-161.
- Kannan N. and Xavier A., 2001 "New Composite Mixed Adsorbents for the Removal of Acetic Acid by Adsorption from Aqueous Solution-A Comparative Study", Toxic. Env. Chem., 79, pp.95-107.
- Kannan, N. and Murugavel, S., 2008 "Comparative Study on the Removal of Acid Violet by Adsorption on Various low Cost Adsorbents", Global NEST Journal, Vol. 10, No 3, pp 395-403.
- McCabe, W.E., Smith J.C., and Harriott, P., 2001, Unit Operation of Chemical Engineering, McGraw Hill, New York.
- McKay G., 1983 "The adsorption of Dyestuff from Aqueous Solution Using Activated Carbon: Analytical Solution for Batch Adsorption Based on External Mass Transfer and Pore Diffusion", Biochem. Eng. J., 27, pp.187-194.
- Ghosh, P.K. and Philip, L., 2005 "Performance Evaluation of Waste Activated Carbon on Atrazine Removal from Contaminated Water", Journal of Environmental Science and Health Part B, pp.425–441.
- Corrêa R. A., Calçada L. A. and Peçanha R. P., 2007, "Development of a Fluidized Bed System for Adsorption of Phenol from Aqueous Solutions with Commercial



- Macroporous Resins”, Brazilian Journal of Chemical Engineering, Vol. 24, No. 01, pp. 15 – 28.
- Ramaswamy, E., Sirinivasakannan, C. and Balasubramaniam, N., 2008, “*Bed Expansion Characteristics of Liquid-Solid Fluidized Bed with Internals*”, Modern Applied Science, 2(2), pp 84-92.
 - Ramu, N. Kannan and S.A. Srivathsan, 1992. “Adsorption of Carboxylic Acids on Fly Ash and Activated Carbon”, Indian J. Environ. Hlth., Vol. 34, No. 3, 192-199.
 - Shahavi, M. H., Najafpour, G. D. and Jahanshahi, M., 2008 “Hydrodynamic Behavior and Biochemical Characterization of a Simple Custom Expanded Bed Column for Protein Purification “, African Journal of Biotechnology Vol. 7 (23), pp. 4336-4344.
 - Volesky, B. & Prasetyo, I., 1994 “Cadmium Removal in a Biosorption Column” Biotechnol. Bioeng. 43, pp.1010-1015.
 - Weber, W. J. and Chakravorti, R. K., 1974, “Pore and Solid Diffusion Models for Fixed-Bed Adsorbers”, J. Am. Inst. Chem. Eng. 20, pp. 228-238.

Table 1: Major characteristics of activated carbon.

Density, kg/m ³	1350
BET surface area, m ² /g	1100
Particle porosity	0.5
Bed porosity	0.41
particle diameter (d_p), mm	0.5

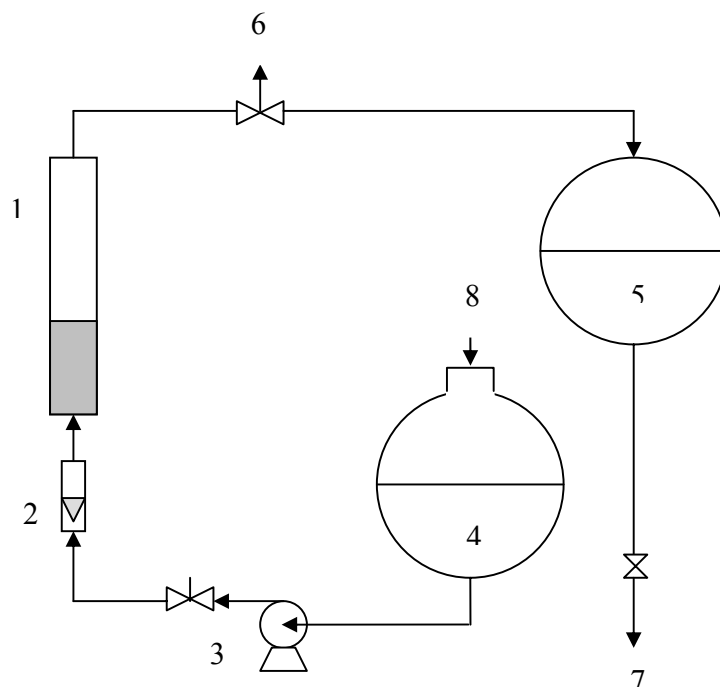


Fig.1: Schematic diagram of opened circuit expanded bed (1.adsorber, 2 flow meter, 3.pump, 4.feed tank, 5.effluent tank, 6.sampling point, 7.to drain, 8.feed).

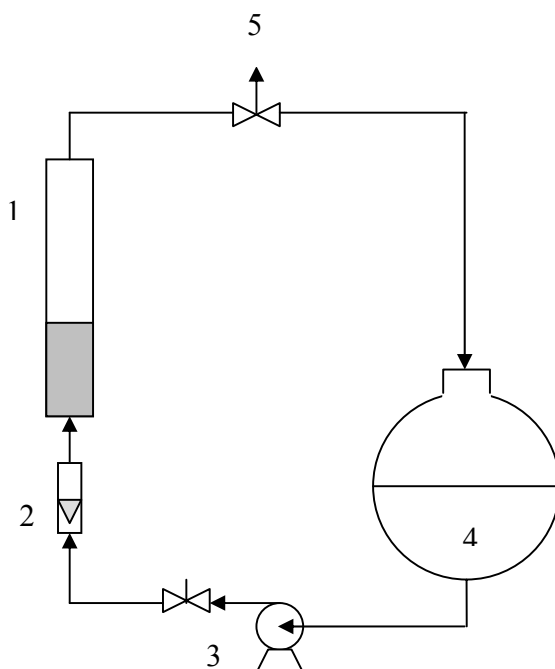


Fig.2: Schematic diagram of closed circuit expanded bed (1.adsorber, 2 flow meter, 3.pump, 4.feed tank, 5.sampling point).

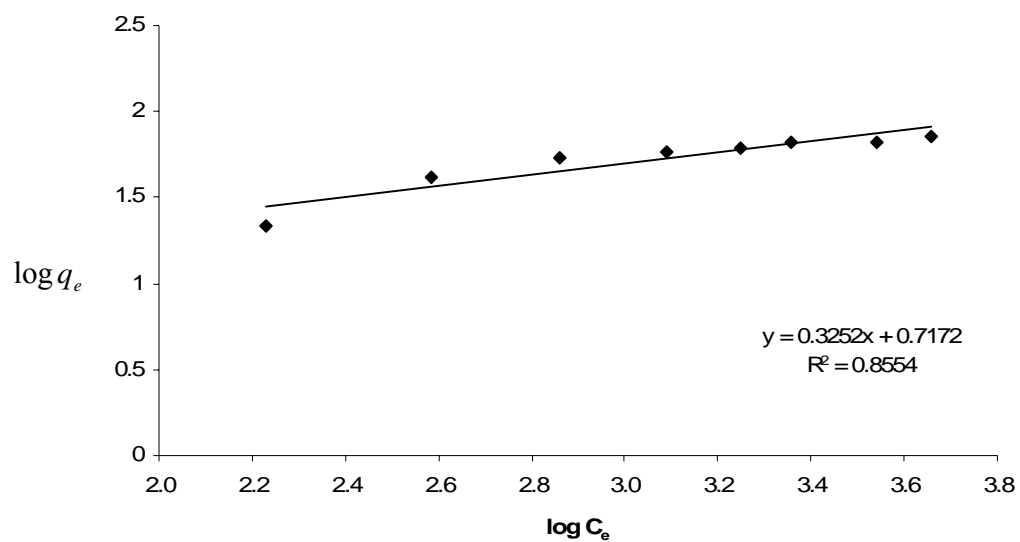


Fig. 3: Linearized Freundlich isotherm for acetic acid adsorption by activated carbon.

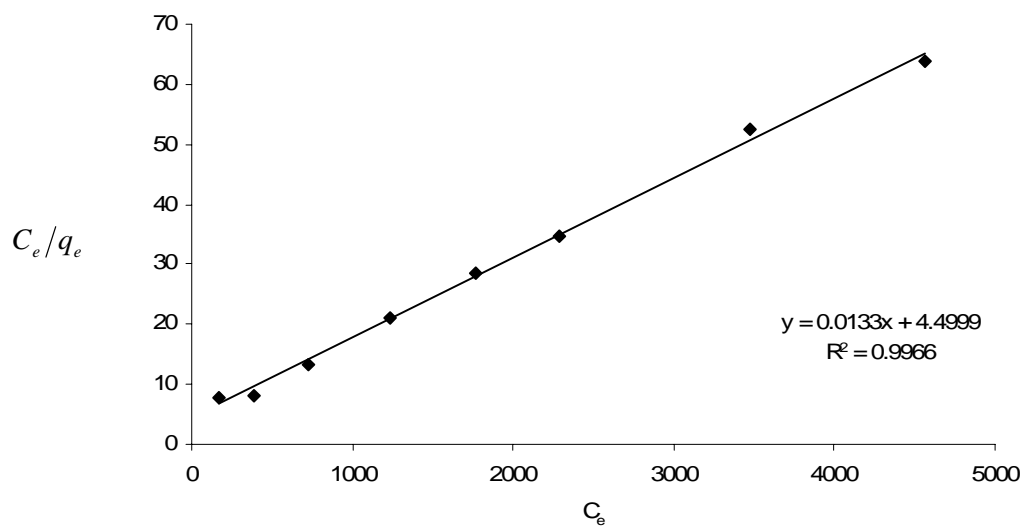


Fig.4: Linearized Langmuir isotherm for acetic acid adsorption by activated carbon.

Table 2: Freundlich and Langmuir parameters of adsorption isotherms for the removal of acetic acid by activated carbon.

Freundlich isotherm			Langmuir isotherm		
n (-)	k (g/l) ^{1/n}	Correlation coeff. (R ²)	a (mg/g)	b (g/l)	Correlation coeff. (R ²)
0.325	5.212	0.8554	75.19	2.96×10 ⁻³	0.9966

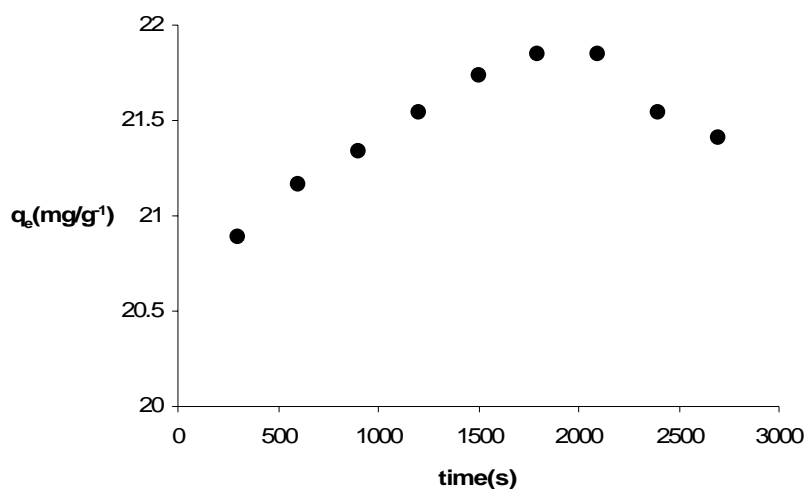


Fig.5: Effect of contact time on the amount of acetic acid adsorbed on activated carbon.

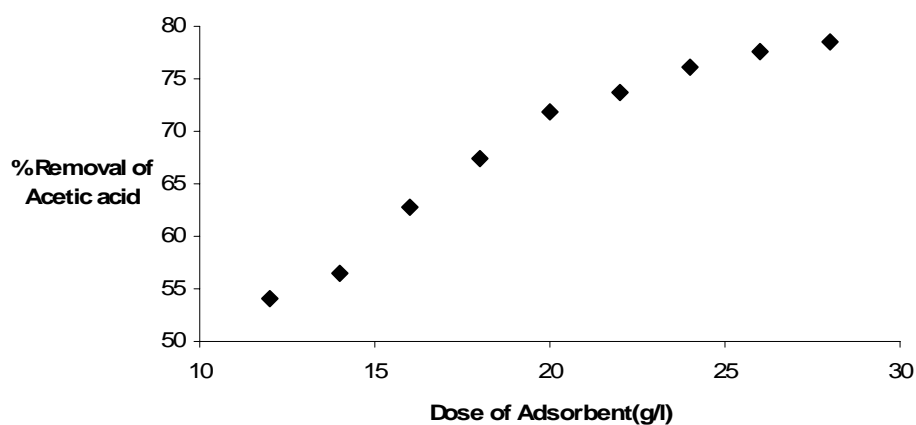


Fig. 6: Effect of dose of adsorbent on the percentage removal of acetic acid.

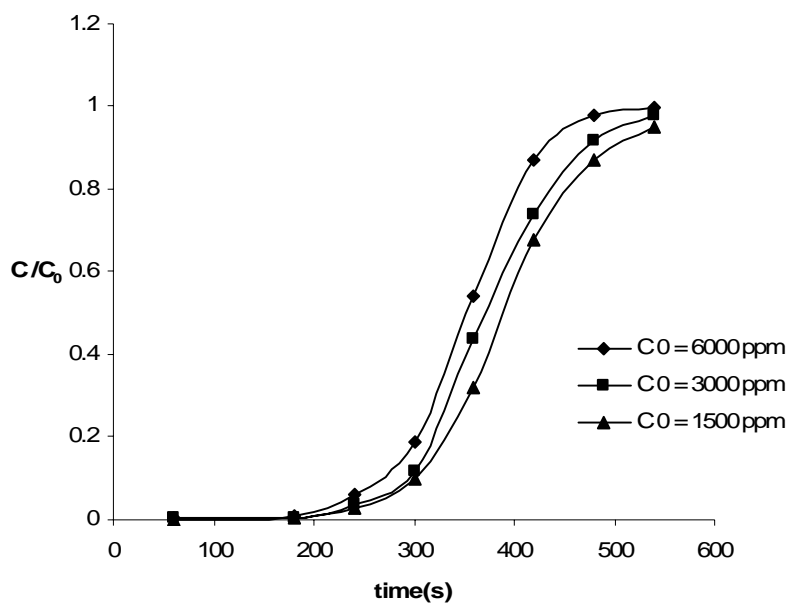


Figure 7: Effect of inlet adsorbate concentration on breakthrough curve.

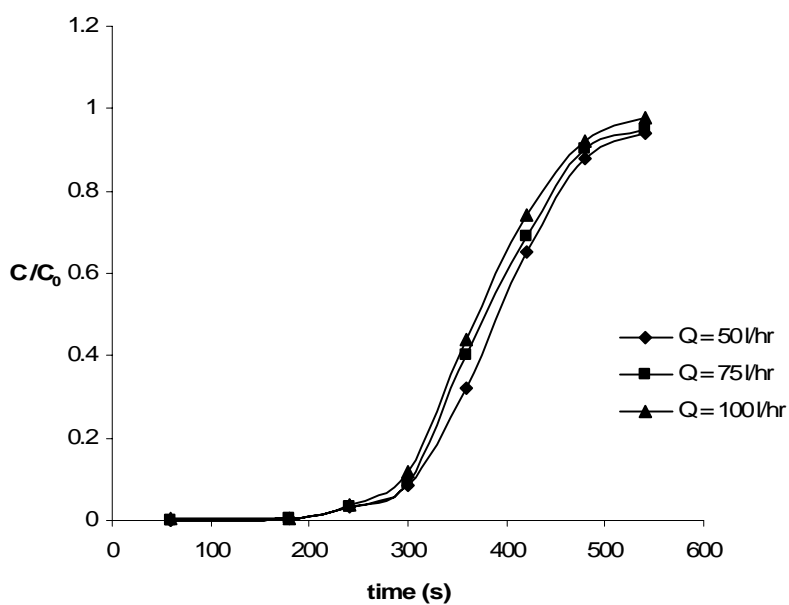


Figure 8: Effect of flow rate on breakthrough curve.

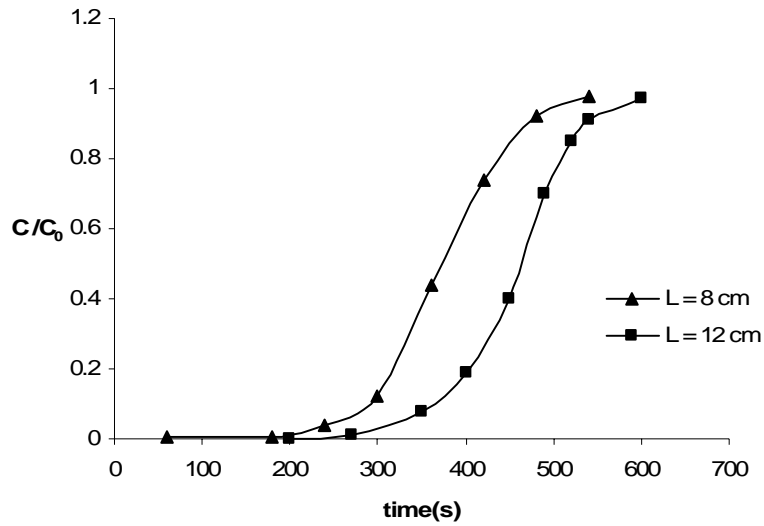


Fig.9: Effect of bed height on the breakthrough curve.

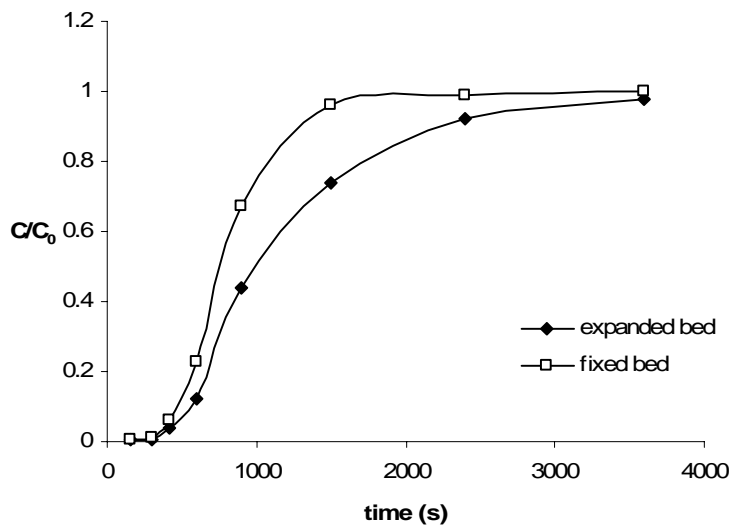


Fig.10: Comparison between fixed-bed and expanded-bed adsorbers.

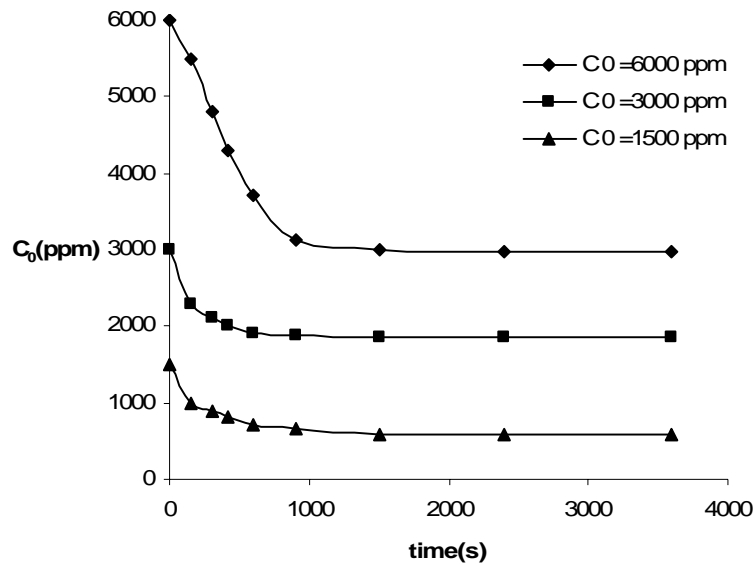


Fig.11: Acetic acid concentration in the closed circuit fluidized bed experiments.



LOW COST AUTOMATIC SUN PATH TRACKING SYSTEM

Mohammed Kasim Al-Haddad
College of Engineering
University of Baghdad

Sameer Sami Hassan
College of Education/Ibn Al-Haitham
University of Baghdad

ABSTRACT

Solar tracking systems used are to increase the efficiency of the solar cells have attracted the attention of researchers recently due to the fact that the attention has been directed to the renewable energy sources. Solar tracking systems are of two types, Maximum Power Point Tracking (MPPT) and sun path tracking. Both types are studied briefly in this paper and a simple low cost sun path tracking system is designed using simple commercially available component. Measurements have been made for comparison between fixed and tracking system. The results have shown that the tracking system is effective in the sense of relatively high output power increase and low cost.

الخلاصة

لقد جذبت أنظمة المتابعة الشمسية المستخدمة لزيادة كفاءة الخلايا الشمسية انتباه الباحثين مؤخراً بسبب كون الاهتمام قد توجه نحو مصادر الطاقة المتجددة. إن أنظمة المتابعة الشمسية هي على نوعين، متابعة نقطة القدرة العظمى (MPPT) ومتابعة طريق الشمس. تم دراسة كلا النوعين في هذا البحث بصورة مختصرة وتم تصميم منظومة مبسطة لمتابعة طريق الشمس باستعمال مواد بسيطة متوفرة في السوق التجارية. تم اخذ قياسات لاجل المقارنة بين المنظومات الثابتة والمتحركة (المتابعة). اظهرت النتائج ان المنظومة المتحركة هي فعالة من حيث الزيادة العالية لقدرة الاخراج وانخفاض الكلفة.

KEY WORDS: solar tracking, MPPT, sun path tracking, solar cell, photovoltaic cell

INTRODUCTION

The resources of most of the energy consumption were and still in the form of fossil fuel, which is either oil, coal or gas. The other source of energy is the nuclear energy. Each one of these types has its own major downside. The increasing consumption of fossil fuel and especially oil has caused the continuing depletion of the world reserve of oil and the lack of new explorations of new reserves that would balance the consumption has led to increase in oil prices for record highs that reached over 140 \$/barrel in 2008 until the global recession brought the prices down to about 80 \$/barrel. Another negative aspect with the fossil fuel is the environmental considerations in regards to carbon dioxide emission that is causing the global warming and climate change that is raising horrible concerns about the future of our planet.

For the nuclear energy, although it does not involve carbon dioxide emission but it is still considered a dangerous source of energy because of the risk of nuclear radiation and on the other hand the nuclear waste that needs to be looked after for several thousand years (10'000 years according to United States Environmental Protection Agency standards). Also, nuclear energy is highly controversial and politics plays a big roll that even if the technical and economical facilities were available, politics can cause agonizing troubles for the developing countries.

For the reasons summarized above, the world has turned to other form of energy sources namely the green energy sources. Green energy is clean in the sense that it does not have a bad impact on the environment, and also it is renewable. Types of green energy sources are:

- Hydropower
- Wind power
- Solar power
- Biofuel
- Wave power
- Geothermal power
- Tidal power

Many developed countries have set strategic goals to explore such types of energy sources to minimize their dependence on the fossil fuel as it is mostly an imported product from the developing countries.

The solar power conversion is one of the most addressed in the field of the renewable energy systems. The available techniques allow converting the solar radiation into two forms of energy: thermal and electrical [1]. The conversion of the solar energy into electrical is done by the photovoltaic (PV) cells or panels. The power supplied by PV panels depend on many extrinsic factors [2], such as irradiation levels affected by weather conditions which limits the amount of the incident solar radiation, temperature, angle of incident radiation and load conditions.

Solar tracking is mainly about achieving the maximum power and hence increasing the efficiency of the PV panels, this is important from the economical point of view, because in total the overall cost should give higher output power. The average solar energy obtained by conventional PV panels during the course of the day is not always maximized [2]. This is due to the static placement of the panels which limit their exposure to the sun. Solar tracking systems usually deal with the two factors namely the load condition and the angle of incidence. The system that adjusts the load condition in order to track the maximum power operating point is called maximum power point tracking (MPPT), these are electronic systems in which high efficiency DC-DC converters are used to control the load current and voltage in order to extract maximum power for a certain PV panels placement and radiation conditions, more explanation about this technique will be presented later. The other type is an electro-mechanical system intended to track the sun path using rotary motors and/or linear actuators to ensure normal incidence of solar radiation on the PV panels and hence maximizing the amount of converted solar irradiation into electrical energy. A combination of both systems can be used to achieve even higher output power.

Many researches have been made about solar tracking with various approaches. Simulations of sun path tracking are presented in [1] that showed efficiency improvement over fixed systems, and in [2] where maximum power is obtained for different environmental conditions. Studies and simulations of the MPPT techniques were presented in [3] and [4] where different algorithms are compared. Analytical calculations for both sun tracking and



MPPT were presented in [5] and the results are compared to fixed system. Hardware implementations were presented in [6-10] using PIC controller or PC-based controllers.

BASICS OF PV CELLS

The solar cell is a non-linear device and can be represented as a current source model as shown in Fig. 1 [4]. The current source generates the photocurrent I_{ph} , which is directly proportional to the solar irradiation or solar insolation (not insulation) in W/m^2 that measures the radiation power from the sun per unit area, which is also equivalent to the light intensity or illumination measured in lux. The two resistances R_s and R_p represent the solar cell internal losses. The series resistance R_s represents the ohmic losses in the surface of the solar cell. The parallel shunt resistance R_p represents the losses due to leakage current.

The I-V characteristics of a solar cell, when neglecting the internal shunt resistance, is given by the equation [3] [4]

$$I_o = I_{ph} - I_{sat} \left[\exp \left(\frac{q}{AKT} (V_o + I_o R_s) \right) - 1 \right] \quad (1)$$

Where I_{ph} is the light generated current, I_{sat} is the reverse saturation current, q is the electron charge, A is the p-n junction ideality factor (a dimensionless factor), K is Boltzmann constant, T is the absolute temperature in Kelvin and R_s is the series resistance of the cell.

The graph of the I-V and P-V characteristics of the solar cell is shown in Fig. 2 [3]. It is clear that the solar cell has non-linear characteristics and these characteristics are affected by the temperature and irradiation level, while the operating point is affected by the load condition. It is also clear from the P-V characteristics that there is only one point of operation where the output power has a maximum value which is desirable operating point for the MPPT techniques that will be discussed next.

As has been mentioned earlier, the term solar tracking means two different techniques; the maximum power point tracking and the sun path tracking. A brief description of both techniques is given below

THE MAXIMUM POWER POINT TRACKING (MPPT)

As can be seen from the curves in Fig. 2, the power curve exhibits a maximum point, i.e. there is an optimum operating point of cell voltage and current at which the load will receive maximum power from the solar cell. The problem is that the load can not be guaranteed to operate at this point for two main reasons. The first reason is that the load condition may not allow to be operated at exactly the desired MPP, and the second reason is that the weather condition and other factor will affect the irradiation level that generates the photocurrent I_{ph} and hence affecting the characteristics curve which in turn will change the MPPT, so, the MPP is virtually unknown. The MPPT is about searching for (or tracking) the values of current and voltage that would produce the maximum power to be extracted from the solar cell. Therefore; high efficiency DC-DC converters are used between the solar array and the load where the switching element is controlled to change the duty cycle that in turn will affect the output voltage and hence the current. Fig. 3 shows a block diagram describing the general idea of MPPT. By using an appropriate algorithm, the MPPT should be achieved under any conditions affecting the solar cell or the load. Different algorithms are used in MPPT, The most widely used are the Perturbation and Observation (P&O) method and the Incremental Conductance (IncCond) method [3] [4]. Below is a brief description of each method.

PERTURBATION AND OBSERVATION METHOD

In P&O method is widely used because of the simple feedback structure and fewer measurements. The tracking algorithm operates by periodically incrementing or decrementing the output voltage, if a given perturbation leads to an increase in the PV array power the subsequent perturbation is made in the same direction, otherwise the subsequent perturbation is made in the opposite direction. In this manner the successive change in the voltage will lead to the MPPT where the voltage will

oscillate around the maximum power point. If the irradiation level changes and hence the characteristics curve changes accordingly, the MPPT will be different than the current operating point but since the perturbation and observation is being done in a continuous manner the P&O algorithm will be able to track the new MPP to be the new operating point.

INCREMENTAL CONDUCTANCE METHOD

The IncCond method is basically a computational method that is based on the fact that maximum power is where the derivative of power with respect to PV array voltage is zero, i.e.

$$P = IV$$

$$\frac{dP}{dV} = I + V \frac{dI}{dV} = 0$$

From which

$$\frac{dI}{dV} = -\frac{I}{V} \quad (2)$$

Equation 2 says that the peak power point is obtained by adjusting the PV array voltage such that the incremental conductance ($\Delta I/\Delta V$) equals the negative of the conductance ($-I/V$). So the role of the algorithm is to increase or decrease the duty cycle of the DC-DC converter until the above condition is satisfied which is equivalent to ($dP/dV=0$). The IncCond method offer good performance under rapidly changing atmospheric conditions (that affect the irradiation level) but it requires more measurements than the P&O method. There are other methods suggested in literature for MPPT [4], but these are beyond the scope of this paper.

SUN PATH TRACKING

Due to the relative motion between the earth and the sun, the incident solar irradiation cannot always be normal to the PV panel that has a fixed placement. Therefore, the intensity of the sunlight falling on the PV panel is greatly reduced. Sun path systems are used to move the PV panel with the sun movement so that the incident sunlight is always normal to the surface of the PV panel.

Before having further discussion of the sun tracking systems, it is useful to define the basic terms associated with the position and motion of the sun.

Zenith: The point directly overhead of the observer. The zenith is used with the west and east as a three-dimensional orthogonal coordinate system to define the sun position.

Solar altitude angle: The angle measured between an imaginary line between the observer and the sun and the horizontal plane the observer is standing on, see Fig. 4a. This angle is positive during day time and negative at night, therefore, the zero value of the altitude angle defines the time of sunrise and sunset. The maximum value of the altitude angle is at solar noon, and the maximum value of the altitude changes with the season for a given location. If the altitude angle is 90° , which usually occurs near the equator, it means that the sun is at the zenith.

Solar azimuth angle: The solar azimuth angle is the angular distance between south (in some literature north) and the projection of the line of sight to the sun on the ground. A positive solar azimuth angle indicates a position east of south, and a negative azimuth angle indicates west of south, see Fig. 4b. The sunrise and sunset do not occur at azimuth angles $\pm 90^\circ$.

Angle of incidence: It is the angle between the sun's rays irradiated on the PV panel surface and the line normal to the PV panel. The objective of the sun path tracking systems is to make this angle zero.

For a fixed point on the surface of earth, the sun position is described by the altitude and the azimuth angles. In sun path tracking systems there can be either a dual axis tracking technique, where the tracking for the azimuth angle or the east-west motion which is due to the daily change of sun position in addition to tracking the altitude angle of the sun due to the seasonal motion. Sometimes, single axis system is sufficient to track the daily east-west motion of the sun because the span of this motion is wider than the span of the seasonal motion.

On the other hand the sun tracking systems are divided into two types according to the way of controlling the alignment of the PV panel to the incident sunlight. They can be either open loop control systems or closed loop control systems.



OPEN LOOP CONTROL SYSTEMS

In this type the controller calculates the tilt angle of the PV panel using special equations or lookup tables for the sun trajectories. Although these systems do not require any measurements but they have the drawback that they require adjustment to a reference point that defines the angles produced by the mechanical system. If that reference point is disturbed, the control system would not sense the resulting error and eventually the alignment of the PV panel will be shifted from its desired location. This type of systems is best suited for theoretical research that calculate the extracted power of the tracking system using mathematical models as used by Armstrong [5].

CLOSED LOOP CONTROL SYSTEMS

This type is a photo sensor based systems, in which the sun position in the sky is detected by photo sensors and the measurements from the photo sensors are fed to the control system, as in Fig. 5. Two photo sensors (for each axis) are positioned in a way that the correct alignment of the PV panel makes equal angles of incidence of the sunlight at two sensors. This produces zero difference (or error) between the measurements of the sensors. When the sun moves, the error will not be zero because the angles are not equal, and the control system will rotate the PV panel to be adjusted in the direction that will make the angles equal and hence eliminating the error as explained in Fig. 6. Although the closed loop systems share the same concept, but the control algorithm can differ widely, they can be simple difference calculating algorithms that can be implemented using PIC controllers [6] or they can be more complex algorithms like genetic [2] algorithms or fuzzy logic control [7] that can only be implemented on a PC. Such systems are able to track the sun path without the need to calculate the sun trajectories.

The sensor based closed loop systems more commonly used than the open loop systems mostly because they are easier to orient and install than the open loop systems in the sense that there is no need for precise adjustment of the mechanical system and if the adjustment is disturbed in the future by external factors, the control system is still able to track the sun path as long as the sun path is within the limits of movement of the mechanical system.

This feature has been tested practically in our proposed system by putting the moving base in an arbitrary orientation, and then the control system starts to adjust the moving base in the direction of the sun until the angle of incidence of sun light is zero without any outside adjustments. The system can then be left to automatically track the sun.

A combination of both the open loop and the closed loop control systems can be used in a way that the angles are calculated first and the PV panel is moved accordingly, then the sensors would detect more accurately the sun position and the PV panel is further adjusted. When there is a cloudy weather condition, the sensors would not be able to accurately locate the sun, therefore, the open loop system takes over the control of the PV panel. This approach is used by Xu [9].

SYSTEM DESCRIPTION

The objective of solar tracking is to increase the efficiency of the PV Panel and hence obtaining higher output power. The overall system is equivalent to having a larger fixed PV panel with output power equals to the smaller PV panel with the tracking system. From the engineering point of view the tracking system must be cost effective in order to justify the cost of the extra equipment required for the tracking system. Therefore, in the design of the proposed tracking system, the cost is considered as a primary factor. Therefore a single-axis tracking system is adopted and since the control and the mechanical parts are the most cost affecting parts of the system, the control part is made using electronic circuit that have the opamp LM324 as the main component. While for the mechanical part, the moving base of the reflector of the satellite receiver antenna is used because of its availability and low cost, in addition to that it well suits the purpose of sun path tracking. For the motor drive part, the H-type drive is used to reverse the direction of the motor motion. Below is a detailed description of the three parts of the system

THE CONTROL PART

The circuit diagram of the controller is shown in Fig 7. It is basically a difference amplifier implemented using the low offset quad opamp LM324. The photo sensor is the 1KLB3B phototransistor that is used to detect the sunlight intensity. Two photo transistor

are positioned on opposite side on the moving base (that carries the PV cell) one to the east side (QE) and one to the west side (QW). With the appropriate choice of the values of the resistors the output of difference amplifiers of opamp A and opamp B are given by [11]

$$V_A = 10(V_{QE} - V_{QW}) \quad (3a)$$

$$V_B = 10(V_{QW} - V_{QE}) \quad (3b)$$

Looking at the characteristics of the phototransistor shown in Fig. 8, it can be seen that this characteristics is different than the characteristics of the normal transistor in the way that the collector current curve is drawn for different values of illumination while for the normal transistor the collector current is drawn for different values of base current. Therefore the illumination will represent the biasing of the phototransistor. Instead of the current gain β which is defined as the ratio between the collector current and the base current I_C/I_B , the current gain of the phototransistor β_p will be defined as the ratio between the collector current I_C and the illumination E_v , i.e.

$$\beta_p = \frac{I_C}{E_v} \quad (4)$$

This will help finding the value of the outputs of the opamps A and B in terms of the illumination E_v . The voltages of the phototransistors QE and QW are given by

$$V_{QE} = V_{CC} - I_{CQE}R \quad (5a)$$

$$V_{QW} = V_{CC} - I_{CQW}R \quad (5b)$$

Substituting eqs (5) and (4) into eq (3) we get

$$V_A = 10 \beta_p R \Delta E_v \quad (6a)$$

$$V_B = -10 \beta_p R \Delta E_v \quad (6b)$$

Where

$$\Delta E_v = E_{vE} - E_{vW} \quad (7)$$

which represents the difference of illumination on the east side phototransistor QE and the west side phototransistor QW. The V_{CC} value is chosen to be 12V, and since the value of R in Fig. 7 is 1kOhm,

the load line can be drawn as shown in Fig. 8 from the point $I_C=12mA$ & $V_{CE}=0$ to the point $I_C=0$ & $V_{CE}=12V$ (these points are outside the graph). The Q point in the middle of the line is approximately $I_C=5mA$, $V_{CE}=5.6V$ and $E_v=200lx$. From eq (4), β_p can be found approximately to be 0.025mA/lx. Taking into account that the value of R is chosen to be 1kOhm, eq (6) becomes

$$V_A = 0.25 \Delta E_v \quad (8a)$$

$$V_B = -0.25 \Delta E_v \quad (8b)$$

The above equation shows that the values of V_A and V_B are sensitive enough for small difference in illuminations on the two phototransistors that will make the controller able to detect any slight movement of the sun. On the other hand V_A and V_B have the same magnitude but opposite signs, this is to determine the direction of movement of the sun.

The next stage of the circuit is the comparators stage where the opamps C and D are used to provide the signaling to the DC motor. The threshold voltage is made variable by a multi-turn potentiometer to the user preference, this is important to stop the movement of the tracker when the magnitude of V_A and V_B which are proportional to the difference of illumination ΔE_v is low. This can happen in a cloudy day when the sun is hidden, so, in such case the tracker is stopped because there is no point of wasting energy by the motors. So when the magnitude of the voltages V_A and V_B are less than the threshold voltage, both outputs of the comparators will be zero. When the magnitude of the voltages V_A and V_B are higher than the threshold, the opamp with negative input voltage will produce zero output and the opamp with positive voltage will produce a positive voltage ($+V_{CC}$) that is fed to the motor drive stage to rotate the motor. When the motor is rotated, the PV panel will be rotated towards the sun along with the phototransistors, and during the rotation the difference in the illumination ΔE_v will decrease until it makes the magnitudes of V_A and V_B fall below the threshold voltage and then the motor stops.

Another element of the controller circuit is the 555 timer whose purpose is to make sure that the controller is not active all the time and there is no continuous unnecessary movement of the motor due to the slow motion of the sun to reduce energy



consumption. Instead, the timer is set to deactivate the controller for about 15 minutes so that the sun will have an appreciable change of position, after that the controller will be activated for about 30 seconds which is enough time for the motor to adjust the position of the PV panel and the having the magnitudes of V_A and V_B below the threshold voltage, this means that the motor will stop before the end of the 30 seconds. The deactivation of the controller is made by pulling to ground the two non-inverting inputs of the opamps A and B so that the outputs V_A and V_B will be both negatives making the outputs of the comparators C and D both zeros.

The Motor Drive

The circuit diagram of the motor drive is shown in Fig. 9, where the H-type drive is used to provide direction reversal of motor motion. The main elements are the four BDX53C Darlington transistors that act as the main switching elements. To rotate the motor in a certain direction one of the control voltages V_1 or V_2 should be set to V_{CC} and the other to ground. If we assume that V_1 equals V_{CC} and V_2 is grounded, the transistor Q_1 will be ON connecting the (+) terminal of the DC motor to ground and the transistor Q_8 will also be ON allowing the base-emitter junction of the PNP transistor Q_6 to be in the forward direction and hence Q_6 will also be ON. This will make the current to flow in the base-emitter junction of the Darlington transistor Q_4 making it ON and this will connect the (-) terminal of the DC motor to V_{CC} and the motor will rotate. For V_2 being grounded the transistors Q_3 , Q_7 , Q_5 and Q_2 will be OFF. If V_1 is grounded and V_2 is set to V_{CC} , the situation is reversed and the motor will rotate in the reverse direction. The motor current was measured and found to be around 0.1A when the moving is far from the end of movement points and the current rises to 0.5A when the moving base is near its end of movement points. These values of current are acceptably small values especially if we consider that the motor is only allowed to rotate for a small amount of time that is determined by the timer of the controller. So, the loading of the motor to the power source of the PV panel is insignificant. The control voltages V_1 and V_2 are taken from the outputs of the comparators C and D and they cannot be both set to V_{CC} , because this will cause damage to the transistors. This condition is guaranteed by

the arrangement of the inputs of the opamps A and B as discussed earlier.

The control voltages V_1 and V_2 are connected to the driver circuit through the normally closed contacts of the switches S_1 and S_2 which are limit switches that are put on the extreme ends of the actuator to ensure that the motor would not rotate the mechanical structure beyond the permissible span.

One last issue about which of the control voltages V_1 and V_2 is to be connected to the output of the comparator C or D, because the wrong connection will make the moving base to move away from the sun. Since there are many factors affecting this decision, like the polarity of the DC motor and its mechanical orientation, the ambiguity can only be resolved by a simple trial and error experiment. A choice is made by connecting, for example, V_1 to output C and V_2 to output D and the motion of the moving base is observed, if the moving base is following the sun then this connection is correct, otherwise if the moving base is moving away from the sun the connection is reversed.

The Mechanical Structure

As has been mentioned earlier the choice of the mechanical structure was made to be a moving base of satellite antenna reflector that is shown in Fig. 10. This choice was mainly because of the availability, low cost and suitability of this moving base for the intended purpose. Although the moving base is having a single motor making the system a single-axis tracking system, but the actuator of the motor is connected to the moving base in a way allowing the base to trace an arc with changing altitude and azimuth angles. This will provide an approximate trace to the exact sun path. The error will be from the difference of the actual altitude of the sun and the altitude angle established by the moving base. The moving base is equipped by a manual mechanical adjustment of the altitude providing the ability to change the range of the altitude angle according to the season. So, the user can make this adjustment every 3 months, for example, to minimize the altitude angle difference error.

This moving base can hold a reflector of 1.5m diameter, that is an equivalent area of 1.77 m² and it was tested to hold with motor rotation 15kg weight. So, any PV panel with such dimensions and weight

can be used with this moving base. In case of larger PV panels are required, a specially designed moving base will be required without modifications to the controller and the driver circuits.

Since the proposed system is only a prototype, the solar cell that was used for the measurement purposes was a small one with open circuit voltage $V_{oc}=7.5V$ And short circuit current $I_{sc}=0.333A$. This solar cell is not powerful enough to rotate the motor, therefore, an external power supply of 12V was used to operate the system. In actual system the output of the solar panel should be used as a power supply of the tracking system.

MEASUREMENTS AND RESULTS

Two sets of measurements were taken for comparison, one for the sun tracking system and one for the fixed system. The altitude angle was calculated for the midday time which is 12:00pm according to the longitude and latitude of Baghdad ($33^{\circ} 20' N$, $44^{\circ} 24' E$) and the date of 12/6 using sun position calculator [12], the calculated value was about 80° [12]. The moving base adjusted according to this angle for noon time and measurements were taken from early morning until afternoon every 15 minutes.

Table 1 shows the output voltage of the moving and fixed solar cells with load termination equals $R_L=25$ Ohm obtained every 15 minutes during the day. The graph of these results is shown in Fig. 11, where it can be seen that the curve of the tracking system is more flat than the fixed system, this means that the load of the tracking system will have a constant voltage for more time that the fixed system. In terms of power, the average power for both systems can be calculated as

$$P = \frac{\sum V_i^2 / R_L}{N} \quad (9)$$

Where N is the number of the measurement points. The amount of power increase using the tracking system over the fixed system can be found to be 57%.

From the economical point of view, we can take an example of a PV panel available in the market of

36W power that costs 200'000ID. As has been stated earlier the cost of our tracking system is 30000ID which is 15% extra cost to the PV panel, in return 57% increase of output power is obtained. Since the cost of the tracking system is the same for a larger PV panel with higher output power, the relative cost will be reduced while obtaining the same percentage of power increase.

CONCLUSION

The purpose of this paper is to motivate for more research in the fields of renewable energy. A design of a sun path tracking system has shown an increase in the output power of 57% of the moving PV panel over the fixed moving PV panel using simple mechatronics with added cost of about 15%. The relative cost can be lowered when using solar panels of higher output power.

REFERENCES

- Alexandru, C.; Pozna, C. "Virtual Prototype of a Dual-Axis Tracking System used for Photovoltaic Panels", IEEE International Symposium on Industrial Electronics, ISIE 2008. June 30 2008-July 2 2008. Cambridge, UK.
- Mashohor, S.; Samsudin, K.; Noor, A. M.; Rahman, A. R. A.; "Evaluation of Genetic Algorithm based solar tracking system for Photovoltaic panels" IEEE International Conference on Sustainable Energy Technologies, 2008. ICSET, 2008. Singapore.
- Hua C.; Shen C., "Comparative study of peak power tracking techniques for solar storage system" 13th Annual Applied Power Electronics Conference and Exposition, 1998. APEC '98. Conference Proceedings 1998. California, USA. Volume: 2.
- Armstrong, S.; Hurley, W.G.; "Self-regulating maximum power point tracking for solar energy systems", 39th International Universities Power Engineering Conference, 2004. UPEC 2004. Bristol, UK. Volume: 2.
- Armstrong, S.; Hurley, W.G.; "Investigating the Effectiveness of Maximum Power Point Tracking for a Solar



- System” IEEE 36th Power Electronics Specialists Conference, 2005. PESC '05. Brazil
- Barsoum, N.; “Implementation of a Prototype for a Traditional Solar Tracking System” Third UKSim European Symposium on Computer Modeling and Simulation, 2009. EMS '09. Athens, Greece.
 - Jung-Sik Choi; Do-Yeon Kim; Ki-Tae Park; Chung-Hoon Choi; Dong-Hwa Chung; “Design of Fuzzy Controller based on PC for Solar Tracking System” International Conference on Smart Manufacturing Application, 2008. ICSMA 2008. South Korea.
 - Omar, A.M.; Shaari, S.; Omar, A.R.; Yahaya, M.R.Y.; “An Automated Solar Photovoltaic Biaxial Tracking System: SolT2A ” IEEE International Power and Energy Conference, 2006. PECon '06. Malaysia.
 - Jing Xu, Kaihua Wu, Li Ma; “All-weather automatic solar tracking method applied in forest fire prevention” 9th International Conference on Electronic Measurement & Instruments, 2009. ICEMI '09. Beijing, China.
 - Hossain, E.; Muhida, R.; Ali, A.; “Efficiency improvement of solar cell using compound parabolic concentrator and sun tracking system” IEEE Canada Electric Power Conference, 2008. EPEC 2008.
 - Millman, J. and Halkias C. “Integrated Electronics”, McGraw-Hill, 1972
 - Sun Position Calculator
<http://www.susdesign.com/sunangle/>

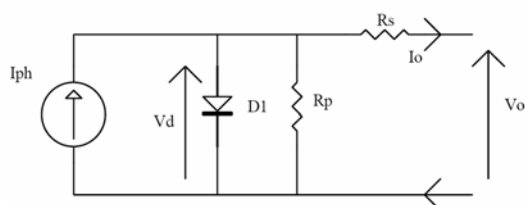


Fig. 1 The solar cell model.

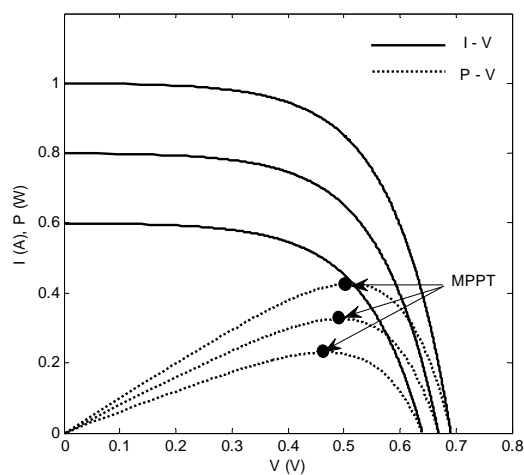


Fig. 2 The I-V and P-V characteristics of the solar cell for different irradiation levels.

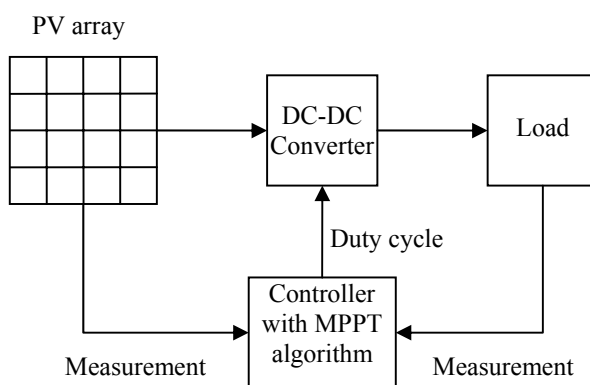


Fig. 3 Block diagram of MPPT technique

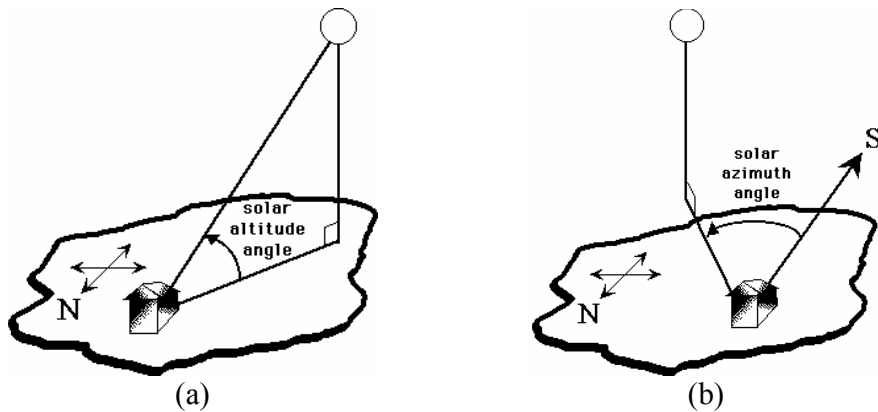


Fig. 4 a: the altitude angle. b: the azimuth angle.

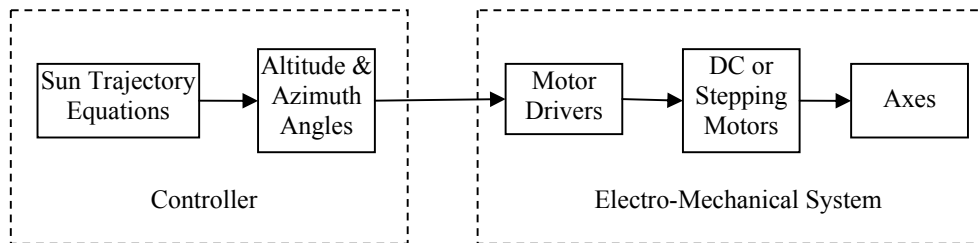


Fig. 4 Open loop control system of the sun path tracking

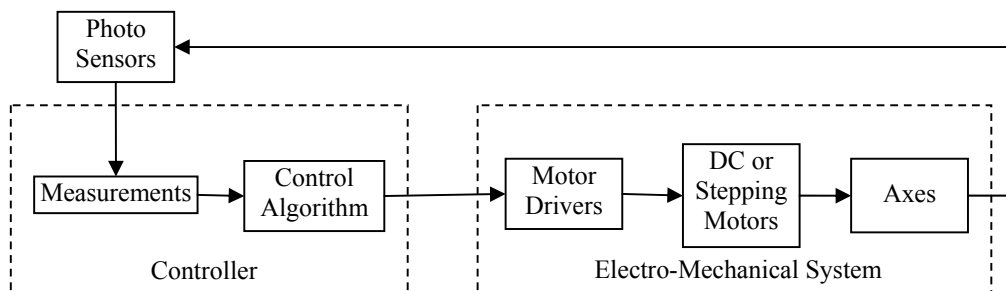


Fig. 5 Closed loop control system of the sun path tracking

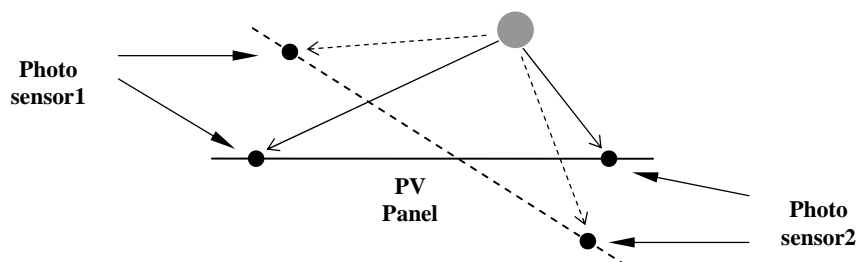
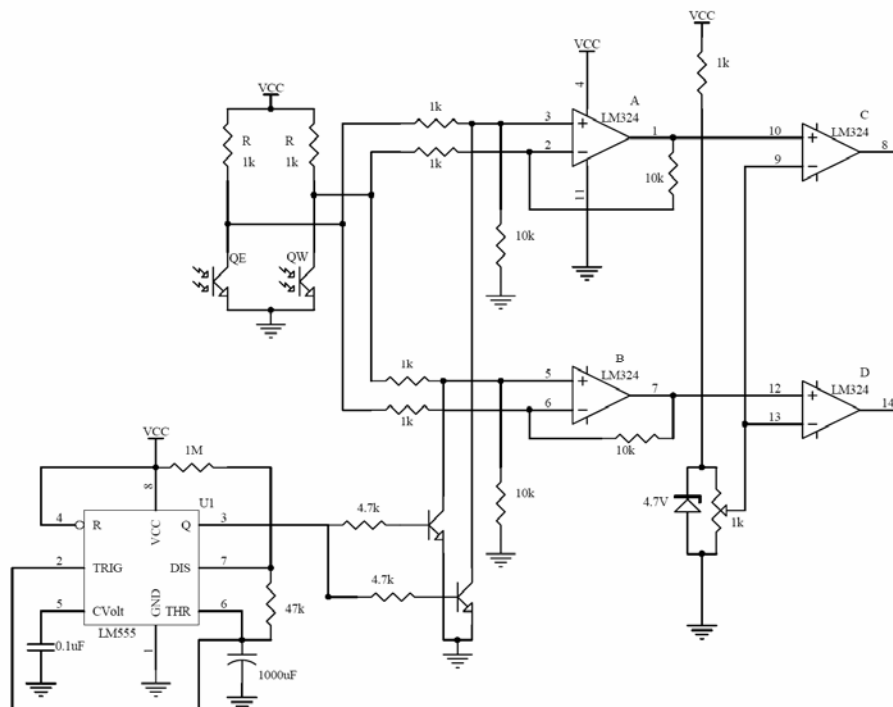


Fig. 6 The adjustment of photo sensors orientation with respect to sun.



The graph plots Collector current I_C (mA) on the y-axis (0 to 10) against Collector-Emitter voltage V_{CE} (V) on the x-axis (0 to 10). A diagonal line represents the load line. Four curves are shown for different base-emitter voltages V_{be} : 400V, 300V, 200V, and 100V. The Q-point is marked at the intersection of the load line and the $V_{be} = 200V$ curve.

V_{CE} (V)	I_C (mA) for $V_{be} = 100V$	I_C (mA) for $V_{be} = 200V$	I_C (mA) for $V_{be} = 300V$	I_C (mA) for $V_{be} = 400V$
0	0	0	0	0
2	2.5	4.5	7.0	9.0
4	2.5	4.8	7.2	9.5
6	2.5	4.9	7.3	9.8
8	2.5	5.0	7.4	10.0
10	2.5	5.0	7.4	10.0

Fig. 8 I_C vs. V_{CE} of the phototransistor for different illumination values.

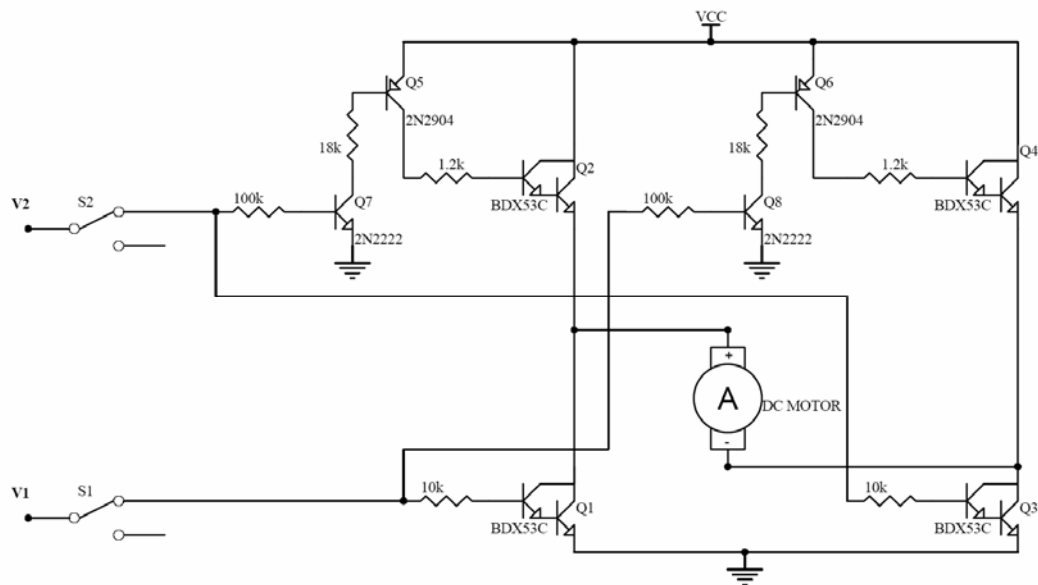


Fig. 9 The circuit diagram of the DC motor driver.

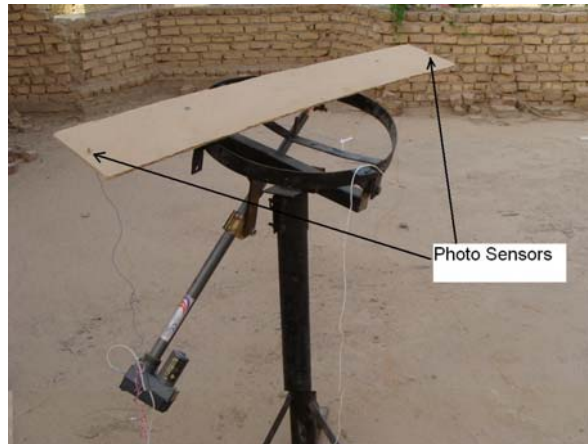


Fig. 10 The moving base with the photo sensors fixed to it.

Table 1: The cost of the designed tracking system

Item	Cost (ID)
Moving base	12'000
Phototransistor 1KLB3B	2x3'500=7'000
Quad opamp LM324	500
Timer 555	500
Transistor BDX53C	4x750=3'000
Transistor 2N2222	4x500=2'000
Transistor 2N2904	2x500=1'000
Board	2x1'000=2'000
Various electronic components	2'000
Total	30'000

Table 2: Practical results

Time (hh:mm)	Tracking PV voltage (V)	Fixed PV voltage (V)	Time (hh:mm)	Tracking PV voltage (V)	Fixed PV voltage (V)
5:30 am	1.05	0.20	12:00 pm	5.76	5.75
5:45 am	2.10	0.41	12:15 pm	5.70	5.65
6:00 am	2.72	0.55	12:30 pm	5.68	5.52
6:15 am	3.14	0.71	12:45 pm	5.63	5.48
6:30 am	3.96	0.92	1:00 pm	5.60	5.44
6:45 am	4.63	1.03	1:15 pm	5.56	5.39
7:00 am	4.72	1.09	1:30 pm	5.51	5.35
7:15 am	4.80	1.14	1:45 pm	5.46	5.31
7:30 am	5.11	1.20	2:00 pm	5.40	5.24
7:45 am	5.30	1.50	2:15 pm	5.35	5.10
7:00 am	5.35	1.80	2:30 pm	5.30	4.95
8:15 am	5.40	2.00	2:45 pm	5.25	4.78
8:30 am	5.45	2.40	3:00 pm	5.20	4.60
8:45 am	5.50	3.26	3:15 pm	5.15	4.30
9:00 am	5.52	3.85	3:30 pm	5.10	3.50
9:15 am	5.51	4.36	3:45 pm	4.96	3.20
9:30 am	5.55	5.00	4:00 pm	4.79	2.90
9:45 am	5.56	5.11	4:15 pm	4.62	2.60
10:00 am	5.57	5.25	4:30 pm	4.38	2.30
10:15 am	5.58	5.36	4:45 pm	4.12	2.00



10:30 am	5.59	5.41	5:00 pm	3.85	1.80
10:45 am	5.61	5.48	5:15pm	3.50	1.60
11:00 am	5.64	5.54	5:30 pm	3.15	1.40
11:15 am	5.71	5.60	5:45 pm	2.70	1.20
11:30am	5.75	5.69	6:00 pm	2.12	1.00
11:45 am	5.76	5.73			

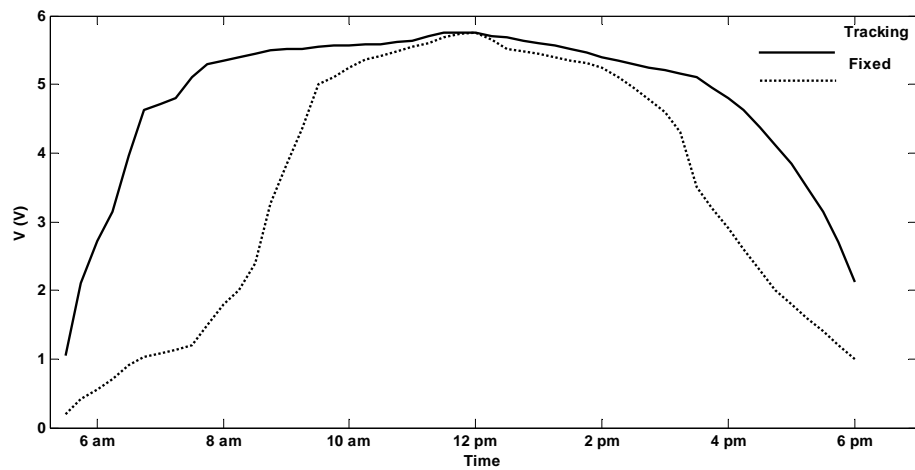


Fig. 11 Graph of the PV cell voltage for both fixed and tracking systems.



PHYSICAL MODEL OF KEROSENE PLUME MIGRATION IN AN UNSATURATED ZONE OF THE SANDY SOIL

Prof. Dr. Rafa H. Al-Suhaili
University of Baghdad
College of Engineering

Hussein A. M. Al -Madany
University of Kufa
College of Engineering

ABSTRACT

Physical model tests were simulated non-aqueous phase liquid (NAPL) spill in two-dimensional domain above the water table. Four laboratory experiments were carried out in the sand-filled tank. The evolution of the plume was observed through the transparent side of this tank and the contaminant front was traced at appropriate intervals. The materials used in these experiments were Al-Najaf sand as a porous medium and kerosene as contaminant.

The results of the experiments showed that after kerosene spreading comes to a halt (ceased) in the homogeneous sand, the bulk of this contaminant is contained within a pancake-shaped lens situated on top of the capillary fringe.

لقد تضمن العمل المختبري تمثيل تسرب السائل العضوي الأخف من الماء في الطبقة ذات البعدين فوق مستوى الماء الجوفي. حيث أجريت أربعة تجارب مختبرية في حوض زجاجي صنع لهذا الغرض وملاً بالرمل. إن استخدام الزجاج يوفر الأماكن المطلوبة لمتابعة تقدم مقدمة الملوثة وبالتالي رسم شكلها خلال فترات زمنية مختلفة. لقد تم اختيار تربة مدينة النجف لتمثيل الوسط المسامي في كل التجارب المختبرية الحالية في حين تم اختيار النفط الأبيض لتمثيل السائل العضوي المتسرب إلى ذلك الوسط.

أظهرت التجارب المختبرية للتربة المتجانسة عند توقف انتشار الملوثة النفطية فإن كمية كبيرة من الملوثة سوف تشكل شكلاً مفلطحاً مستقراً فوق منطقة capillary fringe.

INTRODUCTION

The problem of evaluating the factors controlling the movement of Non-Aqueous phase Liquids (NAPL_s) in shallow subsurface has received increasing attention in the last decade after a number of sites throughout the United States have been found to be contaminated with organic chemicals, mostly petroleum products (McKee et al., 1972; Kramer, 1982), aromatic compounds (Oliveira and Sitar, 1985) and halogenated hydrocarbons. Once a NAPL is released into the subsurface, it continues to travel as a separate liquid phase until it becomes immobile. When the migration of the NAPL reaches its final stage, this contaminant remains as isolated ganglia or pools. These pools act as a source of further contamination by dissolution and vaporization.

Soil and ground water contamination by (NAPL_s) such as organic solvents, gasoline and other petroleum products is widespread due to leaking storage tanks, spills, and improper disposal processing. Although NAPL_s are relatively immiscible with water, understanding the behavior of these liquids in the subsurface is important since solubility may exceed drinking water standards. After release, NAPL migrates as a separate phase downward by gravity with some lateral spreading due to capillary forces. If sufficient NAPL has been spilled, eventually, it may reach the groundwater surface. If it is lighter than water (LNAPL) it will accumulate as a liquid mound that floats on the ground water surface. If it is denser than water (DNAPL) it displaces ground water and continues downward migration until it encounters a hydraulic or capillary barrier as shown in Fig. 1. Floating

LNAPL can partly be removed by creating a pumping well (Mercer and Cohen, 1990). The LNAPL will flow towards the well facilitated by the groundwater table gradient and can be pumped into a recovery tank. Although removing DNAPL is more difficult task, DNAPLs can be pumped out of the subsurface. Not all of the NAPL can

be removed, since some of it is retained in the capillaries of the porous medium. This remaining NAPL can be contained hydrologically or can be removed by other techniques such as air sparging or bioremediation. To predict the NAPL that was left behind in the unsaturated zone after remediation by pumping, the mechanisms that are responsible for the flow and retention of NAPL must be understood. Therefore, such understanding is a major motive for studying the movement, interaction and distribution of three fluid phases, i. e., water, NAPL and air in a porous medium: the subsurface.

The unsaturated zone is a multiphase system, consisting of at least three phases: a solid phase of the soil matrix, a gaseous phase and the water phase (Bear, 1972). Additional phase may also be present such as a separate phase organic liquid. Oil properties such as density, viscosity, interfacial tension, solubility and vapor pressure are important in understanding oil transport and in predicting subsurface contamination.

Al Najaf is one of the most important cities in Iraq. It is the spiritual center of all Moslems because the holy shrine of Al Imam Ali. It is located on high plateau over a sandy ground (Al Shakerchy, 2007). Al Najaf is expected to have a huge development program in the coming years through the construction of many gasoline stations, chemical manufacturing and processing plants and other facilities for storing hazardous materials has led to the installation of underground storage tanks (USTs). Many of installed (old) tanks have exceeded or are currently close to the end of their useful life and are now (or will soon be) leaking, posing a serious threat to soil and groundwater quality as well as to public health and welfare. To establish the most effective soil remediation technology that can be utilized in the control of releases from leaking UST_s and to minimize unreasonable risks to human health and the environment, it is essential to identify likely



contaminants and the severity of contamination from leaking USTs, therefore, Al Najaf sand soil was used here in the experimental works to represent an actual case.

PHYSICAL MODEL

Sand Tank

The sand tank model was built to study the movement of the (LNAPL) in the vadose zone. The simulated spills were performed in a tank 71cm long, 61cm high, and 5cm wide, schematically shown in Fig. 2. Pressure ports and electrodes locations are shown in Fig. 3. The front side of the tank was transparent to allow for visual observations. It consisted of a glass plate for the initial experiments and was later replaced by a Lucite plate in order to accommodate for the design adopted for the saturation measurements. Two pairs of metal reinforcing bars were clamped on the exterior of the tank to prevent bending of the more deformable Lucite plate. The back side of the tank made of stainless steel, was designed to be removable to allow for measurement of the extent of the plume at the back and for examination of the contaminated area within the sample by careful dissection at the end of each experiment. Two vertical perforated stainless steel partitions, covered with stainless steel mesh, provided the lateral boundaries of the sand-filled middle compartment, which had dimensions 61x 61 x 5cm. The purpose of the two outer compartments was to provide constant head reservoirs for controlling the position of the water table within the sand deposited in the middle and, in addition, to control the wetting and drainage of the sand mass.

Materials

A) Soil: Two sizes of available sand, designated #14 (coarse) and #50 (fine), were used for the experiments which brought from Al-Najaf city/Al Adala Quarter. Additional sieving was necessary to achieve

satisfactory uniformity. The sand was also washed to remove fine particles and salts which if dissolved into the water-NaCl solution would alter its electrical properties, as discussed above. The result of the grain size distribution, as shown in Fig. 4, shows that the soil is consisting about of 2.66% gravel, 96.6% sand, and about 0.7% fine. The characteristics of the grain distribution curve give the uniformity coefficient, (C_u) =8.67 and the coefficient of gradation, (C_c) =1.35. According to unified soil classification system, the soil was classified as well graded (Das, 1985). The median grain size of the soil is 0.9 mm.

B) Contaminant Liquid: After considering various organic liquids, kerosene was chosen as the contaminant fluid. The selection was based on the low health hazard of kerosene during experiment, in combination with a number of desirable properties such as specific gravity lower than 1.0, viscosity comparable to that of water, very low solubility in water, and low volatility. The last two properties are necessary to limit the mass transfer between phases during the experiments. The pertinent properties of kerosene are summarized in Table (1). In order to enable visual observations, kerosene was dyed with Sudan III. "Sudan" is trade mark (or name) for a line of dyestuffs, soluble in hydrocarbons; used for the coloring of fats, oils, waxes....etc. Sudan III is a powdered, nonvolatile an organic dye of red color which is insoluble in water.

* SAMPLE PREPARATION

The tests were conducted in a constant temperature room (21°C) which is necessary for such experiments, since electrical properties, and to lesser extent, surface properties are temperature dependent. Sand was then deposited in lifts by dry pluviation. Since uniform sands were used, special packing procedures were not deemed necessary in order to achieve homogeneous samples. The soil density used here is 1.128 gm/cm³ for coarse sand and 1.026 gm/cm³

for fine sand. Before the last lift was placed in the tank a Lucite cylinder, which served as the source of the kerosene, was embedded in the center of the top of the sample and filled with sand to the same final height as the rest of the sample (Fig. 2). The inside diameter of the cylinder was 3.2 cm. The final height of the samples ranged between 49 and 52 cm.

After all the sand was in place, water was slowly introduced via the outer compartments, to form a water table 3-4 cm above the bottom of the tank. More water was permitted to flow from the reservoirs connected to the tank through the outer compartments and into the sample to maintain the water table at the same height, as water infiltrated into the sand due to capillary rise. When the water table stabilized, i.e. when imbibitions of water into the sand ceased, the water table was raised another 3-4 cm, and the same procedure was repeated until the water table finally equilibrated at the top of the sample. The wetting rate was kept slow in order to achieve the maximum water saturation possible while relying only on moistening by capillarity. Wetting of the samples typically lasted 2-3 hours and resulted in water saturation close to 85%.

After the sample was wetted, drainage was initiated by lowering the water table in the outer compartments to the desired height, typically 4 and 16 cm above the base of the tank for the fine and coarse sand, respectively. The two different water table elevations compensated for the different extent of the capillary fringe in the two sands. The samples were allowed to drain overnight, for at least 12 hours. After drainage was completed, three distinct regions appear above the water table. The first is the capillary fringe where there is maximum water saturation under negative pressure. The second zone is the visibly wet area above the capillary fringe where water saturation decreases with increasing distance from the water table. Finally, the third zone is visibly dry (although still moist) region at the top apparently corresponds to the zone where water is discontinuous.

* TEST PROCEDURE

Each experiment began by introducing kerosene inside the cylinder which simulated a leaking underground facility in the sand tank model. In all experiments, a total of 350 cm³ of kerosene was used, equal to approximately 10% of the pore space above the capillary fringe. Kerosene was added as needed to maintain the height of the free liquid inside the cylinder always at 4 cm above the top of the sand, until all of 350 cm³ of kerosene were used. The rate at which kerosene was added to adjust the level at 4 cm was dictated by the rate at which kerosene from the cylinder disappeared into the sand. In this way, in all the experiments kerosene infiltrated under a constant head. The plume was traced at appropriate intervals during both the infiltration (while the source of leak is active) and the redistribution (when no additional kerosene enters the sample) stages, until no significant changes of the front were observed.

Water volume flowing out of the tank was measured and kerosene front was traced (Figs. 4 and 5) at the appropriate intervals. The development of the plume was typically monitored for 24 hours, well after any visible movement of the front had ceased. At the completion of the experiment, the tank was tilted and the back plate was removed in order that the final position of the contaminant front on the back side could be traced. The samples were subsequently dissected, so as to examine the distribution of kerosene in the sand.

A central area which was uniformly contaminated with kerosene was invariably observed, beyond this area, interconnected pockets of kerosene were found which extended to the boundaries of the front as observed through the Lucite plate, indicating minimal boundary effects. A total of 4 simulated spills were performed in homogeneous sands. More specifically, two experiments were conducted with fine sand (#50) and the other experiments with coarse sand (# 14).



* VISUAL OBSERVATION

The experiments with homogeneous coarse (#14) and fine (#50) sands showed that although kerosene infiltrates more rapidly in the coarse sand, the evolution of the contaminant front follows similar patterns despite differences in grain size, provided that the top of the capillary fringe at the same elevation. At the initial stage of the spill, the front retains a regular, circular shape, after few times the front shape becomes ellipsoid as it advances (Figs. 5 and 6). After the contaminant front reaches the boundary between visibly wet dry sand its shape becomes irregular and is characterized by fingering and lateral spreading, as was also reported by Schwille (1984).

When kerosene becomes immobilized and spreading ceases, the final contaminated area consists of two distinct regions, an elongated, pancake-shaped area of high kerosene saturation and the area above it, which was previously swept by the front, at residual kerosene saturation. The top of the kerosene-wet area was slightly above the visibly wet-dry sand boundary in all experiments. The maximum horizontal extent of the kerosene lens occurred at an elevation close to and below the visibly wet-dry sand boundary. Thickness of this pancake-shaped lens was consistently higher in the fine sand.

EXPERIMENTAL RESULTS

A) Propagation of the Contaminant Front:

To quantify the information obtained from the simulated spills, the development of the contaminant front with time was described by the following variables: the volume of kerosene in the sample, the volume of the sample which was contaminated by kerosene, the average kerosene saturation in the contaminated zone, the distance between the lowest point of the front and the water table, and the distance between the source of the leak and the front. The values of these parameters for the fine (#50) and coarse (#14) sands are listed in Table 2. The extent and the

geometry of the final contaminant front were described by the variables listed in Table 3, the percentage of the total volume of the sample which was contaminated by kerosene, the ratio of the volume of contaminated soil to the total volume of the contaminant liquid spilled, and the lens thickness.

A comparison of data for the two sands (Table 2) shows that the final vertical extent of the plume (distance from the leak) is the same for both sands as a result of the same capillary fringe elevations, although the total contaminated area is larger for the fine sand. More specifically, a comparison of the parameters describing the final position of the front (Table 3) shows that the average percentage of the total sample volume contaminated by kerosene is 21.14% for the fine sand, dropping to 19.34% for the coarse sand. Thus the ratio of the kerosene-contaminated sand to the infiltrated kerosene volume is 10.50 in the fine sand and 7.59 in the coarse sand. Kerosene saturation remained consistently lower in the fine sand during all stages of the test, apparently due to the higher initial water saturation in the fine sand, as will be discussed later.

The spreading rate of the contaminant front during kerosene infiltration was also computed from the mean values of the kerosene-contaminated area for the two sands. Spreading rate was calculated based on new volume swept by the front during a time interval (dV/dt), as well as on total volume swept at a time measured from the beginning of infiltration divided by this time (V/t). The two rates are very similar to each other for the same sand, indicating that the spreading rate remains constant during infiltration. The mean values were 18.80 and 86.95 cm^3/min for the fine and coarse sand, respectively.

B) Measurement of Phase Variables: The measurements obtained during two of the experiments, with homogeneous fine and coarse sand, are presented here to illustrate the observed changes in water saturation and the pressure head response. The water table was lowered to 3.9 and 16.0 cm from the

bottom of the tank for the fine and the coarse sand, respectively. Subsequent drainage lasted 14 hours for the fine sand and 12 hours for the coarse sand. At the end of this period water pressures and saturations were changing at a very slow rate indicating that static equilibrium above water table was achieved. Following drainage, a total of 350 cm³ of kerosene was allowed to infiltrate through the Lucite cylinder simulating the leaking facility under a constant head of 4 cm. After all the kerosene was used, infiltration continued under a declining head until all kerosene was in the sand mass and redistribution started. A summary of the two tests is given in Table 4, which also includes the volume of the water that flowed out of the tank during the kerosene infiltration stage.

DISCUSSION

The data from the fully instrumented tests confirm and explain the visual observation regarding the characteristics of the advancing plume and its final extent. On the basis of the visual observations of the kerosene front, it was found that the ratio of spreading rates during infiltration for the coarse and fine sand ($86.95/18.8=4.6$), the ratio of kerosene of infiltration rates was twice as high ($21.6/2.9=7.4$). These results can be explained by considering the different saturation profiles for the two sands. Although the top of the capillary fringe (area of maximum saturation) in both samples is located at the same elevation, the saturation distribution above it is dissimilar due to differences in grain size distribution (higher uniformity in the coarse sand produced a flatter capillary pressure curve). In order to move downward, kerosene has to displace more water in the fine sand than in the coarse sand, as evidenced by the higher saturation changes during infiltration in the fine sand samples and by the larger volume of water displaced at the end of the infiltration stage, 275 cm³ for the fine sand compared to only 145 cm³ for the coarse sand. However, while vertical movement is delayed in the fine sand, kerosene moves

laterally. As a result, although in both cases the kerosene front extends over the same vertical distance 21.7 cm and 22.9 cm for the coarse and fine sand, respectively, the total contaminated area is wider in the fine sand. Again, as a consequence of the different water saturation distribution, as determined from the capillary pressure-saturation curves of the two sands, the final average kerosene saturation is lower for the fine sand.

The results of the comprehensive analysis in Al Najaf city sand (especially for gypsum content) showed that there are two main categories with respect to the changing with depth, first, at depth range of 0.5-2.0m, and second, at depth range of 2.0-12.5m, where at first range, the content of gypsum changes randomly from area to another, so, the average value of gypsum content range of 18-24.19 %. At depth range of 2.0-12.5m, the gypsum content ranged of ≤ 6 % (Al Shakerchy, 2007). When gypseous soils are irrigated, the gypsum is leached and then located and in some cases a gypsum layer is formed which reduces the hydraulic conductivity. This will decreasing trend of contaminant movement.

CONCLUSIONS

The following conclusions are drawn on the basis of the results obtained from the present experimental measurements:

- a) Visual observations from the sand tank model show that the front retains an elliptic shape during the final stages of infiltration, but later on, as it approaches the capillary fringe, it becomes irregular, characterized by fingering and more extensive lateral than vertical movement. After spreading ceases, the contaminated area in homogeneous samples consists of two distinct regions: an elongated pancake-shaped oil lens of high NAPL saturation, which extends from the top of the capillary fringe up to the boundary between visibly wet and dry sand, and the area above it, previously swept by the front, at lower kerosene saturation.



b) The ratio of spreading rates during infiltration for the coarse and fine sand ($86.95/18.8 = 4.6$). While the ratio of kerosene of infiltration rates was twice as high ($21.6/2.9 = 7.4$). These results can be explained by considering the different saturation profiles for the two sands.

c) In order to move downward, kerosene has to displace more water in the fine sand than in the coarse sand, as evidenced by the higher saturation changes during infiltration in the fine sand samples and by the larger volume of water displaced at the end of the infiltration stage, 275 cm^3 for the fine sand compared to only 145 cm^3 for the coarse sand.

d) The experiments with homogeneous coarse and fine sands showed that the kerosene infiltrates more rapidly in the coarse sand, however, while vertical movement is delayed in the fine sand, kerosene moves laterally. As a result, although in both cases the kerosene front (from leak source) extends over the same vertical distance 21.7 cm and 22.9 cm for the coarse and fine sand, respectively.

e) The plume moved faster in the coarse sand, as expected. The total contaminated volume was lower, 2655 cm^3 and 3675 cm^3 for the coarse and fine sand, respectively.

f) Decreasing trend of contaminant movement due to the presence of the gypsum content, fine and other soluble salts in Al Najaf city sand caused the reduction in the hydraulic conductivity, consequently, the reduction in the hydraulic conductivity is due to the plugging of soil pores by the precipitation of the leached gypsum.

- Al Shakerchy, M. S., "Geotechnical Properties of Al Najaf City Soil With Emphasis On Infiltration And Strength Characteristics", A Thesis Submitted To The Building And Construction Engineering Department In The University Of Technology In Partial Fulfillment Of The Requirement For The Degree Of Doctor Of Philosophy In Geotechnical Engineering, 2007.

Bear, J., "Dynamics of fluids in porous media". Elsevier, New York, 1972.

- Das, M. B., "Advance soil mechanics", Mc raw Hill Book Com., 1985.
- Mckee, J. E., F. B. Laverty, and R. M. Hertel, "Gasoline in groundwater". J. Water Pollution Control Fed., 44(2), 293-302, 1972.
- Kramer, W. H., "Ground-water pollution from gasoline", Ground Water Monit. Rev., 2(2), 18-22, 1982.
- Mercer, J.W. and Cohen, R.M. "A review of immiscible fluids in the subsurface: properties, models, characterization and remediation. Journal of contaminant Hydrology, 6:107-163, 1990.
- Oliveira, D. P., and Siter, "Groundwater contamination from underground solvent storage tanks", Santa Clara, California, paper presented at 5th National Symposium and Exposition on

REFERENCE

- Aquifer Restoration and Groundwater Monitoring, Water Well Assoc., Columbus, Ohio, May 21-24, 1985.
- Pantazidou, M., and N. Sitar, "Emplacement Of non-aqueous liquids in the vadose zone". Water Resources Research, 22(1), 25-33, 1993.
 - Thornton, J. S., "Underground movement of gasoline on groundwater and enhanced recovery by surfactants", paper presented at proceedings of the National Conference on Control of Hazardous Material Spills, U.S. Environ. Protect. Agency, Louisville, Ky., May 13-15, 1980.
 - Schuille, F., "Migration of organic fluids immiscible with water, in Pollutants in Porous Media", Ecol. Stud., vol. 47, pp.27-48, Springer-Verlag, New York, 1984.
 - Watts, R. J., "Hazardous wastes: Sources, Pathways, Receptors". John Wiley, USA, 1998.

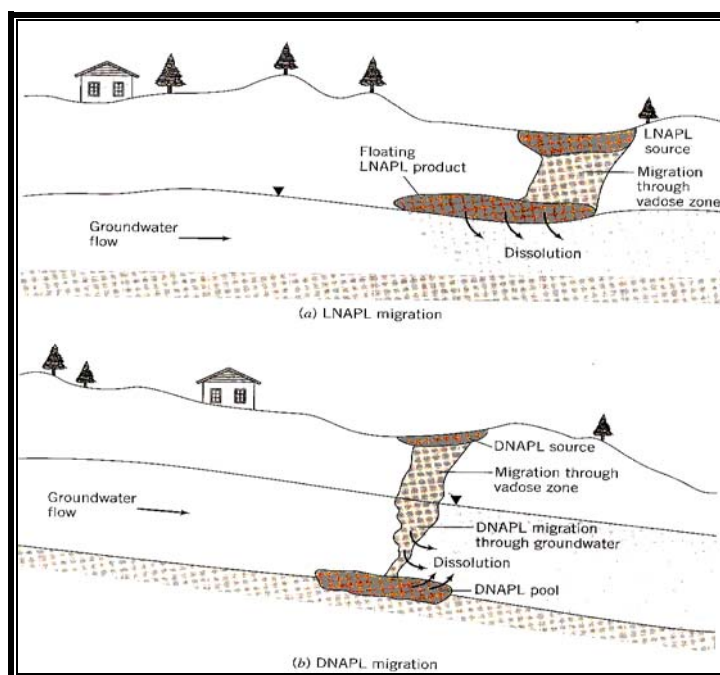


Figure 1: Conceptualized representation of (a) LNAPL and (b) DNAPL migration and contamination of the subsurface (Watts, 1998).

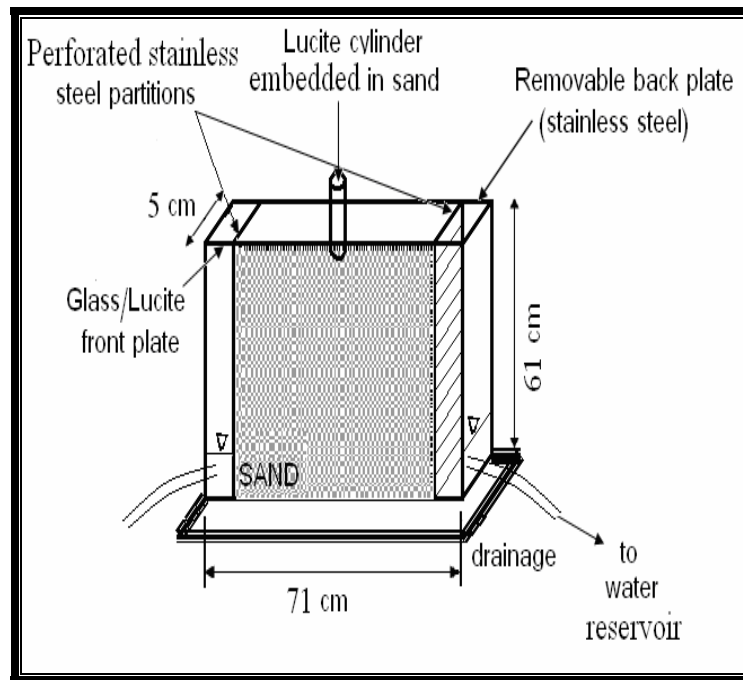


Figure 2: Tank configuration for the sand tank used in the present study.

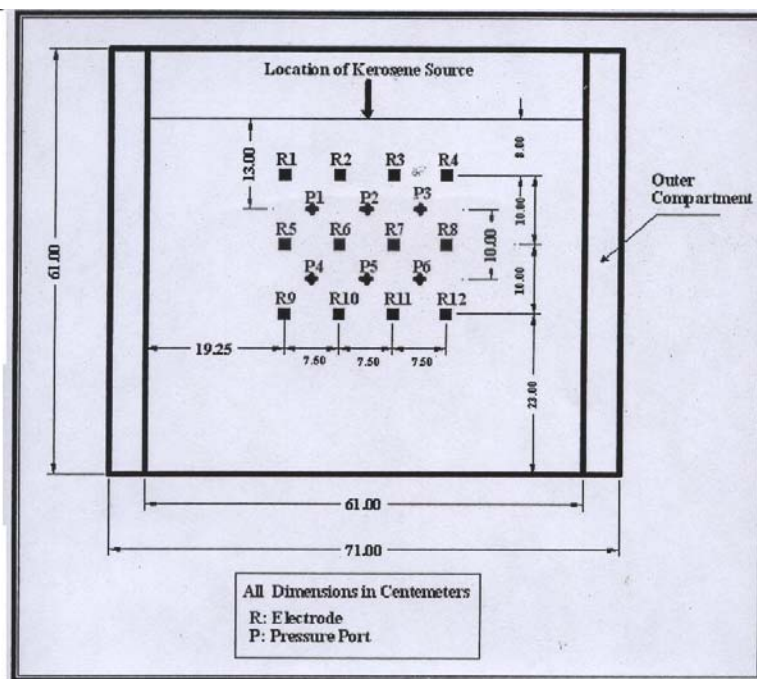


Figure 3: Pressure ports and electrodes locations for the sand tank used in the present study.

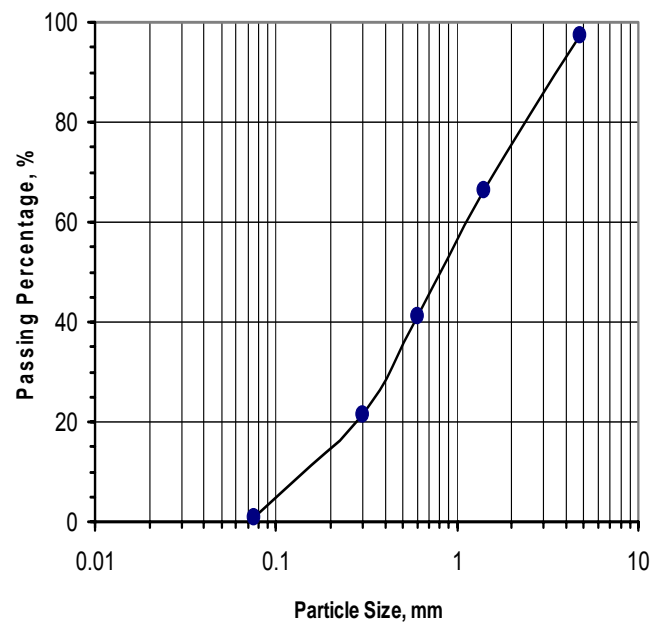


Figure 4: Gradation curve for Al-Najaf city sand.

Table 1: Kerosene properties (Pantazidou and Sitar, 1993).

Parameter	Value
Specific gravity	0.8 at 15 ° C
Viscosity	1.152 CP at 21 ° C
Surface tension: kerosene-air	27.5 dyne/cm at 20 ° C
Interfacial tension: kerosene-water	48 dyne/cm at 20 ° C

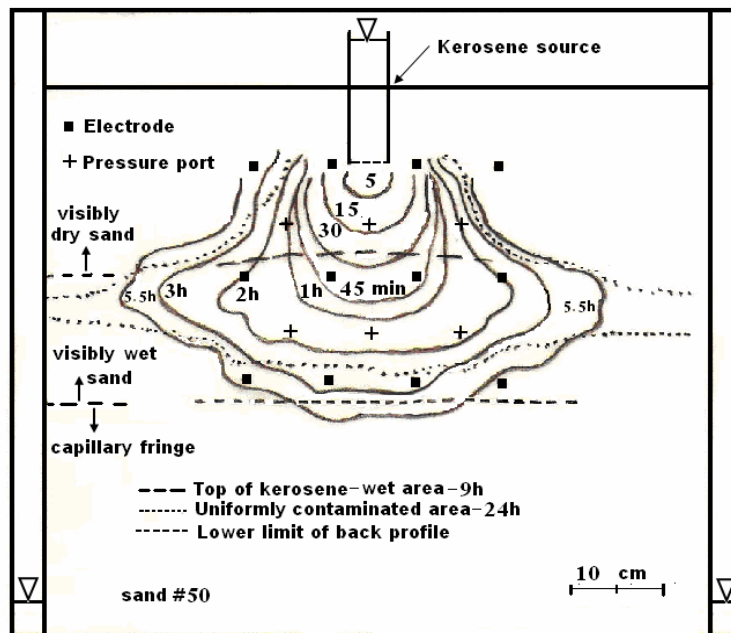


Figure 5: Kerosene front propagation traced during the experiment in the fine sand medium (#50).

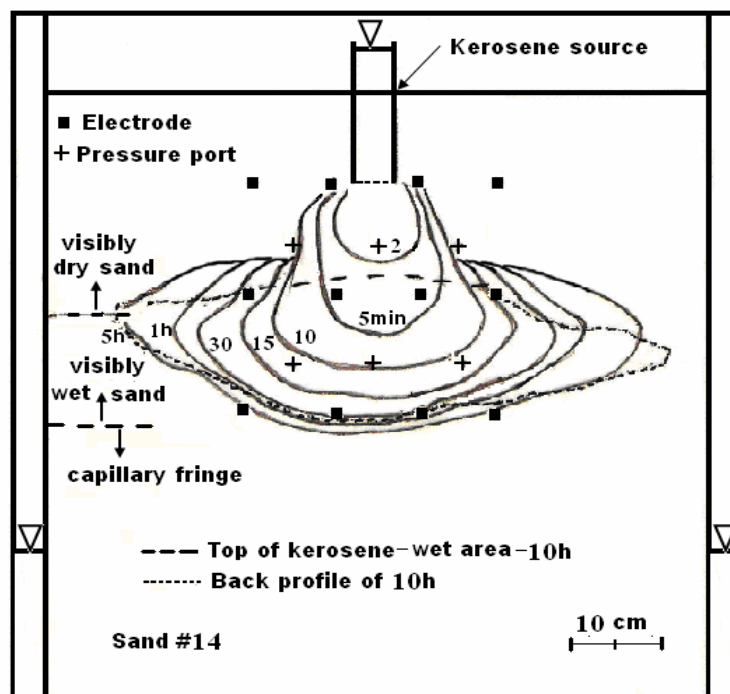


Figure 6: Kerosene front propagation traced during the experiment in the coarse sand medium (#14).

Table 2: Comparison of mean values of front propagation parameters for sands (#14) and (#50).

<i>Time, min</i>	<i>Type of Sand, #</i>	<i>Kerosene Volume, cm³</i>	<i>Contaminated Soil Volume, cm³</i>	<i>Distance from Leak, cm</i>	<i>Distance from Water Table, cm</i>
5	14	107	581	13.1	16.5
	50	-	53	2.7	37.3
10	14	203	1121	17.5	12.4
	50	47	164	4.5	35.4
15	14	350	1718	18.8	10.8
	50	72	262	6.1	33.9
45	14	350	2145	21.2	8.4
	50	135	971	13.5	27.6
Final	14	350	2655	21.7	8.1
	50	350	3675	22.9	17.6

Table 3: Comparison of mean values intervals of final front parameters for sands (#14) and (#50).

<i>Type of Sand</i>	<i>Lens Thickness, cm</i>	<i>Contaminated Soil Volume to Kerosene Volume Ratio</i>	<i>Contaminated Soil Volume, %</i>
#14	11.7	7.59	19.34
#50	16.8	10.50	21.14

Table 4: Summary of two tests of fine and coarse sand.

<i>Type of Sand</i>	<i>Average Porosity</i>	<i>Initial Water Saturation, %</i>	<i>Water Table Height, cm</i>	<i>Infiltration Duration (Constant Kerosene Head/Total), min</i>	<i>Water Displaced at the End of Kerosene Infiltration, cm³</i>
Fine sand (#50)	0.44	84.0	3.9	132/150	275
Coarse sand (#14)	0.41	84.5	16.0	10/11	145



TWO-PARAMETER GAMMA DISTRIBUTION AND LOG NORMAL DISTRIBUTION FOR DERIVATION OF SYNTHETIC UNIT HYDROGRAPH

Mohammed Rashid Dhahir
Computer center ,Baghdad University

ABSTRACT

Most available methods for unit hydrographs (SUH) derivation involve manual, subjective fitting of a hydrograph through a few data points. The use of probability distributions for the derivation of synthetic hydrographs had received much attention because of its similarity with unit hydrograph properties. In this paper, the use of two flexible probability distributions is presented. For each distribution the unknown parameters were derived in terms of the time to peak(**tp**), and the peak discharge(**Qp**). A simple **Matlab program** is prepared for calculating these parameters and their validity was checked using comparison with field data. Application to field data shows that the **gamma** and **lognormal** distributions had fit well.

INTRODUCTION

The term ‘synthetic’ in synthetic unit hydrograph (SUH) denotes the unit hydrograph (UH) derived from watershed characteristics rather than from rainfall-runoff data. **Chow V.T.(1964)** and **Viessman et al. (2007)** provide a good review of the various methods available for (SUH) derivation. Among the available approximate methods for (SUH) derivation as mentioned in **Singh.(1988)**, the method of fitting a smooth curve manually through a few salient points of (UH) is generally practiced. For example, the methods of **Snyder(1938)** [Quoted from **Bhunya et al.(2007)**] and **Espey and Winslow (1974)** utilize empirical equations for the estimation of peak flow(Q_p) [L^3T^{-1}], lag time(t_L)[T], time to peak(t_p)[T], UH widths at 0.5 Q_p and 0.75 Q_p . Thus, beside the involvement of a great degree of subjectivity in such manual fitting, the fitted curves require simultaneous adjustment for the area under SUH to represent unit runoff volume. Due to similarity in shapes, several attempts have been

made in the past to use some probability density functions, (pdf) for UH and its derivation, e.g. **Gray (1961)**, **Sokolov et al.(1976)** and **Ciepielowski(1987)**. [Quoted from **Bhunya et al.(2007)**]. The pdf of the gamma and beta distributions to represent the UH shape were used by **Gottschalk et al.(1998)** and **Haktanir and Sezen(1990)** [Quoted from **Saralees Nadarajah.(2007)**].

Synthetic unit hydrograph methods

- Snyder’s method

Snyder(1938) [Quoted from **Singh. (2000)**], used five variables dependent on catchment characteristics to define a (SUH), (1) catchment lag t_L ; (2) peak discharge rate Q_p ; (3) base time t_b ; (4) width of UH at $Q=0.5Q_p$, W_{50} ;

and(5) width of UH at $Q=0.75Q_p$, W_{75} .
The expressions for t_L and Q_p are as follows:

$$t_L = C_t(LL_C)^{0.3} \quad (1)$$

$$Q_p = C_p \frac{645A}{t_L} \quad (2)$$

in which Q_p = peak discharge rate (ft^3/s); t_L = catchment lag in hours measured from the center of the effective rainfall to the peak of the SUH; L = length of the main stream in miles from the outlet to the upstream divide; L_C = distance in miles from the outlet to a point on the stream nearest to the centroid of the catchment; A = area of the catchment (square miles); and C_t and C_p are coefficients. The coefficient C_t varies from 1.8 to 2.2, generally assumed to be equal to 2. Equation (1) and (2) were obtained from the study of catchments varying in size from 26 to 26,000 km^2 (10 to 10,000 mi^2) in the United States. The expression for time to peak of the SUH, t_p , is:

$$t_p = t_L + t_r/2$$

STATISTICAL DISTRIBUTIONS

TWO PARAMETER LOG NORMAL DISTRIBUTION

The probability density function (pdf) of this distribution is given by [Quoted from Saralees Nadarajah.(2007)].

$$f(x) = \frac{1}{x\sigma_y\sqrt{2\pi}} \exp \left(-\frac{(\ln x - \mu_y)^2}{2\sigma_y^2} \right) \quad (6)$$

Where μ_y and σ_y are the mean and standard deviation of the natural logarithms of x . for $x > 0$, $-\infty < \mu_y < \infty$ and $\sigma_y > 0$. For this distribution, it is known (Johnson and Kot (1970a) that the mode is given by

$$\text{Mode} = \exp(\mu - \sigma^2) \quad (7)$$

Substituting (7) into (6), Yields:

$$t_{pq} = \frac{1}{\sqrt{2\pi}\sigma_y} \exp \left(-\frac{\sigma_y^2}{2} \right) \dots \dots \dots$$

$$\mu_y = \sigma_y^2 + \ln t_p$$

GAMMA DISTRIBUTION

Use of a two-parameter Gamma distribution for representing the UH has a long hydrologic history that started with **Edson. (1951)** [Quoted from **Singh. (2000)**], who presented a theoretical expression for the unit hydrograph assuming Q to be proportional to ($t^x e^{-yt}$) as:

$$Q = \frac{cAy(yt)^x e^{-yt}}{\Gamma(x+1)} \quad (10)$$

where Q =discharge (cfs) at time t ; A =drainage area (square miles); x and y =parameters that can be represented in terms of peak discharge; and $\Gamma(x+1)$ is the Gamma function of $(x+1)$. **Nash (1959) and Dooge (1959)**, based on the concept of n linear reservoirs with equal storage coefficient K , expressed the instantaneous UH (IUH) in the form of a Gamma distribution as:

$$q = \frac{1}{K\Gamma(n)} \left(\frac{t}{K} \right)^{n-1} e^{-t/K} \quad (11)$$

in which n and K are parameters defining the shape of the IUH; and q is depth of runoff per unit time per unit effective rainfall. These parameters have been referred to as Nash model parameters in the subsequent literature. With the suitable change of variables and applying dimensional homogeneity, Eq. (11) can be derived from Eq. (10). The area under the curve defined by Eq. (11) is unity; thus the rainfall and runoff depths are equal to unity. To obtain the



SUH, the parameters of Eq. (11) were related to catchment characteristics [Nash (1960)]. Other attempts to fit a Gamma distribution to hydrographs were by Croley (1980), Aron and White (1982), [Quoted from Saralees Nadarajah, (2007)] and Singh (1998). The procedure given by Croley (1980), to calculate n for known values of (q_p) and (t_p) requires programming to iteratively solve for n . Croley (1980) also proposed procedures to obtain a UH from other observable characteristics.

The method by Aron and White (1982) involves reading the values from a graph, in which errors are introduced. Based on their method, Bhunya (2003) listed a step-by-step procedure to obtain UH, which may be briefly described by the following equations:

$$n = 1.045 + 0.5f + 5.6f^2 + 0.3f^3 \quad (12)$$

in which

$$f = Q_p t_p / A \quad (13)$$

where Q_p is in cubic feet per second; t_p is in hours; and A is in acres. Equations (12) and (13) require careful attention for the units, and these cannot be used as such when $Q_p t_p$ is required to be computed for a value of (n) known from other sources. Hann et al. (1994) [Quoted from Bhunya (2003)] gave the following expression to calculate (n) :

$$n = 1 + 6.5 \left(\frac{Q_p t_p}{V} \right)^{1.92} \quad (14)$$

where V = total volume of effective rainfall. An equation provided by Singh (1998) to obtain the value of (n) may be written as:

$$n = 1.09 + 0.164 \beta + 6.19 \beta^2 \quad (15)$$

where $\beta = q_p t_p$ (dimensionless), in which (q_p) is the peak runoff depth per unit time per unit effective rainfall. Singh observed that the error in n obtained from Eq. (12) is (0.53%) when $(b = 0.25)$ and (0.05%) when $(b = 1.0)$. The error in n calculated from Eq. (15) decreases with increasing values of β .

APPLICATION

The applicability of the proposed method was examined for two cases, (A) and (B). In case (A), the UH was derived from the actual hydrograph; (Q_p) and (t_p) are used from the observation. In case (B), the partial data only, few observations from the actual data, were used only to find q_p and t_p .

Case A

For this case the watershed area is $(A) = 201.6 \text{ KM}^2$. The calculations for the base flow, direct runoff, and unit hydrograph are shown in the table (1) [Quoted from Salas (2006)], also the plot of the observed unit hydrograph is shown in fig(1).

Case B

A watershed area of 54 km^2 , according to Snyder model the $t_p = 5$ (hour), $q_p = 0.13$ (1/hour)

Fig. (3): SUH for case B.

RESULTS:

The results arrived can be summarized as follows.

- The gamma distribution results are closer to the actual data as shown in the fig(2) which shows Comparisons of observed unit hydrograph with SUH obtained from Gamma and Log Normal distributions. Also table(2) shows that the estimated depth of excess rainfall for the Gamma distribution is 0.9913 which is too close to 1 than Log normal distribution with value of 0.9912. Fig(3) shows the comparison between the Gamma, Log Normal distributions and the Snyder model whereas table (3) shows that the estimated depth of excess rainfall for the Gamma distribution is 0.9910 which is very close to 1 as compared to Log normal distribution which value is 0.9851.

CONCLUSIONS

The following conclusions are derived from the study:

- The pdf computed by probability distribution gave results better than the existing synthetic methods i.e methods suggested by **Snyder**(1938), and gave accurate results of the actual pdf parameters, as verified by using observed data.
- The comparison between the gamma distribution and the log normal distribution shows that the gamma distribution is more flexible than lognormal distribution since the estimated depth (0.9913), is nearest to the actual data.

REFERENCES

- **Aron, G., White, E.L., (1982).** Fitting a gamma-distribution over a synthetic unit-hydrograph. Water Resources Bulletin 18, 95–98.
- **Bhunya, P. K., Mishra, S. K. and Berndtsson, R., (2003).** Simplified of synthetic unit hydrograph. J. Hydrol. Eng. ASCE 8 (4), 226–230.
- **Bhunya, P. K., Mishra, S. K., Ojha, C. S. P. and Berndtsson, R., (2004).** Parameter estimation of Beta-distribution for unit hydrograph derivation. J. Hydrol. Eng. ASCE 9 (4), 325–332.
- **Bhunya, P.K., Berndtsson, R., and Ojha, C.S.P., 2007.** Suitability of Gamma, Chi-square, Weibull, and beta distributions as synthetic unit hydrographs. Journal of Hydrology 334, 28–38.
- **Chow, V. T., 1964.** Handbook of Applied Hydrology. Mc Graw-Hill Book Co. Inc., New York.
- **Croley II, T.E., (1980).** Gamma synthetic hydrographs. J. Hydrol. 47, Distributions, vol. 1 Houghton Mifflin Company, Boston.
- **Dooge, J.C.I., (1959).** A general theory of the unit hydrograph. J. Geophys. Res. 64 (2), 241–256.
- **Espey, W. H. Jr. and Winslow, D. E. (1974).** “Urban flood frequency characteristics.” J. Hydraul. Div., 100(2), 279–293.
- **Gray, D. M. (1961).** “Synthetic hydrographs for small drainage areas.” J. Hydraul. Div., Am. Soc. Civ. Eng., 87(4), 33–54.
- **Johnson, N.L., Kotz, S., (1970a),** first ed. Continuous Univariate Mgmt., Alexandria Univ., Egypt, 104–110.
- **Nash, J. E. (1960).** “A unit hydrograph study with particular reference to British catchments.” Proc., Inst. Civ. Eng., London, 17, 249–282.
- **Nash, J.E., (1959).** Synthetic determination of unit hydrograph parameters. J. Geophys. Res. 64 (1), 111–115.
- **Salas, (2006)** .Notes on Unit Hydrographs, Colorado State University, Department of Civil and Environmental Engineering.
- **Saralees Nadarajah, (2007).** Probability models for unit hydrograph derivation. Journal of Hydrology 334, 185–189.
- **Singh, S. K. (1998).** “Reconstructing a synthetic unit hydrograph into a Gamma distribution.” Proc., Int. Conf. on Integrated Water Resour. Mgmt., Alexandria Univ., Egypt, 104–110.
- **Singh, S. K. (2000).** “Transmuting synthetic unit hydrographs into gamma distribution.” J. Hydrologic Eng., 5(4), 380–385.
- **Singh, V. P. (1988).** Hydrologic systems: Rainfall-runoff modeling, Vol. 1, Prentice-Hall, Englewood Cliffs, N.J.



- Viessman, W. Jr., Lewis, G. L., and Knapp, J. W. (2007). Introduction to Hydrology, 5rd Ed.,
- Yue, S., Taha, B.M.J., Bobee, B., Legendre, P., and Bruneau, P., (2002). Approach for describing statistical properties of flood hydrograph. J. Hydrol. Eng. ASCE 7 (2), 147–153.
- Soil Conservation Service _SCS_. (1972). SCS national engineering handbook, Section 4: Hydrology, U.S. Dept. of Agriculture, Washington, D.C.

Table (1): The unit hydrograph calculations for case study (A)[salas (2006)]

Time (hr)	Total Flow (m ³ /s)	Base Flow (m ³ /s)	Direct runoff Qt (m ³ /s)	Unit hydrograph (m ³ /s)
0	125	--	--	--
1	100	100	0	0
2	150	100	50	12.5
3	250	100	150	37.50
4	415	100	315	78.75
5	600	100	500	125.00
6	515	100	415	103.75
7	400	100	300	75.00
8	300	100	200	50.00
9	225	100	125	31.25
10	175	100	75	18.75
11	150	100	50	12.5
12	135	100	35	8.75
13	125	100	25	6.25
14	100	100	0	0
15	100	100	0	0
			$\sum Q_t = 2240$	$\sum u_t = 560$

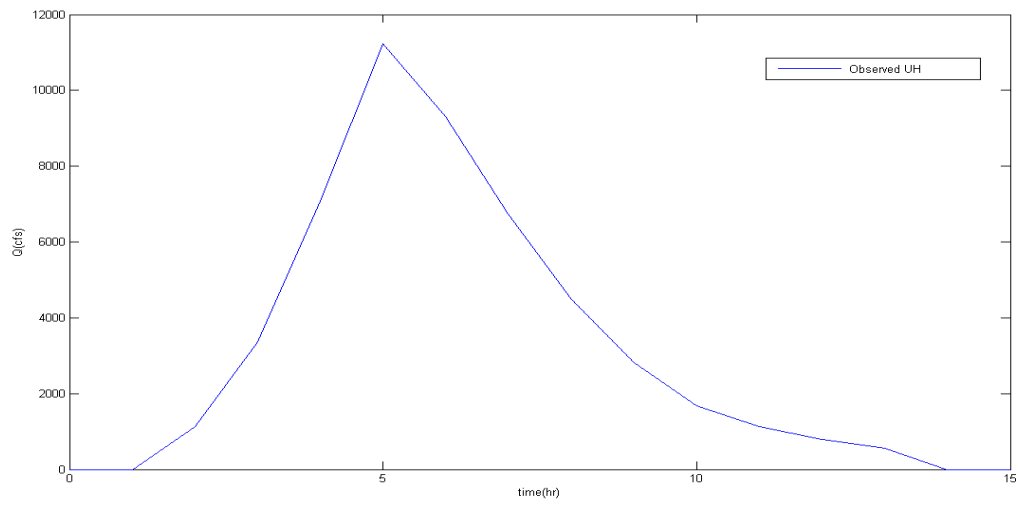


Fig. (1): Unit Hydrograph from observed data table1 [salas(2006)].

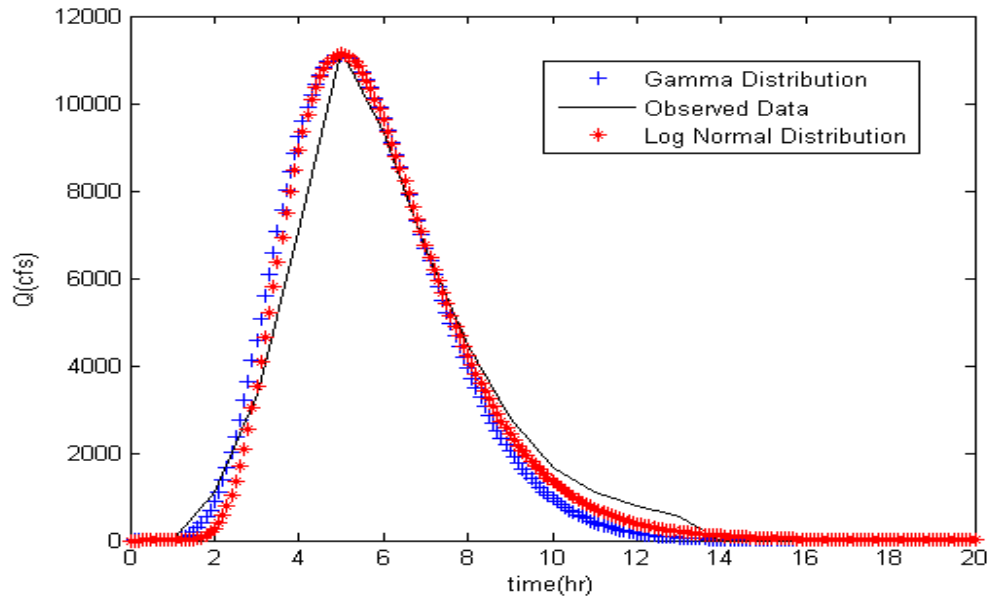


Fig. (2): Comparisons of observed unit hydrograph with SUH obtained from Gamma and Log Normal distributions

Table (2): Estimated depth of excess rainfall over the watershed area using different methods for case (A).

Type of method	Average depth (in)
Observed data	1
Gamma distribution	0.9913
Log normal distribution	0.9912

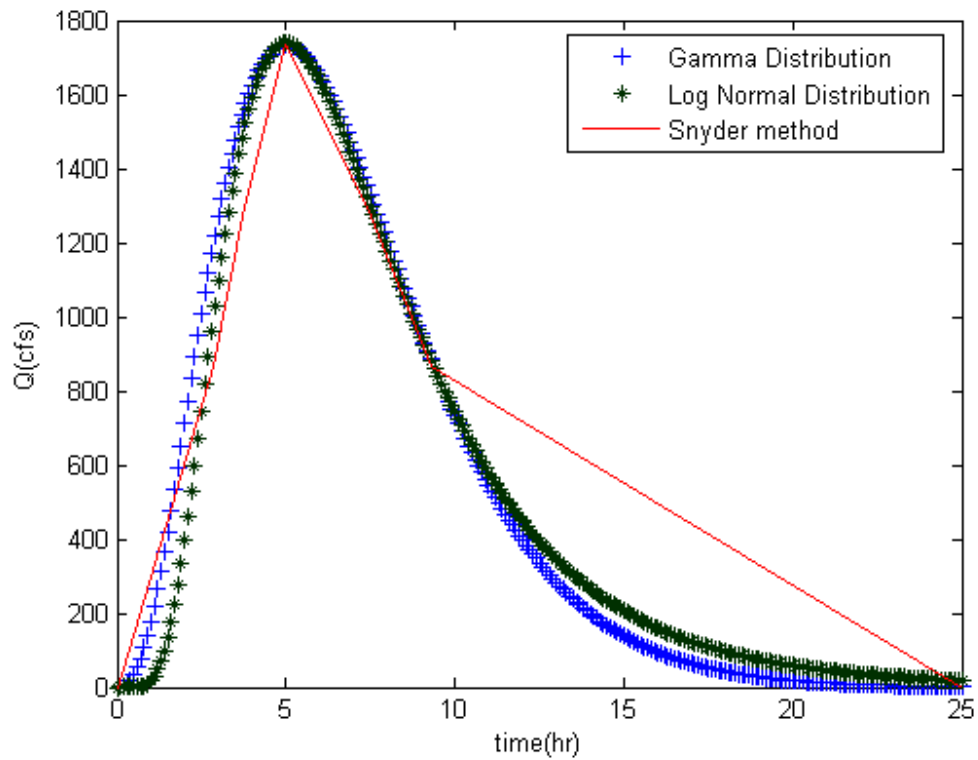


Fig. (3): Comparisons of Snyder unit hydrograph with SUH obtained from Gamma and Log Normal distributions

Table (3): Estimated depth of excess rainfall over the watershed area for different method.

Type of method	Average depth (in)
Snyder method	1.231
Gamma distribution	0.9910
Log normal distribution	0.9851



ORGANOCLAY FOR ADSORPTION OF BINARY SYSTEM OF POLLUTANTS FROM WASTEWATER

Abbass H. Sulaymon
College of Engineering
University of Baghdad

Waleed M. S. Kassim
College of Engineering
University of Baghdad

Mohsin Jasim Nasir
Foundation of Technical
Institutes

ABSTRACT

single and binary competitive sorption of phenol and p-nitrophenol onto clay modified with quaternary ammonium (Hexadecyltrimethyl ammonium) was investigated to obtain the adsorption isotherms constants for each solutes. The modified clay was prepared from blending of local bentonite with quaternary ammonium . The organoclay was characterized by cation exchange capacity, and surface area. The results show that paranitrophenol is being adsorbed faster than phenol . The experimental data for each solute was fitted well with the Freundlich isotherm model for single solute and with the combination of Freundlich-Langmuier model for binary system .

الخلاصة

تم دراسة الامتزاز لنظام احادي والامتزاز التنافسي لنظام ثنائي للفينول و بارا- نايترافينول على سطح الطين المعامل بالامين الرباعي للحصول على ثوابت الامتزاز لكل ملوث . تم تحضير الطين العضوي من مزج البنتونيت المحلي مع الامين الرباعي . ومن ثم فحص الطين العضوي المحضر عن طريق قياس قابلية الطين العضوي للتبادل الايوني الموجب وكذلك فحص المساحة السطحية . بينت النتائج ان بارا- نايترافينول يمتز اسرع من الفينول وكانت النتائج العملية مطابقة لمعادلة فريندلج بالنسبة للأنظمة المنفردة ولمعادلة فريندلج لانكماير للأنظمة الثنائية .

KEY WORDS

Organoclay, adsorption, Freundlich model, wastewater

INTRODUCTION

In recent years, there were a wide range of hazardous waste disposal and contaminated of water in which affect on human health and environmental. The transport of these compounds in the environment is a complex process, depending on such factors as solubility, octanol-water partition coefficient, chemical and biological reactivity. Adsorption process is widely used for removing organic compounds from water. Phenolic compounds are toxic if adsorbed through the skin and may result in death. Contact with the skin also causes dangerous and painful burns. Immediate washing of the skin with ethanol solution and warm water usually removes the phenolic compounds without serious consequences. Phenol and its derivatives induces toxic effect for fish and aquatic life. They induce genotoxic, carcinogenic, immunotoxic, hematological and physiological effects and have a high bioaccumulation rate along the food chain due to its lipophilicity. Thus phenol pollution represents a threat against natural environment and also to human health. When phenol is present in the aquatic environment, fish food consumption, mean weight and fertility are significantly reduced. Excessive exposure may affect the brain, digestive system, eye, heart, kidney, liver, lung, peripheral nerve, skin and the unborn child. The Environment agency aims to ensure that environmental exposures are too low to cause such effects. [Gad and Saad, 2008].

Clay is a representative of 2:1 layered phyllosilicates. These layers are built from two tetrahedral and octahedral cations can be replaced by lower valence cations, such as Al^{+3} and Fe^{+2} or Mg^{+2} respectively. The excessive negative charge of these layers is compensated by metal cations (Na^{+1} , K^{+1} , Ca^{+2} and Mg^{+2}) in the interlayer space, which can be exchanged with various cations, such as quaternary ammonium salts forming the modified clay (organoclay). [Jaynes and Boyd, 1991].

Natural clay is ineffective sorbents for removal of toxic organic compounds from environment. The inorganic exchange cations of natural clays are strongly hydrate in water, producing a hydrophilic environment at the clay surface. The replacement of inorganic exchange cations with organic cations of alkyl hydrocarbon yields organoclay with organophilic properties [Boyd et al, 1988].

Boyd and Jaynes, (1992) divided organoclays into two types, organophilic and adsorptive. Organophilic clays are formed using large alkyl cations, and adsorptive organoclays are formed using small alkyl or small aromatic organic cations. Smith and Galan, (1995), found that organoclays prepared using small organic cations have internal surfaces which can act as hydrocarbon adsorption sites. The objectives of this study are to modify the natural clay to organoclay and to investigate the competitive adsorption between phenol and p-nitrophenol onto prepared organoclay.

- MATERIALS AND METHOD

Adsorbates

Phenolic compounds namely as; phenol and p-nitrophenol were used as adsorbates. These physical properties are listed in table (1).

- Adsorbent (Organoclay)

The organoclay was prepared by adding the required quantity of hexadecyltrimethyl ammonium chloride solution (25% wt./vol.) to the desired quantity of bentonite in a stainless steel container. The bentonite used in this study was a local bentonite in powder form (particle size of 0.075mm) calcium type. It was supplied by the State Company of Geological Survey and Mining (Baghdad). The resulting paste was then introduced into the meat grinder to achieve good mixing. The product was dried in the electrical oven at 85 °C for 48 hours and then ground by agate mortar and screened to desirable particle size of (0.075mm). The physical properties of the prepared



organoclay was measured at the laboratories of the Ministry of Industry and Minerals (Ibn Sina State Company) and at the Ministry of Oil (Institute of Oil Training and Development). The results are presented in Table (2).

Procedure

A series of batch experiments were carried out to determine the adsorption isotherms of Ph and pnp solutions onto organoclay with pH of 6.5-6.8. A certain amount of organoclay (0.05, 0.1, 0.15, 0.2,0.5 g) was placed into 100ml contaminant solution at concentration of 0.05kg/m³ for each solute . The adsorption experiments were conducted at constant shaking at room temperature for 30 hour to achieve equilibrium concentrations. Then, the solutions were filtrated, and their concentration were determined by UV-spectrophotometer at college of engineering, Baghdad university (Model UV-GENESYETM 10) at $\lambda_{max}=270nm$ and $\lambda_{max}=317nm$ for ph and pnp respectively. The adsorption capacity q_e (kg/kg) of each solute onto organoclay was calculated by mass balance relation :

$$q_e = \frac{V(C_o - C_e)}{W} \quad (1)$$

Where C_o and C_e are the initial and equilibrium concentration of adsorbate respectively (kg/m³), V is the volume of solution and W is the weight of the organoclay used (kg).

RESULTS AND DISCUSSION

Characterization of Modified Clay

In order to examine the structural difference of the clay before and after modification with a quaternary amine, clay and their modified organic derivatives are characterized using ordinary as well as modern characterization tools which include determination of cation exchange capacity, surface area and total organic carbon (Hasmukh et al., 2006) as described below:

Cation Exchange Capacity

The clays are characterized by their cation exchange capacities , which can vary widely and depend on source and type of clay.

Cation exchange capacity (CEC) is represented by the weight ratio of amine to bentonite. The cation exchange capacity for Iraqi bentonite is about 80 meq/100gm bentonite (according to the specifications of the supplier) . The weight ratio of amine to bentonite was calculated from its relation with cation exchange capacity percentage. The CEC was calculated according to the following equation [Mousavi et al., 2006] :

$$\frac{\text{Amount of amine, g}}{100g \text{ bentonite}} = \frac{\text{MW. of amine, g/g.mole} \times \text{CEC, meq/100g} \times \% \text{CEC}}{1000} \quad (2)$$

where 80 meq/100gm bentonite represents 100% CEC and molecular weight of amine is 320 g/g mole . The appropriate equation to satisfy this above equation is found to be:

$$\begin{aligned} \text{g amine /100g bentonite} &= 0.256 \% \text{CEC} \\ \text{or : } Y &= 0.256 X \end{aligned} \quad (3)$$

Where : Y is g amine/100g clay and X is %CEC .The results are tabulated in Table (3) :

To choose the best ratio of amine to clay for maximum removal efficiency, a shaker speed of 200rpm was run for 10 hours, containing 0.5g of prepared organoclays (given in Table 2) and 100ml of water polluted with 50ppm of each solute.

The results are depicted in Table (4) indicating the large effect of amine to bentonite ratio on the removal efficiency and as can be seen an increase of the ratio increases the removal efficiency , reaching a maximum value of 35g/100g clay for each solute at 136.72 %CEC . Above this weight ratio no effect on removal

efficiency is obtained ,where the effluent concentrations of Ph and pnp decrease to 8, 5.8 and mg/l respectively.

Alberto et al., (2002) characterized the organophilic clay used in the solidification/stabilization of hazardous waste at %CEC of 150 meq/100g. In this cement-based stabilization/solidification processes hae been used for about two decades for the immobilization organics pollutants in hazardous wastes and contaminated soils.

SURFACE AREA

The surface area of natural clay is found to be 65 m²/g . For an organoclay this decreased to 37.6 m²/g (Institute of Oil Training and Development). Because organoclay is more aggregated than natural clay. The low value of the surface area found with the organoclay was because measurements were made at the external surface only, no internal surface area was accessible to nitrogen .This reason was stated by [Jaynes and Vance,1996]. This may be also attributed to the nearly total blocking of the micropores by the surfactant loaded material.

Estimation of Adsorption Isotherms Constants

The adsorption of a single and binary compound systems of phenol and paranitrophenol onto organoclay in batch experiments were conducted with initial concentration of (0.05 kg/m³) and particle size of (0.075 mm)at room temperature in order to determine the isotherms constants for each system using different models as follows: (Nasir,2010)

- **Freundlich model**

$$q_e = KC_e^{1/n} \quad (4)$$

- **Langmuir model**

$$q_e = \frac{q_m b C_e}{1 + b C_e} \quad (5)$$

- **Radk-Prausnitz model**

$$q_e = \frac{K_{RP} C_e}{1 + \left(\frac{K_{RP}}{F_{RP}} \right) C_e^{1-N_{RP}}} \quad (6)$$

- **Combination of Langmuir-Freundlich model**

$$q_{e,i} = \frac{q_{m,i} b_i C_{e,i}^{1/n_i}}{1 + \sum_{i=1}^N b_i C_{e,i}^{1/n_i}} \quad (7)$$

Single Component System

The adsorption isotherms for single component systems of phenol and p-nitrophenol onto organoclay are shown in figures 1 and 2

Binary Component System

The adsorption isotherms for binary system (Ph-pnp) onto organoclay is shown in figure (3)

The parameters for each model were obtained using non-linear statistical fit of the equations to the experimental data .The Freundlich isotherm model was fitted with experimental data for each solute as a single , while for binary component systems the combination of Langmuir-Freundlich model was used. All parameters with correlation coefficients are summarized in Table 5.



From the figures and tables for single and binary component systems, It can be seen :

- equilibrium isotherm for each solute is of favourable type (i.e somewhat convex upward) and relatively high adsorbent loading were obtained at low concentrations of solute in water.
- The Freundlich model gives the best fit of the experimental data for single solute systems with high correlation coefficients. The equilibrium data for binary component systems were described successfully with Langmuir-Freundlich combination model for competitive adsorption.
- The q_e values for the binary systems were less than those in single systems due to competition between the solutes
- The constant parameters of the Freundlich model were found to be as (2.51 and 2.33) for n and as (0.314 and 0.559) for k for ph and pnp respectively .Where k is related primarily to the capacity of the adsorbent, and n is a function of the strength of adsorption. For fixed values of C_e and n the larger the value of k , the larger capacity (q_e). For fixed values of k and C_e , the smaller the value of n , the stronger the adsorption bond. The high value of k and the lower value of n indicated that the sorption capacity of organoclay for p-nitrophenol was very high compared with Phenol.
- Values of octanol-water coefficient (K_{ow}) (Table 1) shows that phenol is more hydrophilic than p-nitrophenol . This is due to the adverse effect of the OH group on adsorption of phenol, which may be attributed to the capability of this group to form hydrogen bonding with water and then renders the compound less liable to be adsorbed in comparison with pnp.
- The paranitrophenol is adsorbed to greater extent in comparison with phenol itself. This is attributed to the prevention of the formation of

hydrogen bond either by forming an internal hydrogenbond between OH and the substitute group or by offering steric hinderance ,thereby increasing the solvophobic nature (i.e: decreasing solubility) as well as sorption capacity of the solute.

- The adsorption capacity can be compared for the three solutes in terms of (q_e). The maximum adsorptive capacities were (0.03 and 0.0344 kg/kg) for ph and pnp respectively, in which capacity order of $pnp > Ph$.
- There is a weak competition in binary systems in the adsorption capacity of solute in the presence of others , whereas the uptake of phenol is very much reduced by the presence of other solute .
- The competition between solutes in the binary solute systems reduced the sorbed amount of each solute compared with that in the single-solute system .

CONCLUSIONS

- Modification of natural clay to organoclay is resulting through the exchange of quaternary amine (hexadecyltrimethyl ammonium $HDTMA^+$) cation in place of Ca^+ at the surface of bentonite . This modification has been shown by different parameters. The CEC% for natural clay (80) increased to (136.71) for modified clay. The surface area decreased from 65 to 37.6 m^2 /g for natural and modified clay respectively.
- The order of adsorption capacity for binary systems onto organoclay are found to be of $pnp > ph$. This order indicates that substituted phenols are adsorbed to greater extent in comparison with phenol itself.
- The competition between solutes in binary sorption systems caused reduction in the sorbed amount of each solute

compared with that in single solute system.

- The higher adsorption capacity of pnp onto organoclay may be explained by its lower solubility, higher molecular weight and higher octanol-water coefficient in comparison with phenol.

REFERENCES

- Alberto U, Paul L.B., and Neville G.P., (2002) "The influence of pH and temperature changes on the adsorption behaviour of organophilic clays used in the stabilization/solidification of hazardous waste" J. Environmental Engineering Science, Vol. 1, p:123-133.
- Agency for Toxic Substances and Disease Registry ,(1992) Toxicological Profile for dichlorophenol .Atlanta ,Georgia:US Department of Health and Human Services, DHHS (ATSDR) publication. No.TP-91/14.
- Boyd,S.A.,Lee,J. F. and Mortland, M.M.,(1988), "Attenuating organic contaminant mobility by soil modification ", Vol : 333, 345-347.
- Boyd S.A. and Jaynes, W.F. (1992) Role of layer charge in organic contaminant sorption by organoclays . In layer Charge Characteristics of Clays, pre-Meeting Workshope CMS and SSSA. Minneapolis , Minnesota, University of Saskatchewan, Saskatchewan,89-120
- Gad S .and Saad A.S (2008)," Effect of environmental pollution by phenol on some physiological parameters of oreochromis niloticus" Globel Veterinaria,IDOSI Publications, Vol.2, No.6, pp312-319.
- Hasmukh P. A., Rajesh S.S., Hari B. C., and Raksh V. J., (2006) " Nanoclays for polymer nano-composites, paints, ink, greases and cosmetics formulations, drug delivery vehicle and waste water treatment" Indian Academy of Science,Vol.29, No.2, pp 133-145.
- Jaynes,W. F., and Vance,G.F.,(1996), " BTEX sorption by organoclays , cosorptive enhancement and equivalence of interlayer complexes", Soil Science Society American Journal, Vol.60,No.6, pp 1742-1749.
- Jaynes W.F. and Boyd S.A. (1991) " Hydrophobicity of siloxane surface in smectites as revealed by aromatic hydrocarbon adsorption from water" Clays and Clays Minerals, 39,428-436.
- Mousavi, S.M., Alemzadeh, I. and Vossoughi,M (2006),"Use of modified bentonite for phenolic adsorption treatment of olive oil mill wastewater" Iranian Journal of Science and Technology, Transaction B, Engineering,Vol.30,No.B5.
- Nasir M.J., (2010) " Competitive Adsorption of Multi-Organic compounds onto organoclay from simulated wastewater" Ph.D. Thesis, University of Baghdad, College of Engineering.
- Smith, J.A. and Galan, A. (1995) " Sorption of nonionic organic contaminants to single and dual organic cations bentonites from water "Environmental Science and Technology , 29, 685-692



List of Symbols

<u>Symbols</u>	<u>Descriptions</u>
b	Langmuir constant, m^3/kg
C_o	Initial concentration, kg/m^3
C_e	Equilibrium concentration, kg/m^3
F_{RP}	Radk-Prausnitz constant
k	Freundlich adsorption isotherm capacity constant, $(\text{mg}/\text{g}, (\text{mg}/\text{l})^{-1/n})$
K_{RP}	Radk-Prausnitz constant
MW	Molecular weight
n	Freundlich adsorption isotherm intensity constant
N_{RP}	Radk-Prausnitz constant
Ph	Phenol
pnp	paranitrophenol
q_e	Internal concentration of solute in particle at equilibrium, kg/kg
q_m	Adsorption equilibrium constant defined by Lngmuir equation, kg/kg
R	Correlation coefficient
W	Weight of organoclay, kg

Table 1 Main properties of adsorbates used in this study [Agency for Toxic Substances and Disease Registry,1992]

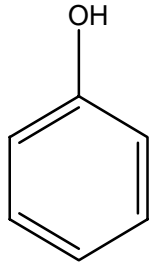
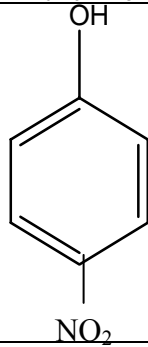
Property	Phenol	Paranitrophenol
Symbol	Ph	pnp
Formula	$\text{C}_6\text{H}_5\text{OH}$	$\text{C}_6\text{H}_5\text{NO}_3$
Structure		
Molecular weight, g/mole	94.11	139
Solubility in water (at 20° C), mg/l	86000	17000
Octanal-Water ,Log (K_{ow})	1.5	1.91
UV wave length (nm)	270	317

Table 2 Characteristics of powdered organoclay (Ibn Sina State Company and Ministry of oil)

Characteristic	Value		Test Location
	Bentonite	Organoclay	
Particle size,mm	0.075	0.75	University of Baghdad
Moisture content, %	7.2	0.36	Ibn Sina Company
Bulk density, kg/m ³	945	1025	Ibn Sina Company
Surface area, m ² /g	65	37.6	Ministry of oil
%CEC, meq/100g	80	136.72	University of Baghdad

Table 3 : Amine/100g bentonite as function of %CEC

%CEC	78.12	97.66	117.18	136.72	156.25	175.8	195.3
Amine/100g bentonite	20	25	30	35	40	45	50

Table 4 : Effect of different weight ratio of amine to bentonite on removal efficiency

Weight Ratio g	phenol C _o =50mg/l		p-nitrophenol C _o =50mg/l	
	Effluent Conc. mg/l	Removal %	Effluent Conc.mg/l	Removal %
20	34	32	30.2	39.6
25	25.8	48.4	21.6	56.8
30	17.2	65.6	13.7	72.6
35	8	84	5.8	88.4
40	10.1	79.8	7.75	84.5

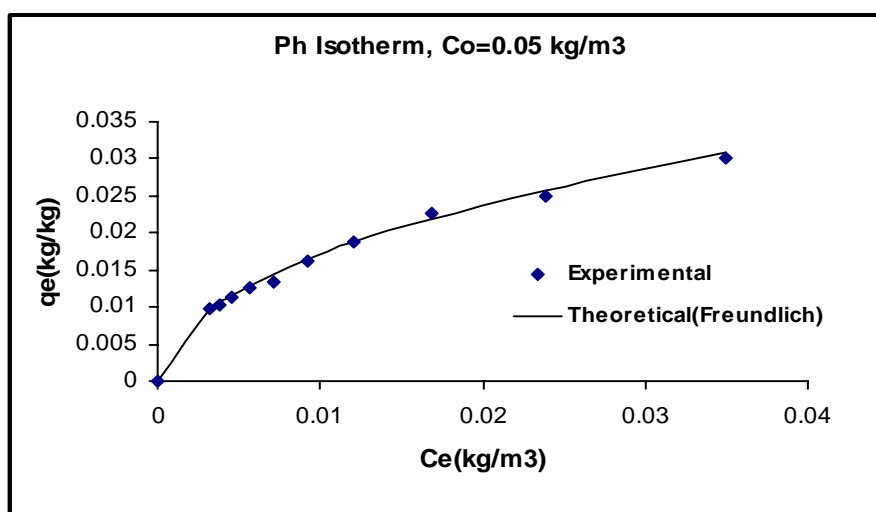


Fig. 1 : adsorption isotherm of phenol onto organoclay

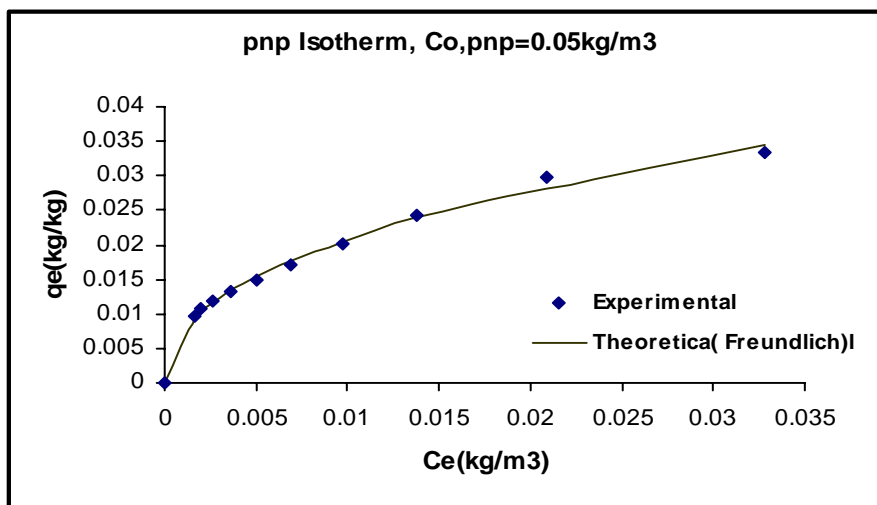


Fig. 2 : adsorption isotherm of p-nitrophenol onto organoclay

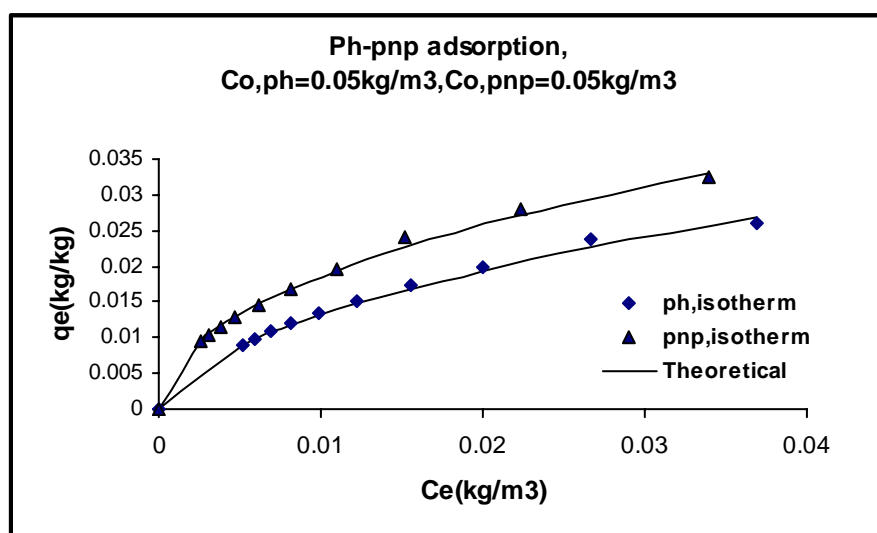


Fig. 3 adsorption isotherm of (Ph-pnp) as binary system onto organoclay

Table 5 :Parameters of single and binary system solutes isotherms for phenol and Paranitrophenol

Model	parameters	phenol	p-nitrophenol
Single Solute			
Freundlich Equation(4)	k	0.314	0.559
	n	2.51	2.33
	R ²	0.9990	0.9992
Langimur Equation(5)	q _m	0.397	0.391
	b	8.51	13.58
	R ²	0.9964	0.9831
Radk-Prausnitz Equation(6)	K _{RP}	15.95	22.15
	F _{RP}	0.48	0.56
	N _{RP}	0.4	0.43
	R ²	0.9942	0.9990
Binary system			
Model	parameters	Ph-pnp	
		Ph	pnp
Combination of Langimuir-Frendlich Equation(7)	q _m	0.391	0.384
	b	5.38	15
	n	1.87	0.577
	R ²	0.998	0.9932



FINITE ELEMENT METHOD FOR INCOMPRESSIBLE VISCOELASTIC MATERIALS

Montadher A. Muhammed
lecturer
Material Engineer
Najaf Technical Institute

ABSTRACT

A numerical method (F.E.) was derived for incompressible viscoelastic materials, the aging and environmental phenomena especially the temperature effect was considered in this method. A treatment of incompressibility was made for all permissible values of Poisson's ratio. A mechanical model represents the incompressible viscoelastic materials and so the properties can be derived using the Laplace transformations technique. A comparison was made with the other methods interested with viscoelastic materials by applying the method on a cylinder of viscoelastic material surrounding by a steel casing and subjected to a constant internal pressure, as well as a comparison with another viscoelastic method and for Asphalt Concrete problem exposed to constant pressure (vehicles load) was done.

The obtained results were very convenient, as well as, a large time steps can be taken than others methods.

الخلاصة

تم اشتقاق أسلوب حل عددي (F.E.M) للمواد اللزجة المرنة غير القابلة للانضغاط، تم إدخال ظاهرة التقادم و الظروف البيئية وخاصة تأثير درجات الحرارة، إضافة إلى معالجة خاصية عدم الانضغاطية لكل القيم المسموحة من نسبة بويسن. تم اعتماد نموذج ميكانيكي يمثل المواد اللزجة المرنة غير القابلة للانضغاط واشتقاق خواص المادة منه باستخدام تقنية لابلاس. تم مقارنة أسلوب الحل العددي مع أساليب حل أخرى للمواد اللزجة-المرنة، وتطبيق ذلك على اسطوانة لزجة-مرنة ذات غلاف خارجي مرن (من الفولاذ) مع وجود ضغط ثابت، إضافة إلى مقارنة مع أسلوب حل لزج-مرن آخر لحالة الإسفلت المتعرض لضغط ثابت (وزن المركبات). أظهرت النتائج تقارب كبير مع باقي الأساليب مع وجود ميزة استخدام خطوات اكبر للزمن.

KEY WORDS/ Viscoelastic, Finite Element, Aging Effect, Incompressibility

INTRODUCTION

The finite element method for many years was used to solve problems depending on the Elastic and Quasi-Elastic theories, few researcher used the finite element depending on the Viscoelastic theories, but the techniques still in short of the aging phenomena.

In this work the aging factor was applied depended on the temperature effect (physical aging)

For Viscoelastic materials aging may be due to a large number of causes: oxidation (with or without the stimulation of light); gradual loss of plasticizer or other low molecular weight additives [Boyer 1998]. Such chemical or physicochemical degradation processes are not considered in this research and only aging processes of a physical nature will be treated (i.e the type of aging that is due to inherent instability of the amorphous glassy state).

Physical aging is a reversible process in general, i.e. by re-heating the aged material to $T > T_g$ The original state of thermodynamic equilibrium is recovered and a renewed cooling to temperature $T < T_g$ will induce the same aging effects as before.

Temperature effects are extremely important in the analysis of viscoelasticity, temperature has three effects [Oza 2003]:

- temperature change causes thermal strains, which must be combined with mechanical strains,

- material module have different values at different temperatures,

- heat flow may occur.

Williams, Landel and Ferry [David Roylance 2001] have proposed that the variations in relaxation time are not primarily due to thermal activation, but to thermal expansion, i.e. the expansion of free volume V_f with increasing temperatures and by using an equation proposed by Doolittle. These authors derived the famous WLF equation:

$$\log a_T = -\frac{c_1(T - T_s)}{c_2 + T - T_s} \quad (1)$$

Where T_s is the reference temperature (which represent material's specific constant for the position of the glass transition of the material).

C_1 , C_2 are constants relating to the choice of reference temperature.

Which will be used in the range of glass transition temperatures to coverage the Physical Aging phenomena.

The finite element technique, which was used to calculate displacements and stress for the elastic case, has been extended to provide analysis capability for the viscoelastic case in this research.

Many researcher have been used different methods to calculate displacement, stress and strain for viscoelastic materials.

(Ghasak 2008) studied the rutting problem for Asphalt concrete which subjected to repeated axle loading using both elastic and viscoelastic model by finite element software (ANSYS 9). He found that the difference between the two approaches (Elastic; Viscoelastic) is about (12%). The rut depth was calculated and compared with two considerable models (Yassoub and Amjad models).

(O.C.Zienckiewicz 1968) developed a completely general method of numerical viscoelastic stress analysis with constant or temperature variable properties. He proved that numerical methods of elastic analysis (and in particular the finite element method) can be extended to deal with wide range of viscoelastic problems of the quasi-static type.

The method is checked against some known solutions. Examples from the field of propellant technology, concrete and rock behaviors are included.

The processes of numerical analysis have been incorporated into two-dimensional finite element analysis program.

An example of propellant is taken as cylinder of viscoelastic material which represents the rocket grain, surrounded by a steel casing and subjected to constant internal pressure P . Contours of maximum compressive stress is plotted at various time

steps and the same contours is plotted but with a moving (burning up) inner boundary.

(Lakes, 2006) formulated a viscoelastic problem in a way that allows to the use of higher order differential equation solution techniques. In this literature the advantages of using Runge-Kutta integration formulae are indicated.

Examples for plane strain problem are developed under the assumption of:

- Linear viscoelasticity with a hereditary integral form of the stress – strain relation.
- Validity of the reduced time hypothesis.
- Bulk modulus constant in time.
- Homogeneous, isotropic material.

This formulation has the advantage that the increase in computational effect for each time step using the higher order formulae is, generally, more than offset by the increase in magnitude of the time step that can be used. This advantage is demonstrated with an example. Also with this approach a means of estimating the error involved in the integration is available. The process described in this literature is valid for a more general form of material representation.

An example of reinforced viscoelastic cylinder subject to constant internal pressure P is indicated here by using the fourth order Runge-Kutta method. Distribution of tangential and radial stress is plotted against the ratio of radius to outer radius for several time steps.

(Rogers 1988) solved stress analysis problems for linear Viscoelastic materials on basis of integral operator stress – strain relations by using the method of simple finite – difference numerical integration . They recommend to take the integral from 0 to t and consider the material is undisturbed for $t < 0$.

(Taylor and Pister 1990) developed a computational algorithm for the solution of uncoupled , quasi – static boundary value problem for a linear Viscoelastic solids undergoing thermal mechanical deformation, they showed that the stresses at a high temperature will decrease faster than at a lower temperature.

In this research a computational method based on finite element technique with using isoparametric element and local coordinate (natural coordinate) will be applied ,viscoelastic solution is obtained using Laplace transform technique.

As an applications of the method , a problem which studied by Zienkiewicz is examined ,as well as, a comparison with another viscoelastic method and for Asphalt Concrete problem exposed to constant pressure (vehicles load) was done, in order to know the efficiency of the procedure and make a comparison with the other methods.

MATHEMATICAL MODEL

Material Representation

For a viscoelastic material , a model can be used to relate components of strain to components of stress.

For incompressible Viscoelastic solid material , the more convenient famous model to represent is called “three parameter model”[Amada 1997], generally, this model used to represent most standard linear Viscoelastic solids as shown in Fig1.

This model which is consistently used in subsequent applications, it is useful to establish systematically its relaxation modules G and creep compliance J using Laplace transform techniques [Gibiansky 1997] as following in **Table 1** :

$$\bar{\varepsilon}(t) = \tilde{J} \bar{\sigma} \quad (2)$$

$$\tilde{J}(s) = \frac{1}{E_1} + \frac{1}{E_2 + s\mu} \quad (3)$$

$$\tilde{G}(s) = \frac{1}{\tilde{J}(s)} = E_1 \frac{s + E_2 / \mu}{s + (1 / \mu)(E_1 + E_2)} \quad (4)$$

Where: ε -strain σ -stress E -elasticity modulus μ -viscosity s - Laplace transform factor.

Applying the inverse Laplace transform and simplifying eqn (3),(4) can be reduced to :

$$J(t) = \left[\frac{E_1 + E_2}{E_1 E_2} - \frac{1}{E_2} \text{EXP} \left(-\frac{E_2}{\mu} t \right) \right] \quad (5)$$

$$G(t) = \left[\frac{E_1 E_2}{E_1 + E_2} - E_1 \text{EXP} \left(-\frac{E_1 + E_2}{\mu} t \right) \right] \quad (6)$$

METHOD OF SOLUTION

The displacement based finite element method is one such numerical procedure ,the effectiveness of the method is due to its conceptual simplicity, assuming that the nodal point displacement of the finite element mesh completely specify the displacement in the body.

This finite element technique , which has demonstrated to provide an excellent analysis method for elastic case , has been extended to provide analysis capability for the Viscoelastic case in this research .

The relation of stress- strain for plane strain case are [Hughes 1987] :

$$\varepsilon_{xx} = \frac{1}{E} (\sigma_{xx} - \nu (\sigma_{yy} + \sigma_{zz})) \quad (7)$$

$$\varepsilon_{yy} = \frac{1}{E} (\sigma_{yy} - \nu (\sigma_{xx} + \sigma_{zz})) \quad (8)$$

$$\varepsilon_{xy} = \frac{2(1+\nu)}{E} \sigma_{xy} \quad (9)$$

$$\text{But : } \nu = \frac{1 - \frac{2G}{K}}{2 + \frac{2G}{K}} \quad (10)$$

$$E = \frac{9K}{1 + \frac{3K}{G}} \quad (11)$$

Then the stress matrix {D}(matrix of properties) can be obtained from eqns (7), (8),(9) in term of relaxation G and bulk K moduli.

$$[\sigma] = [D] [\varepsilon] \quad (12)$$

$$[D] = \begin{bmatrix} K + \frac{4}{3}G & K - \frac{2}{3}G & 0 \\ K - \frac{2}{3}G & K + \frac{4}{3}G & 0 \\ 0 & 0 & G \end{bmatrix} \quad (13)$$

The global coordinate {X} of the node in terms of local coordinate (ξ, η) and displacement field { δ } in isoparametric element is [Zienkiewicz 1989] :

$$\{X\} = [N] \{X_{ii}\} = \begin{bmatrix} x(\xi, \eta) \\ y(\xi, \eta) \end{bmatrix} \quad (14)$$

$$\{\delta\} = [N] \{\delta_i\} = \sum_{i=1}^n \delta_i N_i \quad (15)$$

{N} is a matrix of shape function, which is a function of local coordinate ξ and η .

By differentiation of shape function with respect to global coordinate we can obtain strain quantities. This can be done by a transformation using Jacobian matrix {J} which can be obtained by differentiate Eqn 14 using chain rule.

$$\{J\} = \sum_{i=1}^n \begin{bmatrix} \frac{\partial N_i}{\partial \eta} x_i & \frac{\partial N_i}{\partial \eta} y_i \\ \frac{\partial N_i}{\partial \xi} x_i & \frac{\partial N_i}{\partial \xi} y_i \end{bmatrix} \quad (16)$$

Then local coordinates can be obtained as:

$$[J]^{-1} \begin{bmatrix} d\xi \\ d\eta \end{bmatrix} \begin{bmatrix} dx \\ dy \end{bmatrix} \quad (17)$$

For plane strain case the relation between strain and displacement is [Hughes 1987]

$$\varepsilon_{xx} = \frac{\partial u}{\partial x} \quad (18)$$

$$\varepsilon_{yy} = \frac{\partial v}{\partial y} \quad (19)$$

$$\epsilon_{xy} = \frac{\partial u}{\partial y} + \frac{\partial v}{\partial x} \quad (20)$$

Then the strain matrix $\{B\}$ is obtained by writing eqns (18),(19),(20) in terms of matrix notation and using the following relations [Saabye 2000]:

$$\frac{\partial u}{\partial x} = \sum_{i=1}^n \frac{\partial N_i}{\partial x} u_i \quad (21)$$

$$\frac{\partial v}{\partial y} = \sum_{i=1}^n \frac{\partial N_i}{\partial y} v_i \quad (22)$$

$$[B] = \begin{bmatrix} \frac{\partial N_i}{\partial x} & 0 \\ 0 & \frac{\partial N_i}{\partial y} \\ \frac{\partial N_i}{\partial y} & \frac{\partial N_i}{\partial x} \end{bmatrix} \quad (23)$$

It is incorrect to vary only stress matrix $\{D\}$ with time (the Quasi – static solution) since properties of viscoelastic material varies with time, but it is convenient to differentiate this matrix with respect to time depending on the superposition theory of linear viscoelasticity :

So that :

$$\left[\frac{\partial D}{\partial t'} \right] = - \frac{\partial G(\tau - \tau')}{\partial t'} \begin{bmatrix} \frac{4}{3} & -\frac{2}{3} & 0 \\ -\frac{2}{3} & \frac{4}{3} & 0 \\ 0 & 0 & 1 \end{bmatrix} = \left\{ \bar{D} \right\} \quad (24)$$

$\tau - \tau'$ is the current and past shifted time respectively which can be calculated from WLF eqn No.1.

From the chosen model in Fig.1 and for the incompressible linear viscoelastic material undergoes environmental temperature change, the total stress will expected to be as:

$$\sigma_{total} = \sigma_{elastic} + \sigma_{viscoelastic} + \sigma_{thermal} \quad (25)$$

So that:

$$\{\sigma(t)\} = [D] \{\epsilon(t)\} + \int_0^t [D] \{\dot{\epsilon}(t)\} dt - 3\alpha K [T(x,t) - T(x,0)] \quad (26)$$

α - thermal expansion which is constant in time .

By minimizing the equation of potential energy we can solve Eqn.- 26

The minimum potential energy M can be expressed as [Bath 1995]:

$$M = \frac{1}{2} \int_v [\sigma(t)]^T \epsilon(t) dv - \int_v [\delta]^T F_v dv - \int_s [\delta]^T F_s ds \quad (27)$$

F_v : is the body force per unit volume

F_s : is the load of surface traction

By substituting Eqns 26 , 14 into Eqn 27 and minimization with respect to nodal displacements the total potential energy can be written as :

$$\frac{\partial M}{\partial [\delta^e]^T} = 0 = \int_v B^T D B dv \{\delta^e\} + \int_v B^T D \left[\int_0^t \{\epsilon(t)\} dt \right] dv - \int_v N^T F_v dv - \int_{se} N^T F_s ds - 3K \alpha \int_v B^T (T(X,t) - T(X,0)) dv$$

Solving Eqn 25 will give the values of displacements for all nodes in the structure of interest.

Then stresses can be obtained by solving Eqn 26.

For incompressibility conditions it is more convenient to separate the stress matrix $\{D\}$ into two components (shear and bulk) [Amada 1997] as:

$$[D] = [D]^s + [D]^b \quad (29)$$

And by applying a selective integration procedure [Saabye 2000] , which is third order Gauss rule for shear components and second order Gauss rule for bulk components.

This will make some equilibrium between shear and bulk components.

RESULTS AND DISCUSSION

The first step is obviously to test the rate of convergence and the other features of the process. The process of numerical analysis described in this research is applied into two problems which was solved by Zienkiewicz and Ghasak respectively.

The first problem shown in Fig 2 is a cylinder of Viscoelastic material surrounded by a case of steel and subjected to an internal pressure suddenly applied at $t = 0$ and maintained thereafter at a magnitude P_0 .

The Viscoelastic material is assumed to be isotropic with the following properties [Zienckiewicz 1968]:

$$\frac{1}{K_{creep}} = 0$$

$$G_0 = 2584.125 \times 10^5 \text{ N/m}^2$$

$$K = 6891 \times 10^5 \text{ N/m}^2$$

$$G(t) = 2584.125 \times 10^5 + 3 \times 10^5 e^{-0.57 \tau}$$

$$T_s = 75 \text{ C}$$

The properties of steel case is taken as :

$$E = 206.73 \text{ GPa}$$

$$\nu = 0.3015$$

The results obtained by applying the method of Viscoelastic technique which compared with the solution by Zienckiewicz as shown in Figs 3 and 4, where the variation of radial and circumferential stresses with time is shown.

There are very small differences from the values of the solution by Zienkiewicz.

The points from finite element solution are obtained by averaging stresses across the element boundaries .

The curves presented are obtained by taking a time step of $\Delta t = 0.5$

It can be shown that the main computational advantage of this method over others lies in the fact that larger time steps can be taken. For example in the Quasi-Elastic solution (Zienkiewicz 1968) to obtain the curve in Fig3 at $\tau = 3$, a thirty time steps is used, and this required thirty solutions of a set of equations, the same curve is obtained by the method of this research using six time steps, as well as, the method can cover the environmental phenomenon like aging and temperature effects.

The second problem shown in Fig 5 is a pavement subjected to constant pressure load with **tire print diameter=300 mm(actual contact area) and tire**

load=80 KN, Pressure=550 KPa for the Single tire.

Data input in software of Asphalt concrete are exhibit in Table (3), the elastic solution is used for subbase and subgrade layers except asphalt material will be treat as a viscoelastic material .

The elastic properties for Subbase is $E=350 \text{ MPa}$, $\nu=0.3$ and Subgrade is $E=100 \text{ MPa}$, $\nu=0.4$ respectively, The mesh is shown in Figure 4 (1518 element-4-node). The results of rutting vs. number of load repetitions are shown in Figure 6

Figure 7 shows the comparison of rut depth for various number of axle load repetitions between the proposed technique and Ghasak method (Ghasak 2008). It can be seen that generally there is a small difference between the two techniques ranges from 5% to 7%.

Also this finite element model can be used for both the thermal and stress analysis (thermo-mechanical analysis) , the both thermal and force equilibrium are satisfied in each increment before the analysis proceeds to the next increment.

To capture the transient phenomenon for temperature displacements and applied loads , the time steps was taken small enough.

Using of the shifted time τ in Viscoelastic solution enables us to include the thermal effect by using WLF equation , as well as, using isoparametric element with local coordinates (ξ, η) enable us to use an element with curvilinear shape and cover the change in displacements with time.

The problem of incompressibility is distinguished by testing the ratio of bulk to shear modulus as following

$$\frac{\text{Bulk modulus}(K)}{\text{Shear modulus}(G)} = \frac{2(1+\nu)}{3(1-2\nu)}$$

For incompressible material ν approach 0.5 and bulk modulus becomes large



relative to shear modulus. It is noted that the use of these values in the finite element codes have not been tailored for incompressibility analysis and lead to very serious numerical errors caused by the ill-conditioning resulting from the division by a value which is nearly zero, and more importantly, "mesh locking" may occur, this refers to the inability of an element to perform accurately in an incompressible analysis, regardless how refined the mesh is due to an over-constrained condition and insufficient active degree of freedom.

It is noted that the element lock despite the fact that its area has remained constant, resulting in the prediction of too small of a displacement and too large of stress.

Using of selective integration and separation of bulk from shear components will improve the values of results for all permissible values of Poisson's ratio (ν).

CONCLUSIONS:

Within the limitations of the present work and depending on the results of applying the proposed techniques the following conclusions can be inferred :

- It can be use more time steps with an accurate results in this procedure compare with other method.
- It can coverage the aging phenomena and temperature effects.
- It can coverage the incompressibility phenomena and make a solution for it.
- It can be extend the procedure for most types of viscoelastic materials (compressible, incompressible, linear, non-linear ,.....etc.)
- It is recommended to extend the procedure for non-linear viscoelastic materials and using the procedure for rubber like materials.

REFERENCES

- Amada, S. and Lakes, R. S., "Viscoelastic properties of incompressible material", *Journal of Materials Science*, 32, 2693-2697, (1997)
- Bath ,K.J., *Finite Element Procedures* , Prentice-Hall, Englewood Cliffs,NJ,1995.
- Boyer, D. B., Papadogiannis, Y., Park, H. C., and Lakes, R. S., "Viscoelasticity and aging of composites materials.", *Bio-Medical Materials and Engineering*, Vol. 8, 45-53, (1998).
- David Roylance ,*Engineering Viscoelasticity*, Department of Materials Science and Engineering ,Massachusetts Institute of Technology, Cambridge, MA 02139, October 24, 2001.
- Gibiansky, L. V. and Lakes, R. S., "Bounds on the complex bulk and shear module of a two-dimensional two-phase viscoelastic composite", *Mechanics of Materials*, 25, 79-95, (1997).
- Ghasak E.A, Studying of Rutting in The Flexible Pavements Using Viscoelastic Finite Element Method , thesis, Civil Eng., Babylon University ,2008.
- *Hall H. , *Viscoelasticity* , Encyclopedia of polymers science and Engineering , Vol. 3, pp608 – 609 , Kosaido printing co. Ltd . ,Tokyo . 2006 .
- Hughes ,T.J.R, *The Finite Element Method-Linear Static and Dynamic Finite Element Analysis*, Prentice Hall ,Englewood Cliffs, NJ, 1987.
- Lakes, R. S. and Wineman, A., "On Poisson's ratio in linearly viscoelastic solids", *Journal of Elasticity*, 85, 45-63 (2006).
- Oza, A., Lakes, R. S. and Vanderby, R., "Interrelation of creep and relaxation for nonlinearly viscoelastic

materials", *Rheologica Acta*, Vol.42, 557-568 (2003).

• Rogers T.G. ,E . H. Lee , “*Solution of viscoelastic stress analysis problems using measured creep or relaxation functions*”, *Journal of applied mechanic* , Vol. 55 ,pp 127 – 133 , 1988

• Saabye. N. O, Hans. P, Introduction to the Finite Element Method, Prentice Hall Europe ,2000.

• Taylor Robert I. , Karl .S. Pister and Gerald. L. Goudreal , “*Thermo*

mechanical analysis of viscoelastic solids”, *Int. J. N. M. Eng.* Vol2 , pp 45-59 . 1990

• Zienkiewicz O.C., M. Watson “*A numerical method of viscoelastic stress analysis* ”, *Int . J.mech . Sci*, vol.10 , pp807 – 827 , 1968.

• Zienkiewicz,O.C. and R.I. Taylor,*The Finite Element Method*, (4th ed) Vol. 1, Basic Formulation and linear problems, 1989.

NOMENCLATURE

Symbol	Definition	Units
a _T	WLF shift factor	-
C ₁	WLF eqn. constant	-
C ₂	WLF eqn. constant	°C
E	Elasticity modulus	N/m ²
G	Relaxation modulus	N/m ²
J	Creep compliance	m ² /N
K	Bulk modulus	N/m ²
P	Pressure	N/m ²
T _s	Reference temperature	°C
t	Current time	hr
u	Horizontal displacement	mm
v	Vertical displacement	m
Greeks letters	Definition	Units
ε	Strain	m/m
σ	Stress	N/m ²
μ	Viscosity	N.hr/m ²
ρ	Density	kg/m ³
τ	Current shifted time	hr.
ν	Poisson ratio	-
ξ	Local horizontal coordinate	m
η	Local vertical coordinate	m

Matrices	Definition
[B]	Strain matrix
[δ]	Displacements matrix
[D]	Stress matrix
[F]	Elastic load vector
[J]	Jacobian matrix
[N]	Shape function matrix
[T]	Thermal load vector
[X]	Coordinate matrixP

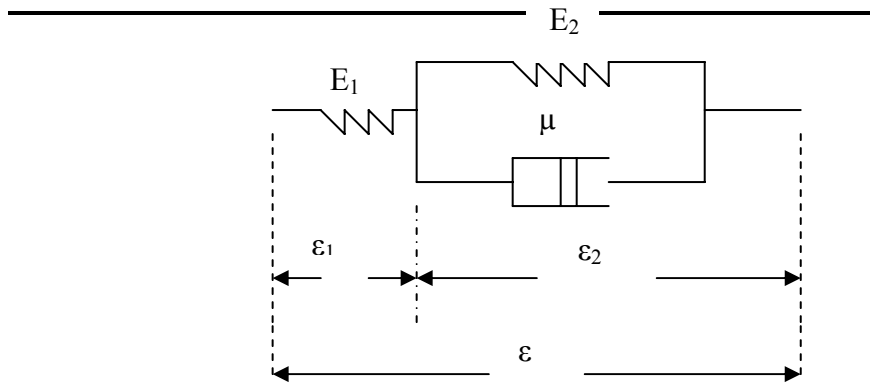


Fig 1. The three parameter model

Table1 : The Laplace transform technique

Constitutive equation.	Laplace transform
$\epsilon_1 = \frac{\sigma}{E_1}$	$\bar{\epsilon}_1 = \frac{\bar{\sigma}}{E_1}$
$\epsilon_2 = \frac{\sigma'}{E_2}; \mu \frac{d\epsilon_2}{dt} = \sigma''$	$\bar{\epsilon}_2 = \frac{\bar{\sigma}'}{E_2}; s\mu \bar{\epsilon}_2 = \bar{\sigma}''$
$\sigma' + \sigma'' = \sigma$	$\bar{\sigma}' + \bar{\sigma}'' = \bar{\sigma}$
$E_2 \epsilon_2 + \mu \frac{d\epsilon_2}{dt} = \sigma$	$(E_2 + s\mu) \bar{\epsilon}_2 = \bar{\sigma}$
$\epsilon_1 + \epsilon_2 = \epsilon$	$\bar{\sigma} \left(\frac{1}{E_1} + \frac{1}{E_2 + s\mu} \right) = \bar{\epsilon}$

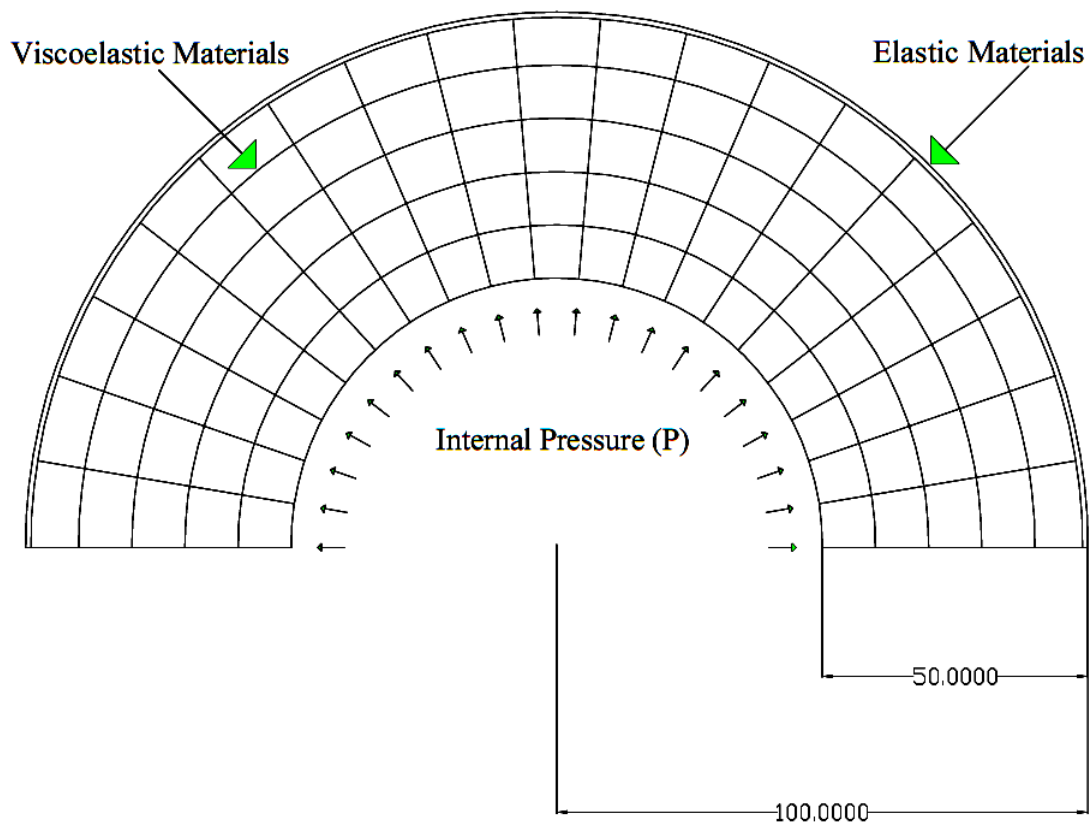
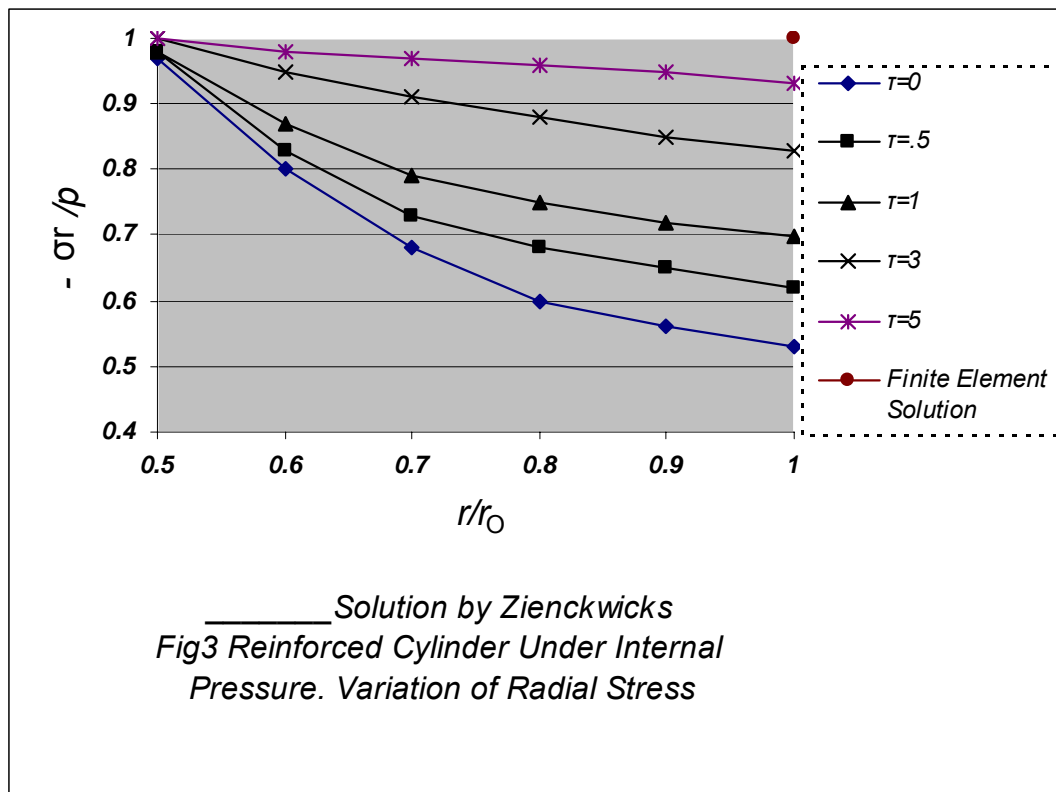
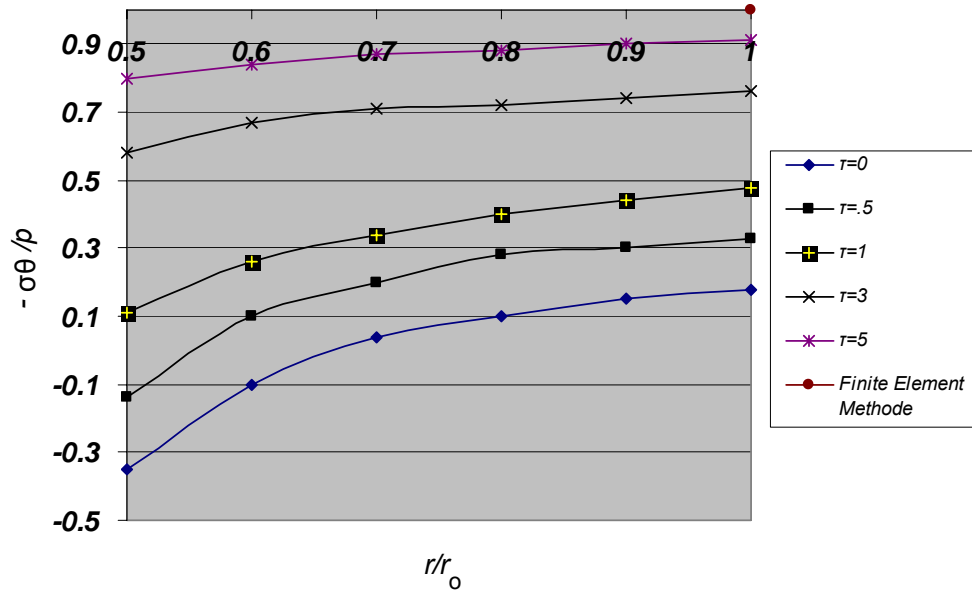


Fig 2: Viscoelastic cylinder surrounded by Elastic metal.





— Solution by Zienckiewicz
Fig4 Reinforced Cylinder Under Internal Pressure. Variation of Tangential Stress.

Table 2 : Comparison of results with the solution by Zienckiewicz at $\tau = 1$

r/r_0	Viscoelastic Solution FEM $-\frac{\sigma_r}{P}$	Solution by Zienckiewicz $-\frac{\sigma_r}{P}$	Viscoelastic Solution FEM $-\frac{\sigma_{\theta}}{P}$	Solution by Zienckiewicz $-\frac{\sigma_{\theta}}{P}$
0.5	0.96	0.97	0.12	0.125
0.6	0.87	0.875	0.24	0.247
0.7	0.79	0.80	0.33	0.34
0.8	0.77	0.78	0.41	0.415
0.9	0.75	0.756	0.45	0.452
1	0.74	0.748	0.48	0.49

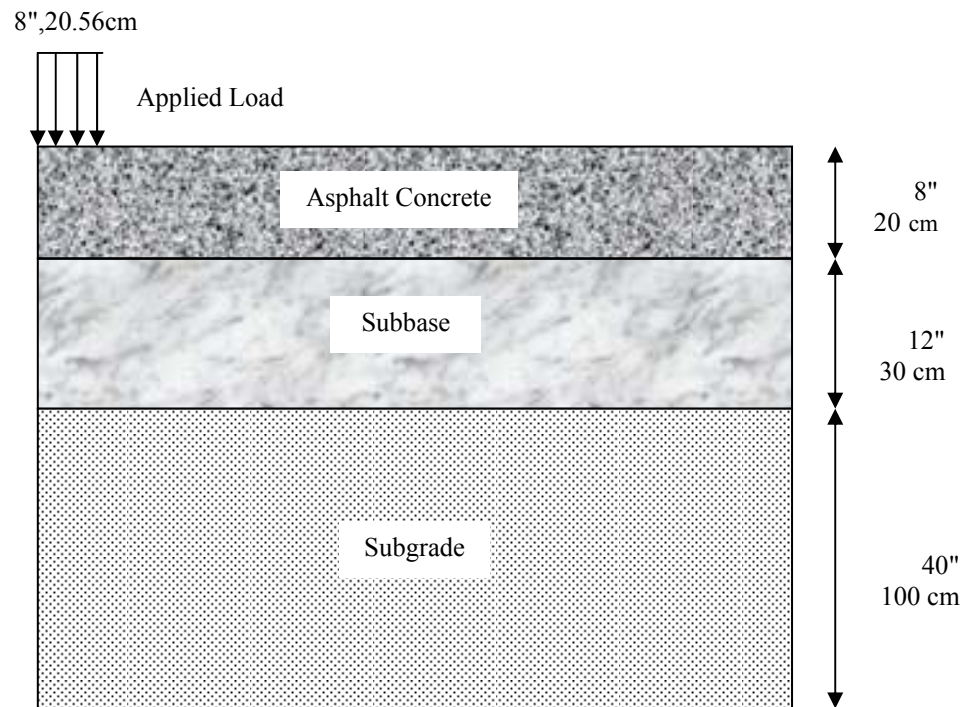


Fig. 5 : Pavement Layer configuration .

Table 2: Viscoelastic Material Properties for Asphalt Layer under Temperature $T_s = 23\text{ }^{\circ}\text{C}$ (Ghasak 2008).

Time of loading	Creep compliance $J(t)$ (1/MPa)	Relaxation modulus $G(t)$ (MPa)	Bulk modulus $K(t)$ MPa
0.1	0.0048	208.43	231.6
0.25	0.0063	158.1	175.7
0.5	0.0084	118.12	131.25
1	0.0092	108.47	120.5
2	0.01	94.63	105.14
4	0.012	83.5	92.78
8	0.0132	75.5	83.9
15	0.017	58.37	64.9
30	0.0198	50.34	55.9
45	0.021	46.75	52

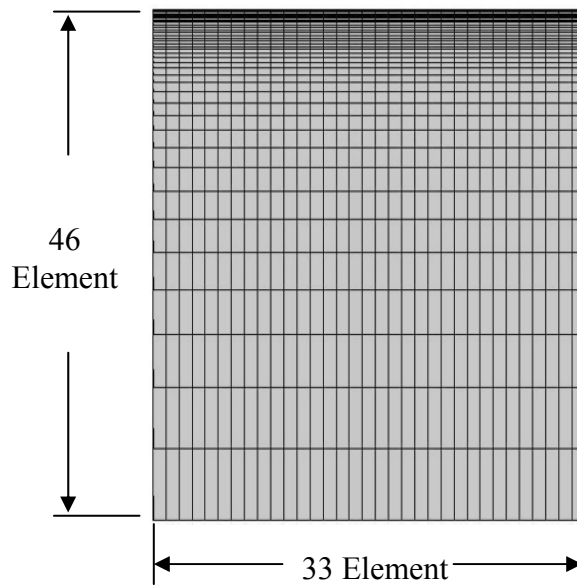


Fig 6 :Finite Element mesh for pavement layers configuration.

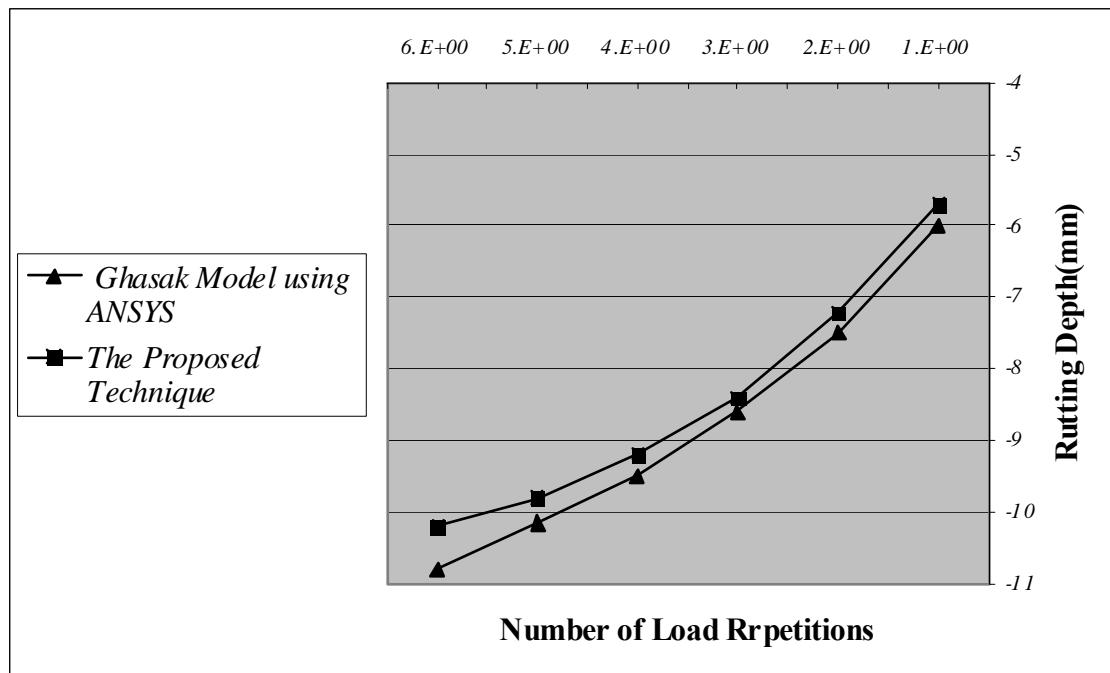
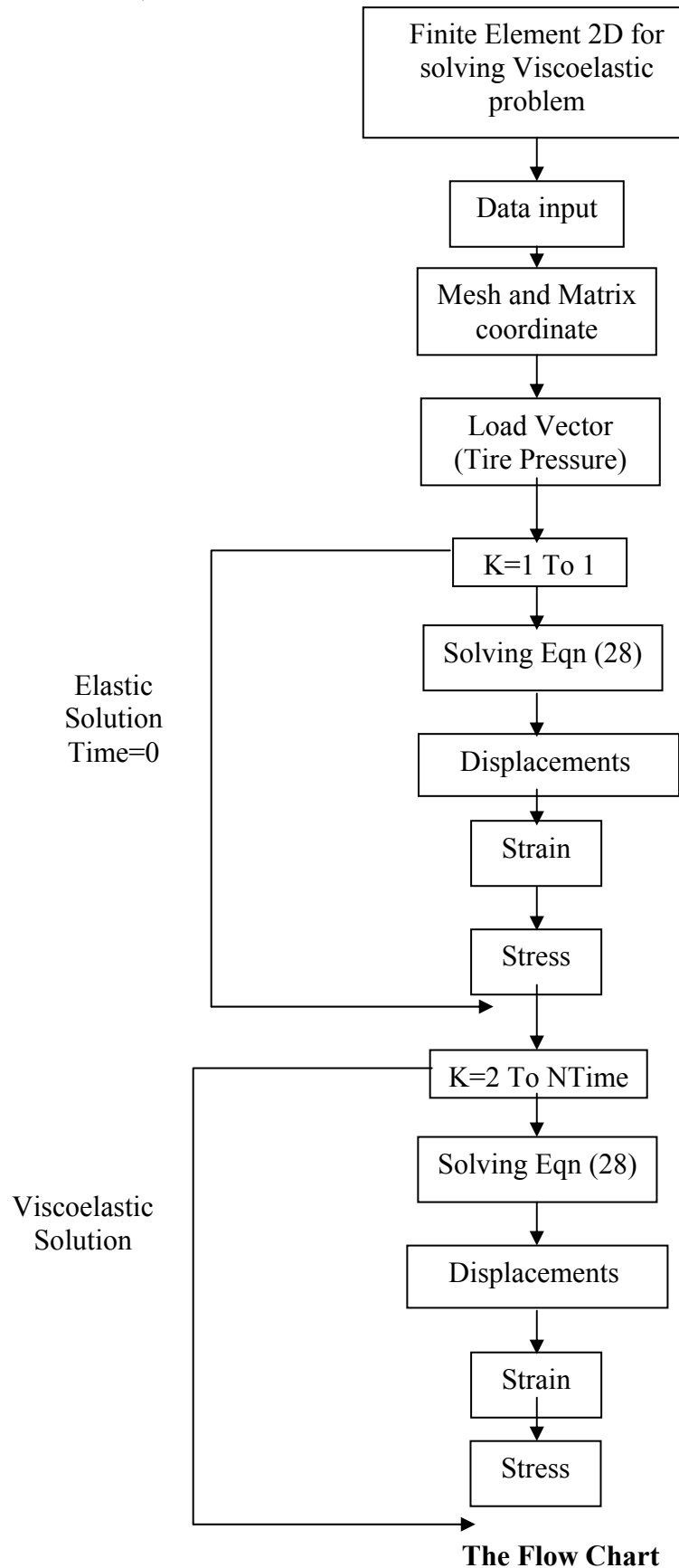


Fig 7 : Comparison between the Proposed procedure and Ghasak method.

APPENDIX





RADAR PARAMETER GENERATION TO IDENTIFY THE TARGET

Prof. Dr. W. A. Mahmoud, Dr. A. K. Sharief and Dr. F. D. Umara

**University of Baghdad
Baghdad, IRAQ**

ABSTRACT

Due to the popularity of radar, receivers often “hear” a great number of other transmitters in addition to their own return merely in noise. The dealing with the problem of identifying and/or separating a sum of tens of such pulse trains from a number of different sources are often received on the one communication channel. It is then of interest to identify which pulses are from which source, based on the assumption that the different sources have different characteristics. This search deals with a graphical user interface (GUI) to generate the radar pulse in order to use the required radar signal in any specified location.

KEY WORDS

Identification ; Target ; Electronic Warfare ; Radar Pulse ; Graphical User Interface.

INTRODUCTION

The continuous growth of air traffic increases demand to determine reliable algorithms and systems to tell where, on what altitude and how fast an aircraft is moving, as well as whether that aircraft of interest is friendly, foe or neutral. In general, this is referred to as a tracking. When something is under tracking, it implies that the current object is a target. In the sequel, tracking can be defined more precisely “as processing measurements obtained from a target in order to maintain an estimate of its

current state, which typically consists of kinematics components (such as position, velocity, acceleration etc.) and other components (radiated signal strength, spectral characteristic, feature information etc.). Emphasis of the word “state” implies that scientists in tracking field are mainly concentrated in estimating the trajectory of the target. The use of the word “state” is

ambiguous, exact meaning depends always on the context [Hau00].

Defense systems dealing with tracking are important in the warfare because the present aircraft and vessels may be quick and destructive. Therefore, tracking systems are required to be as highly intelligent as possible. Software package presented in this paper comprehends GUI [Alb03] to achieve more reliability in tracking system in order to solve a given problem, e.g. the identification problem. This paper is organized as follows: The principles of the target tracking and the electronic warfare system are presented in section 2, and section 3, respectively. While the receiving system and the radar signal description are presented in section 4 and section 5, respectively. The parameters to be identified and the simulated results are presented in section 6 and section 7, respectively, finally the conclusion is represented in section 8 followed by the references.

TARGET TRACKING

In the civilian aviation the target's velocity, height, position and heading can be easily solved, because all targets are cooperative by default. When dealing with defense applications, qualities listed above are not enough. In fact, they are not even considered first. In the military field, the most urgent is to know whether the target of interest is friendly or hostile. After then questions as "What is the type of the target?" and "What is the target threatening?" rise. Problem that deals with the type of the target is referred to as an

identification problem. An example of tracking system, with using identification network (Bayesian network) in association, is illustrated in Fig.(1) [Vac93].

The identification procedure is as follows; Targets emit signals, which can be detected by sensors, when a sensor has detected a signal, it will be modified and transmitted to the identification system. Then identification system processes all observations and results a type probability function, which is returned to the operator. An example of the identification system is illustrated in Fig.(2).

ELECTRONIC WARFARE SYSTEM

Electronic warfare (EW) receivers will be the assumed approach. It takes many distinct forms, such as detecting and degrading the performance of a hostile radar, intercepting and disrupting enemy communications, decoying aircraft and ordinance and confusing the enemy's perception of the tactical area. It represents a necessary investment to protect friendly weapon platforms [Sch86].

The basic concept of EW, is to exploit the enemy's electromagnetic emissions in all parts of the electromagnetic spectrum in order to provide intelligence on the enemy's order of battle, intentions, and capabilities, and to use countermeasures to deny effective use of communications and weapons systems while protecting one's own effective use of the same spectrum [Tsu86].

The modern concept of EW as a vital and basic element of military strategy, which when used in concert with other military assets,

provides a method of neutralizing an enemy force (force divider effect) while simultaneously enhancing the power of a friendly force (force multiplier effect). Thus EW is defined as a military action involving the use of electromagnetic energy to determine, exploit, reduce, or prevent hostile use of the electromagnetic spectrum and action which retains friendly use of the electromagnetic spectrum. Fig.(3) illustrates the functions performed in a modern tactical EW system.

Electronic warfare systems are used in military actions to protect resources from enemy threats. In EW, as in other electronic system, simulation plays a vital role in training the operators to become proficient in using the equipment and recognizing threats. These systems can be organized into the three major categories or divided into three parts:

- Electronic Support Measure (ESM), which collects information on the electronic environment.
- Electronic Countermeasures (ECM), trying to disturb enemy systems.
- Electronic Counter-Countermeasures (ECCM), trying to disturb the enemies ECM [Tsu86].

The ESM and ECCM are referred to as passive systems because they do not radiate electromagnetic energy, while the ECM is referred to as an active system since it tries to disturb the enemy system by sending electromagnetic energy. EW encompasses the two major areas: ESM and ECM [Fan01].

ELECTRONIC WARFARE RECEIVING SYSTEM

A simplified block diagram of an EW receiving system is shown in Fig.(4). The first block is the feature extractor, which represents the radio frequency receiver hardware, the parameter measurement and encoding circuitry.

Figure(5) shows a diagram of the digital receiver. The output of the feature extractor is a pulse descriptor word (PDW), which contains the feature values of the intercepted signal (i.e., frequency, amplitude, pulse width, time of arrival (in some cases) the signal's azimuth and elevation bearing).

The PDW for each intercepted signal is stored in a pulse buffer for further processing. Modern EW receiving systems must operate in an increasingly dense signal environment. Hence, a large quantity and jumble of signals are intercepted that must somehow be stored in a timely and efficient manner so that subsequent actions, such as identifying the signal's origin, can be taken. The third block performs the sorting or deinterleaving function by clustering the incoming radar pulses into groups. In principle, each group or cluster should represent a single radar or emitter.

However, the task of isolating a particular signal from a specific emitter can be difficult to accomplish, since the parameter boundaries between different signals may overlap, and since factors such as measurement error can cause the

measured characteristics of the signal to become inexact or “fuzzy”. A proper choice of the signal parameters that are used for sorting as well as a proper assignment of their relative importance in the decision process can minimize some of the problems caused by inexact or ambiguous signal characteristics. For example, one signal parameter that can be very useful for signal sorting or deinterleaving purposes is the direction of arrival (DOA) of the intercepted signal. Unfortunately, this parameter may not always be available, since many EW systems cannot measure a signal’s DOA. Moreover, in highly dynamic situations, signal’s DOA may be changing too rapidly to be of practical use.

Consequently, many EW systems must rely on other parameters, such as frequency or pulse width, to sort the received signals. Therefore, the problem of making decisions based on inexact or ambiguous evidence will always be present to some degree.

Intercepting and then isolating the signal(s) of interest is(are) not the end goal of a large array of EW receiving systems. In many cases, the intercepted signal must also be ascribed to a specific radar or class of radar in the environment. For example, ECM systems must determine the identity of a victim radar or threat before the appropriate jamming technique can be selected. The task of determining the

identity of an intercepted signal is laden with uncertainty, since the evidence (data cluster) itself contains uncertainty, and since each stage in the identification process introduces additional uncertainties. Nevertheless, an accurate identification must be made; in some cases, an error can be fatal.

The final two blocks support the task of identifying and classifying the intercepted signals. The fourth block, the pattern extractor and tracker (PET), uses the stored information from the deinterleaver to compute any patterns (e.g., the pulse repetition interval (PRI) pattern) that may be contained in each data cluster (emitter) by using the appropriate data item from the PDWs stored in a cluster. The final and fifth block is the classifier, which describes each data cluster in the PET to a particular emitter.

The identity of a particular signal is usually inferred by correlating the observed characteristics of that signal with those that are stored in the electronic order of battle (EOB), which is a list that contains the identity and signal characteristics of all known radars or those likely to be encountered [Vac93]

Major applications of EW receivers serve three purposes in EW system: they warn of enemy radar (radar warning receiver (RWR)), they support electronic jammers (electronic countermeasures (ECM) receiver), and they aid reconnaissance (electronic intelligence (ELINT))

receiver). The requirements for each of these functions are different, and so in most situations they are supported by different receivers [Sch86]

RADAR SIGNALS: CW PULSE, RF PULSE TRAIN AND CHIRPED TYPE SIGNALS

Most radars are designed to transmit a continuous train of RF pulses in order to perform target detection. These RF pulses have the same power, and share a common antenna for transmitting and receiving signals. For Continuous-Wave (CW) radars, the pulse is transmitted continuously, often through a separate transmitting and receiving antenna. Both of these radar designing operate mainly at a single frequency. For a high-resolution modern radar, see eq.(1), it requires a wide radar bandwidth to increase the information about the location and the identity of target,

Radar resolution

$$(\Delta r_s) = \frac{\text{propagation velocity}}{2 \times \text{bandwidth}} \quad (1)[\text{Hau00}]$$

Pulsed radar signals, are predominantly pulsed with widths varying between 0.1micros and tens of microseconds. so they are transmitted as periodic pulse trains.

A chirped pulse is a RF pulse consisting of a sine wave that is phase modulated in such a way that linear frequency modulation results across the pulse duration. By statistical

definition, a linear chirped sinusoidal signal is a non-stationary signal and is described as:

$$s(n) = \sqrt{P_x} \exp j(2\pi f n + \Psi n^2 / 2 \cdot \phi) \quad (2)[\text{Hau00}]$$

Where Ψ is the chirp rate of the signal, f is the centre frequency, n is the time period and ϕ is the constant phase of the signal. The signal amplitude $\sqrt{p_x}$ is constant but the signal is non-stationary due to the chirping of the frequency that sweeps linearly with time. The input signal $x(n)$ is given by:

$$x(n) = s(n) + \eta(n) \quad (3)[\text{Hau00}]$$

where $\eta(n)$ is a zero mean white noise (Gaussian) signal with noise power of P_π . Different radar signal properties are graphically illustrated in Fig.(6) [Bro79,Tin01].

PARAMETERS TO DETECT

A radar receiving system is generally used to extract the features of each input pulse, including RF, amplitude (Amp), pulse width (Pw), angle of arrival (AOA), time of arrival (TOA), and modulation of pulse (MOP). Other parameters measured are pulse repetition interval (PRI) and burst repetition interval (BRI). PRI indicates how often pulses arrive and BRI indicates how often groups of pulses arrive. For a detailed discussion about the quantities that an EW receivers receive, one should refer to chapter three into [Sch86].

According to these features, the deinterleaver wants to cluster pulses which are emitted from distinct emitters into distinct

groups. The ability of a radar system to determine and resolve these important target parameters depends on the characteristics of the transmitted radar signal.

Fig.(7): Pulse train signal with its time frequency

The train of interleaved pulses is processed in the ESM receiver to identify for each pulse the center frequency, amplitude, PW, TOA and bearing (or AOA), see fig.(8) The information is then input to a pulse sort processor, which deinterleaves it into the PRI appropriate to each emitter. Further comparison against a store of known radar types permits the generation of an emitter list, classified with threat significance. Depending on the detected radar signal the pilot of an airplane gets information of the threat he is exposed to.

The receiver subsystem detects the radar pulses and measure the individual parameters, (the digital words a receiver generates and passes to a digital processor). The availability, resolution and accuracy of these measurements must all be taken into account when designing the deinterleaving system. Obviously, the better the resolution and accuracy of any parameter measurement, the more efficiently the preprocessor can carry out its task. However, there are limitations on the measurement process from outside the ESM system (e.g. noise, jamming, and multipath), inside the system (e.g. timing requirement) and from cost-effectiveness considerations.

SIMULATION RESULTS

In the following section different types of the radar signals will be evaluated by the radar_parameter_generation GUI package, from the applied signal flowgraph shown in Fig.(9), the signal shown in Fig.(10), some other samples of generated signals from their applied simulink shown in fig.(11), are shown in Fig.(12) and (13).

As a short summary, the following individual units are used in Fig.(9): they are further divided into different modules and sub-modules in order to manipulate different types of input data.

The Input Unit,
The Digital Signal Processing Unit,
The EA Strategy Unit,
The Human Computer Interface Unit,
The Output Unit,
The Control and Management Unit, and
The Power Calculation and Evaluation Unit.

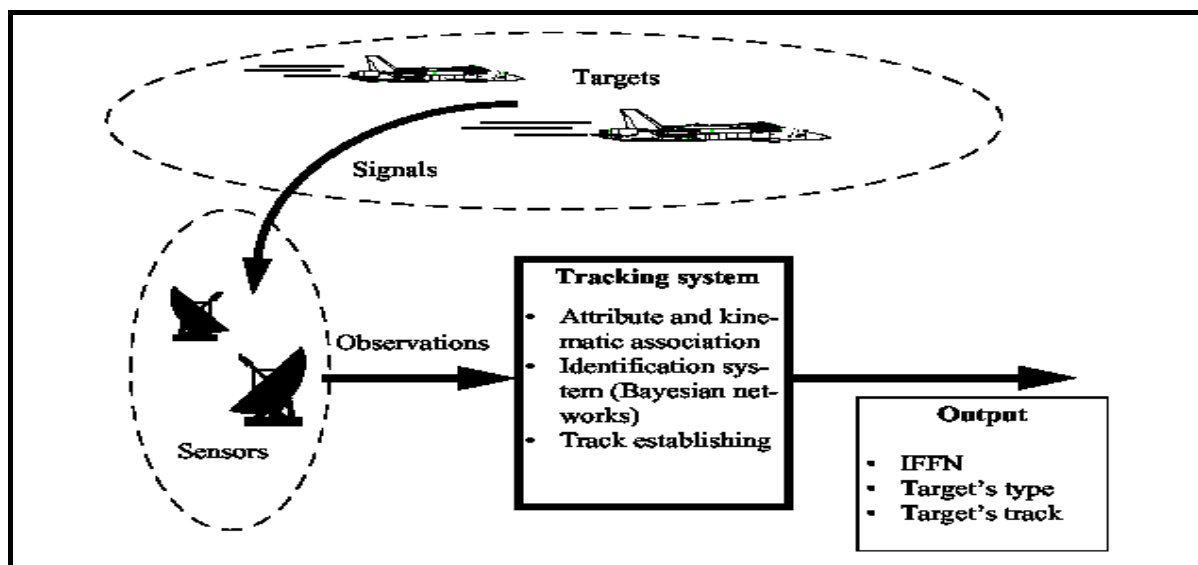
Matlab-Simulink, the processing and analyzing phases applied onto the received IF signals. It has the function of reading out the data samples of the digitized IF signal of constant, chirp, or nonlinear frequency modulation, converting the digitized IF into video signal, measuring processed video pulse parameters and displaying time and frequency drawings of input and video signals. Fig.(11) shows the implemented model.

CONCLUSION

From the above results, the generated electronic order of battle can be obtained, hence, in order to identify any target, the only requirement is to compare it with the available standard table.

REFERENCES

- Albakry B.M., 2003, "Interference Analysis and Generation in Radar System", M.Sc. Thesis, Electrical Eng. Dep., University of Baghdad.
- Fanden P., 2001, "Evaluation of Xilinx System Generator", M.Sc. Thesis, Linköping university Sweden.
- Ting L. K., 2001, "Algorithm and FPGA Implementation of Adaptive LMS-Based Predictors for Radar Pulse Deinterleaving", Ph.D Thesis, Queen's University Belfast.
- Hautaniemi S., 2000, "Target Identification with Bayesian Networks", M.Sc. Thesis, Tampere University of Technology, Finland.
- Vaccaro D.D., 1993, "Electronic Warfare Receiving Systems", Artech House.
- Schleher D.C., 1986, "Introduction to Electronic Warfare", Artech House.
- Tsui J.B., 1986, "Microwave Receivers with Electronic Warfare Applications", John Wiley and Sons..
- Brookner E., 1979, "Radar Technology", Artech House



Fig(1): Illustration of a tracking system

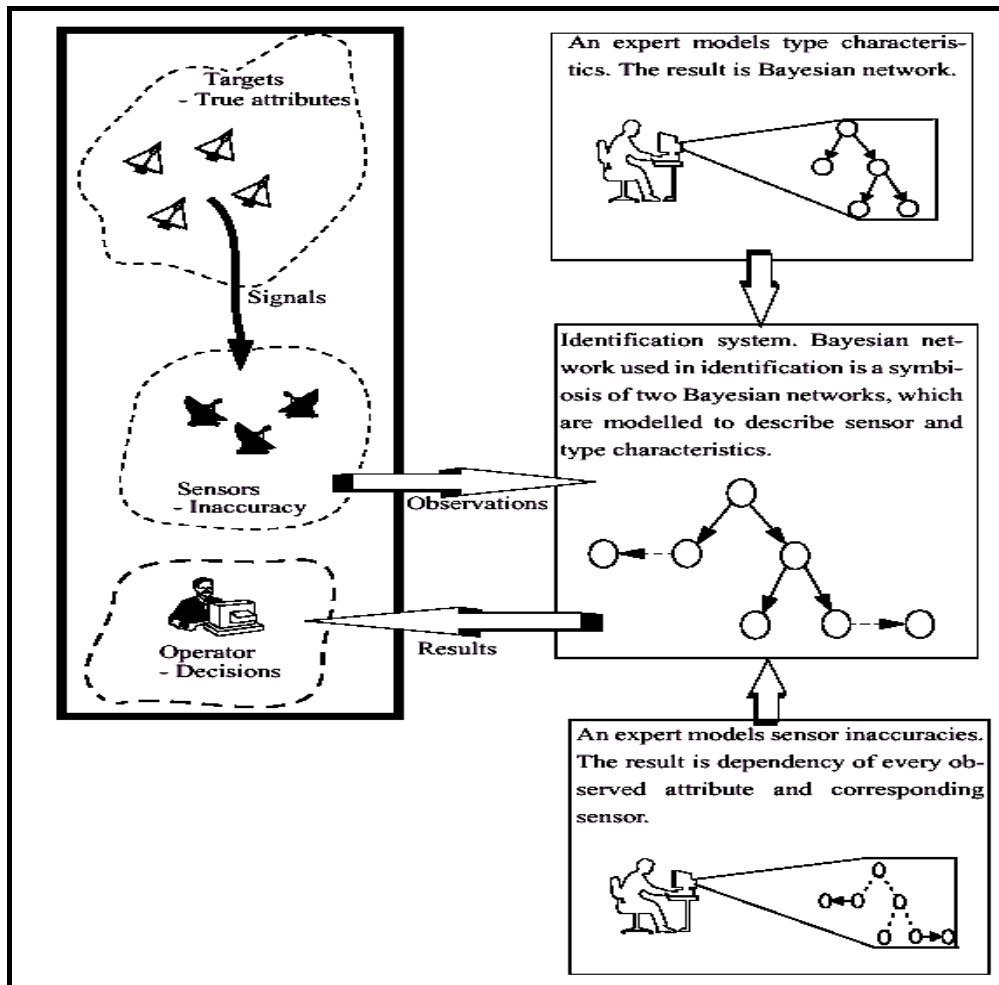


Fig.(2): illustration of the identification procedure.

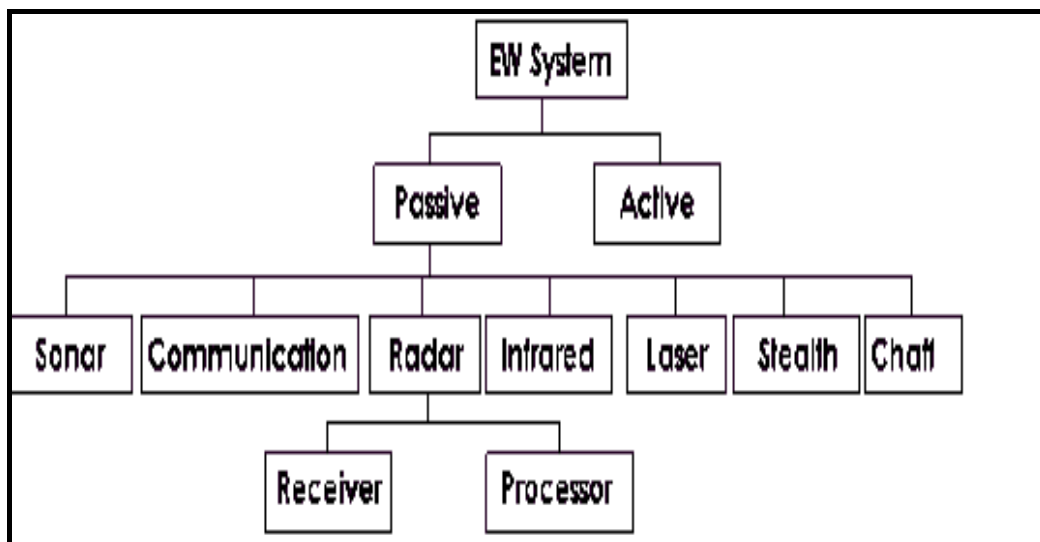


Fig.(3): Functional structure of EW system.

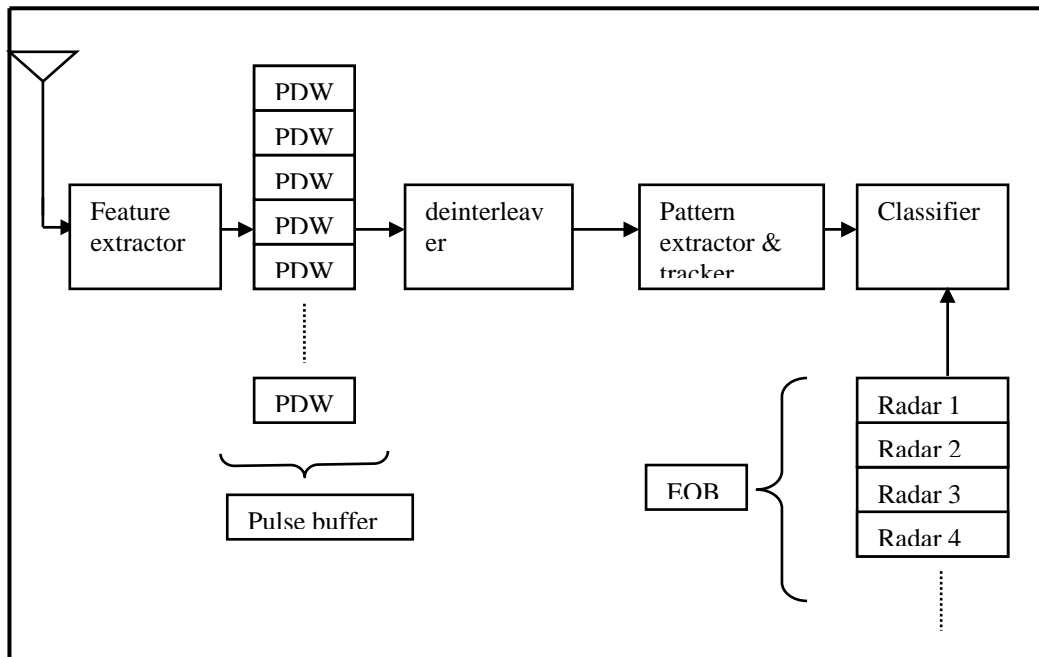


Fig.(4): General block diagram of an EW receiving system

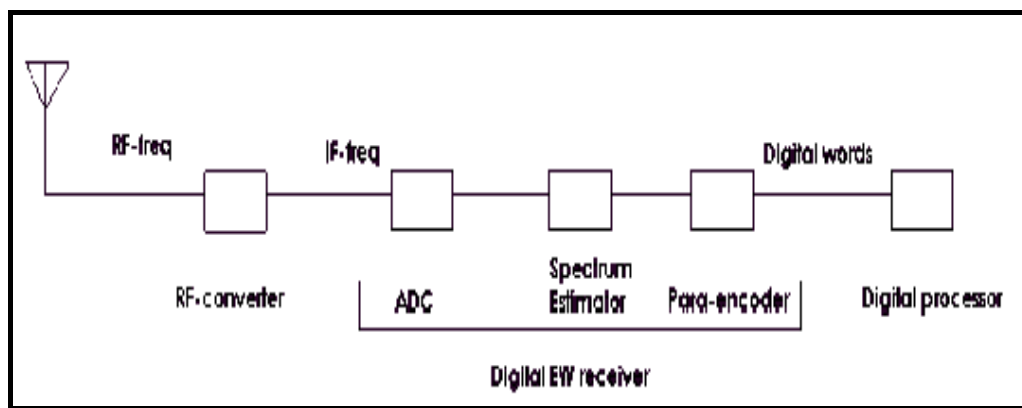


Fig.(5): Functional block scheme of a digital EW receive.

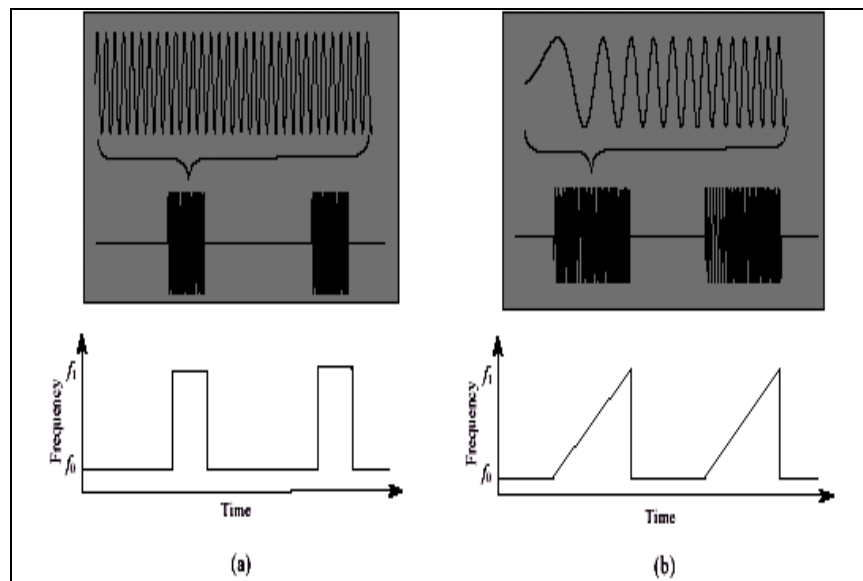


Fig.(7) illustrates (a) CW pulse train signal with its time-frequency representation (b) CW chirped train signal with its time-frequency representation [Bro79].

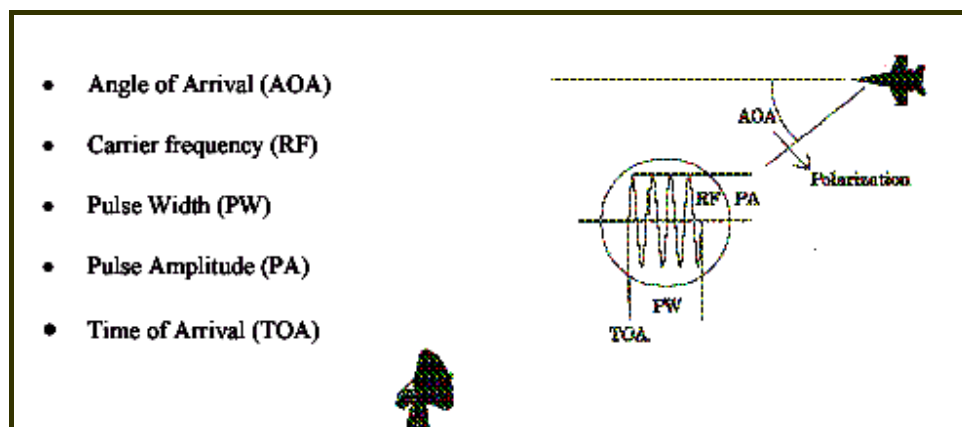
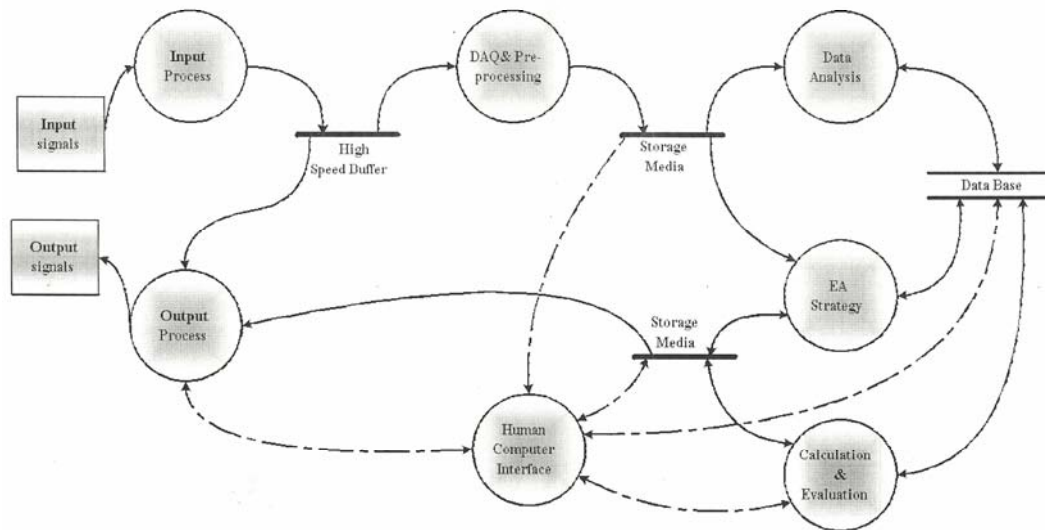


Fig.(8):Parameters measured by receiver.

Fig.(9): Radar Generation signal flow graph.



10

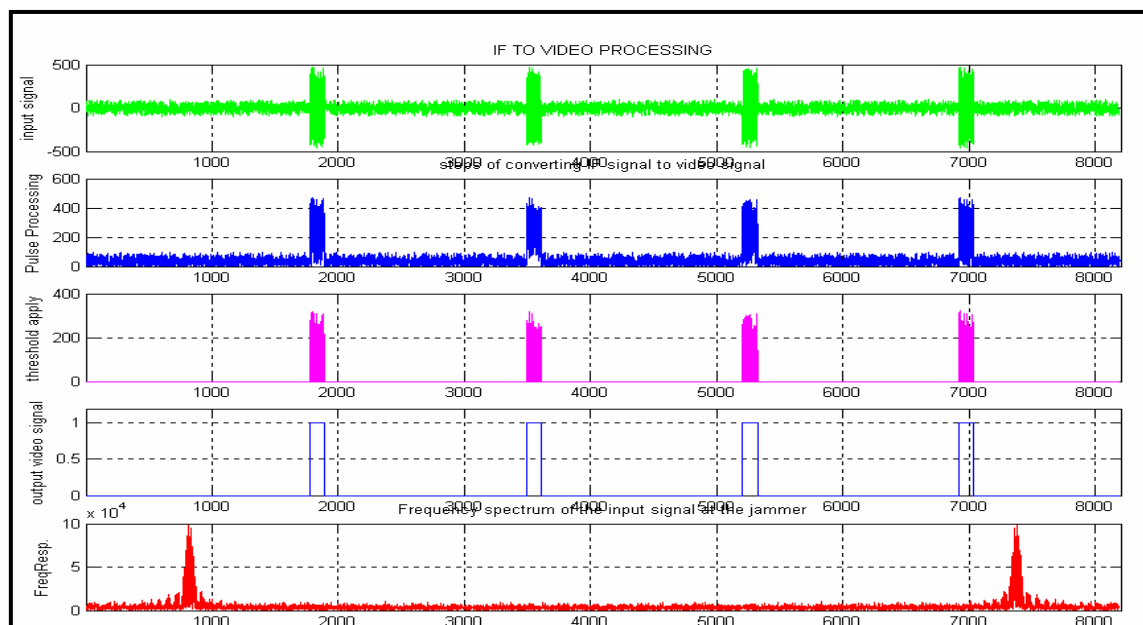


Fig.(10): Simulated sample of Radar signal.

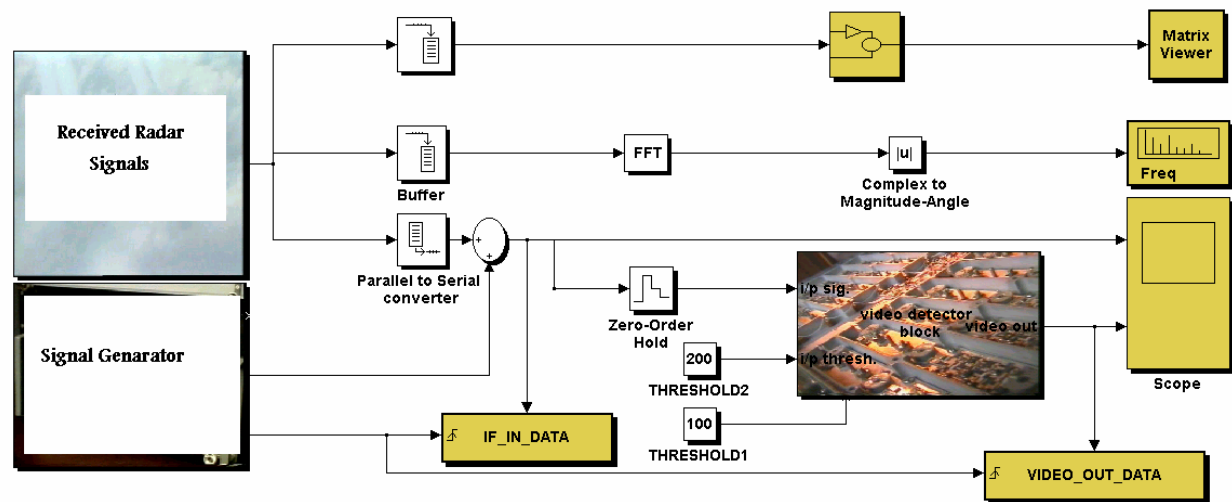


Fig.(11): The simulink to generate a signal.

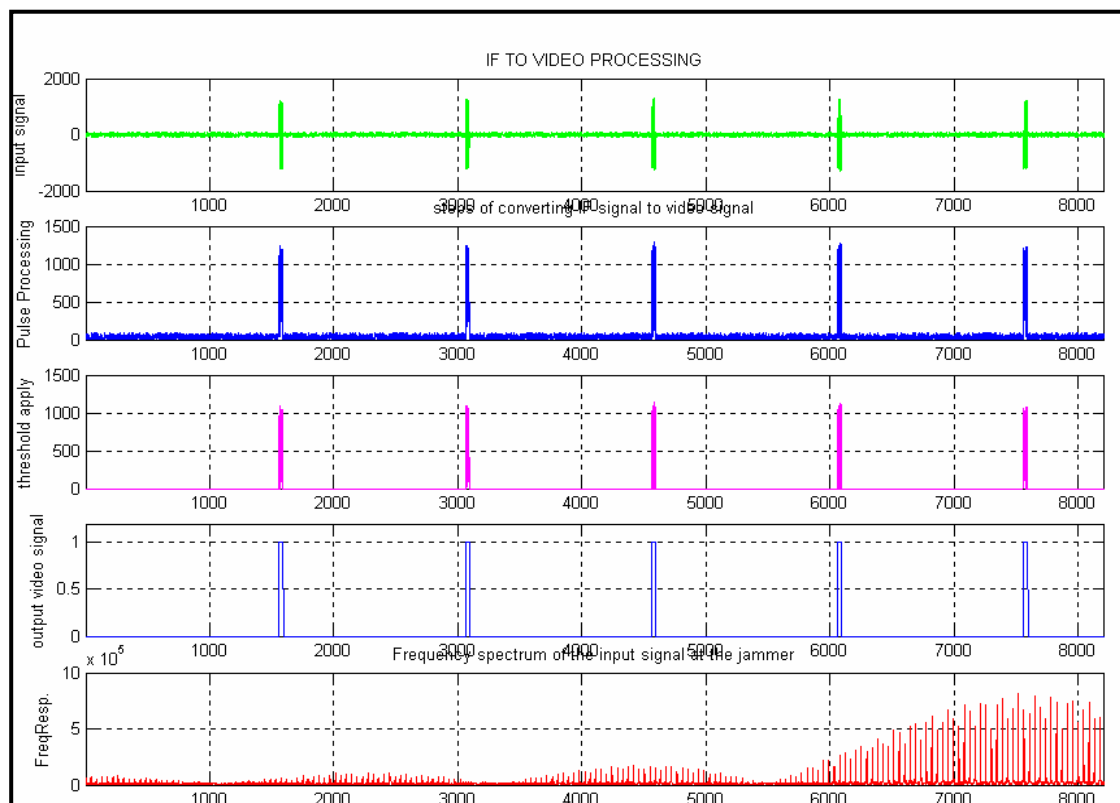


Fig.(11): Second sample of the radar signal.

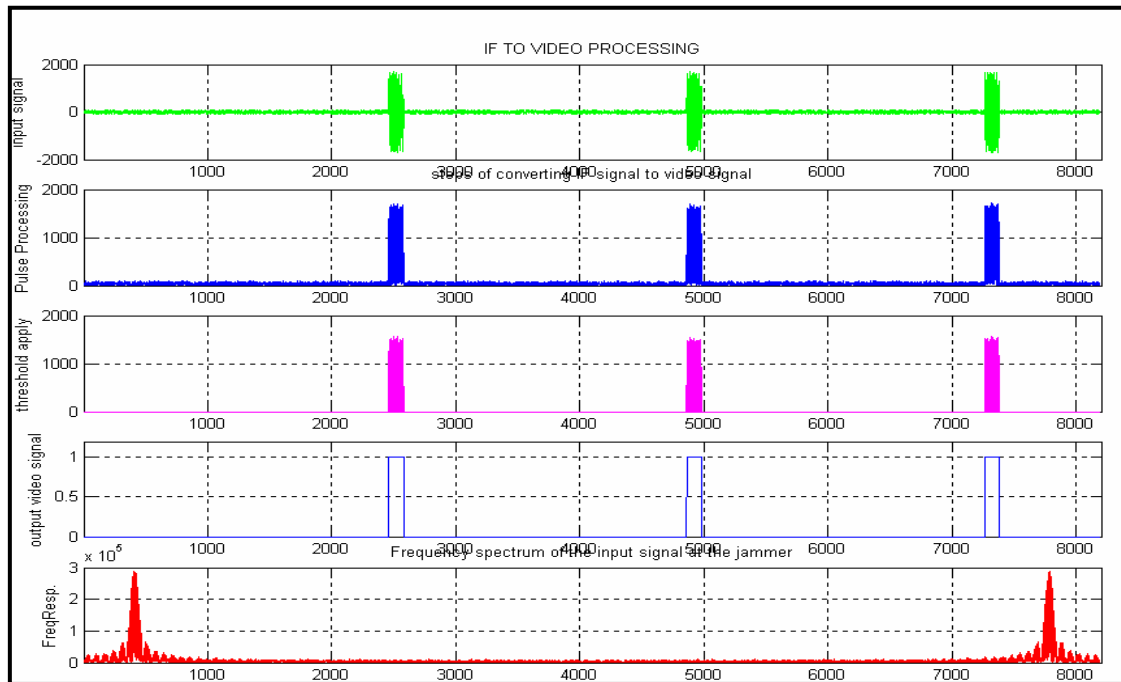


Fig.(12): Third sample of the radar signal.



CONSTRUCTION DELAY ANALYSIS USING DAILY WINDOWS TECHNIQUE

Assist. Prof.: Dr. Sawsan Rasheed Mohammed
University of Baghdad
College of Engineering
Department of Civil Engineering

Salsabeel S . Jafar
University of Baghdad
College of Engineering
Department of Civil Engineering

ABSTRACT:

Delays occur commonly in construction projects. Assessing the impact of delay is sometimes a contentious issue. Several delay analysis methods are available but no one method can be universally used over another in all situations. The selection of the proper analysis method depends upon a variety of factors including information available, time of analysis, capabilities of the methodology, and time, funds and effort allocated to the analysis. This paper presents computerized schedule analysis programmed that use daily windows analysis method as it recognized one of the most credible methods, and it is one of the few techniques much more likely to be accepted by courts than any other method. A simple case study has been implemented to demonstrate the accuracy and usefulness of the proposed delay analysis model. The results of the study indicate that the outcomes of delay analyses are often not predictable that each method may yield different results. The study also revealed that depending on the time and resources available, and the accessibility of project control documentation, one method may be more practical or cost-effective.

KEYWORDS: Construction Management, Scheduling, Delay Analysis, Computer Applications, Claims Management, Construction Law.

:_____

INTRODUCTION:

Delays in construction can cause a number of changes in a project such as late completion, lost productivity, acceleration, increased costs, and contract termination. The party experiencing damages from delay needs to be able to recognize the delays and the parties responsible for them in order to recover time and cost. However, in general, delay situations are complex in nature. A delay in an activity may not result in the same amount of project delay. A delay caused by a party may or may not affect the project completion date and may or may not cause damage to another party. A delay can be caused by more than one party; however, it can also be caused by none of the parties (such as unusually severe weather conditions). A delay may occur concurrently with other delays and all of them may impact the project completion date. A delay may sometimes contribute to the formation of other delays. In construction contracts, schedule delay analysis is commonly conducted to demonstrate cause and effect relationships of time-related disputes. Schedule delay analysis makes use of the as-planned schedule, the as-built schedule, and schedule updates. CPM schedules add another dimension to schedule analysis as they provide schedule analysts with a critical path, float consumption, and the opportunity of utilizing what-if methodology. CPM has long been accepted by courts as an effective tool to evaluate the impact of delays (Arditi and Pattanakitchamroon 2006). There are many delay analysis methods that have been used by researchers and practitioners and these are known by different terminologies among practitioners and researchers. The results of delay analysis may be influenced by the method selected and therefore the selection of the most appropriate method is of importance to all parties concerned.

The objective of the study presented in this paper is to introduce a computerized schedule for delay analysis that incorporates daily windows analysis method and also to develop decision support system for selecting the suitable delay analysis method.

DEFINITION OF DELAY:

Time is the essence of a construction contract. A time period is specified as the contract duration. The legal obligations and rights associated with the concept of delay arise from the obligation implied in every contract that one party will not delay, hinder, or interfere with the performance of the

other party (Vento and D'Onofrio 2007). Thus, whether the owner or the contractor (or subcontractor, as the case may be) is legally and, perhaps, financially responsible for the consequences of delay depends upon a determination of the event(s) and party(ies) contributing to the delay.

The term "delay" in construction contracts has no precise technical meaning. It can be used in different sense to mean different conditions in project execution (Pickavance 2005).

Bramble and Callahan (1987) defined delay as "the time during which some part of the construction project has been extended beyond what was originally planned due to an unanticipated circumstance".

Assaf and Al-Hejji (2006) defined construction delay as "the time overrun either beyond the contract date or beyond the date that the parties agreed upon for delivery of a project".

Delay was also defined as "an acts or events that extend the time necessary to finish activities under a contract" (Stumpf 2000).

However, the term delay which will be addressed in this research means any occurrences or events that extend the duration or delay the start or finish of any of the activities of a project resulting in project late completion and that will only occur when the delay lies on the critical path of the programme.

However, in general, delay situations are complex in nature. A delay in an activity may not result in the same amount of project delay. A delay caused by a party may or may not affect the project completion date and may or may not cause damage to another party. A delay such as unusually severe weather conditions can be caused by none of the parties. Delays can occur in any and all activities, and these delays can concurrently or simultaneously cause delays in the project completion (Arditi and Pattanakitchamroon 2008). A delay may sometimes contribute to the formation of other delays. In other words, a project delay is the accumulated effect of the delays in individual activities.

As an example, a delay in the issue of drawings to a contractor can bring about consequences such as out-of-sequence work, work stoppages and poor morale. Shiet al. (2001) presented schematic cause-effect relationship of project delay as shown in Figure 1.

From causation perspective delays may be categorized under the following types:

*** Delays Caused By the Contractor:**

These include delays caused by parties for whom the contractor is responsible in law. Under most contracts the contractor is neither entitled to extension of time nor recovery of loss and/or expense and may have to pay damages/penalties.

*** Delays Caused By the Owner:**

These include delays caused by parties for whom the owner is responsible in law. In most standard forms, the contractor is entitled to extension of time and recovery of loss and/or expense caused by this type of delay.

*** Delays Caused By Neither Party:**

these include delays for which neither the owner nor the contractor is responsible, e.g. exceptionally adverse weather conditions. Most contracts allow the contractor more time to complete but with no corresponding entitlement to recover any loss and/or expense caused and no damages/penalties assessed.

Identifying delay impacts and allocating responsibility for delay events is more often argumentative because it involves one party's gain and the other party's loss. Delay analysis has developed as a means of providing the justification and quantification of the time and/or cost consequences necessary for resolving the different contentions (Braumah and Ndekugri 2009). It involves detailed

investigation of project records, programmes and their updates, often on retrospective basis, and with the aid of a number of different approaches commonly

termed "Delay Analysis Methodologies"

DELAY ANALYSIS METHODS:

There are four methods often mentioned in the literature that are professionally acceptable. They include:

- As-planned versus as-built schedule analysis method,
- Impact as-planned schedule analysis method,
- Collapsed as-built schedule analysis method, and
- Window analysis method, and they are known by different terminologies among practitioners.

The as-planned vs. as-built method is the observation of the difference between an as-planned schedule and an as-built schedule. The method identifies the as-built critical activities, compares these activities with the activities on the as-planned schedule, assesses the impact of delays on the project, identifies the sequences which actually define the duration of the project, and determines the causation and responsibility of delays that impact project completion.

The impact as-planned method uses only an as-planned or baseline schedule for delay analysis. It is based on the theory that the earliest date by which a project is completed can be determined by adding the delays into the as-planned schedule. New activities that represent delays, disruptions, and suspensions are added to the as-planned schedule and are used to demonstrate the reason why the project was completed later than planned. Contractors, who submit claims that involve a time extension, add only owner-caused delays to the as-planned schedule in the appropriate sequence to document the total project delay caused by the owner.

The collapsed as-built method is also referred to as the "but-for" schedule method. This analysis is popular in claim presentations because it is easily understood. SCL defines it as a method where the effects of delays are "subtracted" from an as-built schedule to determine what would have occurred but for those events (SCL 2002). This approach is a method of choice when a contractor lacks an acceptable schedule during the project, or when no as-planned schedule was required in the contract.

The window analysis method breaks the construction period into discrete time increments called "window" and examines the effects of the delays attributable to each of the project participants as the delays occur. It adopts the as-planned schedule as its baseline, but the as-planned schedule is periodically updated at the end of each planned time period. The windows analysis method is distinguished from the impact as-planned and collapsed as-built analyses in the fact that it incorporates both party delays into the analysis. In addition to this advantage, window analysis also provides a disciplined basis for the contractual parties to keep a project schedule up-to-date and properly adjusted. The majority of the viewpoints reviewed in the literature agree that windows analysis yields the most reliable results. In spite of its advantages, this method still has limitations which are summarized as follows:

- Window size can have a significant impact on the results of the analysis.
- Windows analysis has no mechanism for considering owner directed versus contractor acceleration.
- Windows analysis procedures do not include a systematic approach for calculating the responsibility for delays when multiple baseline updates have been used at different construction stages.
- Windows analysis does not consider the impact of resource over-allocation resulting from delays caused by various parties.

Hegazy and Zhang (2005) introduced changes to the traditional windows analysis method in order to resolve some of the above limitations. They proposed a daily windows approach for apportioning concurrent delays and accelerations. The approach uses a window size of one day to account for all fluctuations that occur in the project's critical path(s). However, this approach still does not consider other factors such as the effect of resource over-allocation and multiple baseline updates. To overcome this problem Hegazy and Menesi (2008) introduce improvements to the daily windows analysis in order to ensure that delay analysis considers multiple baseline updates, resource over-allocation and accurately apportions delays and accelerations among project parties.

EASY PLAN PROGRAMME:

Easy Plan (Hegazy 2007) is a computer programme which integrates estimating, scheduling, resource management, and project control. The Easy Plan program has been developed using the VBA language of Microsoft Excel software. Some of Easy Plan's features that facilitate delay analysis are (Menesi 2007):

- It allows the user to specify up to 3 estimates (duration and cost) for each activity.
- It allows the user to enter up to three key resources and to specify the daily limit of these resources.
- It notifies the user if the resource limits are exceeded.
- It allows the user to change the method of executing any activity.
- It permits more than one baseline to be saved.
- It allows the user to enter the daily progress of an activity as a percentage, or as a delay by a certain party.

- It represents the project progress using two bars for each activity: the top represents the baseline, and the bottom represents the progress. Thus, it shows whether the actual progress is faster or slower than that planned.
- It calculates and shows the actual project duration while the daily progress is being entered, taking into consideration all the delays, accelerations, and slowdowns.
- It allows the user to specify the project deadline and notifies the user if the project duration exceeds the deadline.

The application of this schedule analysis programme is described in the following case study. Figure 2 is proposed as the flow chart describing the procedure of Easy Plan programme.

COMPUTERIZED SCHEDULE ANALYSIS MODEL

CASE STUDY: ANALYSIS OF DELAYS, ACCELERATIONS, LOGICAL RELATIONS AND RESOURCE OVER-ALLOCATION

A computerized schedule analysis with enhanced daily windows analysis has been presented in this study to accurately apportion delays and accelerations among the project parties. The model has been incorporated into a computer program, EasyPlan (Hegazy 2007), which integrates estimating, scheduling, resource management, and project control.

CASE OVERVIEW:

A hypothetical eight-activity project is considered as a case study to demonstrate the daily windows analysis. The activities, their optional estimates, their predecessors (logical relationships), and the amount of resources required for each activity are shown in Table 1.

The contractor submitted an initial (as-planned) schedule that satisfied its own resource constraints and met a 15-day deadline, which was accordingly approved by the owner. Actual progress, however, resulted in some schedule changes. Table 2 summarizes delay events during the course of work. An analysis is required to determine if the contractor is entitled for compensation by the owner, and to investigate whether the owner's delay on day 6 warrants a request for compensation to cover the added expenses of accelerating Activity G. Although this

project is simple, the changes due to delays, accelerations, logical relations and resource over-allocation make its delay analysis complicated.

Using the Easy Plan Programme:

Following the case study information, first, the general data for the project were entered; including the start date, working days, the key resource (L1) and its daily limit (6), project deadline duration (15 days), and other contract provisions, such as a \$5,000 (U.S. dollars) daily penalty and a \$50/day (U.S. dollars) indirect cost (Fig. 3). Next, the activities and their optional estimates were specified in an activities sheet, as shown in Fig. 4.

Then, the predecessors of each activity were entered, as shown in Fig. 5. Since the contractor planned to use the first estimate for each activity (the cheap and slow option), the “method used” column, indicates an index of “1.” Accordingly, the project duration became 15 days. This 15-day schedule meets the deadline and also the six L1 resource limit at a total cost of \$ 48,750. Therefore, the schedule was saved as a “baseline” for the project (Fig. 6).

ACTUAL PROGRESS EVENTS:

When the project moved to the construction stage, all progress events, including delays, along with all parties responsible were entered on a daily basis. In the progress sheet of Fig. 7, each activity has two bars: the top bar (light color) represents the baseline indicated as daily percentages (e.g. duration of two days means a progress of 50% for each day). The bottom activity bar (dark color), on the other hand, allows the user to record the actual events that were experienced during the execution of the activity. Initially, the actual bars were set to be the same as the baseline bars. Actual daily events are entered in one of two ways. They can be entered directly on the actual activity bar (bottom) or the user can click on the “daily progress” button.

The daily events for an activity can be entered as either a progress or a delay. For Day 1 (Fig. 6), the project progressed according to the planned. The contractor delayed Activity A on Day

2, Day 3 and Day 4, which extended the project duration from 15 to 18 days as shown in Fig. 5, while Activity E progressed according to its planned duration.

In response to the actual events that took place after Day 4, the contractor decided to run Activity H in parallel with Activity G and immediately after Activity F as a corrective action in order to accelerate the project by three days and finish the work by the planned date (Fig. 8). Since the owner and the contractor agreed to use a new baseline after this logical relationship change, a new baseline was then saved in Easy Plan.

On Day 6, the owner delayed Activity D by one day. Although the delay did not affect the overall project duration, it caused a resource over-allocation at Day 9, as shown in Fig. 9. This over-allocation implied that the owner’s delay on Day 6 would later force the contractor to change the schedule or even delay some activities to avoid exceeding the resource limit. On Day 9, because of the resource limit, the contractor did not start Activity G due to its inability to proceed with the three Activities D, F, and G in parallel. Thus, Activity E and the project duration would be extended to Day 16, as shown in Fig. 10.

To compensate for this 1-day delay, the contractor decided to accelerate Activity G, and accordingly accelerate the overall project by one day, by changing the method of executing Activity G. The faster and more expensive second method reduced the duration of Activity G to six days instead of seven. Consequently, the project duration became 15 days again (Fig. 11). This change also mandated another adjustment and the approval of a new baseline after Day 9.

(Fig. 12) shows the As-built schedule of the project after entering all the events, in which the project finished on Day 17 with 2 days of net delay.

Delay Analysis for the Case Study:

When the user selects “Windows analysis,” as illustrated in Fig. 13, the analysis is conducted, and a small window containing a summary result is presented (Fig. 13).

The results summary indicates that the owner (O) was responsible for half day of excusable compensable delay, which was compensated by his half day of acceleration while the contractor (C) was responsible for five days of non-excusable delays, but he was compensated for four and a half day of them because of his acceleration. On the other hand, the project duration, however, became 17 days due to an excusable (N) delay of one and a half day.

DISCUSSION OF RESULTS:

Detailed results of the delay analysis are presented in an automated report (Fig. 13), providing a detailed day-by-day analysis. For example (Fig. 14) shows the result of Day 5 to Day 8. At the beginning of Day 5, a new baseline was entered because of the contractor’s corrective action. Since the new baseline duration was 15 and the previous baseline duration was 18, a 3-day contractor acceleration was accumulated. At Day 6, the owner caused a delay to Activity D which is critical. Therefore, no (O) was shown in the cumulative results of Day 5. However, the owner’s event on this day would lead to future resource over-allocation as indicated in the extra day of expected project delay (16 days instead of 15 days), as shown in the third column in Fig. 13. Accordingly, one (N) delay was accumulated in this case since it was not caused purely by the contractor (i.e., the owner was the reason). The report thus gives a traceable account of the basis for the results of the analysis. It should be noted that while the programmer suggests that an (N) is considered as a result of the owner’s impact on resource over-allocation (i.e., the contractor is entitled to a time extension but no cost compensation), it is possible to use any other agreed upon option (e.g., considering a compensable owner delay). In the event that the contractor’s own performance is the cause of its resource over-allocation, the presented schedule analysis approach has the advantage of clearly recognizing the situation and its implications on the remaining schedule and eligibility for delay claims.

This validates the programme’s ability to distinguish the parties causing the delay, acceleration, logical relation and resource over-

allocation. As such, it is suitable for decisions related to cost and time compensation.

CONCLUSIONS:

The main study findings and conclusions are summarized as follows:

- The reliability of delay analysis depends on the programming and record keeping practice. An analyst should meticulously review the data obtained from the project records because none of the methods yields reliable results if the information used is invalid.
- There are a number of methodologies available for analyzing delays and these differ from each other based on the type of schedule techniques required, the baseline schedule used and the mode of application in their use. Therefore, a fair and effective evaluation of delay impact is possible if the most appropriate delay analysis method is selected that provides a reliable solution with the information available and within the time and cost allocated for this purpose.
- None of the existing delay analysis methods is perfect as each has its own strengths and weaknesses. Windows analysis method is clearly accepted by the literature as the most reliable delay analysis method among the four standard methods discussed in this research. However, the transient nature of construction projects not often allowing scheduling data being well documented as well as time and budget limitations lead a number of researchers to suggest that the choice of a simpler method may be sensible.
- Daily windows delay analysis method is considered an accurate method and suitable to use as it takes into consideration the effects of baseline Cumulative resource Expected and the effective Results taken Duration ractor to accelerate the project and minimize potential delays as it usually ignored in delay analysis.
- It is necessary for analyst to be very familiar with the capabilities of the software used in project scheduling and progress control in order to be able to generate legitimate schedules for the analysis.

**REFERENCES:**

- AACEI (2007). "Recommended Practice No. 29R-03, Forensic Schedule Analysis." AACE International, Morgantown, West Virginia, U.S.A.
- Assaf, S. A., and Al-Hejji, S. (2006). "Causes of Delay in Large Construction Projects." *International Journal of Project Management*, 24, 349-357.
- Arditi, D. and Patel, B. K. (1989) "Impact analysis of owner-directed acceleration." *Journal of Construction Engineering and Management*, ASCE, Vol.115, No. 1, pp. 114-157.
- Arditi, D., and Pattanakitchamroon, T. (2006). "Selecting a delay analysis method in resolving construction claims." *International Journal of Project Management*, 24(2), 145–155.
- Braimah, N., and Ndekugri, I. (2007). "Factors influencing the selection of delay analysis methodologies." *International Journal of Project Management* (Paper in Press).
- De la Garza, J. M., Vorster, M. C., and Parvin, C. M. (1991). "Total float traded as commodity." *Journal of Construction Engineering and Management*, ASCE, 117(4), 716–727.
- Hegazy, T., and Menesi, W. (2008). "Delay Analysis under Multiple Baseline Updates." *Journal of Construction Engineering and Management*, ASCE, 134 (8), 575-582.
- Hegazy, T., and Zhang, K. (2005). "Daily Windows Delay Analysis." *Journal of Construction Engineering and Management*, ASCE, 131(5), 505-512.
- Hegazy, T. (2007). "EasyPlan Project Management System." Available from: <http://www.civil.uwaterloo.ca/tarek/EasyPlan.html>.
- Jafar, S. S. (2010) "Construction Delay Analysis Using Daily Windows Technique", M.Sc., Thesis, University of Baghdad.
- Pickavance, K. (2005). "Delay and Disruption in Construction Contracts" 3rd Ed., LLP Reference Publishing, London.
- SCL (2002) "Society of Construction Law. Delay and Disruption Protocol". Print most (Southern) Ltd, England (<http://www.eotprotocol.com>).
- Stumpf, George R. (2000). "Schedule Delay Analysis." *Cost Engineering Journal*, AACE International, 42(7), 32-43.
- Shi, J., Cheung, S., and Arditi, D. (2001). "Construction Delay Computation Method." *Journal of Construction Engineering and Management*, ASCE, 127(1), 60-65.
- Salsabeel S . Jafar (2009) " Construction Delay Analysis Using Daily Windows Technique" M.Sc. Thesis, College of Engineering, Al-Baghdad University.

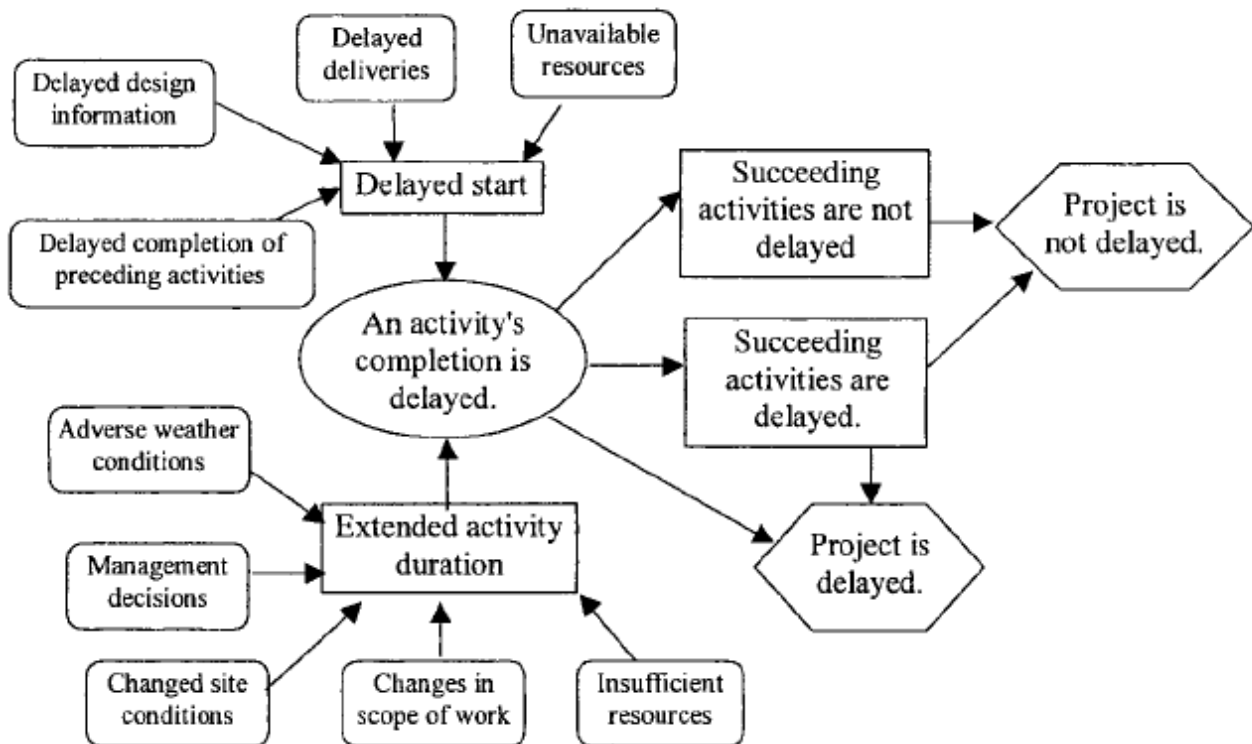


Figure.1 Cause-Effect Relationship of Construction Delays (Shi et al. 2001)

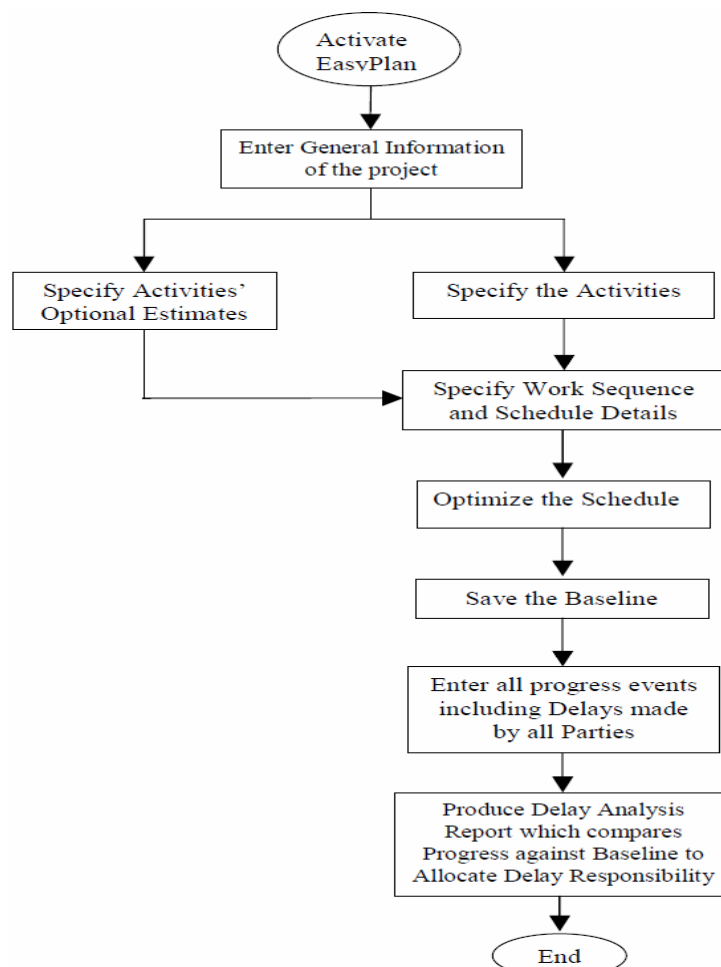


Figure.2 Flow Chart Indicating the Easy Plan's Procedure (Researcher)

**Table 1: The Activities' Estimates and Predecessors**

No.	Activity	Predecessor	Estimate 1			Estimate 2		
			Cost	Duration	Resources	Cost	Duration	Resources
1	A	-	6000	2	3			
2	B	1	6000	3	1	5000	4	1
3	C	1	6000	3	1	5000	4	1
4	D	1	6000	3	2	5000	4	2
5	E	-	6000	5	2	5000	6	2
6	F	2,3,5	6000	4	3	5000	5	3
7	G	2,3,5	6000	7	3	5000	8	3
8	H	4,6,7	6000	3	3			

Table 2: Delay Events and Their Secondary Effects

Day	Description
2,3 and 4	The contractor delayed Activity A (3 days) on Day 2, Day 3 and Day 4, and accordingly, it was expected that the project would finish in 18 days. To recover the three-day delay, the contractor found that the best available option was to run some activities in parallel so that the project duration would be 15 days again.
6	On the sixth day, the owner delayed the start of Activity D, and therefore a resource over-allocation was expected for the next few days.
9	The contractor delayed the start of Activity G to his inability to proceed with three Activities D, F and G in parallel because of the resource limit. Therefore, the contractor voluntarily accelerated the project by using of a more expensive method for Activity G which shortened its duration from 7 days to 6 days.
11	Both the owner and the contractor caused delay to the project. The owner delayed Activity G while the contractor delayed Activity F.
12	The contractor caused delay to both Activities F and G.
14	Activity F was delayed because of the slow progress of the contractor while Activity G was stopped due to inclement weather.
16	The project was accelerated by one-day because of the owner acceleration for Activity G and the contractor acceleration for Activity H.



is used

First baseline was saved on
September 1 2009

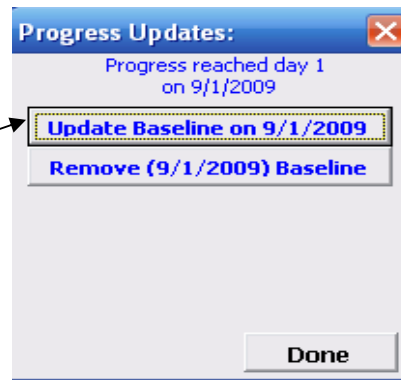


Figure 6: Saving the Project Baseline

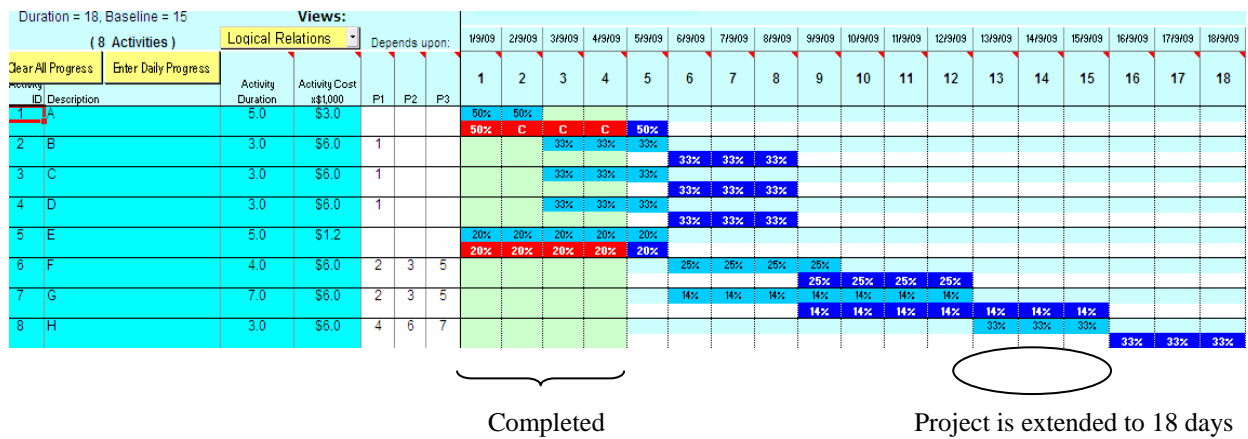


Figure 7: Actual Progress at the end of Day 4

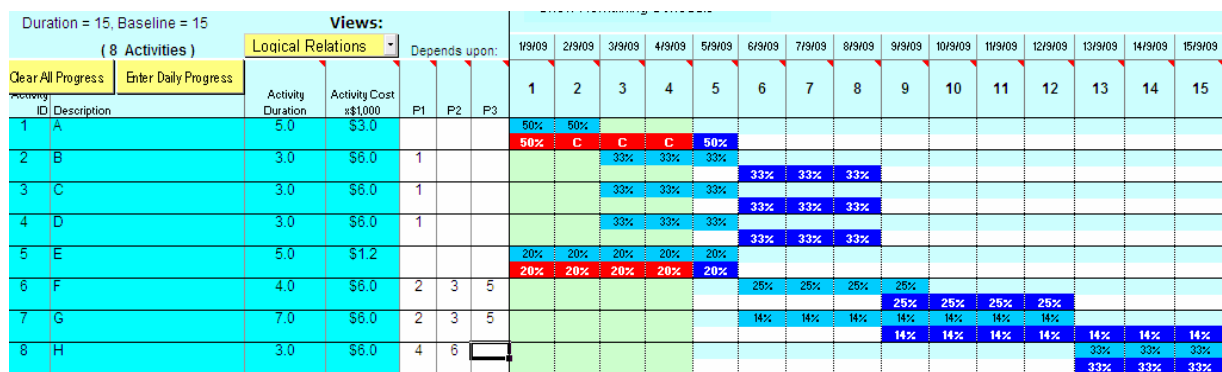


Figure 8: Project Schedule after a Change in the Logical Relations

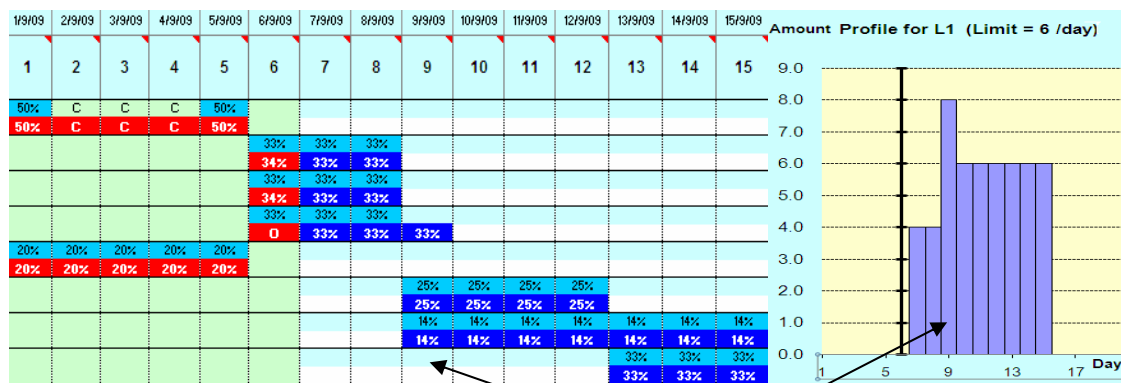


Figure 9: Actual Progress at the End of Day 5

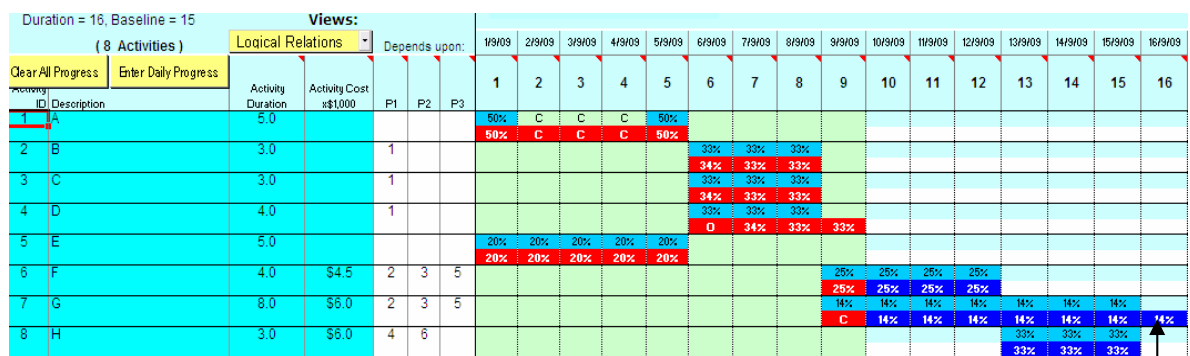


Figure 10: Actual Progress at the End of Day 9

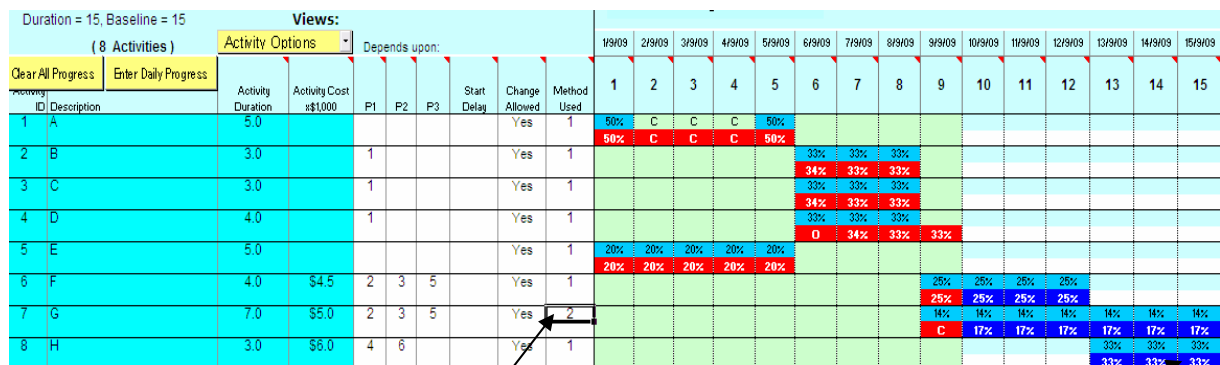


Figure 11: Changing the Method of Executing Activity G



Duration = 17, Baseline = 15				Views:																				
(8 Activities)				Logical Relations	Depends upon:			1/9/09	2/9/09	3/9/09	4/9/09	5/9/09	6/9/09	7/9/09	8/9/09	9/9/09	10/9/09	11/9/09	12/9/09	13/9/09	14/9/09	15/9/09	16/9/09	17/9/09
Clear All Progress	Enter Daily Progress	Activity Duration	Activity Cost \$1,000	P1	P2	P3	1	2	3	4	5	6	7	8	9	10	11	12	13	14	15	16	17	
ID Description																								
1	A	5.0					50%	C	C	C	50%													
2	B	3.0		1			50%	C	C	C	50%	34%	33%	33%										
3	C	3.0		1								34%	33%	33%										
4	D	4.0		1								0	34%	33%	33%									
5	E	5.0					20%	20%	20%	20%	20%	0	34%	33%	33%									
6	F	7.0		2	3	5	20%	20%	20%	20%	20%				25%	25%	25%	25%						
7	G	9.0		2	3	5									C	17%	17%	17%	17%	17%	17%			
8	H	2.0		4	6										C	17%	0	C	17%	N	17%	33%	16%	
																			33%	33%	33%		70%	30%

Figure 12: Actual progress at the end of Day 17

Main Screen File Project Resources Utilities Quick Jumps Help

Excel Menu
Indirect Cost Estimation
Competitor Analysis and Markup Estimation
Site Layout Optimization
Delay Analysis

But-For Analysis
Windows Analysis

Baseline vs Actual
Current Date: (17) 17/9/2009
Cost = \$10,850, Baseline \$ = \$16,250

Duration = 17, Baseline = 15

Windows Analysis

Project As-Built Duration (days) = 17.0
Compensable Owner delays (O) = 0.50, Owner Acceleration = 0.50.
Contractor nonexecusable delays (C) = 5.00, Contractor Acceleration = 4.50.
Execusable other party delays (N) = 1.50.

OK

Figure 13: Summary of Delay Analysis Results

Chapter Five Case Study 1 - Notepad	Cumulative Results	Expected Duration
<p>Analysis of days 5 to 9. A new baseline has been entered.</p> <p>Day: 5 (Saturday, Sep 5 2009)</p> <p>The new baseline saves 3 days, which will be credited as Contractor.</p> <p>Previous Duration = 15.0</p> <p>Current Duration = 15.0</p> <p>Compensable Owner delays (O) = 0.00, Owner Acceleration= 0.00.</p> <p>Contractor delays (C) = 3.00, Contractor Acceleration= 3.00.</p> <p>Excusable delays (N) = 0.00.</p> <p>Considering Resource Allocation:</p> <p>Current Duration = 15.0</p>	<u>New Baseline with 3 contractor accelerations</u>	15
<p>Day: 6 (Sunday, Sep 6 2009)</p> <p>Previous Duration = 15.0</p> <p>Current Duration = 15.0</p> <p>Compensable Owner delays (O) = 0.00, Owner Acceleration= 0.00.</p> <p>Contractor delays (C) = 3.00, Contractor Acceleration= 3.00.</p> <p>Excusable delays (N) = 0.00.</p> <p>Considering Resource Allocation:</p> <p>Current Duration = 16.0</p> <p>Modified (N) Delay= 1.00</p>	<u>Effect of Resource over-allocation</u>	16
<p>Day: 7 (Monday, Sep 7 2009)</p> <p>Previous Duration = 15.0</p> <p>Current Duration = 15.0</p> <p>Compensable Owner delays (O) = 0.00, Owner Acceleration= 0.00.</p> <p>Contractor delays (C) = 3.00, Contractor Acceleration= 3.00.</p> <p>Excusable delays (N) = 1.00.</p> <p>Considering Resource Allocation:</p> <p>Current Duration = 16.0</p>	<u>No Change</u>	16
<p>Day: 8 (Tuesday, Sep 8 2009)</p> <p>Previous Duration = 16.0</p> <p>Current Duration = 16.0</p> <p>Compensable Owner delays (O) = 0.00, Owner Acceleration= 0.00.</p> <p>Contractor delays (C) = 3.00, Contractor Acceleration= 3.00.</p> <p>Excusable delays (N) = 1.00.</p> <p>Considering Resource Allocation:</p> <p>Current Duration = 16.0</p>	<u>No Change</u>	16

Figure 14: Daily Windows Analysis Results of the Second Baseline (Days 5 to 8)

م.م. محمد حسان جيل
قسم الكهروميكانيك
الجامعة التكنولوجية

م.م. امير عبد جدوع
قسم الكهروميكانيك
الجامعة التكنولوجية

د. ابتسام احمد حسن
قسم الكهروميكانيك
الجامعة التكنولوجية

_____:

(Φ)

(m_A)

. ($10^6 \leq Ra \leq 3.96 \times 10^6$)

(m_A)

(δ)

($\Phi=90^\circ$)

(m_A)

. ($\Phi=180^\circ$)

EXPERIMENTAL STUDY FOR A NATURAL CONVECTION HEAT TRANSFER FROM AN ISOTHERMAL HEATED RECTANGULAR PLATE

ABSTRACT

An experimental investigation to know the effect of inclination angle (Φ), perforation ratio (m) and heating level on the rate of heat transfer by natural convection from isothermal rectangular flat plate (with and without rectangular hole) with extension surface. The experiments covered the laminar region with a range of Rayleigh number of order of 10^6 .

The experimental study included the manufacturing of four rectangular models of aluminum (125mm) length, (64mm) width and (10mm) thickness and perforation ratio ($m=0.0, 0.2 \& 0.28$) respectively with heater for each model, and manufacturing a device allow fine movement of the thermocouple in three dimensions above the models surface with a capability of inclination the models up to (180°) with horizon. Practical Experiments achieved by using local measure method for finding the temperature gradient, thermal boundary layer thickness (δ) using thermocouples. The experiment has been done with variable inclination angle from horizon ($0^\circ, 30^\circ, 90^\circ, 145^\circ \& 180^\circ$) and four heating level ($T_w=50, 70, 90 \& 110^\circ\text{C}$) in range of Grashof number ($1.632 \times 10^6 \leq Gr_{Lo} \leq 5.973 \times 10^6$) for each model.

The results show that the boundary layer thickness (δ) decrease while the temperature gradient increase when Grashof number and perforation ratio (m) increase. The boundary layer thickness (δ) for incline position facing upward is more than facing downward while the temperature gradient is less. The average Nusselt number increases with the increase of inclination of plates facing upward to reach to the higher average Nusselt number at vertical position then decreases with increase of inclination of plates. Also Average Nusselt number value increases with increase of perforation ratio and Grashof Number.

KEY WORDS: Natural convection, Rectangular plate, inclination angle.

$$4 \times 10^7$$

$$(180^\circ - 0^\circ)$$

(Kobus

C.J.&Wedekind G.L. 2001)

$$5.2 \leq d \leq 19.97 \text{ mm}$$

$$(9.6 \text{ cm})$$

$$(180^\circ - 0^\circ)$$

(Pera

L.& Gebhart B.1973)

(Waheed A.M. 2001)

(Mohammed J.A. 2002)

(Ali Th. H. 2007)

$$(2^\circ, 4^\circ, 6^\circ)$$

(Wassan N. M. 2009)

(m_A)

(AL

Arabi M.&Riedy M.1976 , AL Arabi M.& Sakr B.
1988)

)

(



(m_A)
(L₀=94.5mm)
(z) 1C
()
1.55×10⁶)
(5.88×10⁶≤Gr_{L0}≤
:
50 °C -)
(70 °C -90 °C -110 °C
Φ 90°,145°,180°)
(=0°,30°,
1
(10 mm) ()
(125 mm) (64mm)
(m_A = 0, 0.2 ,0.28)
 $\left(\frac{dT}{dz}\right)_{z=0}$

(T)

(Fourier's Law)

(U)

()

(Cairnie L.R. &

Harrison A.J. 1982)

$$-k_f \frac{dT}{dz} \Big|_{z=0} = h (T_w - T_\infty) \quad (1)$$

(X,Y & Z)

(1)

.180 ° 0°

:

$$h = \frac{-k_f \frac{dT}{dz} \Big|_{z=0}}{(T_w - T_\infty)} \quad (2)$$

(±0.09)

y x

y

$$\beta = 1/T_f$$

$$\bar{h} = \frac{1}{A} \int_A h \cdot dA \quad (3)$$

اما المتغيرات اللابعدية الاخرى فقد تم تعريفها كما يلي :

$$Gr_{L_0} = \frac{g\beta(T_w - T_{\infty})L_0^3}{\nu^2} \quad Pr = \nu/\alpha \quad Nu_{L_0} = \frac{h \cdot L_0}{k_f} \quad (4)$$

$$Ra_{L_0} = Gr_{L_0} \cdot Pr \quad : \quad (4) \quad (2)$$

$$Nu_{L_0} = \frac{-L_0 \frac{\partial T}{\partial z} \Big|_{z=0}}{(T_w - T_{\infty})} \quad (5)$$

$$Nu_{L_0} = \frac{d\theta}{dz} \Big|_{z=0} \quad (6)$$

(Z-X & (Z-) ()
(Φ =0° 30° 90° 145° 180°) Y)
Φ) .(Gr_{L0}=1.632×10⁶)
(=0°

$$\theta = \frac{T - T_{\infty}}{T_w - T_{\infty}} \quad Z = \frac{z}{L_0}$$

:

$$\overline{Nu}_{L_0} = \frac{1}{A} \int_A Nu_{L_0} \cdot dA \quad (7)$$

$$(\Phi = 90^\circ)$$

$$(\Phi = 180^\circ)$$

$$(T_f)$$

$$(x\text{-axis})$$

$$(\Phi = 0^\circ \& 180^\circ)$$

$$T_f = \frac{T_w + T_{\infty}}{2} \quad (9)$$

 (δ) $(\Phi = 180^\circ)$

4 3

 $(\Phi = 0^\circ)$ $(m_A = 0.2)$ $(m_A = 0.28)$

6,7

 $(Z-Y)$ $(\Phi = 0^\circ)$ $(\Phi = 0^\circ)$ $(\Phi = 30^\circ)$ $(\Phi = 90^\circ)$ $(\Phi = 180^\circ)$ $(\Phi = 145^\circ)$ $(\Phi = 90^\circ)$

(

 $(\Phi = 180^\circ)$

8,9&10

 $(Z-X \text{ \& } Z-Y)$

5

 $(\Phi = 0^\circ)$ $(X-Y)$ (δ) $, 4.856 \times 10^6, 5.973 \times 10^6)$ $(\delta), (Gr_{Lo} = 1.632 \times 10^6, 3.732 \times 10^6)$

)

 (δ) $(\Phi = 0^\circ)$ $(\theta = 0.02)$

()

 $(\Phi = 90^\circ)$ (δ) $(\Phi = 145^\circ)$ $(\Phi = 30^\circ)$

y-)

(x-axis)

14

$$(\delta)$$
 (δ) $\cdot (\Phi = 180^\circ)$ (δ) $(\Phi=90^\circ)$

($m_A=0.28$)

$$.(5.973 \times 10^6)$$

(m=0.28)

 $\cdot (^{\circ}\Phi=90)$

90°

$$(\Phi)$$
 (m_A) (Gr_{Lo})

$$\overline{Nu}_{L_p} = C_1 \times Ra^n \quad (10)$$

($m_A=0.28$)

 $(\Phi=90^\circ)$

n

C₁

0.2

 $(\Phi=180^\circ)$

(STATISTICA 6.0)

$$\left(\begin{array}{cc} & \end{array} \right) \quad \mathbf{12} \quad \mathbf{1}$$
 C_1

13



Int.J.Heat & Mass Transfer . Vol. 16 , PP. 1131-1145.

Waheed A.M. (2001)

"Numerical and Experimental Study of Natural Convection Heat Transfer from Isothermal Horizontal Disks and Rings".M. Sc. Thesis Univ. Technology.

Wassan N. M. (2009)

"Numerical Study For A Three Dimensional Laminar Natural Convection Heat Transfer From An Isothermal Heated Horizontal And Inclined Square Plate And With A Circle Hole".M. Sc. Thesis Univ. Technology.

AL-Arabi M. & Riedy M. (1976)

"Natural Convection Heat Transfer From Isothermal Horizontal Plates of Different Shapes".Int. J.Heat & Mass Transfer . Vol. 19 , PP. 1399-1404.

AL-Arabi M. & Sakr B. (1988)

"Natural Convection Heat Transfer From Inclined Isothermal Plates".
Int. J.Heat & Mass Transfer . Vol. 31 , No. 3 , PP. 559-566.

Ali Th. H. (2007)

"Experimental Study For A Three Dimensional Laminar Natural Convection Heat Transfer From An Isothermal Heated Square Plate".M. Sc. Thesis Univ. Technology.

Cairnie L.R. & Harrison A.J. (1982)

"Natural Convection Adjacent To a Vertical Isothermal Hot Plate with a High Surface-To-Ambient Temperature Difference ".Int. J.Heat & Mass Transfer. Vol. 25, No. 7, PP. 925-934.

Goldstein R.J. & Lau K. (1983)

"Laminar Natural Convection From A Horizontal Plate And The Influence of Plate-Edge Extensions " .J.Fluid Mech. Vol.129 , PP.55-75.

Kobus C.J. & Wedekind G.L. (2001)

"An experimental investigation into natural convection heat transfer from horizontal isothermal circular disks". International Journal of Heat and Mass Transfer PP.3381-3384.

Mohammed J.A. (2002)

"Measurement Of Three Dimensional Natural Convection Heat Transfer From Discs And Rings Facing Upward And Downward At Constant Temperature"M. Sc. Thesis Univ. Baghdad

Pera L.& Gebhart B. (1973)

"Natural Convection Boundary Layer Flow Over Horizontal And Slightly Inclined Surfaces".

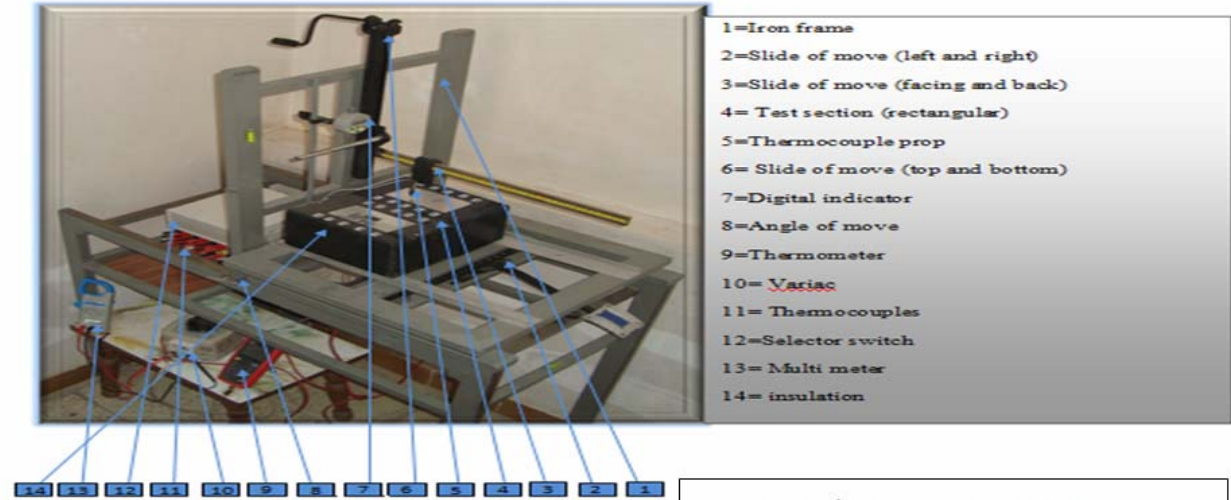
_____:

m^2		A
m		D
m/s^2	التعجيل الأرضي	g
		Gr_{Lo}
$W/m^2 \cdot ^\circ C$	معامل انتقال الحرارة الموضعي	h
$W/m^2 \cdot ^\circ C$	متوسط معامل انتقال الحرارة	\bar{h}
----) (m_A
----		Nu_{Lo}
----		$\overline{Nu_{Lo}}$
----		Pr
----		$R_{\square Lo}$
$^\circ C$		T
$^\circ C$	درجة حرارة الغشاء	T_f
$^\circ C$		T_∞
$^\circ C$		T_w
m		w
m		x, y, z
m^2/s		α
$1/K$		β
Degree		Φ
m^2/s		v
kg/m^3		P
----		θ
mm		δ

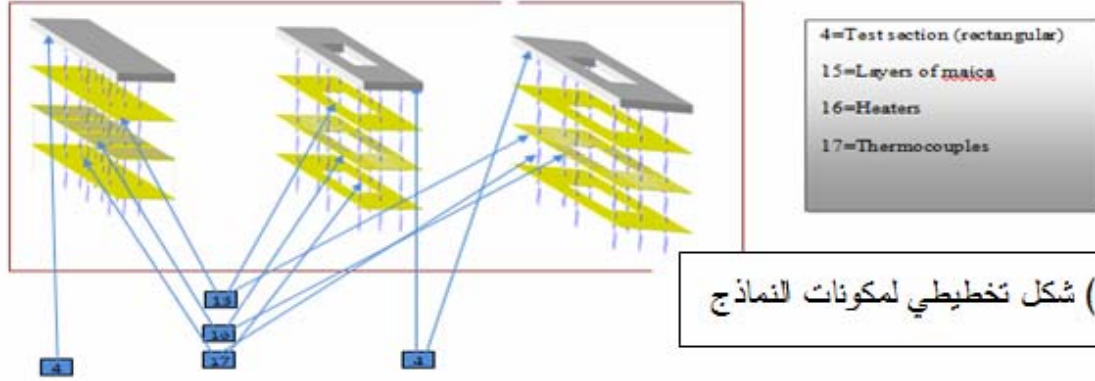


جدول (1) العلاقة بين متوسط رقم نسلت ورقم رالي.

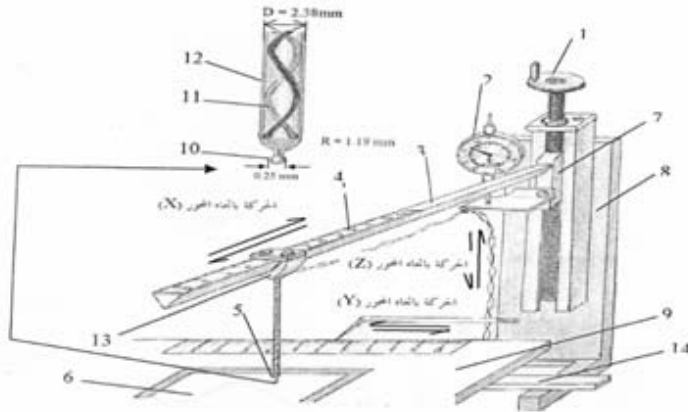
\equiv	\equiv	\equiv	
$Nu_{L0}=1.526 \times Ra_{L0}^{0.2}$	$Nu_{L0}=1.474 \times Ra_{L0}^{0.2}$	$Nu_{L0}=1.274 \times Ra_{L0}^{0.2}$	$\square=90^0$
$Nu_{L0}=1.497 \times Ra_{L0}^{0.2}$	$Nu_{L0}=1.422 \times Ra_{L0}^{0.2}$	$Nu_{L0}=1.212 \times Ra_{L0}^{0.2}$	$\square=145^0$
$Nu_{L0}=1.332 \times Ra_{L0}^{0.2}$	$Nu_{L0}=1.294 \times Ra_{L0}^{0.2}$	$Nu_{L0}=1.119 \times Ra_{L0}^{0.2}$	$\square=30^0$
$Nu_{L0}=0.949 \times Ra_{L0}^{0.2}$	$Nu_{L0}=0.949 \times Ra_{L0}^{0.2}$	$Nu_{L0}=0.949 \times Ra_{L0}^{0.2}$	$\square=0^0$
$Nu_{L0}=1.222 \times Ra_{L0}^{0.2}$	$Nu_{L0}=1.164 \times Ra_{L0}^{0.2}$	$Nu_{L0}=0.871 \times Ra_{L0}^{0.2}$	$\square=180^0$



(1A) صورة للجهاز المختبري مع أجهزة القياس

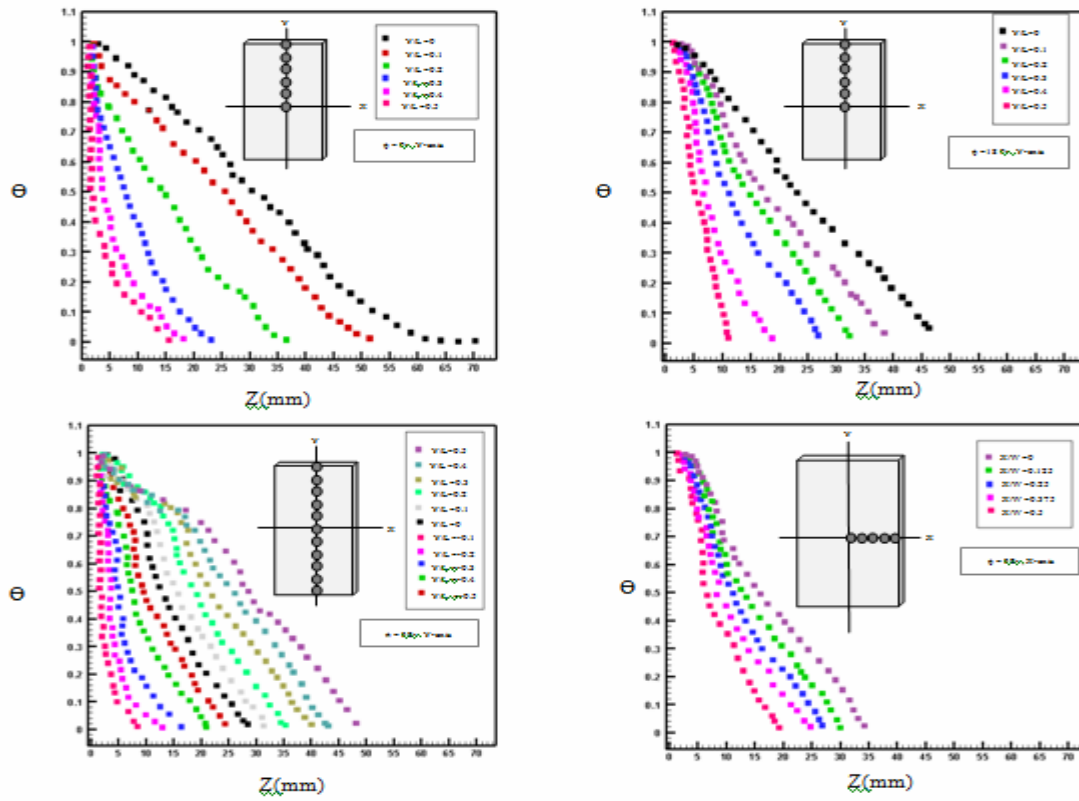


(1B) شكل تخطيطي لمكونات النموذج



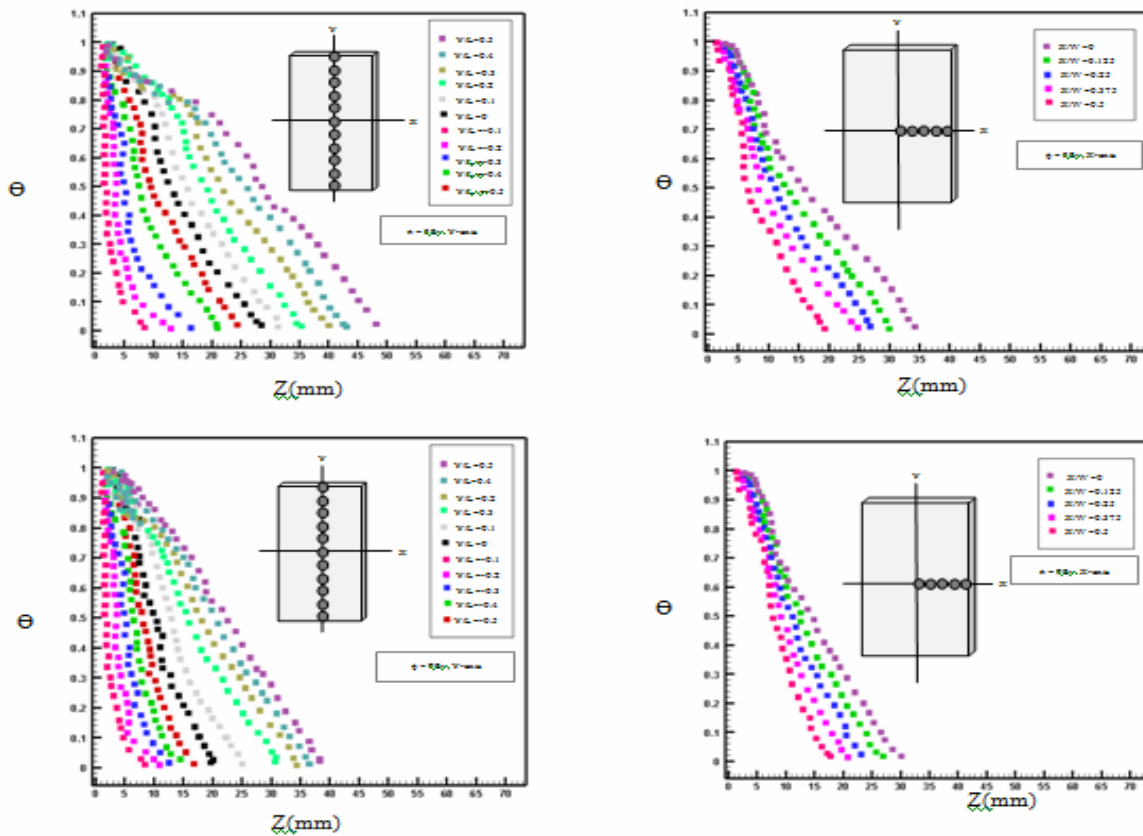
(1C) شكل تخطيطي للجهاز

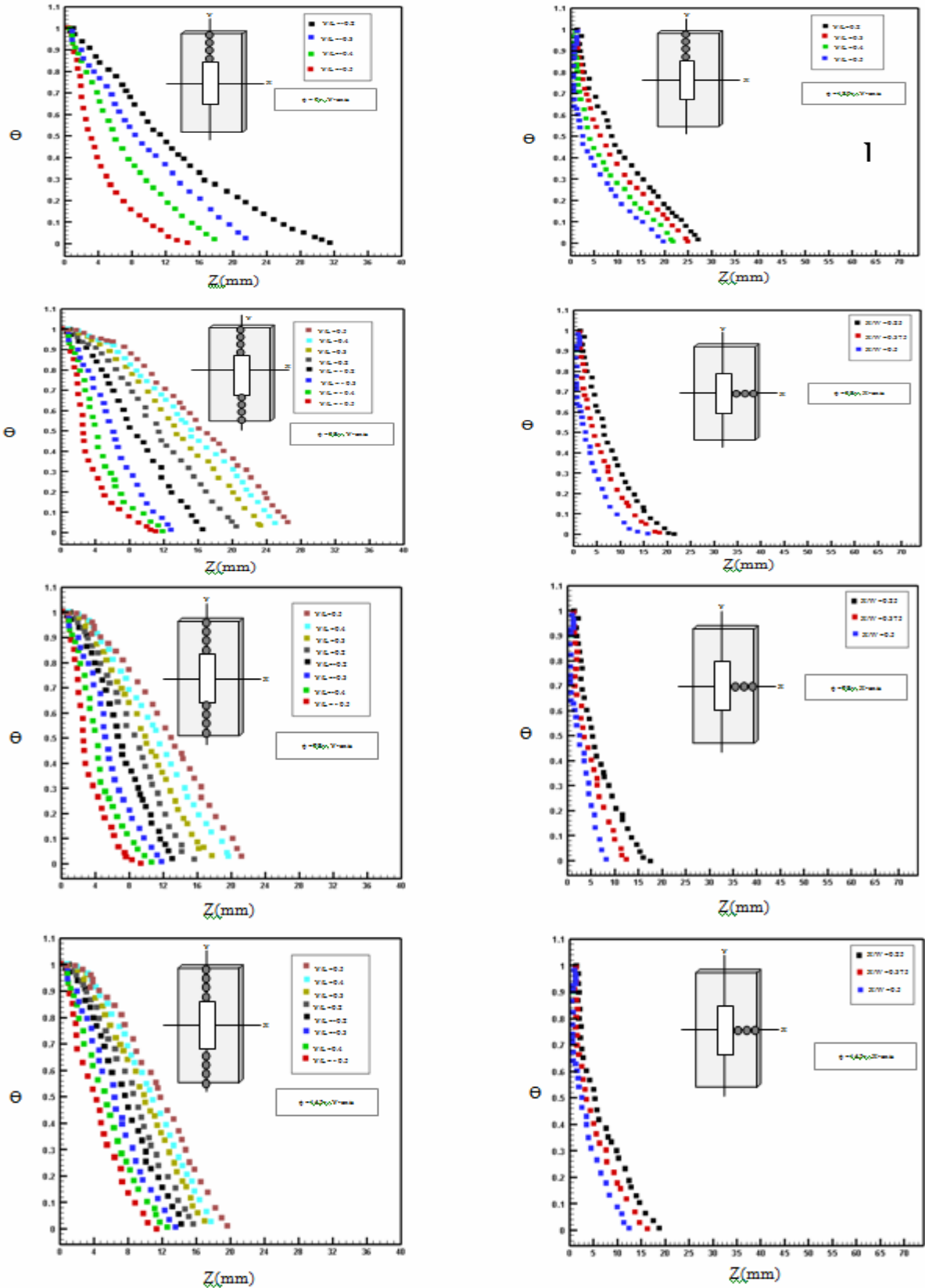
الشكل (1) يوضح أجزاء الجهاز المختبري المستخدم لأجراء القياسات الخاصه بالبحث



$Gr_{Lo} = 1.632 \times 10^6$

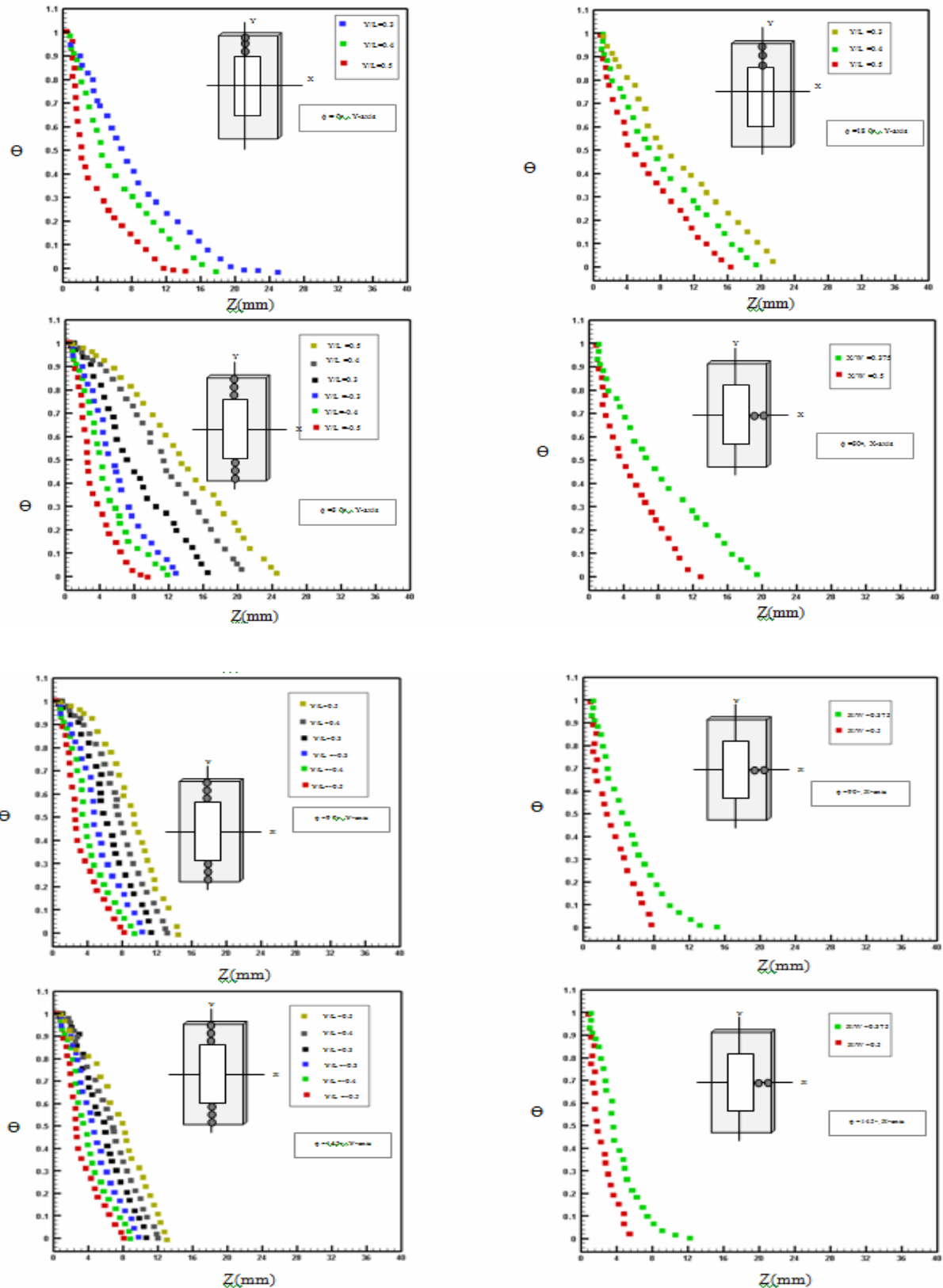
(2)





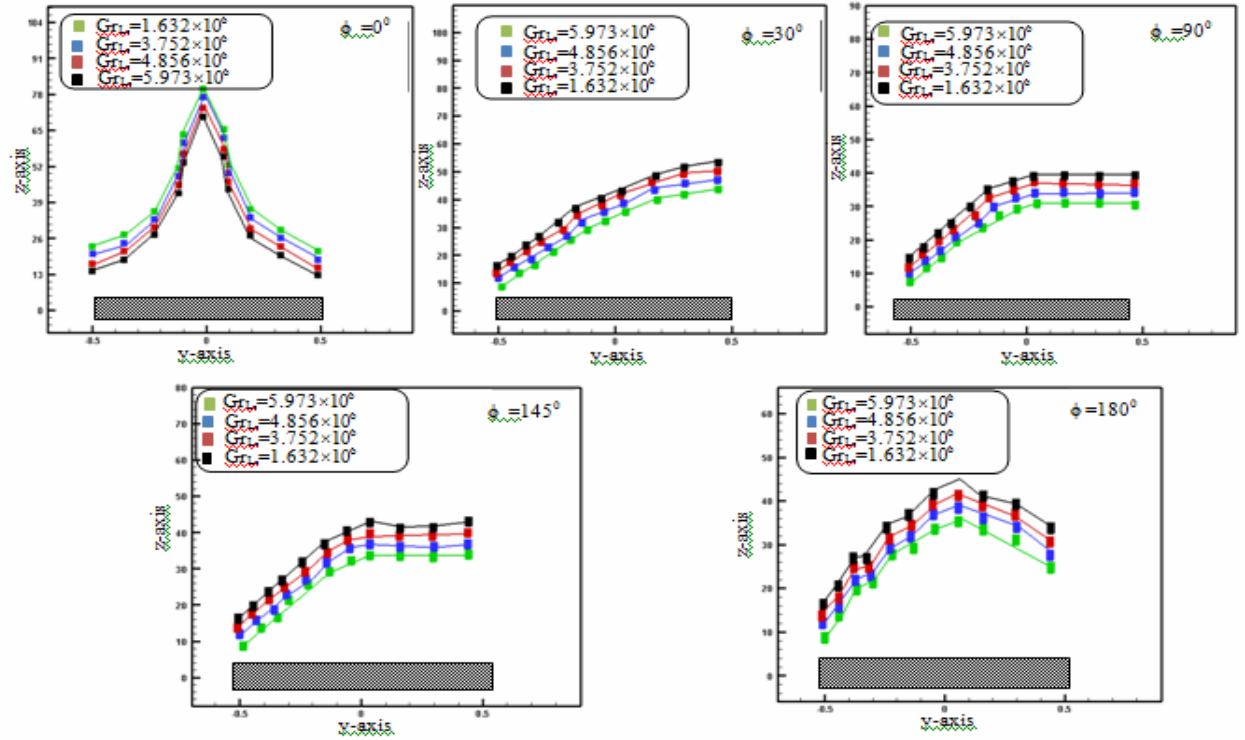
(3)

$$Gr_{Lo} = 1.632 \times 10^6$$

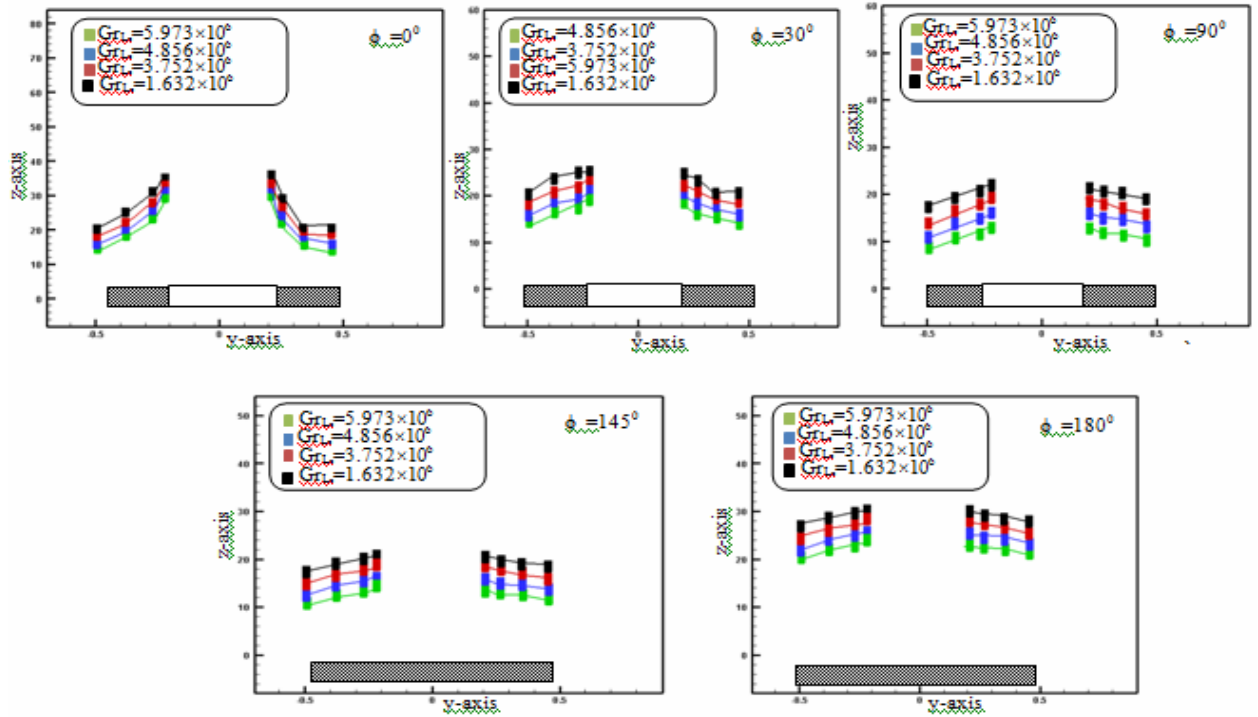


(4)

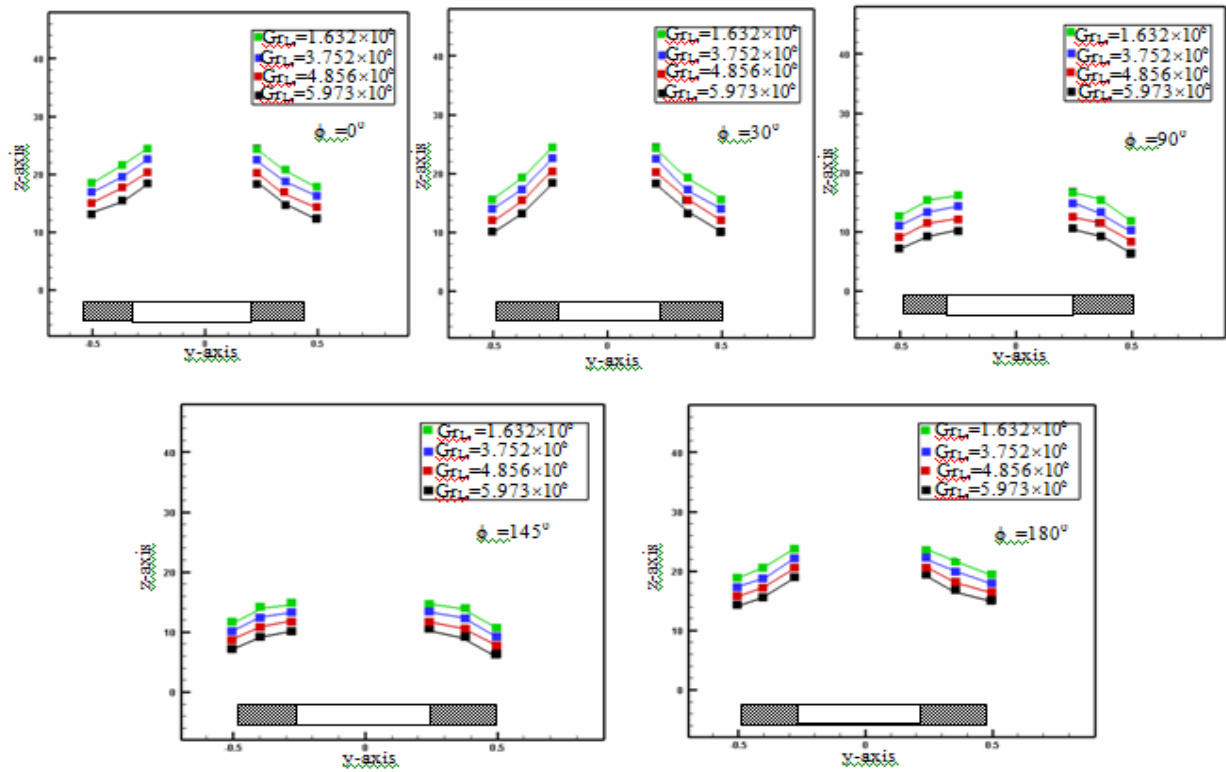
$$Gr_{Lo} = 1.632 \times 10^6$$



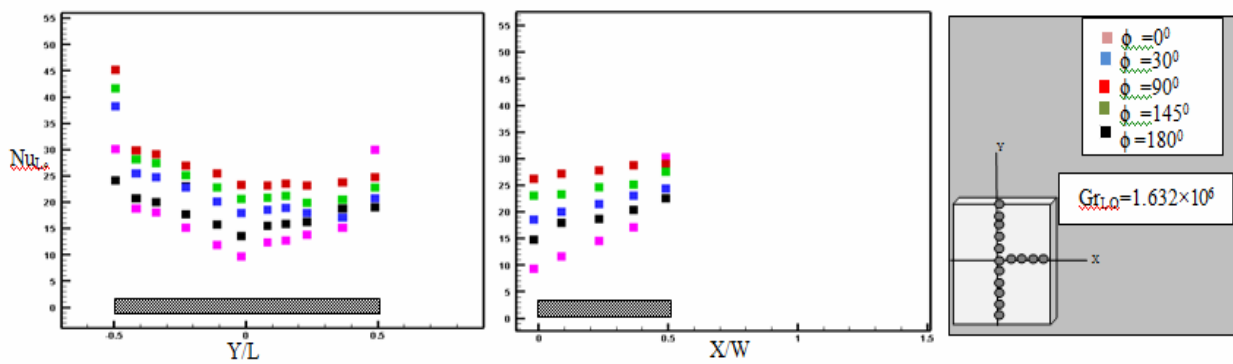
(5)



(6)

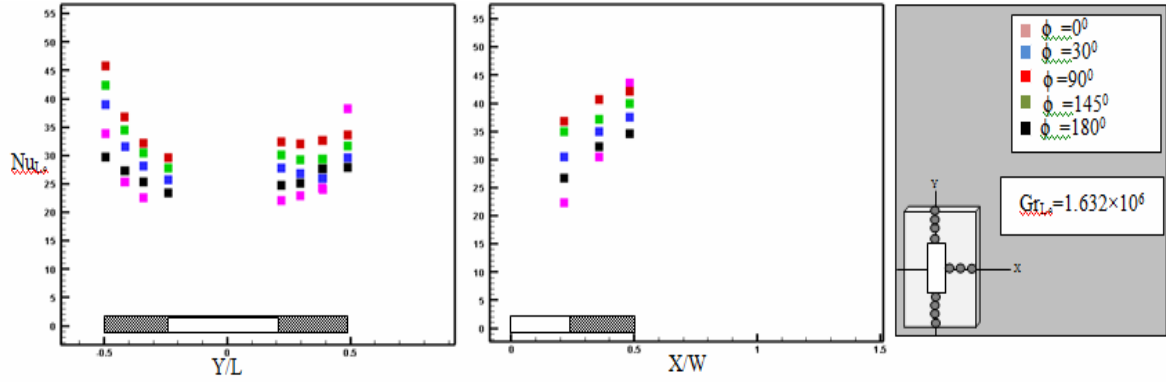


(7)



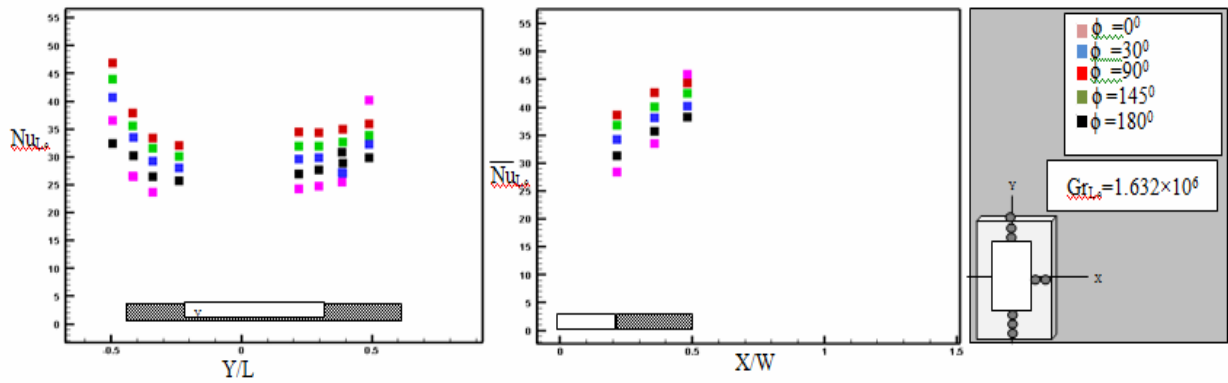
(8)

$$Gr_{L0} = 1.632 \times 10^6$$



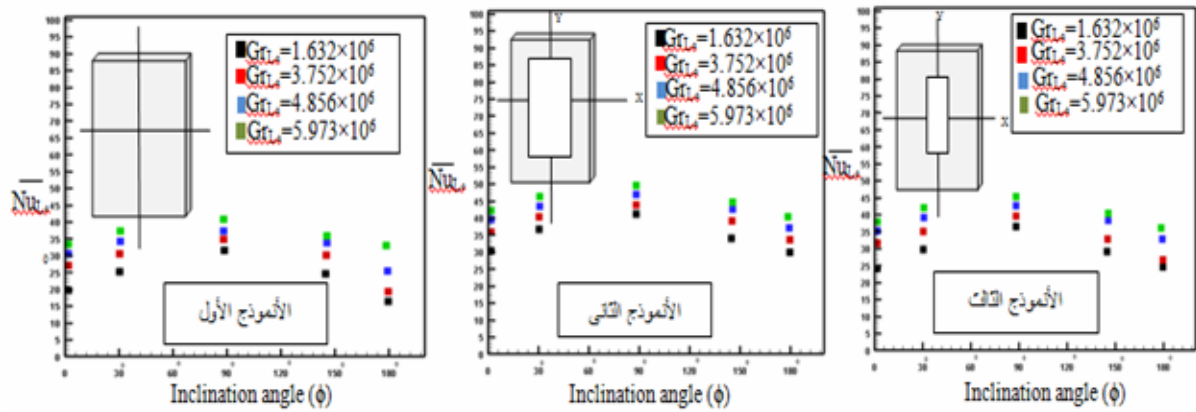
(9)

$$Gr_{Lo} = 1.632 \times 10^6$$

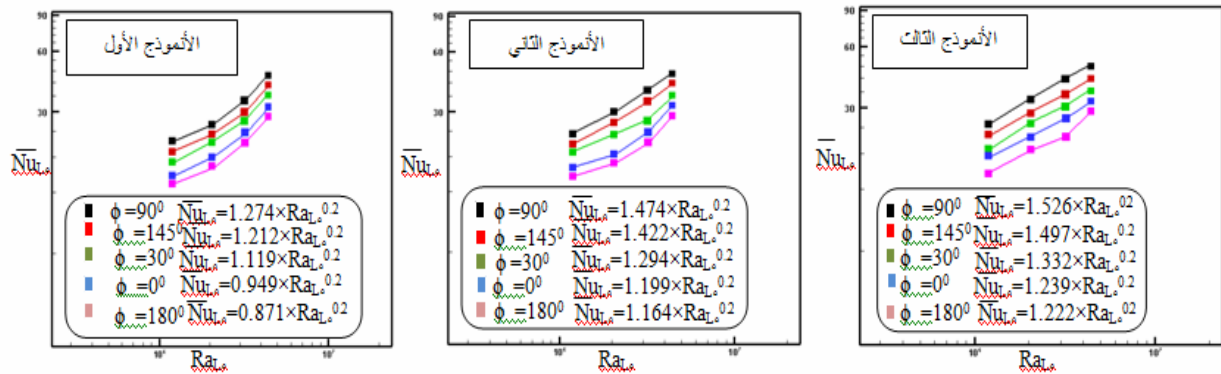


(10)

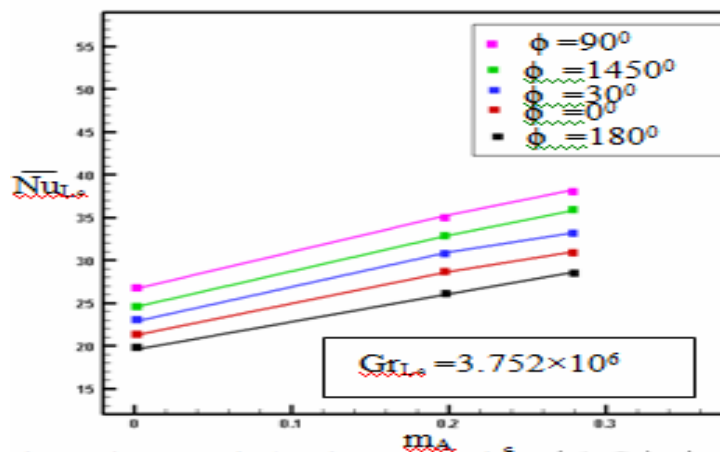
$$Gr_{Lo} = 1.632 \times 10^6$$



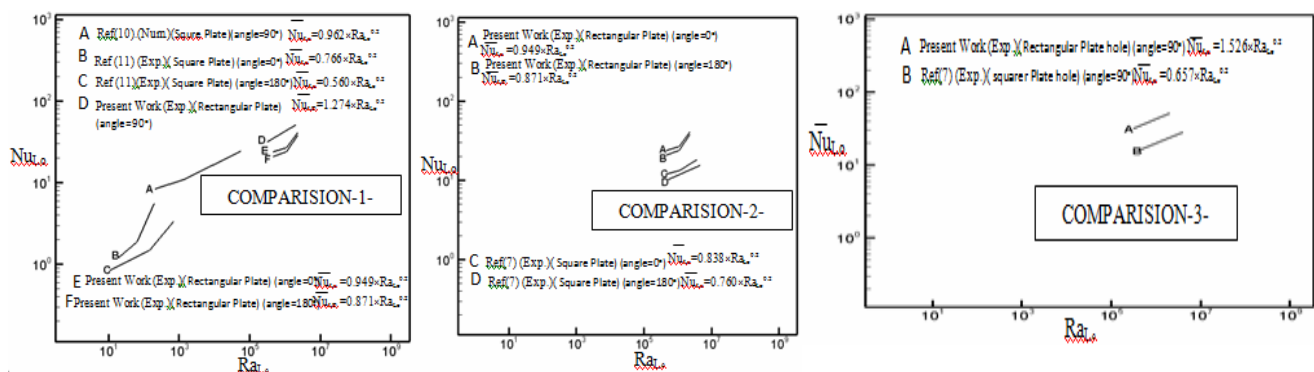
(11)



(12)

 (m_A)

(13)


$$((3 \& 2 \ 1)14)$$



()

بان قيس كبه
قسم الهندسة المعمارية \ جامعة بغداد

غادة موسى رزوقي
استاذ مساعد
كلية الهندسة \ جامعة بغداد

50 (2005).

THE SOCIETY IMPACT ON ARCHITECTURE

ABSTRACT

Designed spaces are usually left unobserved for academic purposes, after they have been brought to physical form, thus there is no broad knowledge base as to how the end user interacts with these spaces depending on certain functional needs and wants. It has been discovered through observation that the vast majority of designed spaces - even smaller scale ones- are very likely to endure alterations. Hence it has proven easier to follow up with and record these architectural alterations within residential projects where living spaces can be changed due to simple and less complex family decisions.

Previous readings of social and sociological type literature with relation to family forms and nature have revealed that there are clear limitations to knowledge involving the effects of society on architectural changes due to the absence of detailed information concerning the impact of social phenomenon on alterations in the architecture of modern Baghdad homes during the past five decades]. Baghdad is perhaps the foremost city in Iraq that has been affected by social changes, firstly, due to it's being the [political and economical] capital of the country and therefore the first in line to absorb changes as opposed to other governorates. Secondly, these alterations in architecture are much clearer in Baghdad due to major political and economical changes which have been witnessed during these past fifty years, changes which have in turn affected the city's social contexts, thus leading to architectural alterations.

Based on the abovementioned reasons, this research aims to prove the existence of a social impact on architectural alteration by:

- Clarifying indications of changes within society in general.
- Clarifying indications of changes within architecture in general.
- Finding the link between both, the architectural and social phenomenon and their directions.
- Showing evidence of changes within Iraqi society in general and within the Iraqi family specifically.
- Showing evidence of changes within Iraqi architecture in general and within Baghdad houses specifically.
- Clarifying the impact of family social changes on the practical manner of living and the designed spaces of residential houses.

The research begins with the exploration of previous related studies of the main variables:

(Society and architecture) and the link between them. After consuming the problem and expressing its aims, the thesis heads towards the exploration of the main aspects: Society, by studying social phenomenon and architecture, by studying its contents and process of change. After the comparison of these two variables, the thesis comes to a sub-conclusion that architectural phenomenon is part of social phenomenon, which leads us to the main discussion of the research, a study of the main events that have affected Iraqi society and the nature of the Iraqi individual, focusing on changes within the Iraqi family as the main unit of society as a whole. The investigation then moves on to changes in the ideas of the Baghdad house. Points should be taken during the course of the study with regards to the elements which represent the main changes in these houses, namely: rearrangement of spaces, adding/subtracting areas, renewals and the moving. The theoretical frame work ends with a case study of 42 residential units in Baghdad and aspects of their social elements (independent factor) and the architectural changes (dependant factor), thus bringing the thesis to its conclusion.

This research does not attempt to provide a description of these houses based upon a certain period of time, but rather why they have come to be the way they appear and the social aspects affecting their appearance.



المقدمة

()

() ()

() -

()

()

()
()

:

*

:

) **50**

.(

(54 1999).

:

:

■

).

■

(35 1987

■

:

:

(48 1987).

-



()

()

(Sorokin,1972,p130)

: Hypothetical Deduction

-

- : (36 1987) .

-

Light

" "

(Lobell,2000,p42) Silence

-

(Encyclopedia of the 20th Century Architecture ,1963,p166))

()

غادة موسى رزوقي)
بان قيس كبه	(

)
 (1999 63)
 (

:
 ()

.
 :
 :
 •
 ()

:
 أ.
 :

ب.



ج.

(
)

(
)
(
)

:"

•

1957

.(Zoning)

—



:()

-

=

=

;

•

() .

.()

()

•

-()

:

.()

-

-()

-

_____.

(42)

:

:()

-

:

:()

-

:

-

غادة موسى رزوقي)
بان قيس كبه	(

•

plan open

_____:

()

•

— :

)

(

() •

•

%70

Kitchenette



عدد تغير متطلبات الدار قاموا بالاستعانة بمكتب الجادرجي والذي كان موقوفاً في حينها فأوصت المهمة الى معماري مكتبه، ولم يرض الجادرجي على التصميم المقترح مع كونه يتواءم مع متطلبات صاحب الدار أولاً وروحية المنشأ المصمم ثانياً، السبب نجده عندما قرأ الطرح الفكري الذي يقوله المصمم في كتاب الاخوضر والقصر البلوري حيث يصف لنا متعة مشاهدة جدار هذا المنزل المحرزي الشابيك المعبرة عن التجربة العالي لفكرة الدار.

وعندما اضيفت المساحة المقترحة للدار الغيت تماماً هذه الفكرة بالإضافة الى مد خط تصريف مياه الامطار على هذا الجدار بالاذن، هنا نجد التباين بين غاية اصحاب الدار وغاية المصمم بالرغم من التقارب الفكري العالي فيما بينهما.

رقم العينة	نوع الأسرة	المنطقة	الوظيفة	الشخص بعدد الأفراد	الادخل	حالة الدار	مساحة الدار م ²	نوع التحويل	سنة التحويل	اسبابه التحويل
22	نوعية	الجادرية	مهندس	بدءاً: 1	عالي	مستقرة	400	اضيف قاطع لغرفة الرياضة لتصبح غرفة نوم بعد مرض رب الأسرة	1976	زواج الابن والرغبة بالاستقلال
				حالياً: 7						



غادة موسى رزوقي)
بان قيس كبه	(

	•	:	—
—			
—	—	—	—
•			
()		
		:	
—		:	—
•			
—	—	:	—
()		
•		:	—
—			—
—			•
)	•		
	(
		:	
	•		
:			%100
:	—		
			()
			.()
:	—		
			•



(adaptations)

()

(

(Extension)

•
()

•

()

()

•



ان طبيعة الحياة التي يعيشها افراد عوائل هذه المنطقة هي لا تختلف كثيراً عن الحياة التي كان يعيشها البغداديون في بداية القرن الحالي، فلا تزال الروابط الأسرية والعلاقات بين افراد العائلة الواحدة والعادات الاجتماعية كما كانت سابقاً، وهذا ما نجده منعكساً في مخططات دورهم.

فهي لا تزال تبني بذات النمط المغلق من التمازج والمفتوح للدخول خدمة للمتطلبات الاجتماعية والوظيفية لسكانها، فلا تزال التنوير ولا تزال المرحاض الشرقي التمازجي ولا تزال الدوخانة -او حجرة الضيوف للرجال، والعكس سكان -او حجرة تجمع النساء، فالبيئة الاجتماعية للمنطقة نجدها منعكسة وبوضوح على الانشاء المعماري للدور السكنية في المنطقة.

رقم العينة	نوع الاسرة	المنطقة	الوظيفة	التغير بعدد الافراد	الدخول	حالة الدار	مساحة الدار م ²	نوع التخوير	منته	اسبابه التخوير
4	مركبة	الثورة	موظف صحي	بدءاً: 11	واطيء	متفادئة	144	اضيفت غرفة وهول	1995	زيادة عدد الساكنين
				حالياً: 13						





-2

- -

•

"

"

80

•

"

"

غادة موسى رزوقي
بان قيس كبه



المساحات الممنعة الجميلة أصبحت والأسف غير مستخدمة فصاحبة الدار تستخدم المطبخ الخمار للجلوس ومعلقة الفطور الغداء والعشاء وفضاء المعيشة الاضائي كفضاء رئيسي للجلوس . وبذلك فان مربع مساحة الدار هي المستخدمة فعليا .





1995

)

(289

_____ :

.1989

.1987

.1995

.1999

.1987

- Encyclopedia of 20th Century Architecture, Thames & Hudson, world of art, New York, 1989.
- Lobell, John. Between Silence & Light spirit and Architecture of Louis Kahn, shamb hala. London, 2000.



— Sorokin, P., Social Mobility, New York, Harper and Brothers 1972